2015

Surface Functionalized Magnetic Nanoparticles for Cancer Therapy Applications

Robert J. Wydra
University of Kentucky, wydrar@gmail.com

SURFACE FUNCTIONALIZED MAGNETIC NANOPARTICLES FOR
CANCER THERAPY APPLICATIONS

DISSERTATION

A dissertation submitted in partial fulfillment of the
requirements for the degree of Doctor of Philosophy in the
College of Engineering
at the University of Kentucky

By
Robert John Wydra

Lexington, Kentucky

Director: Dr. J. Zach Hilt, Associate Professor of Chemical & Materials Engineering

Lexington, Kentucky

2015

ABSTRACT OF DISSERTATION

SURFACE FUNCTIONALIZED MAGNETIC NANOPARTICLES FOR
CANCER THERAPY APPLICATIONS

Despite recent advances, cancer remains the second leading cause of deaths in the United States. Magnetic nanoparticles have found various applications in cancer research as drug delivery platforms, enhanced contrast agents for improved diagnostic imaging, and the delivery of thermal energy as standalone therapy. Iron oxide nanoparticles absorb the energy from an alternating magnetic field and convert it into heat through Brownian and Neel relaxations. To better utilize magnetic nanoparticles for cancer therapy, surface functionalization is essential for such factors as decreasing cytotoxicity of healthy tissue, extending circulation time, specific targeting of cancer cells, and manage the controlled delivery of therapeutics.

In the first study, iron oxide nanoparticles were coated with a poly(ethylene glycol) (PEG) based polymer shell. The PEG coating was selected to prevent protein adsorption and thus improve circulation time and minimize host response to the nanoparticles. Thermal therapy application feasibility was demonstrated *in vitro* with a thermoablation study on lung carcinoma cells.

Building on the thermal therapy demonstration with iron oxide nanoparticles, the second area of work focused on intracellular delivery. Nanoparticles can be appropriately tailored to enter the cell and deliver energy on the nanoscale eliminating individual cancer cells. The underlying mechanism of action is still under study, and we were interested in determining the role of reactive oxygen species (ROS) catalytically generated from the surface of iron oxide nanoparticles in this measured cytotoxicity. When exposed to an AMF, the nanoscale heating effects are capable of enhancing the Fenton-like generation of ROS determined through a methylene blue degradation assay. To deliver this enhanced ROS effect to cells, monosaccharide coated nanoparticles were developed and successfully internalized by colon cancer cell lines. Upon AMF exposure, there was a measured increase in cellular ROS and apoptosis that was attributed to lysosomal disruption since the surface functionalization selected inhibited the Fenton-like surface chemistry. To overcome this surface inhibition, a biodegradable poly(β-amino ester) (PBAE) polymer coating was synthesized to deliver bare iron oxide to intracellular components. Delivering

enhanced ROS to cancer cells is a promising new route of therapy that deserves future studies.

  Robert John Wydra
Student's Signature

  May 1, 2015
Date

SURFACE FUNCTIONALIZED MAGNETIC NANOPARTICLES FOR
CANCER THERAPY APPLICATIONS

By

Robert John Wydra

Dr. J. Zach Hilt
Director of Dissertation

Dr. Thomas Dziubla
Director of Graduate Studies

ACKNOWLEDGEMENTS

Table of Contents

List of Tables

List of Figures

Chapter 1: Introduction

This dissertation investigates the development of tailored novel nanomaterials for cancer therapy. The core nanoparticle utilized was iron oxide which has been previously studied for a wide range of biomedical applications. Iron oxide nanoparticles have the unique physical property of being able to remotely heat when exposed to an alternating magnetic field (AMF). This heat can be used as a standalone therapy, a component of a combination therapy, or be used to activate the release of drug molecules from thermo-responsive matrices. To better utilize this property, appropriate surface functionalization must be performed. This research builds off of two basic platforms previously developed in our lab: co-precipitation synthesis of uncoated iron oxide nanoparticles and one-pot addition of stabilizing molecules to the surface of these nanoparticles. These core nanoparticles were further modified with polymers through atom transfer radical polymerization and surface attachment and biomolecules – monosaccharide and glycerol lipids. Chapter 2 presents a background on the range of polymeric coating used in core-shell architectures to increase stability, decrease toxicity, extend circulation time, and manage the controlled release of therapeutics.

Despite recent advances, development of cancer therapeutics remains one of the most important challenges facing biomedical researchers today. To combat this disease, a multi-modal treatment strategy is often utilized and thermal therapy usually represents one potential aspect of the strategy. Thermal therapy is the process of elevating tumor tissue temperature for therapeutic gains and has been studied for decades, but it has yet to gain widespread clinical recognition either as an independent treatment or in conjunction with traditional therapies. Two temperature ranges have been identified: hyperthermia, 40-45

°C, and thermoablation, ≥46 °C. Hyperthermia can induce cellular death on its own, but it is better suited for enhancing the effects of chemotherapy and/or radiation therapy. Due to the elevated temperature, thermoablation leads to direct cell necrosis and can be used as an independent treatment. Magnetic fluid hyperthermia involves using the remote heating property of magnetic nanoparticles to deliver heat in a controlled localized area. An in depth discussion on the mechanics of hyperthermia and recent advances in magnetic mediated energy delivery can be found in chapter 3. In order to successfully deliver magnetic nanoparticles to the tumor surface, surface modification is necessary. Poly(ethylene glycol) (PEG)-based functionalization is common for biological applications as a means to prevent protein adsorption and thus improve circulation time and minimize host response to the particles. In chapter 4, core-shell nanoparticles were prepared using atomic transfer radical polymerization to coat iron oxide with PEG-based polymer shell. They were developed to achieve thermal therapy that can ablate cancer cells in a remotely controlled manner.

Despite clinical interest in magnetic fluid hyperthermia, researchers have faced a major barrier in that a large ratio of nanoparticles to surrounding cells is necessary to achieve the required elevated temperature. Thus, it is generally considered only applicable for direct injection into solid tumors. Recently, Creixell et al. have created new excitement in the field by demonstrating that targeted nanoparticles that have been internalized by cancer cells can induce cellular death when exposed to an AMF without a measurable temperature rise. Instead of relying on bulk heating, nanoparticles can be specifically tailored to enter cells minimizing potential damage to surrounding tissue. Additionally, this technology raises the possibility of targeting micrometastatic sites previously considered

untreatable.   Understanding the underlying mechanisms of this intracellular energy delivery is one of the provocative questions facing researchers in the field.   In addition to heating effects from the local temperature rise, other chemical effects or mechanical damage from the physically rotation and vibration of nanoparticles in the field may induce toxicity.   One potential chemical effect would be the result of surface mediated production of reactive oxygen species (ROS).   ROS is considered one of the culprits of concentration dependent iron oxide cytotoxicity.   In chapter 5, the effects of an AMF on surface ROS generation was explored.   Using a methylene blue assay, an increase in degradation was observed when a suspension of magnetic nanoparticles was exposed to an AMF indicating there was an increase in the ROS generation in response to the field.   To demonstrate this result *in vitro* nanoparticles functionalized with monosaccharides was explored in chapter 6.   Monosaccharides can provide a level of passivation similar to PEG or polysaccharide coatings while targeting cancer cells which typically over express glucose transporters. While intracellular ROS increased with internalized nanoparticles, the coatings inhibited surface ROS generation meaning the measured cellular effect was due in part to lysosomal disruption.   Lastly, nanoparticles coated with biodegradable polymer coatings were prepared in chapter 7.   The nanoparticles consist of an iron oxide core and biodegradable polymer shell developed to maximize the potential surface reactivity for ROS generation. When tuned properly, such a platform can be combined with targeting ligands to increase treatment efficacy.

1.1. Specific Objectives

The overall objective of this research was to develop novel nanomaterials (i.e., functionalized iron oxide nanoparticles) for cancer therapy. This involved four projects, and the specific objectives of these are outlined below:

1. Synthesis and characterization of PEG-iron oxide core-shell composite nanoparticles for thermal therapy applications

    a. Synthesize core-shell nanoparticles utilizing atom transfer radical polymerization techniques

    b. Perform physiochemical characterizations to verify successful coating

    c. Investigate cytotoxicity by exposing two cell lines to nanoparticles systems

    d. Demonstrate the ability of the core-shell nanoparticles to ablate cancer cells to demonstrate therapeutic potential

2. Accelerated generation of free radicals by iron oxide nanoparticles in the presence of an alternating magnetic field

    a. Synthesize and characterize uncoated iron oxide nanoparticles

    b. Determine the kinetic behavior of the Fenton-like surface chemistry to generate free radicals using a methylene blue degradation assay

    c. Analyze the kinetic data to determine an Arrhenius relationship

    d. Demonstrate an enhancement in ROS generation through AMF exposure

3. The role of ROS generation from magnetic nanoparticles in an alternating magnetic field on cytotoxicity

    a. Synthesize glucose functionalized iron oxide nanoparticles

    b. Perform physiochemical characterizations to verify successful coating

  c. Determine the uptake rate and localization pattern in cancer cells

  d. Demonstrate cellular ROS enhancement with AMF exposure

  e. Investigate surface reactivity of coated nanoparticles

4. Synthesis and characterization of magnetic nanoparticles with biodegradable polymer coatings for the treatment of cancer

  a. Synthesize poly(β-amino ester) for coating

  b. Attach biodegradable coating to nanoparticle surface

  c. Perform physiochemical characterizations to verify successful coating

  d. Determine effects of coating on surface ROS generation

Chapter 2: Polymeric Coatings and Additives on Nanoparticles for Biomedical Applications

2.1. Introduction

Surface modification plays an essential role in determining the successful application of nanoparticles by improving stability, preventing agglomeration, improving biocompatibility, and providing additional functionalities such as targeting and drug release. In recent years, nanoparticles have been studied for a wide range of biomedical applications including enhanced imaging, drug delivery, thermal therapy of cancer, and as bioprobes and sensors. Core-shell architectures allow researchers to combine multiple functionalities on a single nanoparticle. A common example is an inorganic core that is selected for its unique physical properties that is coated with an organic shell that improves the colloidal stability while reducing the core nanoparticle toxicity. However, researchers have been striving for the ultimate goal of a nanosized "smart bomb", where a carefully designed nanoparticle is capable of being safely delivered to the body, carrying its drug payload to a specific location, and only releasing the drug at the target location to minimize any systemic effects [1]. This chapter will focus on the different uses of polymeric coatings in core-shell nanoparticles. Briefly, common core particles and synthesis techniques will be introduced. The different functionalities of the polymeric shell will be discussed, specifically their role in improving colloidal stability, reducing nanoparticle toxicity, increasing circulation time, active targeting, and controlling different mechanisms of drug loading and release.

2.2. Core Nanoparticle Systems

When designing a nanoparticle system for drug delivery, it is of particular interest to select the appropriate core. As highlighted in the introduction, spherical core-shell nanoparticles are of major interest as a way of combining different physicochemical properties from the core and shell materials. In the following section, commonly utilized core nanoparticles will be briefly described.

2.2.1 Magnetic Nanoparticles

Magnetic nanoparticles are the focus of much research due to their many biomedical applications, such as targeted delivery, magnetic resonance imaging (MRI), and the thermal therapy of cancer [2-5]. Magnetic nanoparticles have the unique physical property of being able to remotely heat when exposed to an alternating magnetic field due due to the absorption of energy from the magnetic field and conversion into heat primarily through Brownian relaxation and Neel relaxation [6]. In addition to coating magnetic nanoparticles with a material to improve colloidal stability and biocompatibility, an additional concern is preventing the further oxidation of magnetic core altering its physical properties. In terms of drug delivery, magnetic nanoparticles are potential candidates for drug tracking with magnetic resonance imaging and the thermal delivery of a therapeutic agent.

2.2.2 Gold Nanoparticles

Similar to magnetic nanoparticles, gold is being studied by biomedical researchers for its potential use as a diagnostic or therapeutic agent as a result of its unique chemical and physical properties [7-10]. Gold is considered inert and non-toxic, and it is usually functionalized to carry out an intended biological application; in most cases a facile gold-

thiol surface chemistry is utilized. When irradiated with light, gold nanoparticles interact with the electromagnetic wave through a phenomenon called surface plasmon resonance (SPR). Through SPR, heat can be generated through electron-phonon and phonon-phonon interactions and this heat can act alone as a therapeutic or work to thermally trigger the release of a drug. The plasmonic peak, or excitation wavelength, can be controlled by engineering the shape and structure of the gold nanoparticle; the general structures are classified as spherical gold nanoparticles, gold nanorods, gold nanoshells and gold nanocages. For a detailed review on the role of structure on plasmonic properties, the reader is referred to the review article by M. Hu et al. [11].

2.2.3 Mesoporous Silica Nanoparticles

Mesoporous silica nanoparticles are currently being studied to serve as drug delivery systems based on their unique design. These silica nanoparticles have been templated with porous channels that can serve as potential drug carriers [12, 13]. Unlike magnetic and gold nanoparticles, which rely on a multifunctional platform, these particles are functionalized to better control drug adsorption and release from the pores. It should be noted that silica is considered relatively biocompatible and is sometimes used as a coating to reduce the toxicity of other inorganic nanoparticles [1].

2.3. Nanoparticle Architectures

Core-shell structures provide the opportunity to design nanoparticles with multiple functionalities. In general, core-shell nanoparticles can be prepared in one of two ways based on the way the polymer coating is applied to the surface. 'Grafting to' involves the addition of end functionalized polymers that interact with the nanoparticle surface. 'Grafting from' involves a controlled surface initiated polymerization, whereby an initiator

is bound to the nanoparticle surface and the polymer is grown from the surface. Schematic representations of 'grafting to' and 'grafting from' are illustrated in **Figure 2.1.**

2.3.1 'Grafting to'

In the 'grafting to' approach, the polymer chains are immobilized on the surface either through a chemical adsorption or physical adsorption. In the case of physical adsorption, the bond is non-covalent and therefore easily reversible and susceptible to removal by shear stress or other interactions [14]. Physical adsorption is usually carried out with block co-polymers where one chain segment has an affinity (e.g., electrostatic or hydrophobic interactions) for the nanoparticle surface. Because of the required chain segment, the ability to introduce functional groups is hampered, and a polymer may coat more than one particle introducing clusters [14, 15]. Chemical adsorption results when a covalent bond is formed between the reactive end group of the polymer chain and the nanoparticle surface. Since it is a covalent bond, the resulting functionalization is typically more stable than physical adsorption. Polymer orientation becomes a limiting factor as the end group has to come in contact with the surface. Both 'grafting to' approaches suffer from the limitation of low grafting density. As the polymer chains begin to adhere to the surface, steric crowding limits the possible reaction sites. Despite limitations, it should be noted that 'grafting to' is a very common technique selected for its simplicity of generating a multifunctional core-shell structure.

2.3.2 'Grafting from'

The 'grafting from' technique is a two-step process. First, the nanoparticle surface must be functionalized with initiator group. Depending on the substrate, a variety of known surface chemistries can be used (e.g., thiols on gold and silanes on glass) [14, 16]. A

solution containing catalyst and monomer will be added to the nanoparticles, and the initiator group will be transformed to a radical that is confined to the nanoparticle surface. The radical serves as the site of the polymerization, and the shell is propagated from the surface in a uniform and precise manner. The key advantage of a 'grafting from' approach lies in that the coating is constructed one monomer at a time allowing for a higher polymer density, up to 1 chain/nm2 and a variety of polymer combinations [17]. There are multiple surface initiated polymerization mechanisms utilized to create core-shell nanoparticles. Some of them will be highlighted below, but for an in depth description, the author recommends the following review articles [14, 16, 18-20].

One of the most extensively used surface initiated polymerization is metal catalyzed atom transfer radical polymerization (ATRP), which is selected for its compatibility with a wide range of monomers yielding polymers with low polydispersity indexes (PDI), less stringent experimental conditions, and remains end functionalized with the initiator for the synthesis of copolymers [14, 19]. During the reaction (see **Figure 2.2.a**), the reduction of the alkyl halide by a transition metal complex initiator generates a radical utilized in the propagation of the polymer. The radicals are deactivated by the oxidized form of the transition metal complex, and this reversible activation-deactivation allows control over the polymerization. Typically, the transition metal complexes are copper or iron based, and the initiators are either α-haloesters or benzyl halides.

Similar to ATRP, reversible addition-fragmentation chain transfer (RAFT) polymerization allows for the synthesis of a range of polymers with a narrow PDI and controlled end groups. The polymerization (see **Figure 2.2.b**) is controlled by the degenerative transfer by a dithioester agent. Conventional free radical initiators are used
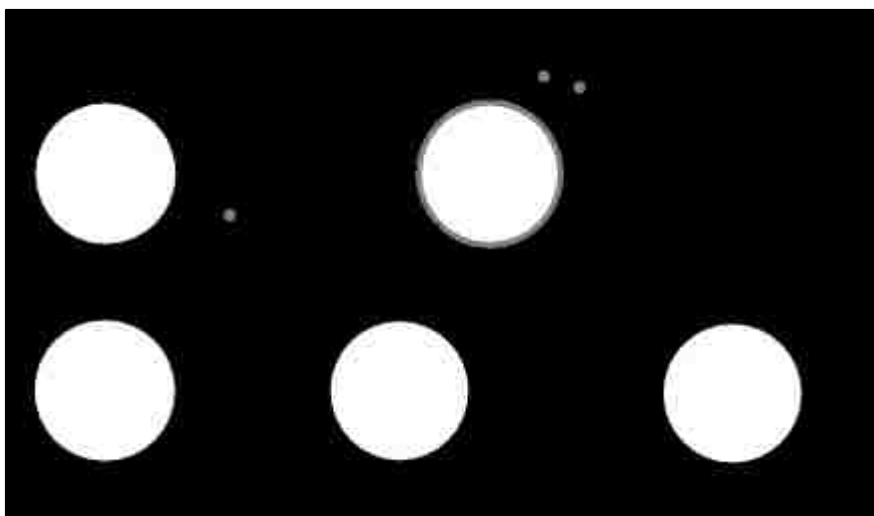
Figure 2.1. Schematic displaying the different surface functionalization methods: 'grafting to' (a) and 'grafting from' (b).
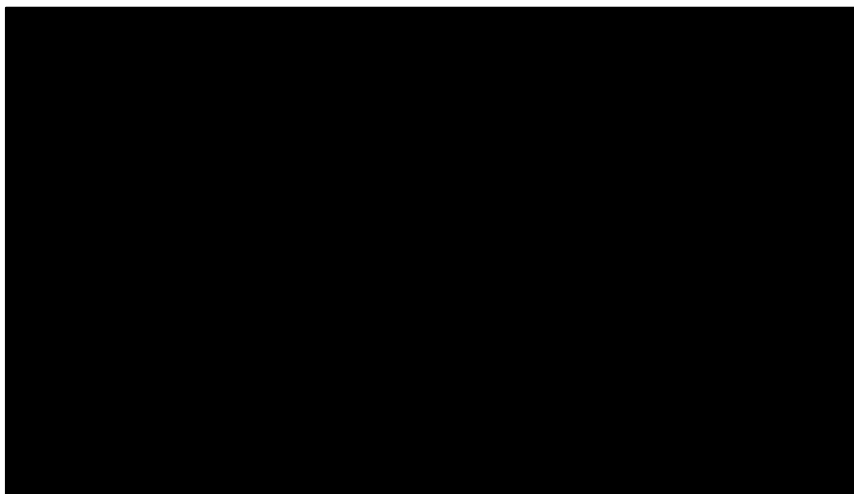
Figure 2.2. General reaction mechanism of (a) ATRP, where X = halogen, Y = transition metal complex, and Y^0 = oxidized form of the transition metal complex and (b) RAFT polymerization where X = transfer agent.

to generate the initial radicals that drive the reversible exchange mediated by the transfer agent.

2.4. Coating Functionality

2.4.1 Colloidal Stability

Nanoparticles, with their high surface area to volume ratio, are prone to aggregation and agglomeration issues unless addressed with a coating to provide colloidal stability. Colloidal stability additives either work by providing electrostatic repulsion (i.e., placing charged groups on the surface to repel nearby particles) or by steric repulsion (i.e., adding non-ionic materials to the surface to prevent surface contact with nearby particles). When selecting a polymeric material for steric stabilization, three factors must be addressed: surface density, layer thickness, and outer surface profile [21]. An illustration of the different surface coatings can be seen below in **Figure 2.3**. In the diagram, the local polymer concentration, denoted as ρ_2, is shown to change with distance away from the particle surface. Brush systems anchored to the surface (**Figure 2.3.a**) have the highest segment density, ρ_2, at the radius of gyration and trail off from there. Brush systems absorbed to the surface (**Figure 2.3.b**) have a higher density closer to the particle surface. Due to lower polydispersity of surfactant layers (**Figure 2.3.c**), the outer concentration profile sharply declines compared to polymeric systems.

Colloidal stability is modeled as the linear combination of the total energy of interaction. These interactions are generally separated into three contributions: attractive (V_A), electrostatic repulsion (V_R), and steric repulsion (V_S) [22]:

$$V_T = V_A + V_R + V_S \qquad \qquad \textbf{Equation 2.1}$$
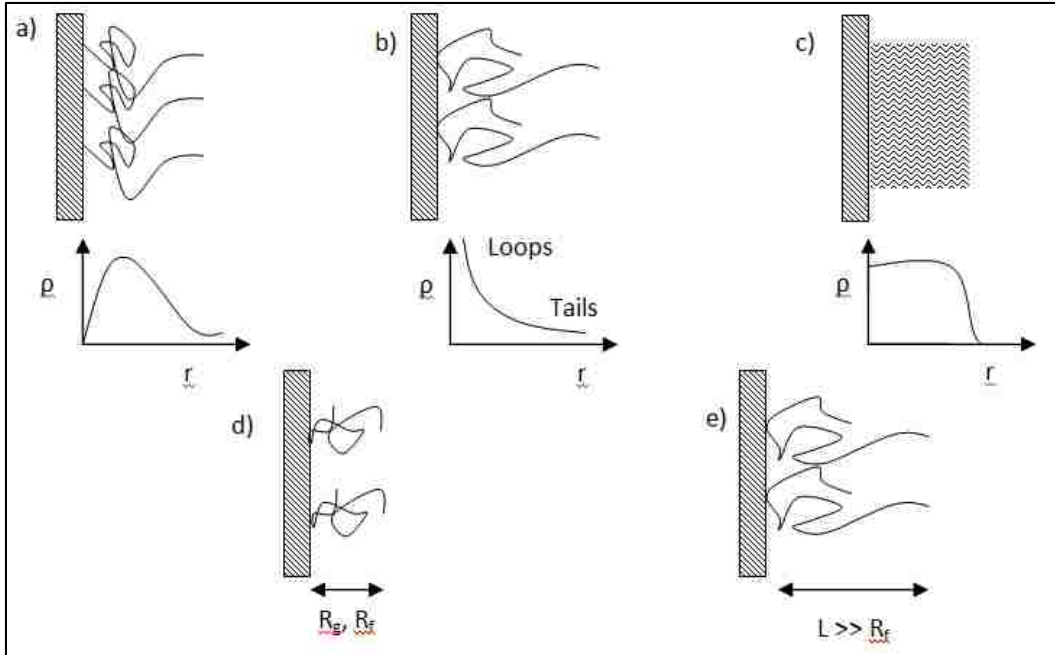
Figure 2.3. Illustration of polymer chains in solution near a surface: a) terminally anchored polymer; b) adsorbed chain; c) adsorbed surfactant layer; and the effects of surface coverage where the Flory radius is in the order of radius of gyration resulting in low coverage (d) and high coverage leading to a brush system (e).
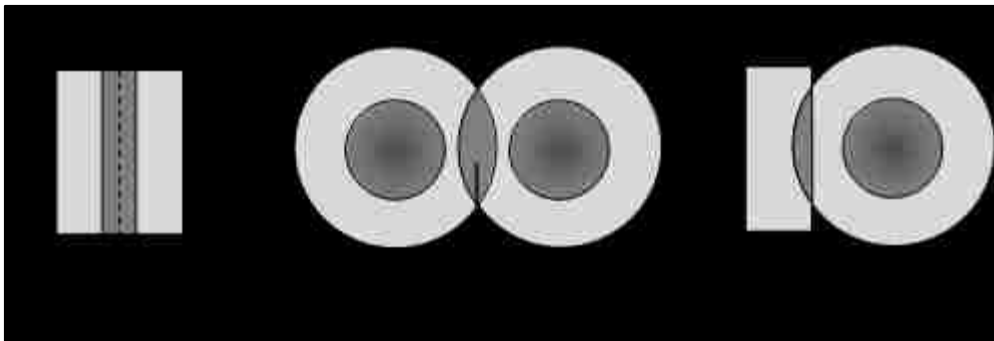
Figure 2.4. Illustration of overlap areas of polymeric stabilizers for a) plate-plate; b) sphere-sphere; and c) plate-sphere.

The classical DLVO theory for spherical nanoparticles neglects steric repulsion and assumes the sum of the electrostatic double layer repulsion and van der Waals attraction [21, 23, 24]. For spheres of identical radius, the van der Waals attraction term can be reduced to the following expression:

$$V_A = -\frac{A}{12H}\left[1 + \frac{H}{2a+H} + \frac{H}{a}\ln\left(\frac{H}{2a+H}\right)\right] \qquad \textbf{Equation 2.2}$$

Where A is the Hamaker constant, H is the closest distance between particle surfaces, and a is the particle radius. Two forms of the electrostatic repulsion are commonly used based on the value of κa, where κ is the inverse Debye length [24]:

$$V_R = 2\pi\varepsilon_r\varepsilon_0 a\psi_\delta^2 \ln[1 + \exp(-\kappa H)] \qquad \textbf{Equation 2.3}$$

$$V_R = 2\pi\varepsilon_r\varepsilon_0 a\psi_\delta^2 \exp(-\kappa H) \qquad \textbf{Equation 2.4}$$

where $\varepsilon_r\varepsilon_0$ is the dielectric permittivity and ψ_δ is the surface potential. **Equation 2.3** is for the case where $\kappa a > 10$, and **Equation 2.4** is for the case where $\kappa a < 5$. When polymer coatings are used for steric stability, the development of the interaction energy equation is of greater interest. **Figure 2.4** displays the overlap areas of different polymer coated surfaces with a thickness of δ and a separation distance of h. The chain concentration is denoted as c_2 and is twice as concentrated in the overlap area resulting in an osmotic pressure, Π_E, that acts to separate the particles. The interaction energy is defined as the integral of force within the overlap area [21]:

$$V_S = \int_{2\delta}^{h} -\Pi_E A dx \qquad \textbf{Equation 2.5}$$

The osmotic pressure can be expressed as a virial expansion in terms of the polymer concentration:

$$\Pi_E = RT\left(\frac{c_2}{M_2} + \left(\frac{\overline{v_2}}{M_2}\right)^2\frac{1}{v_1}(0.5\text{-}\chi)c_2^2 + ...\right) \qquad \textbf{Equation 2.6}$$

Where:

$$B_2 = \left(\frac{\bar{v_2}}{M_2}\right)^2 \frac{1}{\bar{v_1}} (0.5\text{-}\chi)$$ **Equation 2.7**

In the above equations, $\bar{v_1}$ and $\bar{v_2}$ are the molar volumes of the solvent and polymer respectively, M_2 is the number average molar mass, and χ is the Flory-Huggins interaction parameter. The integral of $A dx$ is the overlap volume, which is defined as v_o. Thus, **Equation 2.5** can be reduced to the following:

$$V_s = -(2v_o\Pi_{x=2\delta} - v_o\Pi_{x=h})$$ **Equation 2.8**

Substituting the two term virial expansion for the osmotic pressure gives the final form:

$$V_s = 2RTB_2 C_2^2 v_o$$ **Equation 2.9**

In the case of sphere-sphere interaction, the overlap volume can be defined as the following:

$$v_o = \frac{2\pi}{3} (\delta\text{-}H/2)^2 (3a+2\delta+H/2)$$ **Equation 2.10**

While the above model is relatively simplistic, it does provide insight on the factors that affect colloidal stability which include solvent properties (pH, ionic strength, and χ parameter), solution temperature, surface composition, particle size, and particle concentration.

Colloidal stability in blood is a major concern when designing a nanoparticle system for drug delivery. Preventing aggregation is keen since any particle over 200 nm will be readily cleared by the spleen [25]. Once the nanoparticles enter the vasculature, they will encounter cells, plasma proteins, and various electrolytes. Considering this environment, electrostatic repulsion stabilizers would be rendered relatively useless. The ionic concentration from the electrolytes would screen the electrostatic double layer reducing its potential as a barrier [23, 26]. An additional concern of electrostatic repulsion stabilizers is the increased detection by macrophages leading to reticuloendothelial system

(RES) clearance as nanoparticles of high surface charge, either positive or negative, are readily engulfed by macrophages [27].

A common stabilizing technique is the addition of poly(ethylene glycol) (PEG) based polymer brushes to provide both steric repulsion and stealth properties (discussed in the following sections) [28, 29]. Zhang et al. studied the effects of both conjugation chemistry and molecular weight of PEG on the colloidal stability of gold nanoparticles [29]. Typically, gold nanoparticles are conjugated with PEG through covalently attaching a thiol-terminated chain to the particle surface. An alternative route is to use PEG chains capped with thioctic acid which contains a cyclic disulfide. To evaluate the stability under physiological conditions, the nanoparticles were suspended in a solution of phosphate-buffered saline containing 10% fetal bovine serum at 37 °C while particle size was monitored with dynamic light scattering. The PEG coated systems experienced minimal change in particle size over the 48 hour period, and there was no change in trend from the low to high molecular weight PEG. However, the citrate coated particles which rely on electrostatic repulsion experienced a fivefold increase in particle size over a period of 10 minutes. Similar trends were observed for the 40 nm core nanoparticles; however the 80 nm core nanoparticles were less stable and experienced aggregation over 24 hours.

2.4.2 Biocompatibility

Biocompatibility is a broad term which has come to define an engineered system able to fulfill its intended application while minimizing unwanted interactions with the body. In the case of nanoparticle systems, toxicity is typically the critical factor in defining their biocompatibility [30]. Polymer coatings are added to nanoparticles to reduce their toxicity and help shield them from unintended biological interactions.

2.4.2.1 Poly(ethylene glycol)

One of the most widely studied polymers for biological applications is PEG. PEG is a synthetic hydrophilic polymer that is selected as a means to prevent protein adsorption and thus improve circulation time, which minimizes host response to nanoparticles, and this will be discussed further in the following section [31, 32]. Surface coatings of PEG, which is often referred to as PEGylated, can be arranged as simple polymer brushes extending from the surface or as a hydrogel, a crosslinked hydrophilic network.

For example, Gupta et al. have studied PEG-coated iron oxide and have evaluated their toxicity with both live-dead and MTT assays and effects on cell adhesion and morphology on human fibroblasts (hTERT-BJ1) [33, 34]. At concentrations up to 1.0 mg/ml, PEG-coated nanoparticles remained 99% viable and displayed favorable cell proliferation after a 24 hour period [34]. In comparison, uncoated particles observed a 25-50% decrease in viability starting at a concentration of 250 µg/ml. When studying cell adhesion and morphology, the uncoated particles exhibited a significant decrease in adhered cells and a disruption in cell membrane and disorganized cytoskeleton from endocytosis [33]. PEG-coated particles were still internalized, but they did not display the negative effects to morphology [33].

F. Hu et al. synthesized PEGylated iron oxide nanoparticles through a copper mediated atom transfer radical polymerization [35]. When mouse macrophage cells (RAW 264.7) were exposed to the PEGylated nanoparticles, the live cell count was determined to be >93% of the control indicating no toxic effect at 0.2 mg/ml concentration over a 5 day period. In comparison, uncoated iron oxide nanoparticles observed a 30% loss in viability by the second day, but by the fifth day, the viability improved to 90%.

Studying the amount of particles internalized, the uncoated iron oxide decreased from 154 pg/cell to 58 pg/cell over the 5 days, while the PEG-coated remained less than 2 pg/cell. Due to cell division, the number of cells would have increased resulting in a lower amount of particles internalized per cell.

While the gold surface is considered inert, the surfactant used in synthesis of gold nanorods, hexadecyltrimethylammonium bromide (CTAB), is toxic and remains present on the surface [36]. Three approaches were identified as ways to minimize the toxic effect of CTAB: removal of excess CTAB through centrifugation or filtration, overcoat with a polyelectrolyte such as polystyrene sulfonate (PSS), or through PEGylation. Rayavarapu et al. measured the toxicity using a MTS assay of four independent cell lines exposed to a range of concentrations of as-prepared gold nanorods, filtered nanorods to partially remove CTAB, PSS treated, and PEG-thiol coated. The as-prepared and filtered nanorods displayed 100% death at all concentrations tested. At low concentrations, the PSS treated nanorods had viabilities of 80+% for all cell lines. As the concentration increased, the viability decreased which the authors attributed to desorption of the PSS-CTAB complex from aggregation. Except for one cell line (human leukemia, HL60), the PEGylated particles displayed high viabilities and can be considered nontoxic. The authors performed viability studies and determined dose dependent curves on four independent cell lines: human mammary adenocarcinoma (SKBR3), Chinese Hamster Ovary cells (CHO), mouse myoblast (C2C12), and HL60. The LC50 of the HL60 cell line was 103 pM which is considerable higher than the other nanorod systems. HL60 also displayed lower LC50 values from exposure to the other nanorod systems suggesting it is a less robust cell line. Rayavarapu et al. also observed that the PEGylated nanoparticles were the most colloidally

stable, and the PSS treated and possibly other polyelectrolytes aggregated upon exposure to cell culture media.

2.4.2.2 Poly(vinyl alcohol)

In addition to PEG, poly(vinyl alcohol) (PVA) is another synthetic polymer commonly synthesized as a hydrogel. PVA hydrogels are stable and elastic and can be formed by either physical or chemical crosslinking [31]. Physically crosslinked PVA hydrogels are considered biocompatible and thus have multiple biomedical applications, especially in the field of drug delivery.

An interesting example of the use of PVA coated nanoparticles comes from Petri-Fink et al. where cell interaction and cellular uptake was preferred since it is required in drug delivery [37]. PVA was selected for its ability to form a hydrogel through the hydrogen bonding between chains to provide steric repulsion. Hydrogen bonding also forms between the hydroxylated surfaces of the iron oxide nanoparticles and the polymer chains resulting in an absorbed hydrogel shell. In this study, four variations of PVA were tested to determine which has the most potential interaction with human melanoma cells: unmodified PVA, vinyl alcohol/vinyl amine copolymer, PVA with a random distribution of carboxylic acid groups, and PVA with a random distribution of thiol groups. First, Petri-Fink et al. determined that only the amine modified PVA coated nanoparticles displayed significant interaction by the melanoma cells over 24 hours. Cytotoxicity analysis, measured with a MTT assay, showed that PVA, carboxyl modified PVA, and thiol modified PVA coated nanoparticles were non-toxic at 2 and 24 hours. After 2 hours, the amine modified PVA coated nanoparticles displayed no toxicity at all the polymer/iron ratios tested. However, at 24 hours, the high polymer concentration displayed toxicity. By
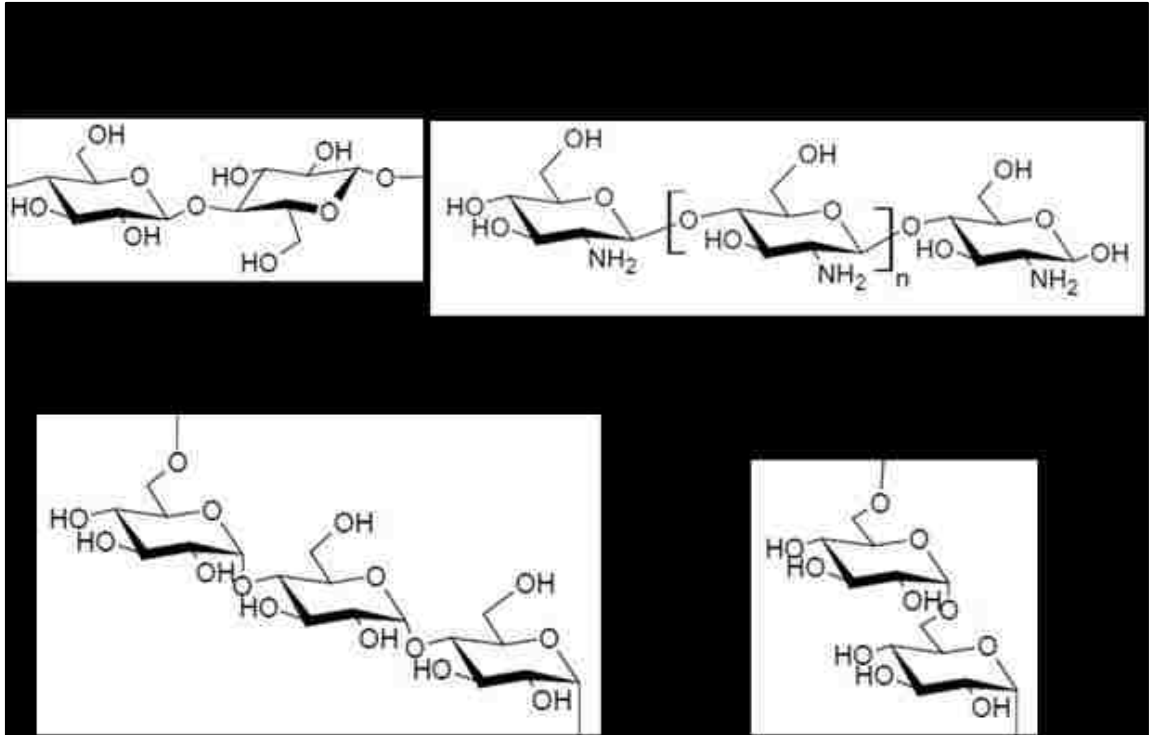
Figure 2.5. Structures of cellulose, dextran, pullulan, and chitosan; note the location of the glycosidic bonds of the glucose unit.

understanding the interaction mechanism, iron oxide shells can be further modified for a range of biomedical applications.

2.4.2.3 Polysaccharides

Natural occurring polysaccharides have been explored as potential coatings to reduce the toxicity of core nanoparticles in addition to PEG or other synthetic polymers. Common polysaccharides utilized for coatings include cellulose, dextran, pullulan, and chitosan; the structures can be found below in **Figure 2.5** [38, 39]. Besides being selected for improving biocompatibility, polysaccharides have the potential for selectively targeting organs or tissues based on recognition of the molecular structure [40].

Iron oxide nanoparticles are a popular candidate for polysaccharide coatings, and currently, dextran coated iron oxide nanoparticles are approved by the FDA for MRI contrast agent use [41]. Dextran molecules can be attached to the surface of iron oxide through various methods, such as the common methods where it is physically adsorbed followed by crosslinking or adsorbed through carboxyl modification to facilitate interaction with iron atoms on the particle surface [42]. However, when placed in phosphate buffer saline solutions, these particles tend to aggregate due to the displacement of the dextran by the phosphate salts. To combat this effect, recently Creixell et al. have devised a strategy to covalently bind carboxymethyl dextran to iron oxide nanoparticles by first attaching an aminosaline to the particle surface and then utilizing carbodiimide chemistry to covalently bind the dextran coating. They have assessed the stability and cytotoxicity, through a resazurin assay, and have determined that the covalently bound carboxymethyl dextran nanoparticles were more stable in cellular media and buffer solutions and displayed minimal toxicity over a 48 hour and one week period compared to

the adsorbed carboxymethyl dextran nanoparticles which displayed significant toxicity at higher concentrations. In addition to dextran-coated iron oxide, Gupta et al. have studied pullulan, a nonionic polysaccharide, coated iron oxide assessing viability and effects on cellular morphology on hTERT-BJ1 fibroblast using a MTT viability assay and visualization [43]. Minimal toxicity was observed by the pullulan coated particles at up to 2.0 mg/ml concentration after 24 hours of exposure, minimal change in adhesion, and there was an enhanced internalization without major disruption of the cytoskeleton due to the surface coating.

Wotschadlo et al. performed an interesting study where they examined the interaction of three different polysaccharide coatings with two different cell lines (i.e., breast carcinoma, MCF-7, and leukocytes) [39]. The polysaccharides were selected to study in the influence of the polymer backbone on cell interaction measured with magnetic separation after brief incubation times of 4, 8, and 12 minutes with nanoparticles. Dextran with its α-1→6 linkage displayed a time dependent interaction with both the cancer cells and leukocytes with greater uptake by the cancer cells. Cellulose with its β-1→4 linkage displayed limited labeling and no time dependent behavior. Pullulan with its mixture of α-1→4 and α-1→6 linkages displayed greater labeling than cellulose and a suggested time dependent behavior with the leukocytes. This seems to imply that the uptake of nanoparticles by cells is partially receptor mediated and the architecture of the shell has influence over the kinetics of uptake, namely that β-linked polymers are barely incorporated in cells.

Chitosan is a natural polymer derived from the exoskeleton of crustaceans and has been of interest to researchers because of its hydrophilic, biodegradable, non-antigenic,

non-toxic, and biofunctional properties [44]. Its structure consists of one amino group and hydroxyl groups in repeating sequence. In acidic pH, the amino group will protonate and can effectively bind to DNA, making chitosan an interesting candidate for non-viral gene carriers that can utilize the oral route of delivery [45]. In addition to native chitosan, hydrophobically modified chitosan is being studied for gene delivery. Bhattarai et al. have grafted N-acylated chitosan on gold nanoparticles resulting in a colloidally stable, relatively non-toxic carrier [45]. Cytotoxicity was evaluated with MTT assay on three different cell lines (i.e., mouse embryo cells, NIH 3T3, colon cancer cells, CT-26, and breast carcinoma, MCF-7) and after 24 hours of exposure, all cell lines demonstrated a concentration dependent behavior. The slight toxicity at higher concentrations was attributed to cell membrane damage from the polycations interacting with the negatively changed membrane. This toxic effect was minimized by the stability of the nanoparticles. At higher concentrations it was still expected that the nanoparticles would aggregate and accumulate around the cell membrane.

2.4.3 Extended Circulation

In addition to cell toxicity, it is important to gain an understanding of how nanoparticles for drug delivery behave in an organism, specifically possessing adequate circulation time to reach the intended target, release its active ingredient, and then be eliminated from the body without any negative side-effects. In addition to the factors affecting colloidal stability, once a nanoparticle enters the blood stream it will encounter phagocytic cells of the RES. Without specific design considerations, nanoparticles are quickly detected and removed from the blood circulation in approximately 10 minutes [46]. This process is mediated by the adsorption of plasma proteins, opsonins, to the nanoparticle

surface rendering the particle more susceptible to phagocytosis either through increased activation of phagocytic cells or the formation of aggregates [47]. Opsonins bind to the surface primarily through hydrophobic interactions, but electrostatic interactions also play a role. Generally, the goal of surface modification is to reduce the nanoparticle hydrophobicity and surface charge density to shield the nanoparticle surface from opsonins.

Along with being selected for its non-toxic properties, PEG is the most widely studied polymer for increasing the circulation time of nanoparticles. The physicochemical properties of PEG (i.e., it is nonionic, flexible, and hydrophilic) allow it to form a steric barrier on a nanoparticle surface preventing opsonization [25, 46, 47]. In addition to hydrophobicity and surface charge, chain flexibility is another factor to consider when designing a polymer coating [25]. If the exposed surface consists of flexible chains, it will be constantly changing surface structure preventing the immune system from adequately designing an antibody around it. The key design parameters for a PEG coating are chain length, shape, and surface density. The surface density has to be high enough to prevent opsonization while not decreasing mobility and flexibility which would decrease circulation time. While significantly increasing circulation time from a few minutes, PEG coated nanoparticles are generally cleared within 24 hours which might be attributed to desorption or degradation of the PEG shell [46].

Polysaccharide coatings are employed to camouflage the nanoparticle surface by utilizing their biomimetic properties. Polysaccharides such as dextran, heparin, hyaluronic acid, and chitosan have been shown to alter the opsonization process and increase circulation times [46]. In comparison to PEG coatings, polysaccharides might have a more

hydrophilic nature but a shorter circulation time [25]. This can be contributed to the decreased flexibility of polymer chain due to steric restrictions of the repeating sugar units. An additional concern is low levels of circulating antibodies for certain polysaccharides which would lead to immunogenic detection and subsequent clearance [46].

2.4.4 Active Targeting

To ensure the effectiveness of an engineered nanoparticle to the application site an active targeting moiety is often utilized. To increase these specific interactions, nanoparticles can be functionalized with a wide range of targeting ligands such as peptides, antibodies, small molecules, and carbohydrates [48-53]. By utilizing an extended circulation strategy discussed above in conjunction with an active targeting agent, the nanoparticles are capable of circulating the body until finding the desired location.

One research area where active targeting schemes are of growing interest is cancer therapeutic applications. Due to the systemic side effects associated with current treatment modalities, development of a tailored nanoparticle capable of localizing treatment is of great interest. Cancer cells proliferate in an uncontrolled manor so targeting cell markers associated with proliferation is a promising area. Folic acid is essential for cell division and cancer cells typically overexpress the folate receptors [50, 54]. For example, chitosan functionalized iron oxide nanoparticles were labeled with folate for imaging applications and displayed preferential uptake by folate receptor over-expressing cells [55]. In addition to folic acid, monosaccharides have been used to not only provide passivation but target glucose transport overexpressing cancer cells [56-58]. The family of human epidermal receptors, epidermal growth factor receptor (EGFR) and human epidermal receptor-2 (HER-2), are responsible for cell signaling for growth and proliferation and thus heavily

researched [59]. EGFR targeted nanoparticles have demonstrated significant selectivity for cancer cells and once internalized, the nanoparticles can induce cellular death when exposed to an alternating magnetic field without a measurable temperature rise [60]. Interestingly, HER-2 targeted nanoparticles are not only capable of reaching the primary tumor but micrometastatic sites as well suggesting nanoparticles are able to treat metastatic diseases [61].

Beyond specific cancer cell targeting, nanoparticles have been designed to target the tumor itself. Recently, Kruse et al. developed CREKA-conjugated iron oxide nanoparticles, utilizing the peptide sequence for tumor homing [62]. They demonstrated the potential of the nanoparticle system to specifically bind to fibrin–fibronectin complexes associated with tumors while at the same time demonstrating a combinational effect of co-delivering heat from the iron oxide core with cisplatin.

2.4.5 Drug Loading

Many drug compounds suffer from poor solubility and poor stability resulting in undesired pharmacokinetic and biodistribution properties. Nanoparticle carriers present a solution to this issue. By incorporating the drug compound into the nanoparticulate system, the drug can be successfully transported in the body while being shielded from early degradation or release. In the growing field of nanoparticle drug delivery, there is interest in developing smart systems capable of the controlled delivery of the therapeutic.

2.4.5.1 Temperature Responsive Coatings

Temperature responsive polymers undergo a reversible phase transition at a certain environmental temperature, known as the lower critical solution temperature (LCST). At the LCST, the polymer phase separates resulting in the shrinking or collapsing of a

crosslinked polymer system (e.g., hydrogel). Poly(N-isopropylacrylamide) (PNIPAAm) undergoes this transition at around 33 °C and is one of the most widely studied temperature responsive polymers studied in the field of drug delivery [31]. By coating nanoparticles capable of absorbing a specific stimulus to generate heat, a remote actuated drug delivery system can be created. A schematic overview of drug loading and release from PNIPAAm core-shell nanoparticles can be seen below in **Figure 2.6**. For example, Wei et al. utilized ATRP to coat gold nanorods with PNIPAAm and loaded norvancomycin into the polymer shell utilizing hydrogen bonding interactions [63]. When irradiated with near infrared light, the gold nanorods generated localized heat which drove the PNIPAAm shell through a phase transition modulating the release of the drug molecules.

Similar to gold nanoparticles, magnetic particles have been functionalized with PNIPAAm coatings for the controlled actuation and release of drugs following an exposure to an alternating magnetic field. Purushotham et al. have developed PNIPAAm coated iron oxide nanoparticles for multimodal cancer therapy consisting of the simultaneous delivery of a chemotherapeutic (doxorubicin) and hyperthermia [64-66]. When performing the release, two different polymer states were utilized with significantly different release rates observed. Initially, the doxorubicin loaded nanoparticles were dehydrated and transferred to PBS at 24, 37, and 42 °C resulting in the cumulative release of 28.8%, 36.3%, and 41%, respectively, after an initial burst release followed by similar steady state release [64]. In comparison, swollen nanoparticles dispersed in PBS at the same temperature observed at cumulative release of 42.6% (24 °C), 63.7% (37 °C), and 78.1% (42 °C) after a longer rapid release phase [66]. Purushotham et al. attribute the difference to changes the PNIPAAm matrix undergoes during the vacuum dehydration. During the dehydration step,
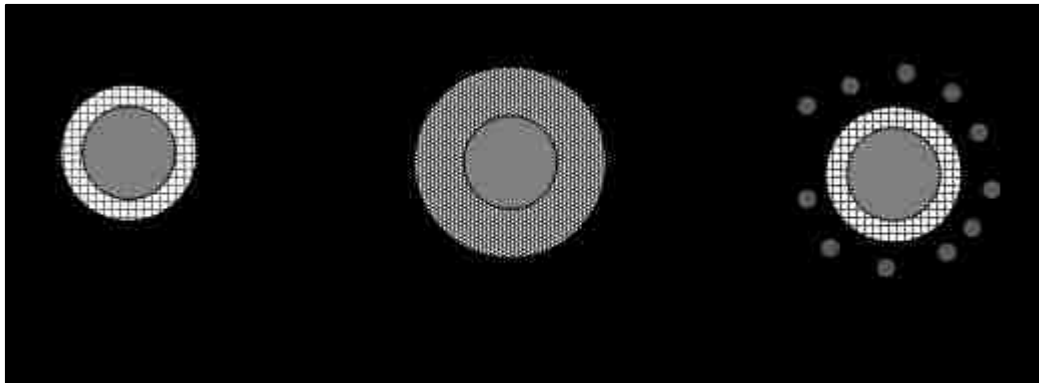
Figure 2.6. Schematic overview of the (a) drug loading and (b) subsequent release experiments at temperatures above the LCST.

there is a heterogeneous distribution of doxorubicin from the migration of water due to evaporation and the re-swelling behavior of the shell is altered. The collapse of the NIPAAm shell above the LCST was only observed in the swollen state nanoparticles making triggered response experiments feasible. Purushotham et al. demonstrated that drug release can be controlled by cycling the temperature across the LCST [66]. In addition to developing the nanoparticle system, they set out to develop a mathematical model to predict the performance in multimodal cancer therapy [65]. Using the experimental data highlighted above to determine the diffusion coefficient of doxorubicin, D_{dox}, the different release profiles of nanoparticles of different sizes and drug loaded were modeled with the following equation derived from Fick's second law of diffusion:

$$\frac{M_t}{M_\infty} = 1 - \frac{6}{\pi^2} \sum_{n=1}^{\infty} \frac{1}{n^2} \exp\left(-\frac{D_{dox} n^2 \pi^2 t}{R^2}\right)$$ **Equation 2.11**

where M_t is the cumulative mass of drug released in time t, M_∞ is the cumulative mass of drug released at infinite time (assumed to be the total drug loaded in the nanoparticles), and R is the radius of the composite nanoparticles. The model demonstrates that drug release occurs faster at higher temperatures and decreased shell thickness. By changing the shell thickness the release rates can be tuned to meet the designer's needs.

One of the key pitfalls to PNIPAAm loaded shells is that the drug compound of choice must be hydrophilic, while most novel drugs tend to be hydrophobic. To deliver hydrophobic drugs, different nanoparticle carriers had to be developed.

2.4.5.2 Cyclodextrin Functional Groups

Cyclodextrin molecules are cyclical formations of glycosidic bonds that have been studied as potential drug carriers. When arranged in this cyclical structure, the hydroxyl groups from the sugar molecules are oriented on the outside resulting in a relatively

hydrophobic core. Since solubility is a major issue with most pharmaceutical agents, hydrophobic drugs can be successfully loaded into the cavity improving the solubility of the compound. The drug is held in the cavity through hydrophobic interactions which can be depressed by the application of heat thereby accelerating the release of the compound [67]. Hayashi et al. have developed β-cyclodextrin (CD) functionalized magnetic nanoparticles with folic acid targeting ligands for the controlled delivery of tamoxifen (TMX) to breast cancer tumors. They demonstrated a pulsatile release behavior of TMX from the CD functionalized nanoparticles when an alternating magnetic field is applied. Similarly, Yallapu et al. has synthesized CD functionalized iron oxide nanoparticles for the encapsulation and delivery of curcumin for cancer therapy [68]. In addition to CD, the nanoparticle was further functionalized with a pluronic F127 (co-polymer containing PEG and polypropylene chains) coating to add additional stability to the system.

2.4.5.3 Gatekeeping Structures

Mesoporous silica nanoparticles (MSNs) provide the opportunity to directly load the therapeutic agent into the core nanoparticle and then using a stimuli-responsive shell as the gatekeeper to regulate the encapsulation and release. Potential candidates to act as gatekeepers are smaller nanoparticles, organic molecules, or supramolecular chemical entities [12]. For example, Slowing et al. have used cadium sulfide (CdS) nanoparticles to block drug loaded pores preventing any premature release [69]. CdS was held in place with a chemically cleavable disulfide linkage that was cleaved by the addition of a reducing agent allowing up to 85% of the loaded molecules to be released. Hong et al. developed a core-shell architecture by coating MSNs in PNIPAAm coating using RAFT polymerization where the polymeric coating acts as the gatekeeper [70]. Unlike drug loading in the

polymeric network, the active compounds can be loaded in the pores of the core nanoparticle allowing compounds with various chemical properties. When the temperature falls below the LCST, the polymeric shell expands allowing drug release.

2.5. Conclusions and Perspectives

This chapter has explored a variety of coatings and additives incorporated onto nanoparticles in a core-shell architecture for biomedical applications. An emphasis was placed on coatings selected for improving colloidal stability, reducing nanoparticle toxicity, increasing circulation time, active targeting, and controlling different mechanisms of drug loading and release, but those are only few of the functions imagined by researchers. As nanotechnology progresses, researchers will become more and more creative in the quest to develop a perfect nanoparticle capable of being safely delivered to the body, actively finding the optimal location for delivery, and delivering the payload in a controlled fashion.

2.6. References

References are located at the end of the dissertation subdivided by chapters.

Chapter 3: Magnetic Nanoparticle Mediated Energy Delivery for Cancer Therapy

3.1. Introduction

Magnetic nanoparticles are being studied for a wide range of biomedical applications usually relaying on the theranostic capabilities of the magnetic core to provide alternating magnetic field mediated thermal therapy and enhanced contrast in magnetic resonance imaging [1-4]. Thermal therapy is the process of elevating tumor tissue temperature for therapeutic gains and has been studied for decades, but has yet to gain widespread clinical recognition either as an independent treatment or in conjunction with traditional therapies. To overcome the barriers of traditional hyperthermia methods – such as localizing the heat, tumor targeting, and even temperature distribution across the tumor – it is of particular interest to utilize the remote heating of magnetic nanoparticles known as magnetic fluid hyperthermia (MFH) [5]. This chapter will explore the use of magnetic nanoparticles as a means to deliver thermal therapy. Briefly, the underlying physics of magnetic nanoparticles will be discussed followed by mechanisms of thermal therapy. The chapter will end with the most recent advances in the area of magnetically mediated energy delivery (MagMED) therapy, which holds great promise in treatments.

3.2. Magnetic Properties

3.2.1 Magnetic States

Magnetic materials are classified based on the arrangement and behavior of their magnetic dipole moments. In the presence of an external magnetic field, the material's response is characterized by the magnetic susceptibility, χ, defined by the following equation:

$$\chi = M/H \qquad\qquad\qquad \textbf{Equation 3.1}$$
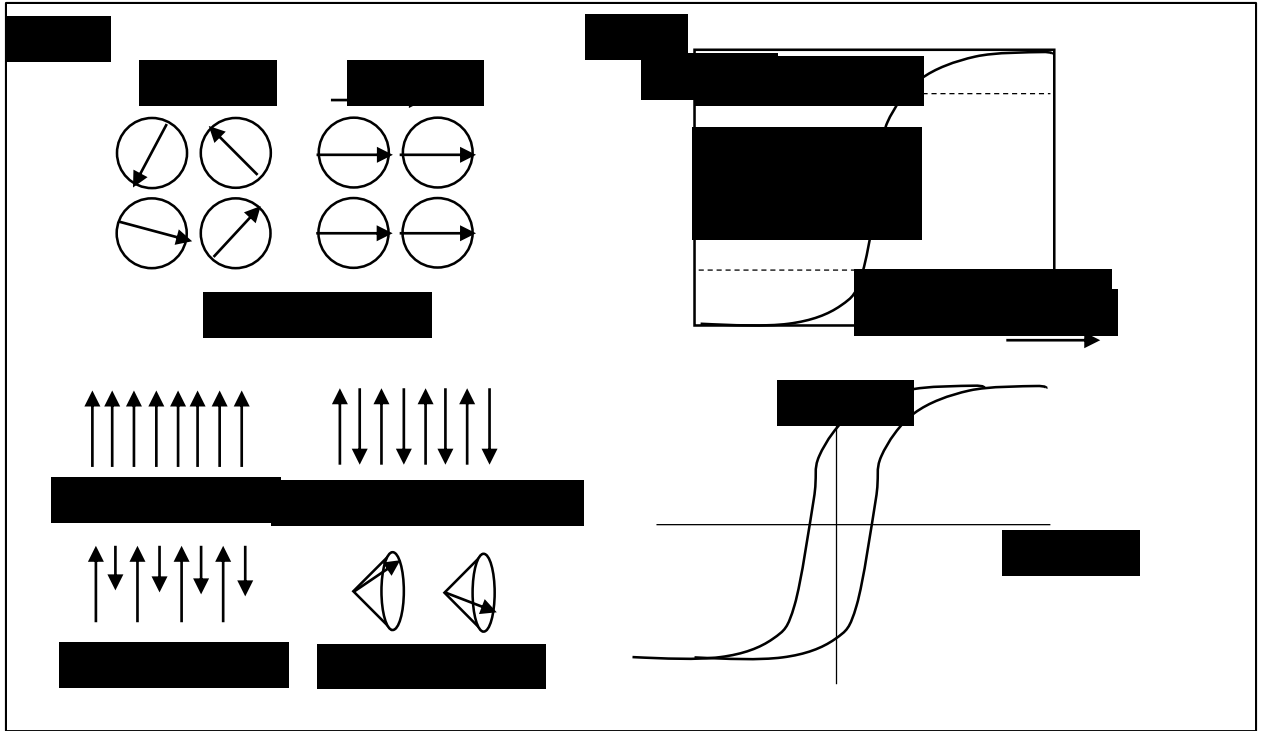
Figure 3.1. Arrangement of magnetic dipoles for different magnetic materials where H indicated the direction of an external magnetic field (a). Representative magnetization curves highlighting the dominant processes and hysteresis loop (b).

where *M* is the magnetization of the material defined by the magnetic moment per unit volume and *H* is the macroscopic magnetic field intensity [6]. Materials with a negative magnetic susceptibility are called diamagnetic since the induced moment is opposite of the external field. Materials with a positive susceptibility are called paramagnetic since the induced moment is aligned with the external field. Once the external field is removed, the material does not retain a magnetic moment as thermal fluctuations randomize the dipoles. When a material has an ordered array of magnetic moments without an external field present, they can be classified as ferromagnetic, ferromagnetic, antiferromagnetic, helical or more complex forms. Illustrated in **Figure 3.1a** are the various arrangements on magnetic dipoles in the presence and absence of an external magnetic field.

Actual macroscopic materials are composed of magnetic domains, or small regions where the local magnetization is uniform. In a multi-domain material the moments are not necessarily parallel. When a magnetic field is applied, the magnetization of material undergoes a typical closed loop response curve. In a weakly applied field, favorable orientated domains increase in size at the expense of unfavorable oriented domains. As the field strength increases the domain magnetization rotates with respect to the field direction until saturation is reached. When the field is shut off, the material will retain residual magnetization and a reverse field is required to reduce the induction back to zero. In a multi-domain material, the energy required to move the domain walls and overcome anisotropic energy results in an irreversible path illustrated as the typical hysteresis loop in **Figure 3.1b**.

Below a certain particle size, multi-domains become energy unfavorable and the particle becomes a single domain [7, 8]. In the case of magnetite, this single domain state

occurs around 30 nm in diameter [9]. At this small particle size, the magnetic reversal energy is small enough that the dipole moment becomes thermally unstable at ambient temperature [10]. This phenomenon is known as superparamagnetism. The magnetic response curve of superparamagnetic materials have zero hysteresis since thermal energy is sufficient to destabilize the magnetic moments to the initial orientation.

3.2.2 Heat Generation

In an alternating magnetic field, magnetic materials dissipate heat in response to the reversal in magnetization. Heat generation occurs primarily though hysteresis losses and relaxation losses. In the case of multi-domain materials, area between the hysteresis loops quantifies the magnetic energy delivered as heat. Single domain materials can display similar hysteresis losses when the external field exceeds the coercivity field [7]. However, in relevant clinical settings such parameters would rarely be achieved [11]. Thus, the heating properties of superparamagnetic particles are dominated by Brownian and Neel relaxation losses [12]. Neel relaxation is defined by the rotation of the internal magnetic moment in response to the magnetic field. As a suspension of particles is free to rotate, the Brownian relaxation is defined as the physical alignment with respect to the alternating magnetic field.

Since Brownian and Neel relaxations occur in parallel, the effective relaxation time is given by the following equation:

$$\frac{1}{\tau} = \frac{1}{\tau_B} + \frac{1}{\tau_N}$$ **Equation 3.2**

where τ_B and τ_N are the Brownian and Neel components respectively. These relaxation times are defined by the following relationships:

$$\tau_B = \frac{3\eta V_H}{k_B T}$$ **Equation 3.3**

$$\tau_N = \tau_0 \exp\frac{KV}{k_B T}$$ **Equation 3.4**

where η is the viscosity of the fluid, V_H is the hydrodynamic volume, k_B is the Boltzmann

constant, T the absolute temperature, τ_0 is the characteristic flipping time (on the order of

10-9 s), K is the magnetic anisotropy, and V is the magnetic volume. From the above

equations, the Brownian relaxation is governed by the hydrodynamic properties of the

system. For example, if the particles become constrained by viscosity the relaxation time

increases and Neel relaxation component dominates. The Neel relaxation is governed by

the energy barrier against magnetization reversal and thus an inherent material property.

The specific loss power, SLP, is a means of quantifying the heat generated by the

particle system in response to the alternating magnetic field. Assuming the system is

monodispersed, it can be expressed as the following:

$$SLP = \chi_0 H_0^2 \mu_0 \pi \frac{2\pi f^2 \tau}{1+(2\pi f \tau)^2}$$ **Equation 3.5**

where χ_0 is the initial susceptibility, H_0 is the field amplitude, μ_0 is the permeability of free

space, f is the field frequency, and τ is the relaxation time. The initial susceptibility, χ_0, can

further be determined through the Langevin equation such that it becomes a function of

domain magnetization and volume fraction of particles [12]. From **Equations 3.2-5**, the

heat generated by particles is dependent on field properties (strength and frequency),

material properties (domain magnetization, anisotropy constant, particle size) and fluid

properties (viscosity, hydrodynamic size, and concentration).

While the above SLP equation is effective for modeling the theoretical performance

of a particle system, experimental quantification typically relies on the specific absorbance

rate (SAR) value. SAR reports the heat output normalized to mass and serves as a means

of comparing the heating performance of different magnetic particle systems. SAR can be calculated as:

$$SAR = (\sum_i C_i m_i)/m * (\Delta T/\Delta t)$$ **Equation 3.6**

where C_i is the heat capacity, m_i is the individual mass of the components heated (fluid and particles), m is the mass of the component generating heat, and $\Delta T/\Delta t$ is the initial slope of the heating profile. SAR should be noted for its inherent simplicity to calculate based on experimental data and material properties. However, it does not incorporate the field parameters which makes direct comparisons of particle systems difficult.

3.3. Thermal Therapy

Two temperature ranges of thermal therapy have traditionally been identified: hyperthermia, 40-45 °C, and thermoablation, ≥46 °C. Hyperthermia can induce cellular death on its own, but it is better suited for enhancing the effects of chemotherapy and/or radiation therapies [13-16]. The exact cause of the increased sensitivity is still under investigation, but it is believed to be a combination of cellular effects – changes in the cell membrane, impaired transport, cytoskeleton damage, and impairment and damage to cellular proteins and DNA – and physiological effects – changes in the vasculature, increased perfusion, and oxygen levels [15, 17, 18]. Due to the elevated temperature, thermoablation leads to direct cell necrosis and can be used an independent treatment [19]. The main issue facing hyperthermia is a clinical means to deliver the elevated temperature to the tumor site. Current methods are characterized by the amount of surrounding tissue heated and subdivided into whole body hyperthermia (water baths or heating chambers), localized hyperthermia (antennas emitting microwaves or ultrasound), and regional hyperthermia (array of antennas) [13, 15]. Localizing the heat, tumor targeting, and even

temperature distribution across the tumor are some of the shortcomings of the current methods of delivering hyperthermia. Localization of the thermal therapy is necessary to prevent damage to the surrounding tissue and minimize patient discomfort and even heating is necessary to guarantee therapy effectiveness.

As discussed in the previous section, nanoparticles can generate heat when exposed to an alternating magnetic field. Magnetic fluid hyperthermia (MFH) involves the collection of nanoparticles at the tumor site through either active or passive targeting or direct injection, and the application of the alternating magnetic field to provide localized heating throughout the tumor. This therapy overcomes the barriers of traditional hyperthermia methods by treating deep-seated and poorly accessible tumors, delivering heat specific to tumor ensuring less damage to healthy tissue, providing uniform temperature distribution, and a higher rate of heat transfer for improved efficacy [20, 21].

3.3.1 Physiological Effects

Despite being written over a decade ago, the hallmark paper examining the physiological effects of hyperthermia remains the review by Hildebrandt et al. [17]. While assessing in vitro studies, Hildebrandt et al. observed that toxicity at increasing temperatures often displays a two-step curve where initial damage results in cellular arrest and with additional heat the trend displays exponential cell death. This trend indicates protein denaturing as the thermal dose required to reach the irreversible cell death corresponds to the energy required to denature proteins. Hyperthermia was observed to be most lethal in the M and S phase where the mitotic apparatus and chromosomes are most susceptible to damage. During heating both RNA and DNA synthesis is impaired along with the inhibition of repair mechanisms to compound the initial damage. Beyond protein

denaturing, the fluidity and stability of the cell membrane is altered along with transport proteins being impeded. However, it appears that this observation is more tied to early indications of apoptosis instead of a direct effect. When multiple cycles of hyperthermia are applied, cells often display a thermal tolerance explained by the activation of heat shock proteins protecting unfolded proteins.

When applying hyperthermia in vivo specific features become apparent. The application of heat above 42 °C decreases blood flow exacerbating the already hypoxic and acidic environment of the tumor. Initial studies with whole body hyperthermia have demonstrated that despite changes in blood flow, healthy tissue has better thermoregulation and remains relatively unaffected. However, moderate hyperthermia (< 42 °C) may have the opposite effect and increase blood supply to the tumor. Such an effect would improve oxygen flow and thereby improve the efficacy of radiation therapy. Initial clinical studies during the 1980's and 1990's were performed without any molecular basis and future research needs to account for the mechanisms of action to improve the efficacy of treatment.

3.3.2 Combinational Effects with Chemotherapy

When used in conjunction with chemotherapy, hyperthermia has the potential of producing synergistic effects. Elevated temperatures are able to influence the pharmacodynamics aspects by accelerating the primary mode of drug action and increasing intracellular drug concentration [22]. The pharmacokinetic aspects are also affected whereby drug uptake, distribution, and metabolism are altered. When selecting a chemotherapy for dual therapy it is important to consider the mechanism of action so the therapies will not work against each other. A recent review by Torres-Lugo and Rinaldi

provides a detailed summary of common chemotherapeutics used in conjunction with hyperthermia [23]. Perhaps most interesting from the summary is that the local delivery of heat via magnetic nanoparticles often improves chemotherapy efficacy more than bulk delivered heat suggesting a localized effect.

Beyond a co-delivery of magnetic nanoparticles with chemotherapeutic, nanoparticles are being functionalized to be drug carriers for dual therapy applications. Such functionalization allows the possibility to track drug location with MRI and utilize magnetic targeting [24-26]. One of the most common techniques is to load the drug into a polymer coating or polymer particle composite [27, 28]. Release is based on diffusion and the increased temperature during hyperthermia accelerates the release rate. A concern with this technique is sufficient drug loading and the nanoscale release path. However, Purushotham et al. predicts that the amount of doxorubicin required and loaded into nanoparticles is similar to the amount of particles required for hyperthermia [11]. More complex structures can be employed such as attaching the drug to the particle surface or tethering a drug loading group to the surface. For example, Hayashi et al. provide an interesting strategy of attaching cyclodextrin groups to the surface to transport hydrophobic drugs [29]. An in-depth discussion of drug loading in polymeric coatings was explored in the previous chapter.

To determine the effectiveness of dual therapy, Babincova et al. described a simple synergy test for combinational therapy based on a model previously established for two drug systems [30, 31]. Their nanoparticle system consisted of cisplatin functionalized to the particle surface. In the synergy test the following variables were defined [A], [B], and [A+B] as the percent viability of hyperthermia, chemotherapy, and combinational therapy

40

respectively. The combined effect is quantified as: [A+B] < [A] x [B] / 100, synergistic; [A+B] = [A] x [B] / 100, additive; [A] x [B] / 100 < [A+B] < [A], if [A] < [B], subadditive; [A] < [A+B] < [B], interference; and [B] < [A+B], if [A] < [B], antagonistic.

Dual magnetic particle delivered hyperthermia and chemotherapy has recently been studied by our research group. Meenach et al. explored the potential of utilizing bulk nanocomposite hydrogels to deliver paclitaxel and heat [32]. Paclitaxel was released from the hydrogel in a non-Fickian profile. Three independent cell lines were exposed to the combinations of therapy and it was determined that hyperthermia improved the efficacy of paclitaxel in A549 cells. Kruse et al. studied the co-delivery of CREKA-conjugated iron oxide nanoparticles with cisplatin [33]. CREKA was selected for its tumor homing properties. The effectiveness of the combination of cisplatin and magnetic nanoparticle delivered hyperthermia was found to be additive using the equation described above.

3.4. Intracellular Hyperthermia and MagMED

A major translational hurdle of magnetic nanoparticle mediated hyperthermia is that a large concentration of nanoparticles is required to achieve the necessary increase in temperature in vitro and especially in vivo, thus limiting the application to direct injection into solid tumors for in vivo application [34, 35]. Medical imaging would be required to facilitate guided injection into a solid tumor in which the advantages of MFH over traditional surgical resection or other localized treatments would become minimal or nonexistent. While utilizing the enhanced permeability and retention effect has been proposed for systemic delivery of nanoparticles, concerns over achieving sufficient tumor accumulation has been raised [36, 37]. When MFH was in its infancy, Gordon et al. hypothesized that intracellular hyperthermia would be more effective than extracellular by

41

overcoming a potential thermal barrier created by the cell membrane [38]. Intracellular hyperthermia would negate the clinical issue of high nanoparticle concentrations as only the cells themselves and not the surrounding tissue would have to be heated to the hyperthermia range. To facilitate nanoparticle internalization, nanoparticles have been functionalized with a wide range of targeting ligands such as peptides, antibodies, small molecules, and carbohydrates [39-44]. Usually, these targeting ligands were developed for medical imaging and diagnostic purposes. Combining the therapeutic potential and enhanced contrast properties of nanoparticles has created the new field of theranostics. For a more detailed discussion on this field, the authors refer the reader to the following reviews [45-47].

Following successful results demonstrating the potential for MFH, researchers turned their attention to intracellular hyperthermia [48-50]. For example, Jordan et al. explored the internalization of dextran and amine functionalized nanoparticles by four cell lines in vitro [51]. Based on the internalization, they observed a three-fold decrease in clonogenic survival by nanoparticle mediated hyperthermia compared to water bath mediated hyperthermia, which demonstrated the potential to deliver heat to the targeted cells. Fortin et al. studied anionic coated maghemite and cobalt ferrite and determined that cancer cells sufficiently internalize the particles at the rate of about 25 pg per cell over the course of 1 hour [52]. These cells were collected and dispersed at a concentration of 20 million cells per 0.3 ml and generated sufficient heating in a magnetic field to achieve the hyperthermia range. The authors explored the heating contributions from the two relaxations and concluded that Neel relaxation is dominant during intracellular hyperthermia as the Brownian contribution was minimized while entrapped in intracellular

vesicles. Thus, future designed particles should emphasize the Neel contribution. Iron oxide based nanoparticles can be doped with various transitional metals to generate different physical and magnetic properties to improve the likelihood of successful intracellular hyperthermia [53, 54]. However, concerns over the toxicity of transition metals in the body have stalled future advances.

Despite promising initial results and room for conceptual development, the mechanism and feasibility of intracellular hyperthermia has been debated for over a decade. The debate stems from the heat transport calculations by Rabin that demonstrated theoretically that the relative heat transfer should be insufficient to induce damage to a cell [55]. In the paper, Rabin explored three length scales: nanoscale (5-100 nm), microscale (2-20 µm), and macroscale (20 mm). For a typical particle, the steady state temperature difference for a single particle is no greater than 10-5 °C implying that a single particle is incapable of thermal damage. Scaling up to the microscale, in order to achieve a local threshold of 43 °C would require a cluster of nanoparticles close to 200 µm in diameter – far larger than a single cell. If the local scale is changed to just heating a single cell of 15 µm is used, the heating power required would be two times what is typically achieved in literature. At the macroscale, the analysis modeled a spherical tumor containing uniformly distributed nanoparticles. He determined that the minimal diameter required would be 1.1 mm limiting the therapy to large tumors. All calculations were performed in the absence of blood perfusion which would add an additional cooling effect to the macroscale calculations.

However, ground breaking work by Creixell et al. demonstrated that internalized targeted nanoparticles can induce cellular death when exposed to an alternating magnetic

field without a measurable temperature rise [56]. The iron oxide nanoparticles were coated with carboxymethyl-dextan and conjugated with epidermal growth factor (EGF) targeting ligands. The targeted nanoparticles were internalized by breast cancer cells at a greater rate than non-targeted, and when exposed to the alternating magnetic field, a 99.9% reduction in cell viability was demonstrated. By utilizing appropriate targeting ligands and this observed intracellular effect where internalized nanoparticles deliver therapeutic gains without perceived temperature rise, the possibility of using magnetic nanoparticles to treat metastatic lesions could be realized instead of being limited to solid tumors. For example, HER-2 targeted nanoparticles are not only capable of reaching the primary tumor but micrometastatic sites as well and could be a good targeting ligand for this form of therapy [57]. This potential therapy has been coined as 'magnetically mediated energy delivery' (MagMED), and it represents a promising field of therapeutics [58]. The provocative question now facing researchers is the exact mechanism of cytotoxicity, and this still needs to be explored. Possible mechanisms at play are local heating effects, physical-mechanical effects (rotational or vibrational movements), or chemical effects, and each of these will be explored below.

Experimental evidence demonstrating local or nanoscale heating usually involves changes in a fluorescent polymeric shell or involves nanoparticles in the direct vicinity of a liposomal carrier increasing the permeability of the bilayer [59-61]. For example, Polo-Corrales and Rinaldi developed iron oxide nanoparticles coated with a poly(N-isopropylacrylamide) shell with a fluorescent tagged acrylamide incorporated into the polymeric coating [60]. The polymeric shell is temperature responsive undergoing a lower critical solution temperature at 35 °C, at which the fluorescence intensity increases with

the changes in local solvent polarity. It was observed with magnetic field exposure that the surface temperature of the nanoparticles was able to immediately drive this transition temperature while the solution temperature lagged behind. The localized heating effect observed experimentally may attribute to the cytotoxicity of the therapy by directly heating and damaging local subcellular components.

In the presence of the alternating magnetic field, the nanoparticles would be physically rotating and realigning themselves in chains along the field. The mechanical forces from magnetic nanoparticle actuation on the range of femto to piconewton have been reported in literature to cluster cellular receptors, distort ion channels, and stimulate the cytoskeleton [62-64]. These mechanical forces could be used to induce apoptosis through lysosomal membrane permeabilization. Increasing the permeability of lysosomes will induce cellular death through the release of cathepsins from the lysosomal compartment into the cytosol where they participate in apoptotic pathways [65-67]. Such a strategy is attractive to researchers as it has been shown to induce cellular death in cancer cells which typically have resistance to apoptotic pathways [68]. In follow-up work with the EGF targeted iron oxide nanoparticles developed by Creixell et al., Domenech et al. observed that the nanoparticles were specifically being internalized into lysosomal compartments [69, 70]. Upon exposure to the alternating magnetic field, they observed an increase in lysosomal permeability and decreased viability as a result of their intracellular treatment. They attributed this observation to either heat dissipation or mechanical disruption of the lysosomes. Zhang et al. developed iron oxide nanoparticles coated with lysosomal protein marker antibodies to specifically accumulate along the lysosome membrane [71]. In this case, the alternating magnetic field applied was at 20 Hz where only physical rotations by
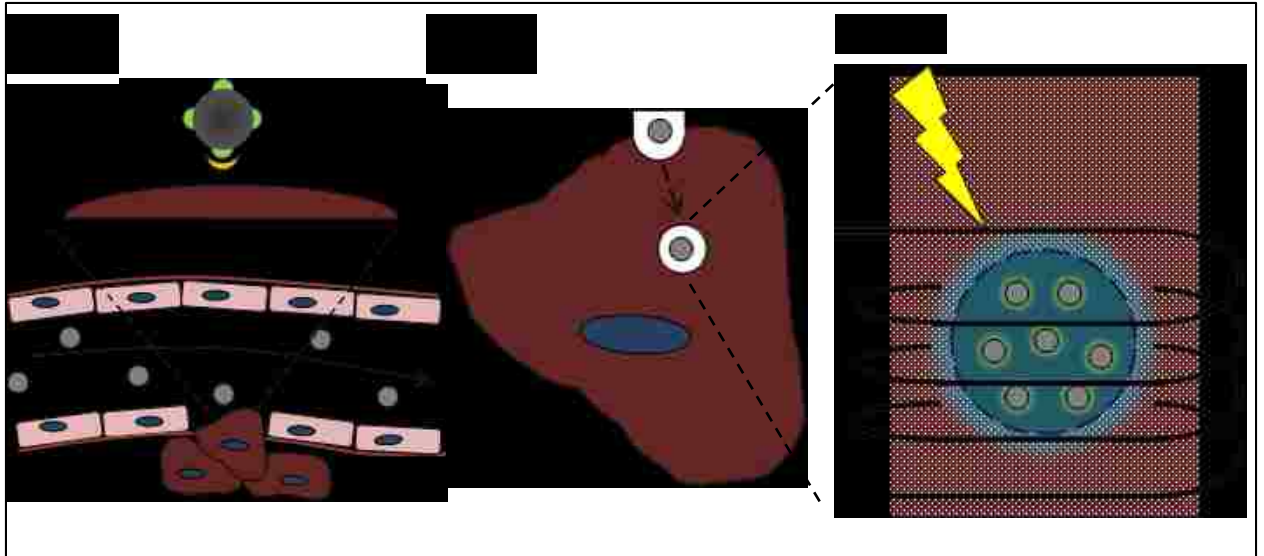
Figure 3.2. Schematic of envisioned route of MagMED therapy through apoptosis triggered by lysosomal membrane permeabilization. Targeted nanoparticles would circulate the body until coming into contact with cancer cells. The targeting ligand binds to the respective cell marker (A) and the nanoparticles are internalized by the cell entering lysosomes (B). When the alternating magnetic field is turned on the nanoparticles are actuated and the energy delivered disrupts the lysosomal membrane spewing the contents (C).

the nanoparticles would be actuated. The resulting cellular apoptosis occurred due to the lysosomal disruption from the rotational forces. A schematic of magnetic nanoparticle actuated lysosomal membrane permeabilization can be found below in **Figure 3.2**.

Further evidence of lysosomal membrane permeabilization was also observed by Sanchez et al. through iron oxide nanoparticles conjugated with a synthetic replica of gastrin to target CCK2R receptors frequently overexpressed by cancer cell lines [72]. Despite a relatively low heating power from the core nanoparticles and low amount of internalization, with alternating magnetic field exposure the cells displayed lysosome membrane permeabilization followed by the leaking of cathepsin B resulting in cellular death. In follow-up work, the authors fabricated a miniaturized electromagnet to produce an alternating magnetic field while cells are studied in real-time using confocal microscopy [73]. Within 30 minutes of alternating magnetic field exposure, the cells displayed elevated reactive oxygen species levels and lysosomal permeabilization. Interesting, in some cells the lysosomes were influenced by the field and organized in needle-like formations. Considering the wide variety of assays available, this technology opens the possibility to gain fundamental knowledge of cellular and molecular mechanisms occurring during treatments.

One potential chemical effect would be the production of reactive oxygen species (ROS) from iron oxide nanoparticles. In the presence of endogenous hydrogen peroxide, free radicals are generated through Fenton-like chemistry [74, 75]. Free radical generation results in cellular oxidative stress, which is believed to be one of the key underlying mechanisms of concentration dependent cytotoxicity [76, 77]. In previous work, we have demonstrated that targeted antioxidant nanoparticles of polytrolox are able to suppress

ROS generation and protect cells from concentration dependent iron oxide cytotoxicity [78]. One of the interesting questions in this field is whether the source of the Fenton-like chemistry is homogeneous or heterogeneous catalytically driven. Voinov et al. have demonstrated through spin-trapping EPR that γ-Fe_2O_3 nanoparticles produce hydroxyl radicals on the surface at a 50-fold increase compared to dissolution of free ions [79]. However, accounting for nanoparticles primarily being internalized into lysosomes, the shift in pH (~4.5) would result in some dissolution of iron oxide to iron ions. These free ions have the potential to leave the lysosome to the cytosol, mitochondria, or endoplasmic reticulum where they would encounter conditions more favorable to Fenton-like chemistry in terms of available hydrogen peroxide [74, 80-83]. While studying the roles of silica coatings for surface passivation, the toxicity of iron oxide nanoparticles were tied to intracellular release of iron ions which would react with mitochondrial hydrogen peroxide [84]. Limited research has been performed studying the effects of magnetic nanoparticles in an alternating magnetic field on ROS production. Recently, we have demonstrated that the generation of ROS is enhanced in presence of an alternating magnetic field [85]. At nanoparticle concentrations where there was no observable temperature rise, we observed a significant increase in ROS generation compared to the Arrhenius prediction. We believe that as a result of the local nanoscale heating the heterogeneous catalytic generation of ROS is accelerated. However, in follow up work we studied the role of nanoparticle coatings and observed the ROS generation was significantly impaired (submitted to Acta Biomaterialia). One of the coated systems involved glucose functionalization, and it was efficiently internalized into lysosomes and induced significant apoptosis compared to the other nanoparticles, reinforcing the physical or thermal mechanisms discussed above.

Despite this one study, heterogeneous catalysis coupled with the enhanced reactivity though nanoscale heating is another route of MagMED worth exploring.

While not a direct chemical effect, Ito et al. has provided an interesting example of intracellular hyperthermia inducing an immune response in cancer cells demonstrating the potential to deliver immunotherapy [86]. Antibody targeted liposomes containing iron oxide nanoparticles were synthesized capable of being internalized by cells and providing sufficient heating to achieve hyperthermia. The authors determined this therapy to have two mechanisms of actions revolving the expression of heat shock proteins (HSP). When sub lethal damage is applied, the cells over express HSP, which in-turn increase the amount of surface MHC peptide complexes, which recruit cytotoxic T cells. Alternatively, the heat generated by the nanoparticles is capable of inducing necrosis. This sudden cellular death releases the cell content including HSP complexes, which interact with neighboring tumor cells and recruit monocytes. Thus, if any targeted therapy only effectively eliminates the outer cells of a tumor, the resulting immune response could assist in eliminating core cells.

3.5. Conclusions and Perspectives

Through MagMED, cancer cells are eliminated without a macroscopic temperature rise, and this mode of therapy opens the possibility of applying magnetic nanoparticles in ways previously not imagined. Previously, the focus was improving the heating capabilities to overcome the thermal delivery limitations, and now, the attention is shifting to intracellular targets. Further studies need to be performed to gain a better fundamental understanding of the mechanisms at play. However, an exciting prospectus is to combine the knowledge gained through combined chemotherapy and MFH with this new therapy. Novel nanoparticle architectures can be synthesized to deliver the chemotherapeutic

intracellular, relying on the nanoscale effects to improve efficacy. For example, the nanoscale heating could be used trigger drug release or the mechanical effects could increase the lysosomal permeability facilitating better drug leakage to the cytosol. The future of cancer medicine is personalized care, and novel architectures should be designed with interchangeable targeting ligands and chemotherapy payloads to tailor treatment to each individual patient and disease.

3.6. References

References are located at the end of the dissertation subdivided by chapters.

Chapter 4: Synthesis and Characterization of PEG-Iron Oxide Core-shell Composite Nanoparticles for Thermal Therapy

In this study, core-shell nanoparticles were developed to achieve thermal therapy that can ablate cancer cells in a remotely controlled manner. The core-shell nanoparticles were prepared using atomic transfer radical polymerization (ATRP) to coat iron oxide (Fe_3O_4) nanoparticles with a poly(ethylene glycol) (PEG) based polymer shell. The iron oxide core allows for the remote heating of the particles in an alternating magnetic field (AMF). The coating of iron oxide with PEG was verified through Fourier transform infrared spectroscopy and thermal gravimetric analysis. A thermoablation (55 °C) study was performed on A549 lung carcinoma cells exposed to nanoparticles and over a 10 minute AMF exposure. The successful thermoablation of A549 demonstrates the potential use of polymer coated particles for thermal therapy. The information included here is adapted or directly taken from work previously published:

> <u>Robert J. Wydra</u>, Anastasia M. Kruse, Younsoo Bae, Kimberly W. Anderson, J. Zach Hilt. Synthesis and Characterization of PEG-Iron Oxide Core-Shell Nanoparticles for Thermal Therapy. Materials Science and Engineering C: Materials for Biological Applications, 33(8): 4660-4666, 2013.

Reprinted with permission from Elsevier.

4.1. Introduction

Due to their unique physical properties, iron oxide nanoparticles are being studied for a wide range of biomedical applications such as imaging, targeted delivery, and thermal therapy of cancer [1-4]. Superparamagnetic nanoparticles remotely heat in an alternating magnetic field primarily due to the Brownian relaxation (physical rotation of the particles)

and Neel relaxation (rotation of the magnetic moment) [5-7]. The particles absorb the energy from the magnetic field and convert it into heat through the aforementioned relaxations [8]. Surface modification plays an essential role in determining the success of nanoparticles in their application by improving stability, preventing agglomeration, improving biocompatibility, and providing additional functionalities (e.g. targeting antibodies) [9-13]. PEG-based functionalization is common for biological applications as a means to prevent protein adsorption and thus improve circulation time and minimize host response to the particles [14]. One method of functionalizing the particles is utilizing a surface initiated atom transfer radical polymerization (ATRP) [15-17]. This method first involves attaching an initiator group to the surface that serves as the seed for polymerization. Various polymeric systems can be grafted from the surface making ATRP a very flexible platform. For *in vivo* applications, PEG functionalization would be essential for the stability of the nanoparticles by preventing premature clearance [18]. To date, most surface initiated polymerizations have been utilized to coat iron oxide nanoparticles with a polymer brushes [19]. PEG brushes have been successfully used to prevent rapid clearance by macrophages, resist protein adsorption, and have reduced cytotoxic effects [20-22]. By utilizing a PEG-based hydrogel coating, similar biological properties are expected while having the additional benefit of future applications such as drug loading for controlled delivery. Coating stability is an additional concern to guarantee the long term effectiveness of a nanoparticle system. Miles et al. have demonstrated that carboxylic acid anchors can be displaced by phosphate ions effecting colloidal stability [23, 24]. In the case of a crosslinked hydrogel shell, the stability of the coating will not be affected by anchoring group displacement as a continuous shell entraps the core nanoparticle.

Thermal therapy is the process of elevating tumor tissue temperature for therapeutic gains and has been studied for decades, but has yet to gain widespread clinical recognition [25-27]. Two temperature ranges have been identified: hyperthermia, 40-45 °C, and thermoablation, ≥46 °C. Hyperthermia can induce cellular death on its own, but it is better suited for enhancing the effects of chemotherapy and/or radiation therapy [25, 28-30]. The exact cause of the increased sensitivity is still under investigation, but it is believed to be a combination of cellular effects: changes in the cell membrane, impaired transport, cytoskeleton damage, and impairment and damage to cellular proteins and DNA; and physiological effects: changes in the vasculature, increased perfusion, and changes in oxygen levels [29-31]. Due to the elevated temperature, thermoablation leads to direct cell necrosis and can be used as an independent treatment [32]. The main issue facing thermal therapy is a clinical means to deliver elevated temperatures to the tumor site. Current methods are characterized by the amount of surrounding tissue heated and subdivided into whole body hyperthermia (water baths or heating chambers), localized hyperthermia (antennas emitting microwaves or ultrasound), and regional hyperthermia (array of antennas) [28, 30]. Localizing the heat, tumor targeting, and even temperature distribution across the tumor are some of the shortcomings of the current methods of delivering hyperthermia. Localization of the thermal therapy is necessary to prevent damage to the surrounding tissue and minimize patient discomfort and uniform heating is necessary to guarantee therapy effectiveness. It is of particular interest to utilize the remote heating of the nanoparticles to overcome the barriers of traditional hyperthermia methods [33]. It has recently been demonstrated that hyperthermia induced by magnetic nanoparticles has an advantage over conventional hyperthermia methods in inducing cell death *in vitro* [34]. By

passive targeting, nanoparticles can collect at the tumor site and by the application of the alternating magnetic field provide localized heating throughout the tumor.

In this study, core-shell nanoparticles were prepared using ATRP to coat iron oxide (Fe_3O_4) nanoparticles with a PEG-based polymer shell. Cytotoxicity on two independent cell lines was examined to determine potential systemic effects. Thermal therapy application feasibility was demonstrated *in vitro* with a thermoablation (55 °C) study on A549 lung carcinoma cells.

4.2. Materials and Methods

4.2.1 Materials

Iron (III) chloride hexahydrate ($FeCl_3 \cdot 6H_2O$); iron (II) chloride tetrahydrate ($FeCl_2 \cdot 4H_2O$); 2, 2 bipyridine (Bpy); copper (I) bromide (CuBr); and copper (powder <425 micron) were obtained from Sigma Aldrich (St Louis, MO). Citric acid monohydrate (CA) was obtained from Fisher Scientific and ammonium hydroxide (NH_4OH) from EMD Chemicals (Gibbstown, NJ). 3-bromopropyl trimethoxysilane (BPTS) was obtained from Gelest Inc. (Morrisville, PA). Poly(ethylene glycol) (N = 400) dimethacrylate (PEG400DMA) was obtained from Polysciences Inc. (Warrington, PA). All materials were used as received.

4.2.2 Iron Oxide Nanoparticle Synthesis

A one-pot co-precipitation method was used to prepare the core citric acid coated iron oxide nanoparticles [35]. Aqueous solutions of $FeCl_3 \cdot 6H_2O$ and $FeCl_2 \cdot 4H_2O$ were combined in a 2:1 molar ratio in a sealed three-neck flask under vigorous stirring and an inert N_2 environment. Once 85 °C was reached, 5 mL of NH_4OH was injected into the vessel followed by 4 ml of 2 M citric acid. The reaction was carried out for 1 hour. The
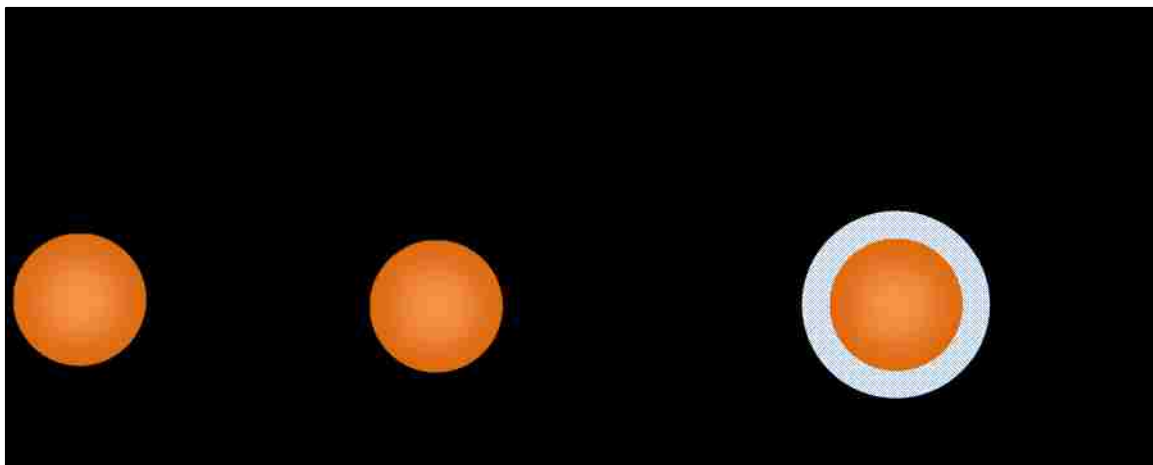
Scheme 4.1. Chemical structures of materials utilized in the iron oxide functionalization: (a) citric acid (CA), (b) 3-bromopropyl trimethoxysilane (BPTS), (c) Poly(ethylene glycol) (N = 400) dimethacrylate (PEG400DMA). (d) Schematic of ligand exchange and ATRP reaction on the nanoparticles.

particles were washed with ethanol and retrieved with magnetic decanting. Following the wash the particles were dried and stored under vacuum.

4.2.3 Silane Initiator

Through a ligand exchange, the citric acid coating was replaced with a silane initiator, BPTS. The particles and initiator were mixed in a 1:2.5 mass ratio in a water-ethanol solution. The mixture was stirred for 24 hours at room temperature. The particles were washed with ethanol and retrieved by magnetic decanting.

4.2.4 Surface Initiated Polymerization

The initiator coated particles were re-suspended in ethanol for the ATRP reaction. The amount of Bpy and CuBr catalyst was determined as a ratio to macromer. The ratios used were 1:0.01 for CuBr and 1:0.04 for Bpy. 4-5 crystals of Cu(0) were combined with the catalyst in 15 ml of ethanol. The catalyst solution and particles were placed in a flask under N2 flow and heated to 50 °C. 5 g of PEG400DMA macromer was diluted in 10 ml of ethanol and injected into the vessel once the temperature reached 50 °C. The reaction was carried out for 24 hours and after which the particles were magnetically decanted and washed and stored under vacuum.

4.2.5 Characterization

Fourier Transform infrared (FTIR) spectra. Attenuated total reflectance FTIR (ATR-FTIR) was used to determine surface functionalization with a Varian Inc. 7000e spectrometer. Dried samples were placed on the diamond ATR crystal and the spectrum was obtained between 700 and 4000 cm^{-1} for 32 scans.

Thermal gravimetric analysis (TGA). TGA was used to quantify the mass percent of the iron oxide core particle. Measurements were performed using a Netzsch Instruments STA

449A instrument. Approximately 10 mg of dried sample was loaded and a heat rate of 5 °C/min under constant air flow was used. At 120 °C, the sample was held isothermal for 10 minutes to vaporize residual solvent and potential water vapor. The sample continued to heat at 5 °C/min until 600 °C. The presented values are normalized to the mass at 120 °C.

Dynamic Light Scattering (DLS). DLS measurements were obtained using a Malvern Zetasizer, Nano ZS90 instrument. Dried nanoparticles were diluted in DI water to a concentration of 200 μg/mL and dispersed using ultrasonication.

Alternating Magnetic Field heating. The AMF heating profile was observed using a custom made Taylor Winfield magnetic induction source and temperature was measured with a Luxtron FOT Lab Kit. Dried particles were diluted in DI water to a concentration of 5 mg/mL. One ml of solution was placed in a 2 ml centrifuge tube and placed in the center of the coil. The solution was heated in a field of approximately 55 kA/m in strength at 300 kHz frequency for 10 minutes.

4.2.6 Cytotoxicity Studies

NIH 3T3 murine fibroblasts (ATCC, Manassas, VA) at passages 6-8 were cultured in Dulbecco's Modified Eagle's Medium supplemented with 10 % v/v calf bovine serum, 10 μg/mL Fungizone (Invitrogen, Carlsbad, CA), and 2 μg/mL Penicillin-Streptomycin-Glutamine (ATCC) in an incubator at 37°C and 5% CO_2. The fibroblasts were then seeded into 12-well plates at 5000cells/cm^2 and incubated for 24 hours. A549 lung carcinoma cells (ATCC) at passages 5-8 were cultured in F-12K medium supplemented with 10% fetal bovine serum, 10 μg/mL Fungizone, and 2 μg/mL Penicillin-Streptomycin-Glutamine and seeded into 12-well plates at 6000cells/cm^2 and incubated for 24 hours. After 24 hours,

the cells were exposed to the various concentrations of nanoparticles. Nanoparticles were added to cell media at concentrations of 100 μg/mL, 500 μg/mL, and 1000 μg/mL. The nanoparticle solutions were made by dissolving dry nanoparticles into the respected cell media. After removal of the spent media, one milliliter of the nanoparticles solutions was added to each well containing the cells. The control wells also underwent a change with fresh media. The well plates were returned to the incubator for 24 and 48 hours. Cytotoxicity was determined using a Live/Dead Viability Assay, calcein AM and ethidium homodimer-1 were obtained from Invitrogen. The cells were imaged with fluorescent microscopy (Nikon Eclipse LV 100) and counted using the NIS-Elements BR 3.0 imaging software.

4.2.7 *In Vitro* Thermal Therapy

A549 lung carcinoma cells at the same passages as the cytotoxicity studies were used for *in vitro* thermal therapy. The cells were seeded into 6-well plates and 35 mm culture dishes at 6000 cells/cm^2 and incubated overnight. The cells were then exposed to 10 mg/mL nanoparticle solutions and allowed to incubate for 3 hours to allow interaction between the cells and the particles. After the 3 hour incubation period, the cells in the 35 mm dishes were exposed to the AMF source (citric acid coated: 27.9 kA/m at 301 kHz; PEG400DMA coated: 30.1 kA/m at 301 kHz) for 10 minutes while the real time temperature was measured with the fiber optic thermometer inserted into the center of the dish. Following the AMF exposure, the cells were returned to the incubator and allowed to incubate for 2 hours to allow time for the cellular response. Results of the thermal therapy were determined using the Live/Dead Viability Assay.
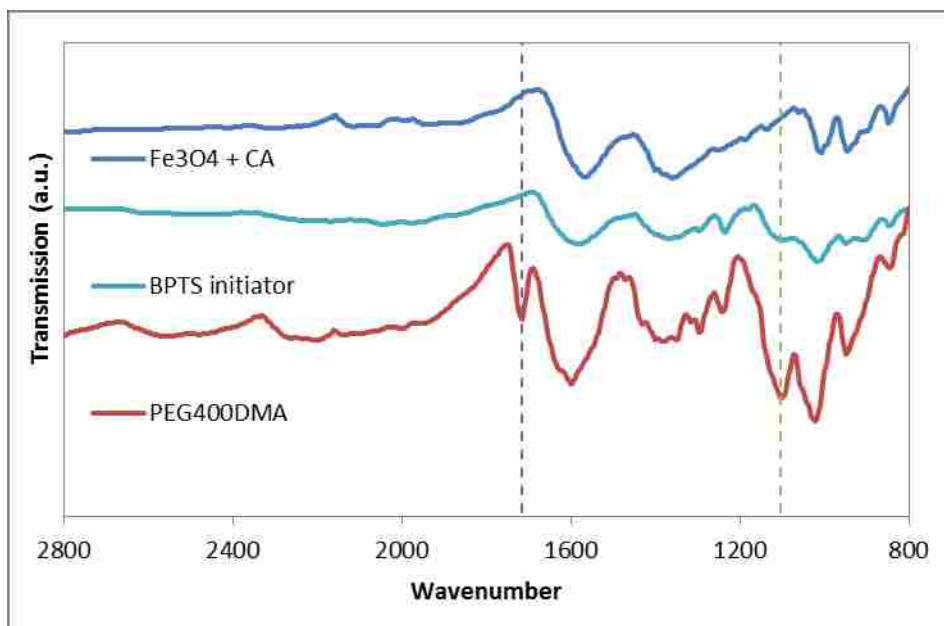
Figure 4.1: FTIR spectra of citric acid coated nanoparticles, particles after the BPTS ligand

exchange, and particles functionalized with PEG400DMA.
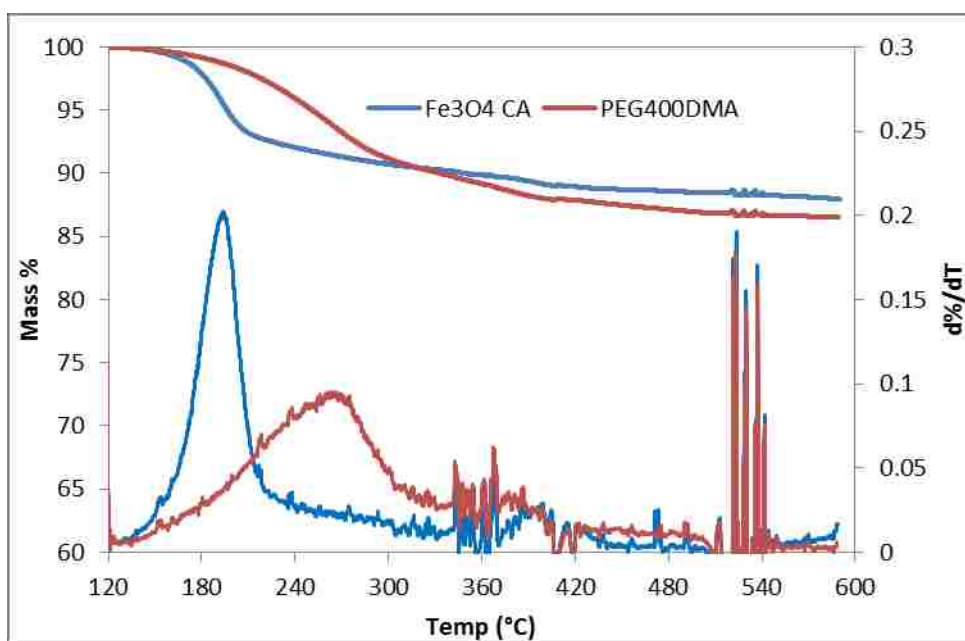
Figure 4.2: Mass loss and derivative profile of citrate and PEG400DMA coated iron oxide.
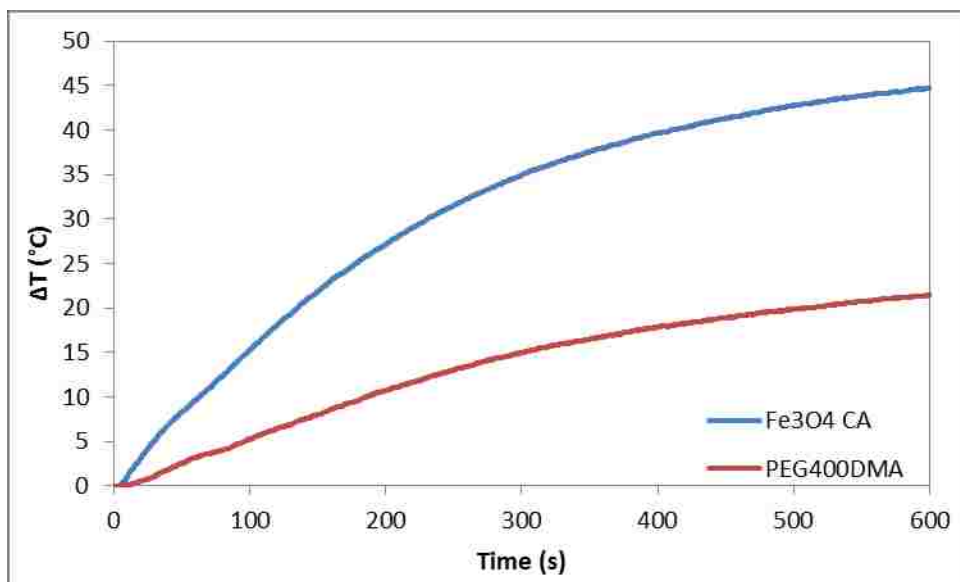
Figure 4.3: ΔT heating profile for citrate and PEG400DMA coated particles. Note: starting temperature was room temperature.

4.2.8 Statistical Analysis

Statistical analysis of the cytotoxicity and thermal therapy studies was performed using a two sample Student's t-test comparing viability to the control. To indicate significant toxicity defined by the following ranges: $p < 0.05$, $p < 0.001$ and $p < 0.001$, a single, double, or triple asterisk was included in the figures.

4.3. Results and Discussion

4.3.1 Nanoparticle Characterization

Confirmation of the successful ATRP reaction was observed in the FTIR spectra in **Figure 4.1** by the presence of peaks indicated by vertical lines at 1715 cm-1 and 1102 cm-1 corresponding to the carbonyl (C=O) stretch band and ether (C-O-C) stretch band from the PEGDMA coating.

From **Figure 4.2**, TGA indicated similar mass loss for both citrate and PEG400DMA coated particles, approximately 12 and 14% respectively, however a change in the profile was observed indicating different compounds. The citrate coating displayed its greatest mass loss between 150 and 220 °C which is similar to the values reported by Frimpong et al. [35]. PEG400DMA coated particles underwent its greatest mass loss between 200 and 320 °C. Hu et al. similarly reported the elimination of poly(ethylene glycol) chains from PEGylated magnetic nanoparticles by 350 °C which further confirms the presence of the polymer coating [20].

The hydrodynamic size of the particles was determined with DLS and reported as Z-average. Citrate coated nanoparticles were 62 nm with a PDI of 0.337% and PEG400DMA coated particles were 198 nm with a PDI of 0.227%. The larger size of the PEG400DMA coated particles may be the result of a cluster of iron oxide nanoparticles

forming the core due to aggregation during the synthesis and washing steps. Previous work with TEM has determined the citrate coated nanoparticles to be on the order of 10 nm.

The heating characteristic of the nanoparticle systems in an AMF was examined, and the heating profiles can be seen below in **Figure 4.3**. The specific absorption ratio (SAR) was calculated:

$$SAR = (\sum_i C_i m_i)/m * (\Delta T/\Delta t)$$ **Equation 4.1**

where C_i is the heat capacity, m_i is the individual mass of the components heated (in this case water and iron oxide nanoparticles), m is the mass of the component generating heat (iron oxide), and $\Delta T/\Delta t$ is the initial slope of the heating profile (the 25 and 30 second time points were used to calculate the slope). Calculations were based on specific heat capacities of 0.65 and 4.18 J/g*K for iron oxide and water respectively. The SAR values were determined to be 177.45 W/g and 62.26 W/g for citrate coated and PEG400DMA coated iron oxide respectively. The difference in SAR values can be explained by the citrate coated nanoparticles are in a freely dispersed stage while in aqueous solution allowing the iron oxide to be available for better heat effects [36].

4.3.2 Cytotoxicity Evaluation

Initial cytotoxicity studies have been carried out on both NIH 3T3 fibroblasts and A549 lung carcinoma cells with the PEG400DMA and citric acid coated iron oxide nanoparticles. The fibroblasts were selected to represent a general toxicity screen and the results are displayed below in **Figure 4.4**. At the 100 µg/mL concentration, the particles were relatively non-toxic as viability remained in the 80-85% range. As the concentration increased to 500 µg/mL and 1000 µg/mL there was a very significant decrease in viability for both particle systems. Looking at the fluorescent overlaid on the bright field images at
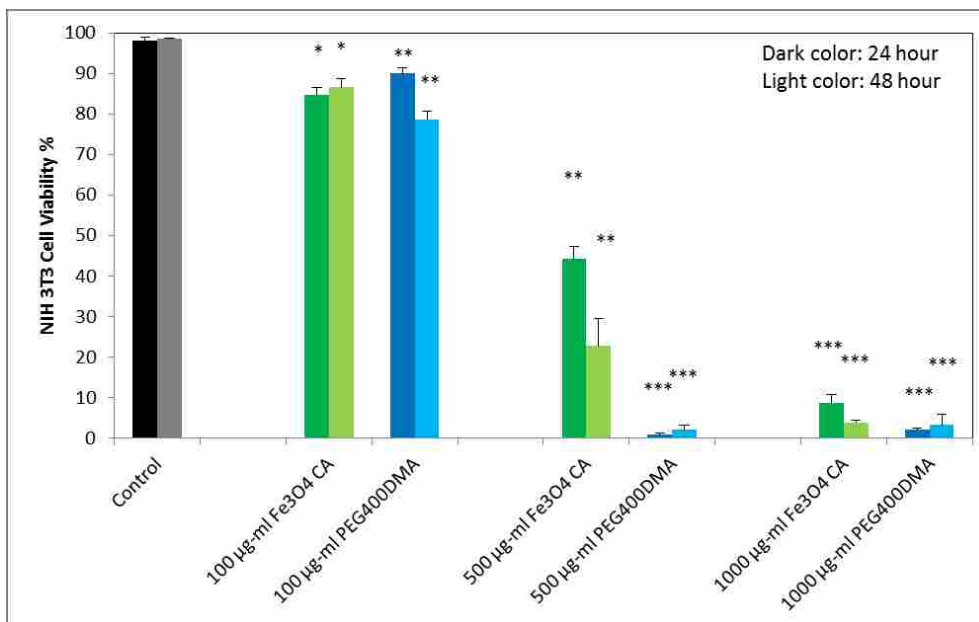
Figure 4.4: Percent viability of NIH 3T3 fibroblasts exposed to Fe_3O_4+CA and PEG400DMA coated nanoparticles. The error is reported as standard error.
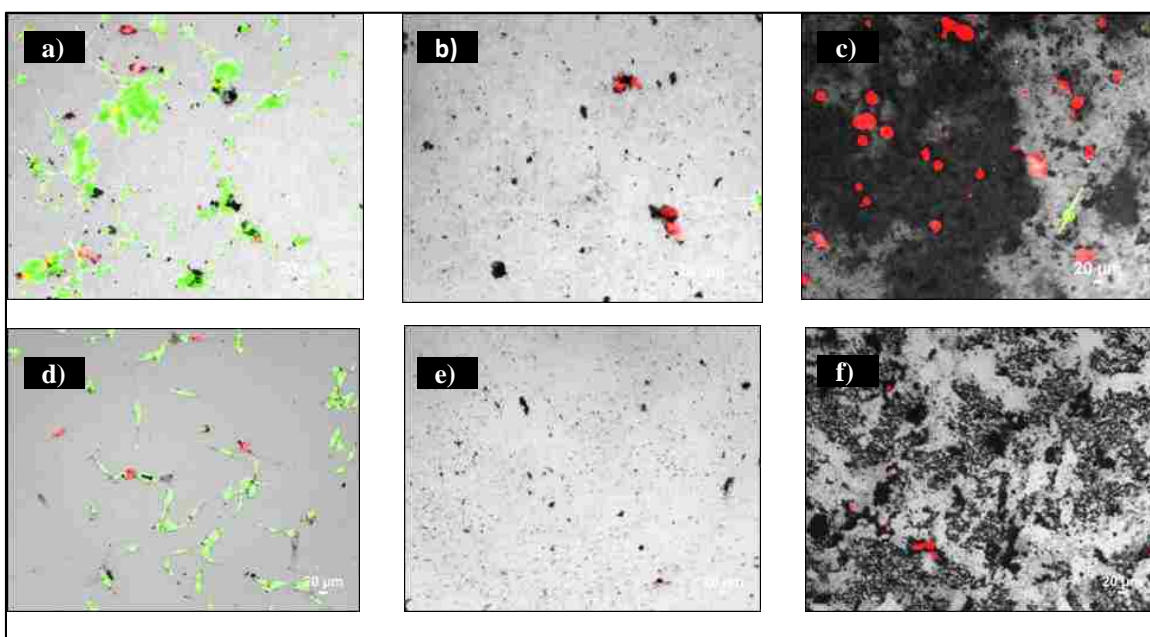
Figure 4.5: Fluorescent overlaid on bright field images for citrate coated particles at 100 μg/mL (a), 500 μg/mL (b), and 1000 μg/mL (c); and PEG400DMA coated particles at 100 μg/mL (d), 500 μg/mL (e), and 1000 μg/mL (f).
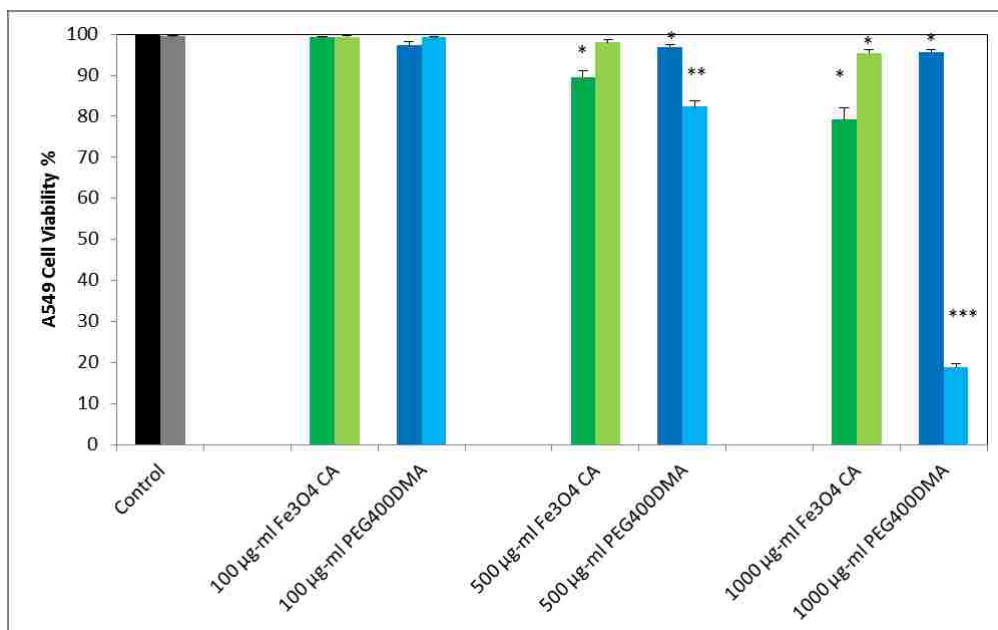
Figure 4.6: Percent viability of A549 lung carcinoma cells exposed to Fe_3O_4+CA and

PEG400DMA coated nanoparticles. The error is reported as standard error.
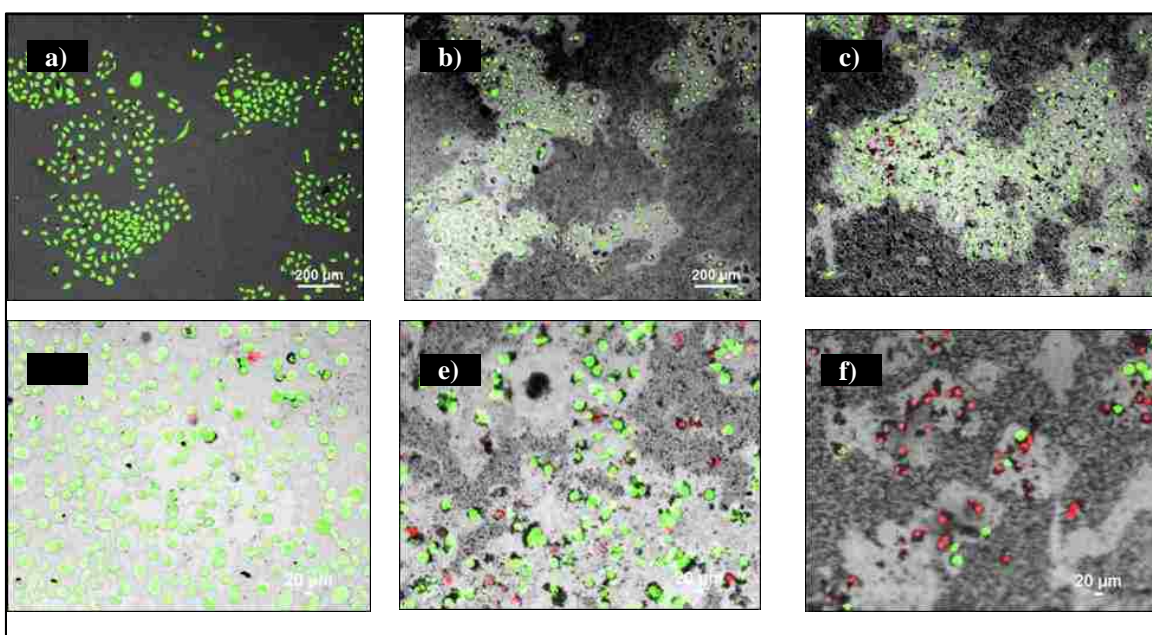
Figure 4.7: Fluorescent overlaid on bright field images for citrate coated particles at 100

μg/mL (a), 500 μg/mL (b), and 1000 μg/mL (c); and PEG400DMA coated particles at 100

μg/mL (d), 500 μg/mL (e), and 1000 μg/mL (f).

48 hour (**Figure 4.5**), the stability of the particles was an issue and the increased settling may have caused physical damage or had a suffocation effect on the cells.

A549 lung carcinoma was the cell line was selected for thermal therapy studies, so it too underwent the toxicity screening (**Figure 4.6**). Unlike the NIH 3T3 fibroblasts, minimal toxicity was observed until the 48 hour 1000 μg/mL PEG400DMA trial. At all three concentrations, the citric acid coated nanoparticles observed a bounce back behavior between 24 and 48 hours. This suggests that there was an initial stress from the exposure of the nanoparticles, but the cells recovered and continued to grow. PEG400DMA systems did not display this behavior and instead observed a decrease in viability between 24 and 48 hours at the higher concentrations. Representative images with the fluorescent overlaid on the bright field at 48 hours are shown in **Figure 4.7** and nanoparticle instability is observed as was the case with **Figure 4.5**. Since PEG is capable of preventing cell adhesion, perhaps the nanoparticles that have aggregated and coated the bottom of the well plate limited the space for cell growth and affected the cell viability between 24 and 48 hours.

From the NIH 3T3 results, we speculated that stability plays a major role in determining viability. The agglomeration of nanoparticles could have a physical suffocating effect by landing on top of the cells or occupying the space needed for propagation. However, a similar amount of particles can be seen out of solution in the PEG400DMA study where there was a minimal toxic effect at the higher concentrations, except for the 48 hour 1000 μg/mL PEG400DMA. Particle stability may still play a role since the local concentration of particles would increase over time, but cancer cells, generally being more resilient cell lines, and are able to withstand the higher local

concentration and physical effects especially during the first 24 hours. The results from the A549 screen indicate that high concentrations of nanoparticles can be used over a short time of exposure with limited toxicity.

4.3.3 Thermal Therapy Demonstration

The ability of the nanoparticle systems to kill cancer cells was explored by exposing cells doped with nanoparticle solutions to the AMF and heating to the thermoablation range. **Scheme 4.2** displays the set up utilized in this trial. Since the 35 mm dish was larger than the 0.625"ID coil, there was a distinct region in the center of the well where the field was the strongest and the particles heated more resulting in greater cellular death [37]. When determining the viability, images were taken from both the periphery and the center to demonstrate the two regions.

During the 10 minute field exposure, the real time temperature at the center of the well was monitored with a fiber optic thermometer. As seen in **Figure 4.8**, both nanoparticle systems heated to 55 °C, 9 °C above the thermoablation threshold which is indicated by the light blue line. The temperature surpasses the hyperthermia range within the first 100 seconds and steady state temperature is achieved after the 250 second mark.

When performing the live/dead assay, two regions were studied – the center of the well, where the field was the strongest, and the periphery, where the field strength is weaker and less nanoparticle heat is generated in this region. Particle systems exposed to the AMF are indicated by 'F' and systems remaining in the incubator are indicated by 'NF.' The control underwent a fresh media change at the same time as the samples dosed with nanoparticles. **Figure 4.9** displays the viability for each of the systems – both the center and periphery viabilities are displayed. During the relatively short exposure time, minimal
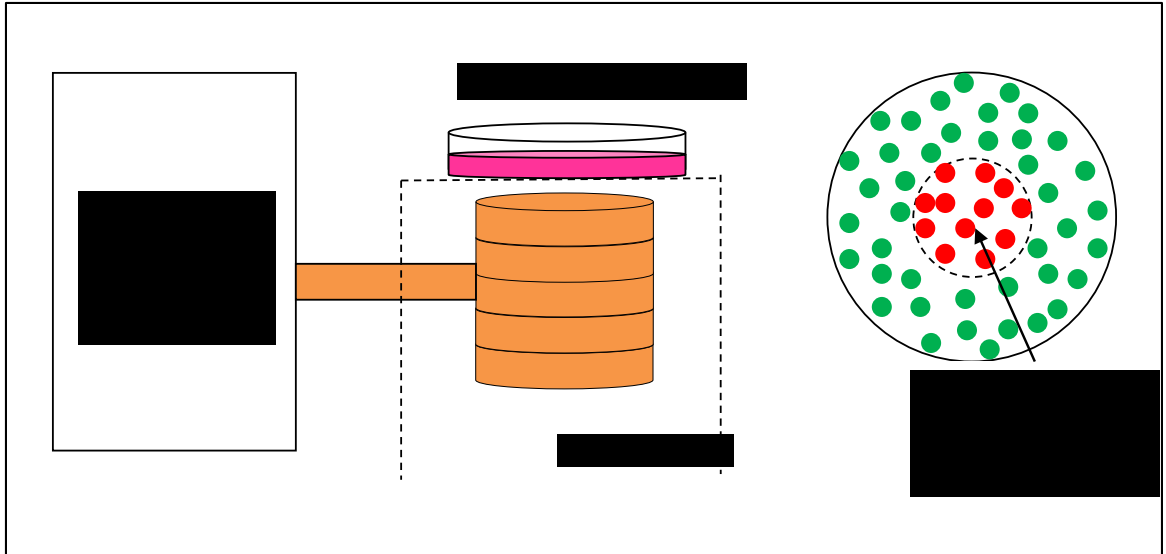
Scheme 4.2: (Left) Illustration of the alternating magnetic field set up and location of the 35 mm dish. (Right) Illustration of the distinct live/dead regions due to the greater heat generated in the center of the well.
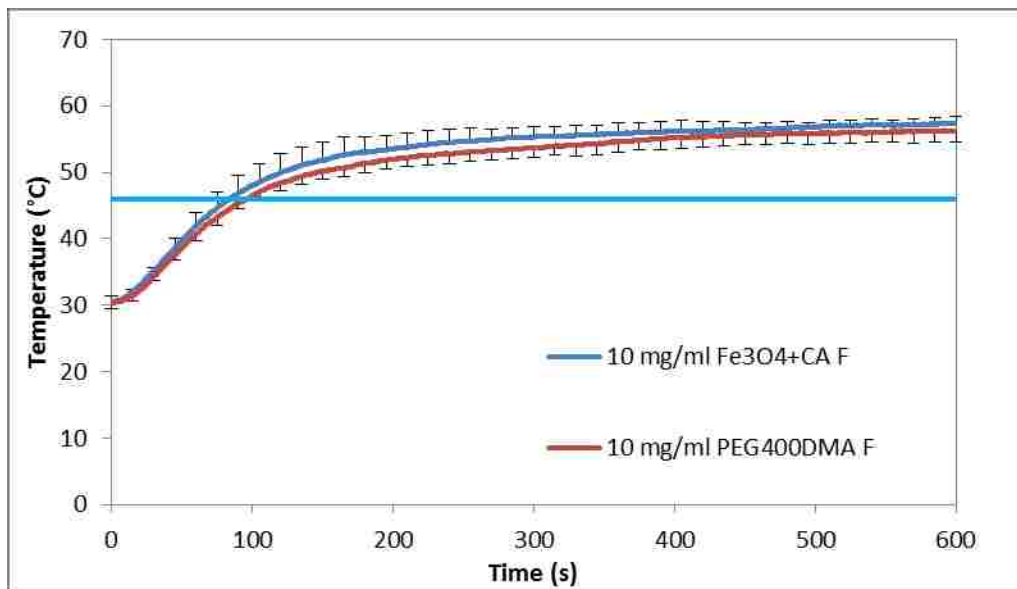
Figure 4.8: Real time temperature data measured at the center of the 35 mm dish. The light blue line indicates 46 °C, the thermoablation threshold. Citric acid coated particles have positive error bars (standard deviation) and PEG400DMA have negative error bars at every 15 s time point.
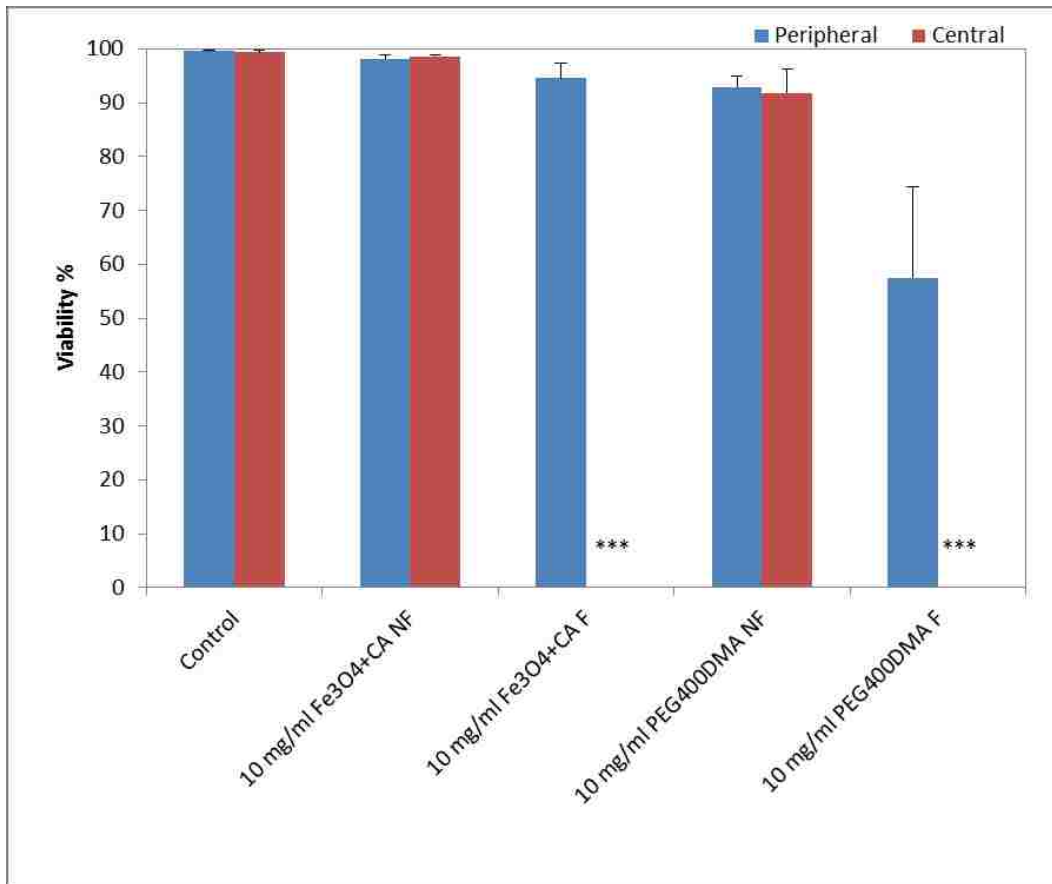
Figure 4.9: Cell viability of A549 lung carcinoma cells exposed to both citrate and PEG400DMA coated particles and AMF exposure (F – field exposure, NF – no field exposure).

toxicity was observed in the systems with nanoparticle solutions and no field exposure indicating that any cellular death with field exposure would be the result of the nanoparticle heating and not cytotoxicity. When the field was applied, there was total death at the center of the well for both the citric acid coated and PEG400DMA coated nanoparticles. This was expected since the thermoablation range was achieved and the cells underwent intense heating inducing necrosis. In the case of the citric acid coated nanoparticles, there was minimal toxicity in the periphery, and the viability was similar to the nanoparticle only systems. The PEG400DMA had a lower viability (60% range) but the two distinct regions of live/dead were observed.

4.4. Conclusion

This study reports the use of ATRP to successfully coat iron oxide nanoparticles with a PEG-based polymer shell and studied the thermoablative properties. During the 24 and 48 hour cytotoxicity studies, the viability of the NIH 3T3 fibroblasts decreased with increasing concentration, and the lower viability for cells exposed to PEG400DMA coated particles was likely a result of stability issues with that system. Using a relatively short exposure time, higher concentrations of magnetic nanoparticles were shown to be effective in thermal therapy studies demonstrating cellular death in the center of the well where the field was the strongest and the temperature achieved was in the thermoablative range. This nanoparticle system can further be explored as a means of co-delivering thermal therapy at hyperthermia temperatures with chemotherapeutics to improve the treatment efficacy.

4.5. References

References are located at the end of the dissertation subdivided by chapters.

Chapter 5: Accelerated Generation of Free Radicals by Iron Oxide Nanoparticles in the Presence of an Alternating Magnetic Field

The surfaces of iron oxide nanoparticles are capable of catalytically generating reactive oxygen species (ROS) through the Fenton and Haber-Weiss reactions. When exposed to an alternating magnetic field (AMF), iron oxide nanoparticles absorb the energy from the magnetic field and convert it into heat. In this study, we observed an increase in the degradation of methylene blue when a suspension of magnetite (Fe_3O_4) nanoparticles was exposed to an AMF indicating there was an increase in the ROS generation in response to the AMF. The increase in ROS generation compared to the Arrhenius prediction was both time and concentration dependent; in which we observed a decrease in ROS enhancement with increased time of exposure and concentration. We postulate that the decrease is due to agglomeration in the presence of the field. As the nanoparticles agglomerate, there is a decrease in surface area per mass limiting the reaction rate. The information included here is adapted or directly taken from work previously published:

> Robert J. Wydra, Catherine E. Oliver, Kimberly W. Anderson, Thomas D. Dziubla, J. Zach Hilt. Accelerated Generation of Free Radicals by Iron Oxide Nanoparticles in the Presence of an Alternating Magnetic Field. RSC Advances. 5: 18888-18893, 2015.

Reprinted with permission from The Royal Society of Chemistry.

5.1. Introduction

Magnetic nanoparticles are of great interest to a wide range of applications due to their unique physical properties [1, 2]. These applications include catalysis, biomedical imaging, anemia supplement, drug delivery, thermal therapy, and environmental

remediation [3-9]. One physical property that has presented itself as a double-edged sword is the generation of free radicals attributed to Fenton and Haber-Weiss chemistries. In the case of biomedical applications, the generation of free radicals leads to oxidative stress which is believed to be one of the key underlying mechanisms of concentration dependent cytotoxicity [10-16]. At the same time, iron oxide nanoparticles are combined with hydrogen peroxide and successfully used as advanced oxidation processes for the removal organic contaminates from wastewater [17]. In both cases, iron oxide nanoparticles act as a homogeneous and heterogeneous catalyst for the degradation of hydrogen peroxide into free radicals. The catalytic mechanism is based on the environment. Under neutral conditions, Voinov et al. have demonstrated through spin-trapping EPR that γ-Fe_2O_3 nanoparticles produce hydroxyl radicals primarily on the surface rather than dissolution of free ions [18]. At lower pH, such as the microenvironment of a lysosome, iron ions can be released from the nanoparticle surface resulting in a greater extent of homogeneous catalysis [19].

When exposed to an alternating magnetic field (AMF), magnetic nanoparticles absorb the energy from the magnetic field and convert it into heat through primarily through Brownian relaxation (physical rotation of the particles) and Neel relaxation (rotation of the magnetic moment) [20]. This heat generation has been extensively studied as magnetic fluid thermal therapy for the treatment of cancer [21, 22]. Until recently, intracellular hyperthermia has been considered improbable due to heat transport calculations by Rabin that demonstrated theoretically the heat generated from a single nanoparticle or cluster of nanoparticles would be negligible to the cell [23]. However, work by Creixell et al. has demonstrated that internalized targeted nanoparticles can induce

cellular death when exposed to an alternating magnetic field without a measurable temperature rise [24]. In follow-up work, the surface temperature of the nanoparticles was shown to instantly increase and to drive a temperature responsive polymer beyond its lower critical solution temperature of 35 °C without an immediate increase in solution temperature [25]. Thereby, they demonstrated that the localized heating from the nanoparticle surface is capable of altering surrounding chemistry and possibly a mechanism of the previously reported toxicity. The exact mechanism of toxicity is still under debate, however the evidence of a local heating effect provides interesting scenarios where the energy dissipated by the nanoparticles can be utilized to only alter the near surrounding volume.

The kinetic behavior of the advanced oxidation process involving magnetic nanoparticles to mineralize pollutants has been extensively studied [26-29]. Temperature is one of the driving factors of the Fenton-like reaction up to about 40 °C [30]. Above this temperature, hydrogen peroxide begins to degrade into oxygen and water limiting the reaction. To date, no one has studied the effect of AMF exposure on the generation of free radicals from iron oxide nanoparticles.

The main objective of this study is to determine the influence of AMF exposure on the degradation of methylene blue by magnetite nanoparticles (Fe_3O_4) and hydrogen peroxide. Three iron oxide concentrations were selected based on their ability to heat the surrounding media. The low concentration of iron oxide nanoparticles did not heat the solution above the radiant heat from the inductive source coil; whereas the high concentration actively heated the solution. The kinetic behavior was first determined using temperature controlled water baths. This data was used to extrapolate an Arrhenius

relationship which provided theoretical values based on the temperature achieved during AMF exposure. The reported enhancement was defined as the ratio of the experimental degradation observed compared to the theoretical value.

5.2. Materials and Methods

5.2.1 Materials

Iron (III) chloride hexahydrate ($FeCl_3 \cdot 6H_2O$); iron (II) chloride tetrahydrate ($FeCl_2 \cdot 4H_2O$); hydrogen peroxide (H_2O_2); and methylene blue (MB) were obtained from Sigma Aldrich (St Louis, MO). Ammonium hydroxide (NH_4OH) was obtained from EMD Chemicals (Gibbstown, NJ). All materials were used as received.

5.2.2 Iron Oxide Nanoparticle Synthesis

A one-pot co-precipitation method was used to prepare the iron oxide nanoparticles as similarly reported previously [31]. Briefly, aqueous solutions of $FeCl_3 \cdot 6H_2O$ and $FeCl_2 \cdot 4H_2O$ were combined in a 2:1 molar ratio in a sealed three-neck flask under vigorous stirring and an inert N_2 environment. Once 85 °C was reached, a 1.5 M solution of NH_4OH was injected into the vessel and the reaction was carried out for 1 hour. The nanoparticles were initially decanted via magnetic decantation to remove majority of the impurities. After, they were resuspended in water and transferred to a dialysis bag for 48 hours of dialysis. Following the washing steps, the particles were stored in suspension.

5.2.3 Nanoparticle Characterization

Dynamic Light Scattering (DLS). DLS measurements were obtained using a Malvern Zetasizer, Nano ZS90 instrument. Nanoparticles were diluted in DI water to a concentration of 200 μg/mL and dispersed using ultrasonication.

Alternating Magnetic Field heating. The AMF heating profile was observed using a custom made Taylor Winfield magnetic induction source and temperature was measured with a Luxtron FOT Lab Kit. Nanoparticles were diluted in DI water to a concentration of 5 mg/mL. One ml of solution was placed in a 2 ml centrifuge tube and placed in the center of the coil. The solution was heated in a field of approximately 60 kA/m in strength at 292 kHz frequency for 5 minutes.

5.2.4 Methylene Blue Degradation

The methylene blue degradation experiments were performed in 2 ml microcentrifuge tubes in either temperature controlled water baths or exposed to an AMF. One ml samples were prepared by diluting stock concentrations of methylene blue to 5 µg/ml and iron oxide nanoparticles to 37.5, 75, and 150 µg/ml. The samples were placed in the water bath for 10 min to equilibrate to the set temperature. The degradation was initiated by spiking the samples with 25 µl of 30% H_2O_2 to a working concentration of 245 mM. After given time intervals the samples were centrifuged for 30 s using a Phenix Quickspin Centrifuge, magnetically decanted, and measured using UV-visible spectroscopy (maximum absorbance at 665 nm) with a Varian Cary. To account for nanoparticle scattering from the nanoparticles that remain in suspension, samples containing only nanoparticles were measured and subtracted out from the sample absorbance.

Samples exposed to the AMF were prepared as described above. They were placed in water baths which corresponded to the expected steady state temperature as a result of field exposure. The samples were exposed to a magnetic field of approximately 51.0 kA/m
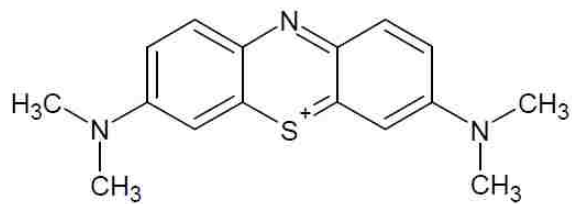
Scheme 5.1. Molecular structure of methylene blue.
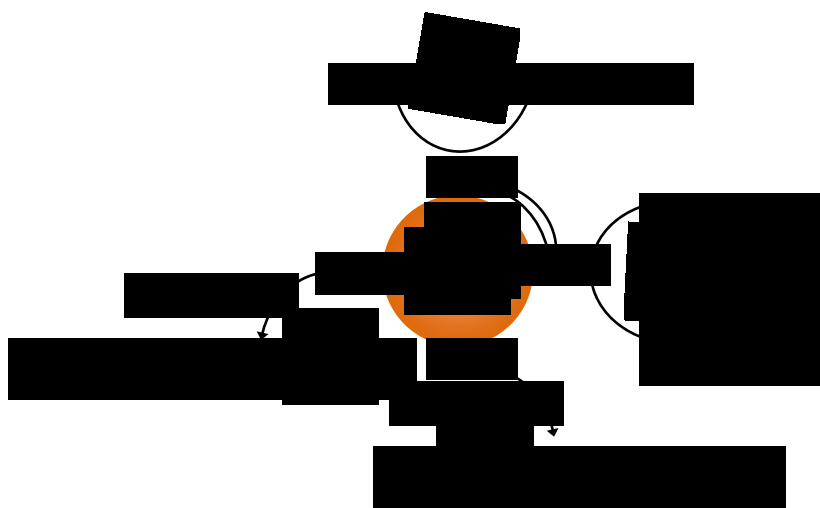
Scheme 5.2. Diagram of potential Fenton/Haber Weiss reactions initiated by iron oxide nanoparticles.
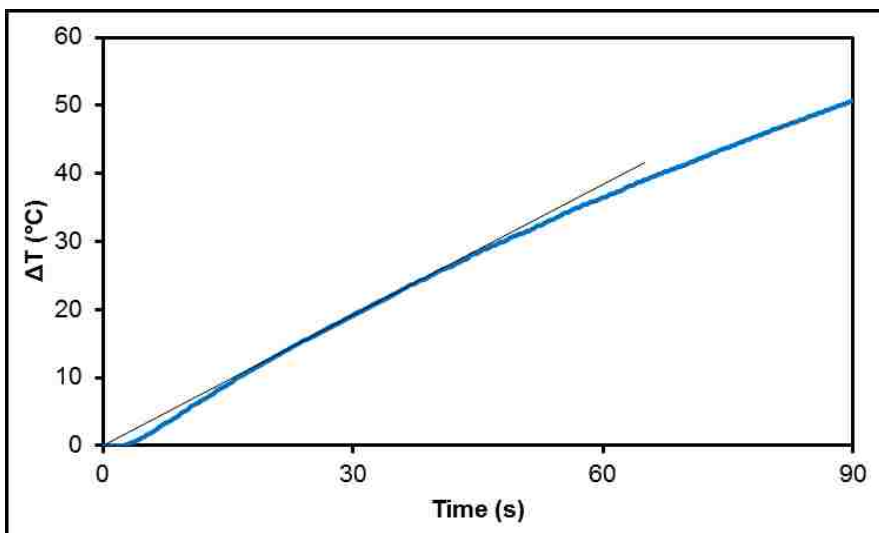
Figure 5.1. ΔT heating profile uncoated iron oxide a nanoparticle where starting

temperature was room temperature. The tangent line indicated the slope used in the SAR

calculations.

76

in strength at 292 kHz frequency while temperature was measured with a Luxtron FOT Lab Kit.

5.2.5 Statistical Analysis

Statistical analysis of the enhancement factor was determined using a one sample t-test where the hypothetical mean was set to 1. To indicate significant enhancement a single, double, or triple asterisk corresponding to $p < 0.05$, 0.01, and 0.001 respectively were included in the figure.

5.3. Results and Discussion

5.3.1 Nanoparticle Characterization

The hydrodynamic size of the particles was determined with DLS and reported as Z-average. Iron oxide nanoparticles were 107 nm with a PDI of 0.176 when dispersed in water. Previous work with TEM has determined the core nanoparticles to be on the order of 10 nm. As these are uncoated nanoparticles with no stabilizing group, agglomerates are likely contributing the in the increase in hydrodynamic size compared to the crystal size observed in TEM.

The heating characteristics of the nanoparticle systems in an AMF were examined, and the heating profiles can be seen below in **Figure 5.1**. The specific absorption ratio (SAR) was calculated:

$$SAR = (\textstyle\sum_i C_i m_i)/m * (\Delta T/\Delta t) \qquad\qquad \textbf{Equation 5.1}$$

where C_i is the heat capacity, m_i is the individual mass of the components heated (in this case water and iron oxide nanoparticles), m is the mass of the component generating heat (iron oxide), and $\Delta T/\Delta t$ is the initial slope of the heating profile (the 25 and 35 second time points were used to calculate the slope). Calculations were based on specific heat

capacities of 0.65 and 4.18 J/g*K for iron oxide and water respectively. The SAR value was determined to be 535.5 ± 25.8 W/g at an AMF of approximately 60 kA/m in strength at 292 kHz frequency.

5.3.2 Methylene Blue Degradation

The rate of radical generation was determined by analyzing the rate of methylene blue (**Scheme 5.**1) degradation. In a Fenton-like system, as illustrated in **scheme 5.2**, iron ions react with hydrogen peroxide to generate highly reactive hydroxyl and superoxide radicals. These radicals attack bonds on methylene blue fracturing the molecule into colorless intermediates. Possible splitting sites include the C-S+=C and the C-N=C of the central ring or hydroxylation of the aromatic side rings [32, 33]. It was determined that the degradation of methylene blue was catalyst driven, as there were negligible effects of hydrogen peroxide alone or adsorption onto the nanoparticle surface on measured absorbance.

The kinetic data was initially fit to a pseudo-first-order and second-order models as explored previously in literature [34, 35]. Relating concentration as a function of relative absorbance, we had the following rate models:

$$d(A_t/A_o)/dt = -k_1(A_t/A_o) \qquad \textbf{Equation 5.2}$$

$$d(A_t/A_o)/dt = -k_2(A_t/A_o)^2 \qquad \textbf{Equation 5.3}$$

Where k_1 and k_2 are the first and second order rate constants, and A_t is the measured absorbance at a given time normalized to the initial absorbance, A_o. Integrating equations 2 and 3 results in the following:

$$\ln(A_t/A_o) = k_1 t \qquad \textbf{Equation 5.4}$$

$$1/(A_t/A_o) = k_2 t + 1 \qquad \textbf{Equation 5.5}$$
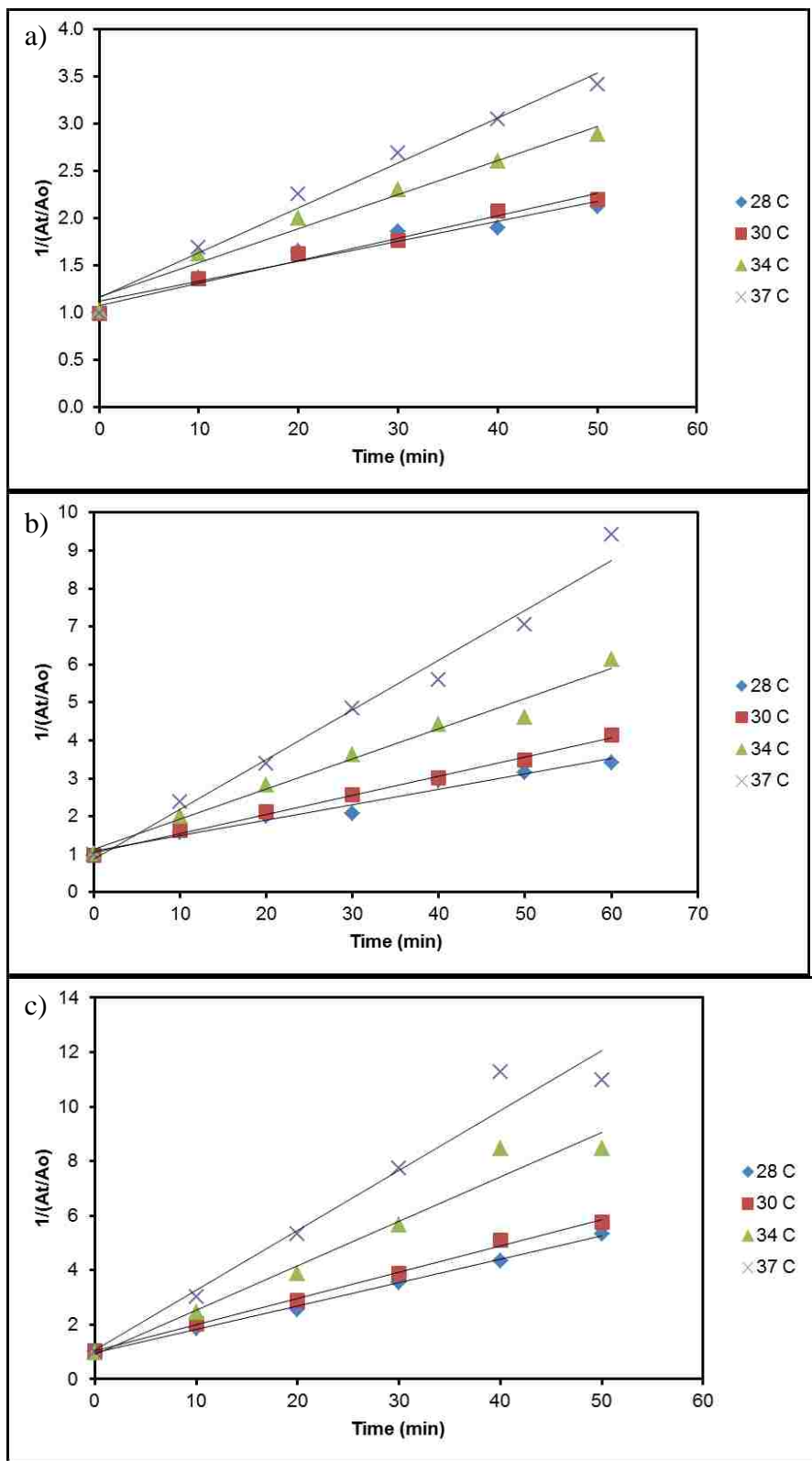
Figure 5.2. Second-order kinetic plots of methylene blue degradation at 37.5 µg/ml (a), 75

µg/ml (b), and 150 µg/ml (c) iron oxide concentration.

The methylene blue degradation data was fit using the above equations to determine the respective rate constants using a linear regression. The pseudo-first-order model was rejected because the y-intercept never approached 0 for any of the concentrations or temperatures tested. The second-order model, seen in **Figure 5.2**, fit the methylene blue degradation as observed previously [35]. The linear correlation coefficients ($R2$) were in the neighborhood of 0.95 again confirming the accuracy of the linear model.

By studying methylene blue degradation at various temperatures, an Arrhenius type relationship was determined. Based on the slopes observed in **Figure 5.2** the reaction was temperature dependent where there was an increase in reaction with increased temperature as expected by Fenton-like chemistry. Using the Arrhenius equation:

$$k = A\exp(-E_a/RT) \hspace{4cm} \textbf{Equation 5.6}$$

where A is the pre-exponential factor, E_a is the activation energy, R is the ideal gas constant, and T is the reaction temperature. Converting **Equation 5.6** into a linear relationship between $\ln(k)$ and $1/T$, the previously determined reaction rates were plotted into **Figure 5.3**. The derived activation energy and pre-exponential factor are listed in **Table 5.1** for the given concentration of iron oxide studied.

Deriving an Arrhenius relationship was essential to provide a comparative basis for the AMF studies. The three iron oxide concentrations studied were selected based on their ability to heat the surrounding media. When the AMF source is activated, the copper coil heats instantaneous and begins to radiate heat to the sample. At the AMF field amplitude used, a solution of methylene blue would heat to 32-32.5 °C. At 37.5 µg/ml iron oxide concentration, the measured solution temperature never exceeded this range with 15 minutes of heating. This implies that the amount of heat generated from the nanoparticle

surface is insufficient to significantly heat the surrounding volume of water. At 75 µg/ml iron oxide, the measured solution temperature was 33.5-34 °C, and at 150 µg/ml, the measured temperature was 36-36.5 °C resulting in a 1.5 and 4 °C temperature rise respectively. At these concentrations the heat generated from the nanoparticle surface actively heated the solution temperature. From the measured steady state temperature of each sample, a theoretical concentration was calculated using the Arrhenius relationship. This value was compared to the experimentally measured absorbance through the following enhancement factor (EF) equation:

$$EF = (1-(A_t/A_o)_{exp}) \: / \: (1-(A_t/A_o)_{theo}) \hspace{2cm} \textbf{Equation 5.7}$$

Where $(A_t/A_o)_{exp}$ is the experimental concentration and $(A_t/A_o)_{theo}$ is the theoretical concentration of methylene blue. The enhancement factor results are displayed in **Figure 5.4**. The lowest concentration, 37.5 µg/ml, displayed very significant ROS enhancement over the three time periods studied. At 5 minutes of exposure, 75 µg/ml was significant, but the enhancement decreased to no measurable enhancement by 15 minutes. The highest concentration never displayed a significant enhancement.

At the lower concentrations of nanoparticles, the local nanoscale heating effects would be more pronounced than at the highest concentration. At these concentrations, energy would be dispersed to the local area driving the catalytic degradation of methylene blue. This energy, however, is insufficient to heat the surrounding volume resulting in no measurable temperature rise. Thus, we would expect the kinetic behavior to be similar to the temperature elevated a few degrees resulting in the observed enhancement. At the highest concentration the measured temperature corresponds closer the local surface temperature and hence no enhancement.

81
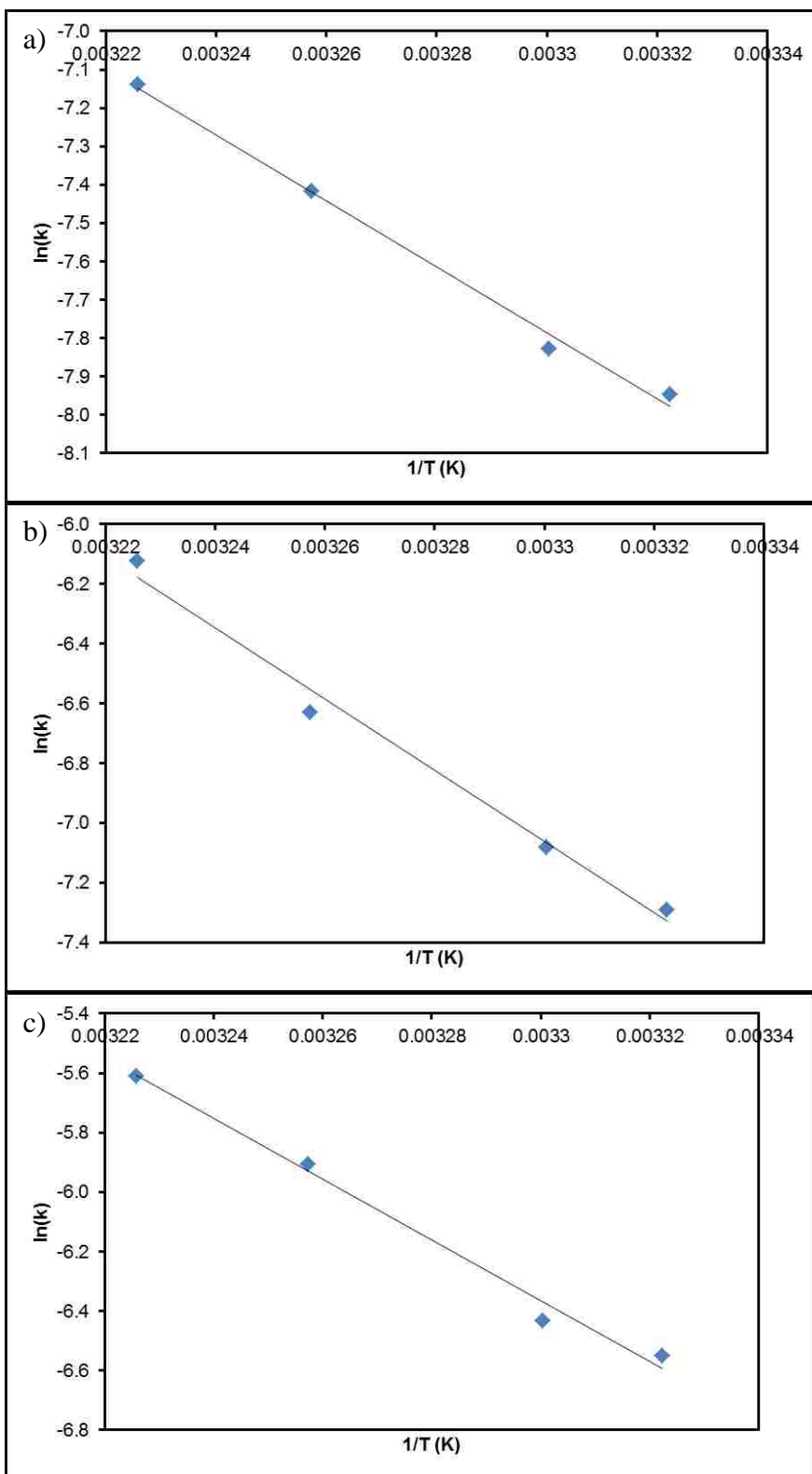
Figure 5.3. Arrhenius plots derived from second order kinetic model from methylene blue degradation at 37.5 µg/ml (a), 75 µg/ml (b), and 150 µg/ml (c) iron oxide concentration.

Table 5.1. Arrhenius constants of methylene blue degradation at various concentrations of

iron oxide nanoparticles.

Concentration	$-E_a$ (J/mol)	A (s^{-1})
37.5 µg/ml	7.15e4	8.79e8
75 µg/ml	9.91e4	1.05e14
150 µg/ml	8.48e4	7.27e11
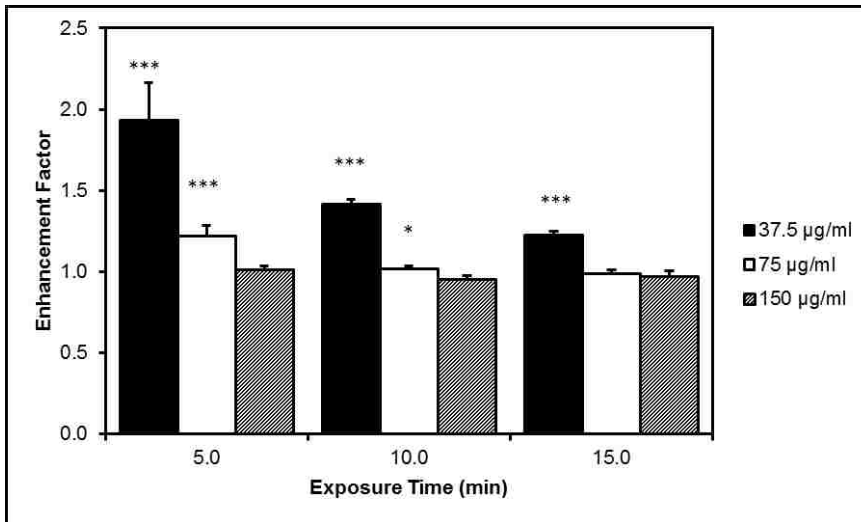
Figure 5.4. Enhancement factor comparing extent of methylene blue degradation based on

experimental and theoretical values at different concentrations of iron oxide nanoparticles

and length of AMF exposure.

When enhancement was observed, the degree of enhancement declined with length of AMF exposure. One possible explanation is the reversible agglomeration of the nanoparticles induced by the magnetic field. Being paramagnetic, the nanoparticles would be attracted to each other resulting in aligned chains or clusters [36, 37]. In this agglomerated state, the available surface area of the nanoparticles would be reduced affecting the catalyst potential. This further confirms a recent observation made by Sharma et al. where the degree of cellular oxidative stress was a function of iron oxide nanoparticle surface area as opposed to mass delivered [38]. Nanoparticle concentration is one of the hallmark factors of colloidal stability and could explain why no enhancement was observed at the highest concentration. Elevated concentrations of magnetic nanoparticles display observable changes in colloidal stability when exposed to the AMF. While not significant, the enhancement factor of the 150 µg/ml system was below 1 at the 10 and 15 minute exposure times. Future experiments investigating the role of aggregation state on the magnetic field heating enhancement factor are warranted.

This study provides a direct example of utilizing the accelerated surface reactivity with AMF exposure for the degradation of a model pollutant. When translating this material property to a biological system such as within the cellular environment, however, there is room for scholarly debate. For starters, the intracellular concentration of H_2O_2 is typically around 0.5-0.7 µM but can be as high as 1 µM during proliferation signaling [39]. Cancer cells are known to have higher levels of H_2O_2 due to erratic signaling, so the intracellular level could conceivably be even higher than 1 µM, but these levels are significantly lower than the levels used in this study. With the decrease in relative concentrations of reactants, the reaction rates would predictably be slower. Most cancer

cells display an overexpression of Akt which causes them to be more susceptible to oxidative stress induced apoptosis [40]. Thus, even acute fluctuations of ROS levels from iron oxide catalyzed Fenton chemistry could have a detrimental effect on cancer cells. Here in the best case, we have demonstrated upwards of a two fold increase in ROS generation with AMF exposure. Future research should investigate whether this ROS generation corresponds with an effective concentration of iron oxide nanoparticles triggering a cytotoxic event.

5.4. Conclusions

This study reports the observed enhanced degradation of methylene blue by free radicals generated by iron oxide nanoparticles heated in an alternating magnetic field. The kinetic behavior of methylene blue degradation was modeled using a second-order reaction, and an Arrhenius relationship was extrapolated from the temperature dependence. When exposed to an alternating magnetic field, the nanoparticles at lower concentrations and exposure time are capable of degrading methylene blue at a greater extent than predicted by the Arrhenius relationship. This observation has multiple future applications, such as improving intracellular hyperthermia processes and reaction rates in advanced oxidation processes.

5.5 References

References are located at the end of the dissertation subdivided by chapters.

Chapter 6: The Role of ROS Generation from Magnetic Nanoparticles in an Alternating Magnetic Field on Cytotoxicity

Monosaccharide coated iron oxide nanoparticles were developed to selectively target colon cancer cell lines for magnetically mediated energy delivery therapy. The nanoparticles were prepared using a coupling reaction to attach the glucose functional group to the iron oxide core, and functionality was confirmed with physicochemical characterization techniques. The targeted nanoparticles were internalized into CT26 cells at a greater extent than non-targeted nanoparticles, and the nanoparticles were shown to be localized within lysosomes. Cells with internalized nanoparticles were exposed to an alternation magnetic field (AMF) to determine the potential to delivery therapy. Cellular ROS generation and apoptotic cell death was enhanced with field exposure. The nanoparticle coatings inhibit the Fenton-like surface generation of ROS suggesting a thermal or mechanical effect is more likely the source of the intracellular effect. The information included here is adapted or directly taken from work submitted for publication:

> Robert J. Wydra, Piotr Rychahou, B. Mark Evers, Kimberly W. Anderson, Thomas D. Dziubla, J. Zach Hilt. The role of ROS generation from magnetic nanoparticles in an alternating magnetic field on cytotoxicity. Acta Biomaterialia. (In review).

6.1. Introduction

Magnetic nanoparticles are being studied for a wide range of biomedical applications such as diagnostic imaging, drug delivery, and thermal therapy of cancer [1-4]. In the case of thermal therapy, the particles absorb the energy from the magnetic field and convert it into heat through the Brownian and Neel relaxation [5]. In most cases, the

nanoparticles rely on passive targeting to systemically circulate and accumulate in tumors via the phenomenon known as the enhanced permeability and retention effect [6]. To increase specific interactions with cells, nanoparticles can be functionalized with appropriate targeting ligands such as peptides, antibodies, and carbohydrates [7-9]. It has recently been demonstrated that targeted nanoparticles are not only capable of reaching the primary tumor but micrometastatic sites as well [10]. Coupled with the ground breaking work by Creixell et al. demonstrating that internalized targeted nanoparticles can induce cellular death when exposed to an alternating magnetic field without a measurable temperature rise, there is great interest to develop targeted nanoparticles for the treatment of metastatic cancer [11]. This intracellular effect, where the internalized nanoparticles deliver therapeutic gains without perceived temperature rise, has been coined as 'magnetically mediated energy delivery' (MagMED) represents a promising field of therapeutics but the exact mechanism of cytotoxicity still needs to be explored [12].

Intracellular hyperthermia was previously considered improbable due to heat transport calculations by Rabin that demonstrated theoretically the heat generated from a single nanoparticle or cluster of nanoparticles would be negligible to the cell or surrounding tumor [13]. However, it has been observed that the surface temperature of the nanoparticles is able to significantly exceed the solution temperature suggesting that a localized heating effect may attribute to the toxicity of the therapy [14]. In addition to a heating effect, chemical effects or mechanical damage from the physical rotation and vibration of the nanoparticles may induce toxicity. One potential chemical effect would be the result of surface mediated production of reactive oxygen species (ROS) from the iron oxide nanoparticles [15]. Free radical generation results in cellular oxidative stress which is

believed to be one of the key underlying mechanisms of cytotoxicity [16, 17]. When temperatures are raised to the hyperthermia range, ROS levels are amplified resulting in long-term cellular death [18]. This observation can be attributed to increased kinetic activity of the Fenton-like reaction with temperature or the decreased ability of cancer cells to scavenge ROS at the elevated temperature [18-20]. Recently, we have demonstrated that the generation of ROS is enhanced in presence of an alternating magnetic field [21]. At nanoparticle concentrations where there was no observable temperature rise, we observed a significant increase in ROS generation compared to the Arrhenius prediction.

Carbohydrate coated nanoparticles, or glyconanoparticles, are an attractive functionality in order to study molecular and cellular targeting by combining the physicochemical properties of the core nanoparticle with receptor interaction, stabilization, and relatively inexpensive compared to other targeting ligands (i.e. antibodies) advantages from carbohydrates [22-26]. Functionalizing nanoparticles with monosaccharides can provide similar passivation to poly(ethylene glycol) (PEG) while at the same time providing a targeting strategy for cells overexpressing glucose transporters [27-29]. Demonstrating therapeutic potential, gold nanoparticles functionalized with glucose were internalized at a greater rate by ovarian cancer cells and used as a sensitizer to enhance radiation therapy [30]. Specifically, we were interested in designing a nanoparticle system to target colon cancer liver metastasis. To date, fluorine-18-deoxyglucose has been successful in the accurate detection of colon cancer liver metastases with positron emission tomography suggesting glucose may be an interesting ligand to study [31].

In this paper, monosaccharide targeted nanoparticles were developed and assessed for their ability to be selectively internalized by colon cancer cell lines. Glucose coated

nanoparticles were synthesized using a two-step process (**Scheme 6.1**). Iron oxide core nanoparticles, selected for their ability to remotely heat in an AMF, were prepared utilizing a facile one-pot co-precipitation technique where a citric acid stabilizer was added during the core synthesis. Next, glucose functionality was attached to the surface through an amine-carboxyl coupling reaction involving D-glucosamine and the citric acid stabilizer. Once internalized, the cells containing nanoparticles were exposed to an alternating magnetic field and cellular ROS was measured. After exposure, we observed a significant increase in cellular ROS and an associated increased level of apoptotic cells.

6.2. Materials and Methods

6.2.1 Materials

Iron (III) chloride hexahydrate ($FeCl_3 \cdot 6H_2O$), iron (II) chloride tetrahydrate ($FeCl_2 \cdot 4H_2O$), D-(+)-glucosamine, and fluoresceinamine isomer I were obtained from Sigma Aldrich (St Louis, MO). Ammonium hydroxide (NH_4OH) was obtained from EMD Chemicals (Gibbstown, NJ). Citric acid monohydrate (CA) was obtained from Fisher Scientific and N-hydroxysuccinimide (NHS) and 1-ethyl-3-(3-dimethylaminopropyl) carbodiimide (EDC) were obtained from Thermo Scientific (Waltham, MA). All materials were used as received.

6.2.2 Synthesis of Iron Oxide Nanoparticles

A one-pot co-precipitation method was used to prepare the core citric acid coated iron oxide nanoparticles as reported previously [32]. Briefly, aqueous solutions of $FeCl_3 \cdot 6H_2O$ and $FeCl_2 \cdot 4H_2O$ were combined in a 2:1 molar ratio in a sealed three-neck flask under vigorous stirring and an inert N_2 environment. Once 85 °C was reached, 5 mL of NH_4OH was injected into the vessel followed by 4 ml of 2 M citric acid. The reaction
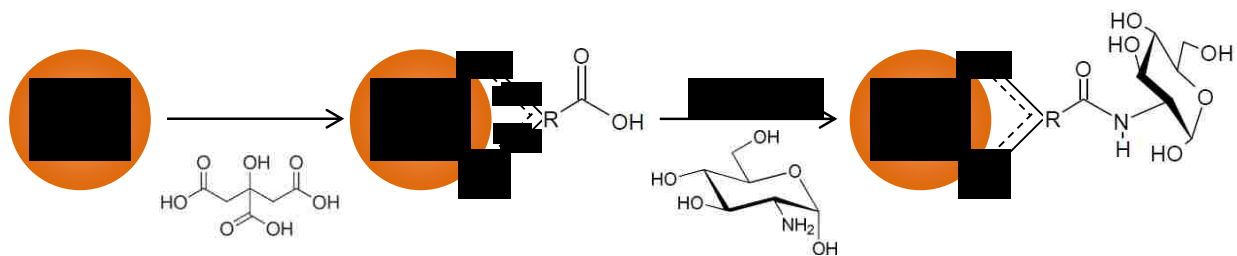
Scheme 6.1. Reaction schematic of monosaccharide coating of iron oxide nanoparticles displaying the attachment of the citric acid stabilizer and subsequent addition of D-glucosamine via amine-carboxyl coupling reaction.

was carried out for 1 hour. The particles were transferred to a dialysis tube for 24 hours of dialysis to remove unreacted chemicals.

6.2.3 Glucose Functionalization

Monosaccharide functional groups were attached to the nanoparticle surface through an amine-carboxyl coupling reaction utilizing NHS/EDC. A molar ratio of 10:1 molar EDC to carboxyl groups was used where the amount of citric acid per nanoparticle was estimated from TGA data. The NHS to EDC ratio was 5:2 molar and glucosamine was used in 10 fold by mass excess to the amount of nanoparticles. In a typical reaction, a stock 10 mg/ml suspension of citric acid coated nanoparticles was mixed with EDC/NHS in aqueous solution to facilitate activation of the carboxyl groups for 30 minutes. Glucosamine solution was prepared in PBS and added to the work up for a final working concentration of 5 mg/ml nanoparticles and allowed to react for 6 hours. Following the reaction, the nanoparticles were washed with dialysis.

6.2.4 Particle Characterization

Fourier Transform infrared (FTIR) spectra. Attenuated total reflectance FTIR (ATR-FTIR) was used to determine surface functionalization with a Varian Inc. 7000e spectrometer. Dried samples were placed on the diamond ATR crystal and the spectrum was obtained between 700 and 4000 cm^{-1} for 32 scans.

Thermal gravimetric analysis (TGA). TGA was used to quantify the mass percent of the iron oxide core particle. Measurements were performed using a TA Instruments SDT Q600 TGA/DSC instrument (New Castle, DE). Approximately 10 mg of dried sample was loaded and a heat rate of 5 °C/min under constant nitrogen flow was used. At 120 °C, the sample was held isothermal for 10 minutes to vaporize residual solvent and potential water

vapor from the atmosphere. The sample continued to heat at 5 °C/min until 450 °C. The presented values are normalized to the mass at 120 °C.

Dynamic Light Scattering (DLS) and zeta potential. DLS and zeta potential measurements were obtained using a Malvern Zetasizer, Nano ZS90 instrument (Westborough, MA). Nanoparticles from stock suspensions were diluted in DI water for DLS and 10 mM NaCl to a concentration of 200 µg/mL and dispersed via probe sonication.

6.2.6 Uptake and Localization

CT26 colorectal cancer cells were cultured in Dulbecco's Modified Eagle's Medium supplemented with 10 % v/v calf bovine serum, 10 µg/mL Fungizone (Invitrogen, Carlsbad, CA), and 2 µg/mL Penicillin-Streptomycin-Glutamine (ATCC) in an incubator at 37°C and 5% CO_2. The cells were seeded in a 35 mm culture dishes at 15000 cells/cm^2 and were allowed to become confluent. Dehydrated nanoparticles were suspended in DMSO at 5 mg/ml stock concentration. The nanoparticles were diluted to 200 µg/ml in cell media prior to exposure. The cells were exposed to nanoparticles for 0.5, 1, and 2 hours. After, the cells were washed 2x with warm DPBS, trypsinized, counted, and dehydrated prior to the Prussian Blue colorimetric assay. 100 µl HCl was used to digest the dry cell pellet and 10 µl of the digested pellet was transferred to a microcentrifuge tube where the reducing agent, hydroxylamine, was added for at least 8 hours. Finally, the iron ions were stained with a 5% potassium ferricyanide solution for 1 hour. Absorbance at 700 nm was measured with a GENios Pro fluorescence spectrophotometer (Tecan, Switzerland). Iron concentration standard curves were prepared using ferrous and ferric chloride salts.

To visualize the nanoparticle internalization a co-localization technique was utilized. First, the nanoparticles were fluorescently tagged with fluoresceinamine, isomer I through a competitive carboxyl-amine coupling reaction. The reaction work-up and purification was the same as the glucose functionalization step described above with a fluoresceinamine isomer I to glucosamine ratio of 0.02:1. The fluorescently tagged nanoparticles were diluted to 50 µg/ml and incubated with CT26 cells overnight. The cells were washed 2x with DPBS and stained with DAPI and Lysotracker Red. Post staining, the cells were imaged utilizing a fluorescent microscope and analyzed for internalization (Nikon Elements 4.2).

6.2.7 Cellular Response to Alternating Magnetic Field

Similar to above, CT26 cells were seeded in a 35 mm culture dishes at 15000 cells/cm^2 and were allowed to become confluent. The cells were doped with iron oxide nanoparticles from 5 mg/ml DMSO stocks and incubated for an additional 1 hour. The media was removed, washed 2x with warm DPBS, and cells were detached using trypsin. Cells were split into samples with and without field exposure and doped with 50 mM 6-carboxy-2',7'-dichlorodihydrofluorescein diacetate (carboxy-DCFDA) (Invitrogen). Cells were incubated at 37 °C for 30 minutes to facilitate stain internalization, exposed to the field for 30 minutes (Taylor Winfield magnetic induction source; approximately 60 kA/m in strength at 292 kHz frequency), and returned to the incubator for 30 minute post incubation. Cells were analyzed using an Accuri C6 flow cytometer (BD Biosciences, San Jose, CA). A ratio of the mean fluorescence between samples exposed to the AMF and the samples that remained in the incubator was used to determine the enhanced ROS generation attributed to the nanoparticles in the AMF.

To determine the effects of the treatment, a Caspase 3/7 Apoptosis assay (Invitrogen) was utilized. Following the intracellular procedure described above, the cells were stained with the reagent per the manufactures protocol immediately following the AMF exposure and allowed to incubate for 30 minutes. After the incubation period the cells were analyzed with flow cytometry. A ratio of the mean fluorescence between samples exposed to the AMF and the samples that remained in the incubator was used to assess the effects of the field exposure.

6.2.8 Surface ROS Generation

To determine the amount of ROS generated from the surface the nanoparticles a methylene blue degradation assay was used. The degradation experiments were performed in 2 ml microcentrifuge tubes where one ml samples were prepared by diluting stock concentrations of methylene blue to 5 µg/ml and iron oxide nanoparticles to 75 µg/ml. The samples were placed in the water bath for 10 min to equilibrate to the expected steady state temperature as a result of field exposure. The degradation was initiated by spiking the samples with 25 µl of 30% H_2O_2 to a working concentration of 245 mM. The samples were exposed to a field of approximately 51.0 kA/m in strength at 292 kHz frequency while temperature was measured with a Luxtron FOT Lab Kit. After given time intervals the samples were centrifuged for 30 s using a Phenix Quickspin Centrifuge, magnetically decanted, and measured using UV-visible spectroscopy (maximum absorbance at 665 nm) with a Varian Cary. To account for nanoparticle scattering from the nanoparticles that remain in suspension, samples containing only nanoparticles were measured and subtracted out from the sample absorbance.
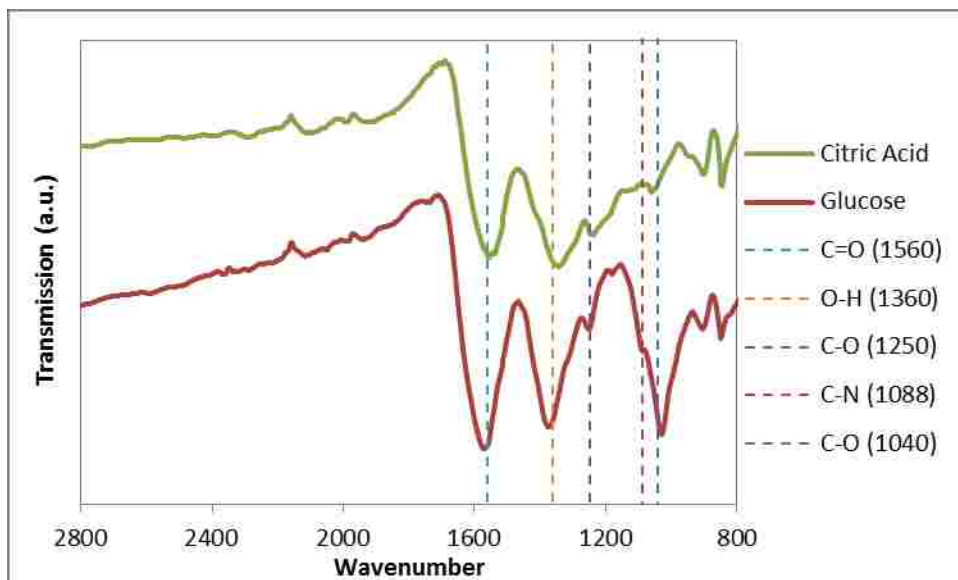
Figure 6.1. FTIR spectra of citric acid coated iron oxide and glucose coated samples. The vertical line at 1088 cm^{-1} indicates the location of a C-N vibration and at 1040 cm^{-1} indicated the location of C-O stretch peak attributed to the D-glucosamine. The vertical lines 1560 cm^{-1}, 1360 cm^{-1}, and 1250 cm^{-1} indicate the location of the C=O stretch, O-H bend, and C-O stretch bonds, respectively, typically attributed to citric acid coated particles.
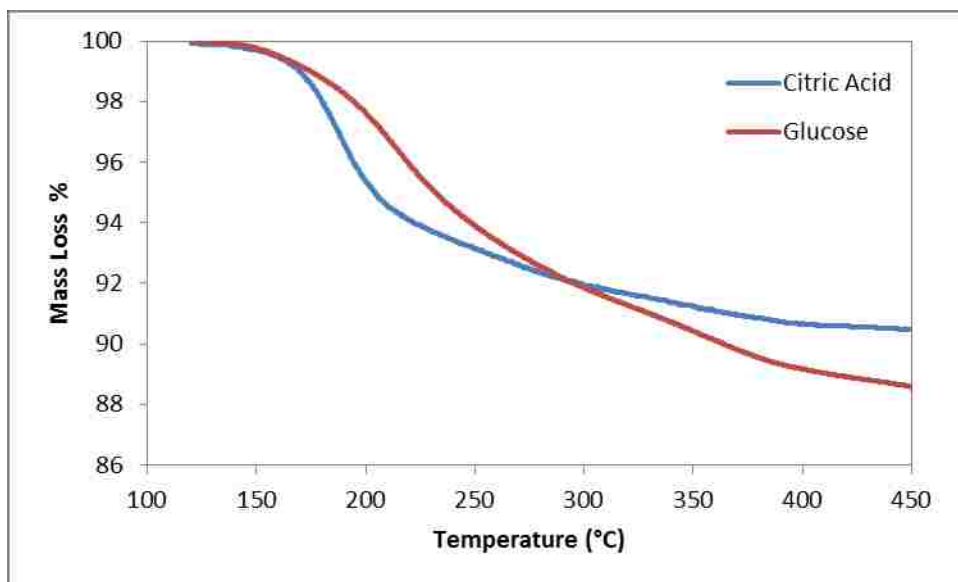
Figure 6.2. Mass loss profile of citric acid and glucose coated iron oxide.

Table 6.1. Results from DLS and Zeta potential measurements of coated nanoparticles.

	Zavg (nm)	PDI	Zeta (mV)
Citric Acid	75.36	0.207	-34.7
Glucose	70.06	0.193	-20.3

6.2.9 Statistical Analysis

Statistical analysis of the ROS generation and apoptosis assay were performed using a two sample Student's t-test comparing viability to the control. To indicate significant differences defined by the following ranges: $p < 0.05$, $p < 0.01$ and $p < 0.001$, a single, double, or triple asterisk was included in the figures.

6.3. Results and Discussion

6.3.1 Characterization of Nanoparticles

Following the reaction, the nanoparticles were characterized to confirm the success of the functionalization. FTIR was utilized as an initial screen to verify the presence of predicted functional groups. In **Figure 6.1**, there is a change in signature between the citric acid and the glucose coated nanoparticles with the key peaks of interest being a shoulder at 1088 cm^{-1} attributed to the C-N vibration and a pronounced peak at 1040 cm^{-1} indicating the location of C-O stretch peak attributed to the glucosamine. It should be noted that the loss of the primary amine peak from glucosamine further confirms a covalent bond instead of electrostatic interactions between the carboxyl and amine groups.

In **Figure 6.2**, TGA indicated similar mass loss for both citrate and glucose coated particles, approximately 10 and 12% respectively, however a change in the profile was observed indicating different compounds. The citrate coating displayed its greatest mass loss between 150 and 200 °C which is similar to the values reported by Frimpong et al. [32]. Glucose coated particles saw its greatest mass loss shift to between 200 and 300 °C.

The nanoparticle systems were further characterized with DLS and Zeta Potential to determine the hydrodynamic size of the particles and surface charge (**Table 6.1**). Citrate coated nanoparticles were 75 nm in diameter with a PDI of 0.207 and glucose

functionalized particles were 70 nm with a PDI of 0.193. The addition of the monosaccharide functional group resulted in no increase in hydrodynamic size. This result also indicated that there was no aggregation induced during the additional synthesis and washing steps. Previous work with TEM has determined the core iron oxide crystal size to be on the order of 10 nm. The zeta potential displays a distinct shift from -34.7 to -20.3 mV. During the functionalization step, carboxyl groups from the stabilizing agent are being partially replaced by the monosaccharide molecules resulting in a diminished surface charge.

6.3.2 Uptake and Localization

A Prussian blue colorimetric assay was used to quantify cellular uptake of uncoated, citric acid coated, and glucose coated iron oxide nanoparticles into CT26 cells. In **Figure 6.3**, the glucose coated nanoparticles display a greater extent of internalization compared to the non-targeted nanoparticles. Over the three time points measured, glucose coated nanoparticles display a 2-3 fold increase over the citric acid coated nanoparticles. Internalization of the glucose coated nanoparticles increased with time and slightly more than doubles between 0.5 and 2 hours. The internalization of the uncoated nanoparticles remains relatively constant between 5-8 pg iron per cell. Citric acid coated nanoparticle internalization doubles between 0.5 and 1 hour but then remains constant.

To visualize the location of the nanoparticles in CT26 cells, the glucose coated iron oxide nanoparticles were functionalized with a green fluorescent tag. Co-localization studies were performed with the addition of DAPI blue and Lyso-tracker red stains to visualize the location of the nucleus and lysosomes respectively. Representative images can be found below in **Figure 6.4**. In the control figure, there is a diminished presence of
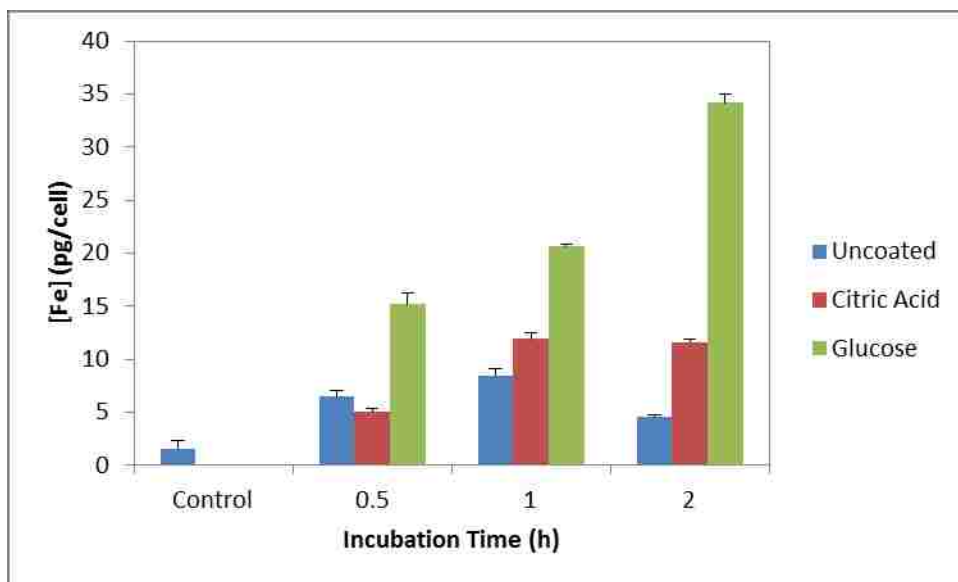
Figure 6.3. Iron content in CT26 cells when exposed to 200 µg/ml of nanoparticles over 0.5, 1, and 2 hours of incubation. Control group consists of cells never exposed to nanoparticles but underwent similar culturing conditions.
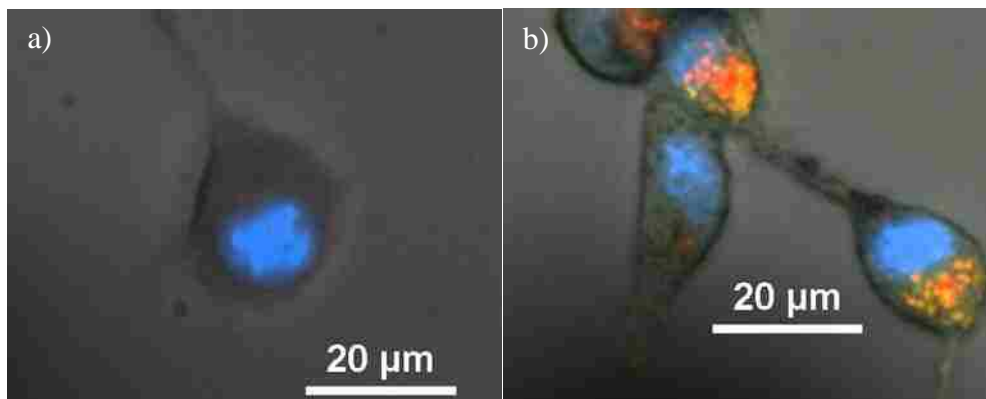
Figure 6.4. Representative localization images of control (a) and 50 µg/ml fluorescently tagged glucose coated nanoparticles (b) incubated with CT26 cells.

naturally occurring lysosomes. In the case of nanoparticle exposure, there are areas of yellow-orange overlap from the green nanoparticles and red lysosomes suggesting the nanoparticles are being internalized in lysosomes. Previously, it was determined that glucose coated iron oxide nanoparticles were internalized by cells via a caveolae dependent pathway culminating in lysosomes [33]. While working with similarly designed glucose functionalized nanoparticles, Shan et al. studied the effects of using a GLUT-1 inhibitor on the rate of internalization [28]. They determined that the internalization was retarded to rates similar to control nanoparticle system. However, glucose transporters are more attuned to transporting small molecules across the cell membrane, not nanoparticles on the order of 70 nm. We picture that the glucose functionalized nanoparticles are sticking to the cell surface via glucose transporters, internalized via caveolae, and eventually compartmentalized into lysosomes.

6.3.3 Alternating Magnetic Field Response

After determining the selectivity of the glucose coated nanoparticles, cells with internalized nanoparticles were exposed to the AMF to demonstrate the potential of the system to deliver MagMED therapy. To study the changes in cellular ROS levels, a DCFDA assay was used. In the presence of ROS, the acetate groups are cleaved converting the molecule from non-fluorescent to fluorescent. The cells were exposed to the AMF for 30 minutes while the temperature was measured with a Luxtron FOT Lab Kit. At the power setting used (approximately 60 kA/m in strength at 292 kHz frequency), the radiant heat from the copper coil heated cellular media to 37-38.5 °C, and there was no difference in heating profile between the control group and the nanoparticle systems. The presence of nanoparticles altered the absolute measured fluorescent value, so a ratio of samples

exposed to the AMF and the samples that remained in the incubator was used. **Figure 6.5** displays the field enhancement ratio of the various systems tested with CT26 cells. There is negligible enhancement in the control group, and any minor increase was attributed to deviation away from ideal culture conditions. Significant enhancement was observed with nanoparticle exposure. Glucose coated nanoparticles displayed an additional enhancement compared to the other non-targeted nanoparticle systems. The increase in ROS enhancement is thought to be associated with the amount of nanoparticles internalized by the cells.

Increased intracellular ROS generation from engineered nanomaterials typically leads to a cytotoxic event. A Caspase 3/7 Apoptosis assay was utilized to determine the effects of the increased ROS enhancement and to demonstrate the potential as a therapeutic. Through the activation of caspase 3/7 in apoptotic cells, the reagent is activated and becomes fluorescent when bound with cellular DNA. Similar to above, **Figure 6.6** displays the ratio of fluorescent values between exposed to the AMF, and the samples that remained in the incubator. Only the glucose coated nanoparticles displayed a significant increase in caspase 3/7 activity compared to the control and the non-targeted nanoparticle systems. The increase in ROS generation during AMF exposure is capable of the triggering the apoptotic pathway leading the cellular death.

To determine the source of the ROS generation, we examined the surface generation through a methylene blue dye degradation assay. The surfaces of iron oxide nanoparticles are capable of catalytically generating ROS through the Fenton and Haber-Weiss reactions. In a Fenton-like system, iron ions react with hydrogen peroxide to generate highly reactive hydroxyl and superoxide radicals which in turn attack bonds on
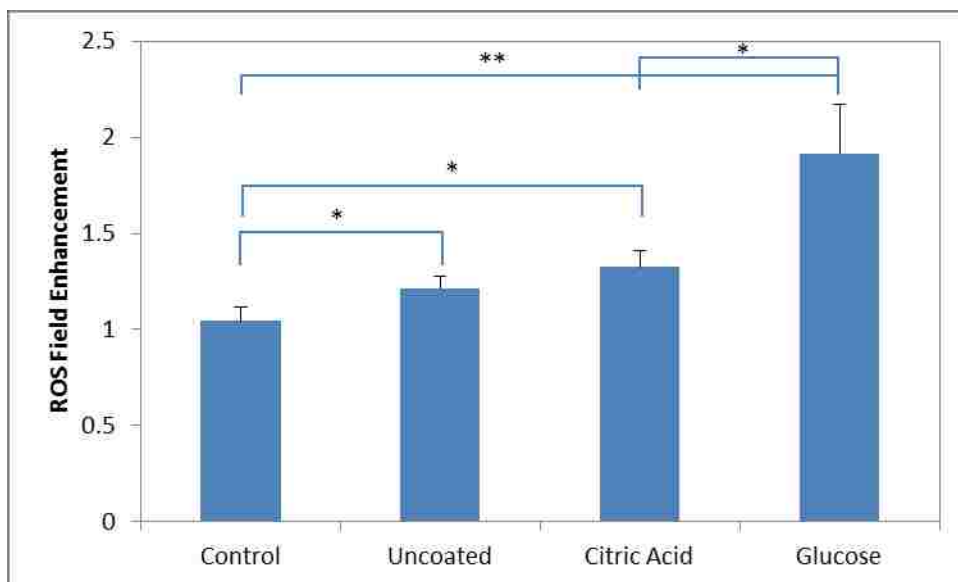
Figure 6.5. Measured ROS enhancement with field exposure determined by dividing the relative fluorescent means from the samples with field exposure by no field exposure. Significant differences between groups are indicated as $*p < 0.05$, $**p < 0.01$.
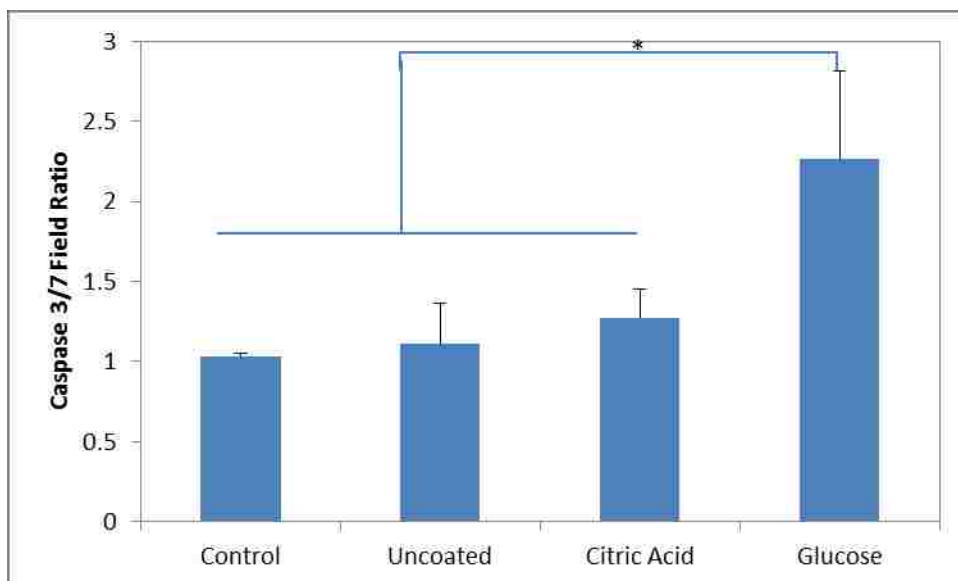
Figure 6.6. Ratio of Caspase 3/7 fluorescence of cells with and without field exposure when exposed to various nanoparticle systems. Significant differences between groups are indicated as $*p < 0.05$.
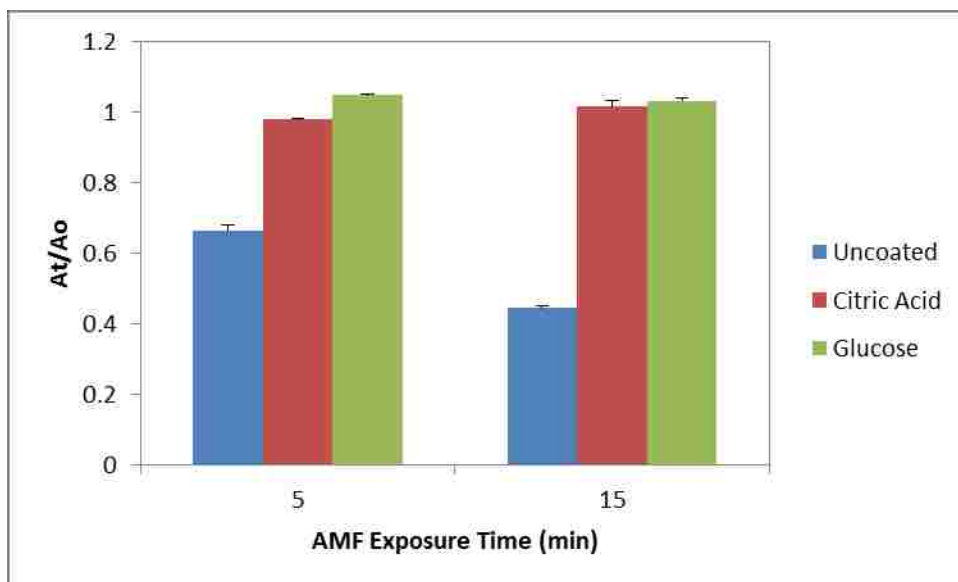
Figure 6.7. Fenton-like generation of ROS by nanoparticle systems measured by methylene blue dye degradation. 75 µg/ml nanoparticles were exposed to the AMF for 5 and 15 minutes in the presence of 0.75% H_2O_2.

methylene blue fracturing the molecule into colorless intermediates. By measuring methylene blue colorimetrically, the amount of degradation can be determined. **Figure 6.7** below displays the amount of methylene blue degraded by the various nanoparticle systems when exposed to the AMF for 5 or 15 minutes. The concentration of nanoparticles selected was 75 µg/ml where there is minimum, 1.5 °C, temperature rise of the solution attributed to nanoparticle heating. Previously at this concentration we observed a statistical enhancement in ROS generation with uncoated nanoparticles compared with the Arrhenius prediction [21]. The uncoated nanoparticles display significant degradation on the order of 40-60%. However, the coated systems display negligible degradation indicating our coating inhibits the Fenton-like reaction.

Toxicity associated with iron oxide nanoparticles is typically attributed to Fenton-like catalytic generation of free radicals with endogenous hydrogen peroxide [34, 35]. Based on previous results, our initial hypothesis was cellular ROS generation would be enhanced through the local heating of the nanoparticles driving the Fenton-like chemistry. Since our coated systems do not display this behavior suggests that another mechanism is at play beyond a chemical effect. In the presence of the alternating magnetic field, the nanoparticles would be physically rotating and realigning themselves with the field. If bound to the cell membrane or internalized within lysosomes these physical motions would induce stress within the cell. The ROS generation in response to these physical stresses would correspond with the amount of nanoparticles internalized. In the case of EGFR targeted iron oxide nanoparticles, Domenech et al. observed an increase in lysosomal permeability correlating with increased ROS generation and decreased viability as a result of their intracellular treatment [36]. They attributed this observation to heat dissipation or

mechanical disruption of the lysosomes. Similarly, iron oxide nanoparticles were coated with lysosomal protein marker antibodies to specifically accumulate along the lysosome membrane [37]. In this case, the alternating magnetic field applied was at 20 Hz where only physical rotations by the nanoparticles would be actuated. The resulting cellular apoptosis occurred due to the lysosomal disruption from the rotational forces.

Accounting for the location of the nanoparticles in lysosomes, the shift in pH (~4.5) would result in some dissolution of iron oxide to iron ions. These free ions have the potential to leave the lysosome to the cytosol, mitochondria, or endoplasmic reticulum where they would encounter conditions more favorable to Fenton-like chemistry in terms of available hydrogen peroxide [34, 38-41]. The toxicity of iron oxide nanoparticles has been directly tied to intracellular release of iron ions which would react with mitochondrial hydrogen peroxide [42]. Considering the theoretical heating calculations, there remains doubt whether the nanoscale heating isolated in lysosomes would be able to effect the kinetics in neighboring organelles [13, 43]. Experimental evidence demonstrating nanoscale heating involves changes in a fluorescent polymeric shell or nanoparticles in the direct vicinity of a liposomal carrier increasing the permeability of the bilayer [14, 44, 45]. Lysosomal membrane permeabilization from free radicals has been demonstrated by elevating the intralysosomal iron content through iron loaded silica particles [46, 47]. The source of the intralysosomal hydrogen peroxide is a direct result of membrane bound NADPH oxidase stimulation by the silica particles [48]. However, uncoated iron oxide nanoparticles do not similarly stimulate NADPH oxidase with endocytosis [49]. Thus in our case, even if the coating is displaced, the only potential source of lysosomal hydrogen peroxide available would have to escape catalase degradation and freely diffuse into the

compartment. With our specific nanoparticle systems, we can likely eliminate a chemical effect and point to either a thermal or mechanical effect disrupting the lysosomal membrane as the source of enhanced ROS generation and associated apoptosis.

6.4. Conclusions

This study reports the use glucose coated iron oxide nanoparticles for the selective internalization and assessed for their potential to deliver MagMED therapy to a colorectal cancer cell line. The targeted nanoparticles displayed increased internalization compared to non-targeted nanoparticles, and co-localization suggests the nanoparticles are internalized into lysosomes. With exposure of an alternating magnetic field, the glucose coated nanoparticles displayed a significant increase in cellular ROS and apoptotic cell death with no measurable increase in media temperature. To determine if the mechanism of toxicity was attributed to a chemical effect, we investigated the surface generation of ROS through Fenton-like chemistry. The coated systems displayed negligible ROS generation compared to uncoated nanoparticles. These observations suggest the cellular ROS measured is attributed to a thermal or mechanical effect of the internalized nanoparticles.

6.5. References

References are located at the end of the dissertation subdivided by chapters.

Chapter 7: Synthesis and Characterization of Magnetic Nanoparticles with Biodegradable Polymer Coatings for the Treatment of Cancer

Iron oxide nanoparticles provide theranostic capabilities through alternating magnetic field (AMF) mediated therapy and enhanced contrast in magnetic resonance imaging. The enhanced local generation of reactive oxygen species (ROS) with AMF exposure has the potential to be a direct toxic effect associated with magnetically mediated energy delivery (MagMED) therapy or can work in conjunction with chemotherapeutics to enhance the drug efficacy. However, coatings essential to the delivery of the nanoparticles can retard the surface generation of ROS, which occurs at the surface through Fenton-like chemistry. To circumvent this issues, we developed a biodegradable coating based on a poly(beta-amino ester) macromer. The reactivity of the nanoparticles was assessed using a methylene blue degradation assay. Unfortunately, with the coating degraded, the nanoparticles did not improve in reactivity and future work is warranted to determine the role of surface anchoring groups.

7.1. Introduction

With their unique physical properties, magnetic nanoparticles are of great interest to nanomedicine researchers with applications in diagnostic imaging, drug delivery, and thermal therapy of cancer [1-4]. Traditionally, nanoparticles often relied on passive targeting to systemically circulate and accumulate in tumors via the phenomenon known as the enhanced permeation and retention effect [5]. Current nanoparticle research has looked to functionalize the surface with appropriate targeting ligands such as peptides, antibodies, and carbohydrates to increase cellular interaction and even target intracellular organelles such as the lysosome [6-10]. The therapeutic potential of magnetic

nanoparticles stem from their ability to remotely heat when subjected to an AMF. Magnetic fluid hyperthermia has been studied for decades, but recent advances with intracellular energy delivery has become an area of interest to researchers [11]. Targeted magnetic nanoparticles can combine their therapeutic potential and enhanced contrast properties as theranostics particles.

MagMED builds off the work established by Creixell et al. demonstrating that internalized targeted nanoparticles can induce cellular death when exposed to an AMF without a measurable temperature rise [11, 12]. In follow-up work, with the specific targeting ligands utilized, local delivery of heat or physical/mechanical forces was shown to disrupt lysosomes and trigger cellular death [13-15]. Beyond these mechanisms, a third potential effect of the local energy delivery involves the generation of reactive oxygen species (ROS). We have recently demonstrated the generation of ROS from the surface of uncoated iron oxide nanoparticles is enhanced in presence of an alternating magnetic field [16]. However, in follow up work, we studied the role of nanoparticle coatings and observed the ROS generation was significantly impaired (submitted to Acta Biomaterialia). One of the coated systems involved glucose functionalization, and it was efficiently internalized into lysosomes and induced significant apoptosis compared to the other nanoparticles, reinforcing the physical or thermal mechanisms discussed above. Building off this research, a potential next generation strategy is to develop a biodegradable coating with a targeting strategy to locate bare nanoparticles next to a biological relevant source of hydrogen peroxide [17-21]. An interesting targeting candidate would be lipophilic triphenylphosphonium (TPP) [22, 23]. Due to its cationic head group, targeted nanoparticles have been observed to escape endosomes and lysosomes and cross into the

mitochondria matrix from charge gradients. We hypothesize that through mitochondrial targeting the chemical effect would be most pronounced. Heterogeneous catalysis coupled with the enhanced reactivity though nanoscale heating is another route of MagMED worth exploring.

Beyond being a direct toxic effect, the enhanced ROS generation can be used to enhance chemotherapeutics [24]. For example, Huang et al. developed iron oxide loaded pH responsive micelles loaded with the anticancer drug β-lap [25]. They determined that iron ions were released and further reacted with hydrogen peroxide generated from the β-lap. The surface of iron oxide nanoparticles can catalytically generate radicals at a 50-fold rate compared to iron ions [26]. Thus, if a biodegradable coating were utilized and the surface of the iron oxide nanoparticles were made available for this above therapy, the efficacy could greatly be improved.

Poly(beta-amino esters) (PBAEs) are a class of biodegradable polymers extensively studied due to their tunable physical properties [27, 28]. For example, by varying the hydrophilic/hydrophobic contributions in the form of the ratios of poly(ethylene glycol) diacrylate (PEGDA) and diethylene glycol diacrylate (DEGDA), significantly different degradation profiles can be achieved [29]. In terms of composite nanoparticle work, Fang et al. provides an interesting example of iron oxide nanoparticles coated with a PBAE copolymer containing doxorubicin [30]. The doxorubicin is released as the PBAE is degraded resulting in a novel theranostic system. By utilizing a PEG-based PBAE polymer coating, the nanoparticles will avoid reticuloendothelial system clearance, increasing their circulation time [31].

In this paper, biodegradable PBAE coated nanoparticles were synthesized and assessed for their ability to catalytically generated ROS. Iron oxide core nanoparticles, selected for their ability to remotely heat in an AMF, were prepared utilizing the facile co-precipitation technique. A PEG-based PBAE polymer with varying amount of anchoring group will be added the nanoparticle surface. This coating would degrade and would re-expose the iron oxide surface to the surrounding environment. We hypothesize that, once the coating is degraded, the nanoparticles will display similar reactivity to the uncoated nanoparticles.

7.2. Materials and Methods

7.2.1 Materials

Iron (III) chloride hexahydrate ($FeCl_3 \cdot 6H_2O$); iron (II) chloride tetrahydrate ($FeCl_2 \cdot 4H_2O$); and isobutylamine (IBA) were obtained from Sigma Aldrich (St Louis, MO). Ammonium hydroxide (NH_4OH) was obtained from EMD Chemicals (Gibbstown, NJ). 3-aminopropyl trimethoxysilane (APTMS) was obtained from Gelest Inc. (Morrisville, PA). Diethylene glycol diacrylate (DEGDA) and poly(ethylene glycol) (N = 400) diacrylate (PEG400DA) was obtained from Polysciences Inc. (Warrington, PA). All materials were used as received.

7.2.2 Synthesis of Iron Oxide Nanoparticles

A one-pot co-precipitation method was used to prepare the iron oxide nanoparticles as similarly reported previously [32]. Briefly, aqueous solutions of $FeCl_3 \cdot 6H_2O$ and $FeCl_2 \cdot 4H_2O$ were combined in a 2:1 molar ratio in a sealed three-neck flask under vigorous stirring and an inert N_2 environment. Once 85 °C was reached, a 1.5 M solution of NH_4OH was injected into the vessel and the reaction was carried out for 1 hour. The nanoparticles

were initially decanted via magnetic decantation to remove majority of the impurities. After, they were resuspended in water and transferred to a dialysis bag for 48 hours of dialysis. Following the washing steps, the particles were stored in suspension.

7.2.3 PBAE Macromer Synthesis

Macromers were synthesized similar to a method and nomenclature previously described [33]. The diacrylate and amine were used in a molar ratio of 1.2:1. The diacrylates consisted of DEGDA (A) and PEGDA (H) kept in a 1:2 molar ratio. The amines consisted of IBA (6) and APTMS (9) in two different ratios based on amount of APTMS anchoring group. Each chemical was pipetted into a 20 mL glass vial with magnetic stirrer. Once the chemicals were added, the vial was transferred to an oil bath set to a temperature of 85°C. The synthesis time period of 48 hours is defined as the point where the chemicals are first mixed at room temperature. The macromer was labeled AH69 10% and AH69 2.5% with the percentages indicating the amount of anchoring group.

7.2.4 Synthesis of PBAE Coated Iron Oxide and Degradation

AH69 coated Fe_3O_4 composite nanoparticles were synthesized via a surface addition reaction. Dried uncoated iron oxide nanoparticles were suspended in anhydrous DMSO at a concentration of 5 mg/ml through probe sonication. Once dispersed, AH69 was added directly to the nanoparticle suspension in a 10:1 mass ratio. The mixture was vigorously mixed for 24 hours to facilitate the macromer addition. The nanoparticles were washed via magnetic decantation with the initial precipitation in ether and then washed three times with acetone. The particles were dried in a vacuum oven and the dry powder was stored under desiccation.

Following the synthesis, AH69 coated Fe_3O_4 were suspended in water at a concentration of 5 mg/ml. The nanoparticle suspension was transferred to a dialysis bag and dialyzed against water for 72 hours. After dialysis, the nanoparticles were magnetically decanted and washed with water. The particles were dried in a vacuum oven and the dry powder was stored under desiccation.

7.2.5 Particle Characterization

Fourier Transform infrared (FTIR) spectra. Attenuated total reflectance FTIR (ATR-FTIR) was used to determine surface functionalization with a Varian Inc. 7000e spectrometer. Dried samples were placed on the diamond ATR crystal and the spectrum was obtained between 700 and 4000 cm^{-1} for 32 scans.

Thermal gravimetric analysis (TGA). TGA was used to quantify the mass percent of the iron oxide core particle. Measurements were performed using a TA Instruments SDT Q600 *TGA/DSC instrument (New Castle, DE).* Approximately 10 mg of dried sample was loaded and a heat rate of 5 °C/min under constant air flow was used. At 120 °C, the sample was held isothermal for 10 minutes to vaporize residual solvent and potential water vapor. The sample continued to heat at 5 °C/min until 500 °C. The presented values are normalized to the mass at 120 °C.

Dynamic Light Scattering (DLS). DLS measurements were obtained using a Malvern Zetasizer, Nano ZS90 instrument. Nanoparticles were diluted in DI water to a concentration of 200 μg/mL and dispersed using ultrasonication.

Alternating Magnetic Field heating. The AMF heating profile was observed using a custom made Taylor Winfield magnetic induction source and temperature was measured with a Luxtron FOT Lab Kit. Particles were diluted in DI water to a concentration of 2

mg/mL. One ml of solution was placed in a 2 ml centrifuge tube and placed in the center of the coil. The solution was heated in a field of approximately 58.1 kA/m in strength at 292 kHz frequency for 5 minutes.

7.2.6 Surface ROS Generation

To determine the amount of ROS generated from the surface the nanoparticles a methylene blue degradation assay was used. The degradation experiments were performed in 2 ml microcentrifuge tubes where one ml samples were prepared by diluting stock concentrations of methylene blue to 5 µg/ml and nanoparticles to 75 µg/ml. The samples were placed in the water bath at 34 °C for 10 min to equilibrate to the expected steady state temperature as a result of field exposure. The degradation was initiated by spiking the samples with 25 µl of 30% H_2O_2 to a working concentration of 245 mM. After given time intervals the samples were centrifuged for 30 s using a Phenix Quickspin Centrifuge, magnetically decanted, and measured using UV-visible spectroscopy (maximum absorbance at 665 nm) with a Varian Cary. To account for nanoparticle scattering from the nanoparticles that remain in suspension, samples containing only nanoparticles were measured and subtracted out from the sample absorbance.

7.3. Results and Discussion

7.3.1 Characterization of Nanoparticles

The PBAE is synthesized through a Michael addition reaction between the amine and acrylate groups resulting in a covalent linkage of amines and esters (**Scheme 7.1.a**). The inclusion of APTMS into the PBAE backbone provides an anchoring group to the nanoparticle surface through siloxane bonds. The ester groups of the PBAE backbone are susceptible to hydrolysis into diols and β-amino acids. These smaller degradation products
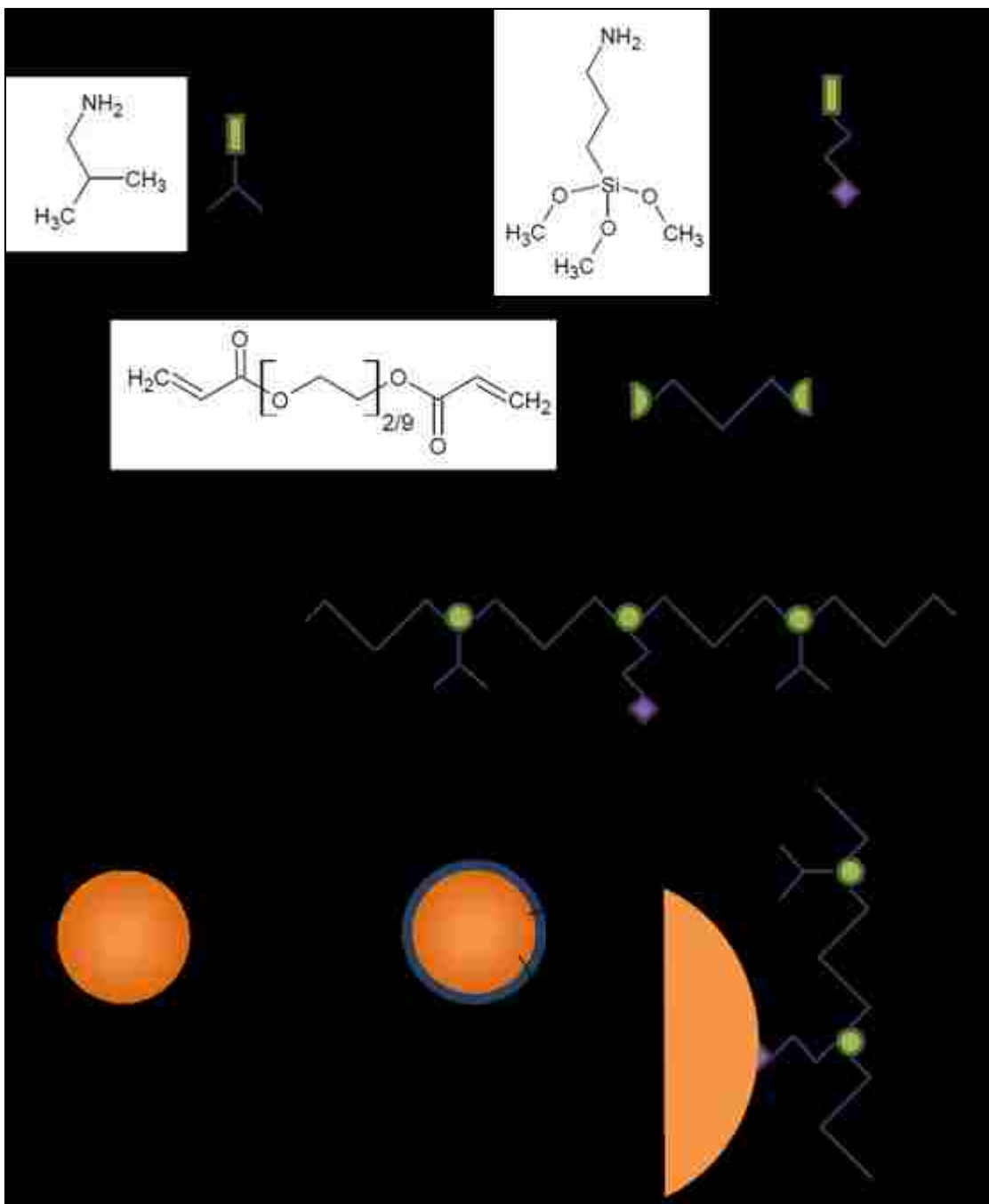
Scheme 7.1. Reaction schematic of the AH69 macromer synthesis (a) and subsequent nanoparticle coating (b). The macromer was made using a 1.2:1 ratio of diacrylate to amine, 1:2 molar ratio of DEGDA to PEG400DA, and 10 or 2.5 mol% APTMS. AH69 attachment was facilitate through siloxane bonding of the anchoring group to the iron oxide surface.

are washed out during dialysis leaving behind a small fraction of the original PBAE as anchoring groups on the nanoparticle surface. Following the reaction and degradation, the nanoparticles were characterized to confirm the successful addition and removal of AH69. FTIR was utilized as an initial screen to verify the presence of predicted functional groups. The spectra of the core uncoated nanoparticles and AH69 coated and degraded nanoparticles with 10 and 2.5% anchor groups are displayed in **Figure 7.1**. Key peaks of interest are indicated by vertical lines at 1715 cm^{-1} and 1110 cm^{-1} corresponding to the carbonyl (C=O) stretch band and ether (C-O-C) stretch band from the PBAE background and at 1015 cm^{-1} corresponding to the siloxane anchoring group. After degradation, the indicative peaks are diminished, and the spectra resembles that of uncoated iron oxide.

Figure 7.2 displays the TGA thermograms of the various nanoparticle systems tested. The uncoated nanoparticles display a 3.1% loss in mass, which can be attributed to chemically adsorbed water and iron oxide hydroxyl groups. With the addition of AH69, the mass loss approaches 10% and occurs in two stages: 250-300 °C and 350-400 °C. The first stage closely corresponds to the elimination of poly(ethylene glycol) previously observed by us in a cross-linked hydrogel coated system [34]. The second stage, around 400 °C, corresponds to the range observed by Galeotti et al. studying a variety saline grafting agents [35]. After degradation, the amount of mass loss decreases to 93.8 and 95.1% for the 10 and 2.5% anchor group systems respectively, confirming the loss of the PBAE backbone. However, the anchoring groups remain as the profile displays the similar elimination range between 350-400 °C. The differences in mass loss profile corresponds the amount of anchoring groups involved in the initial macromer synthesis.
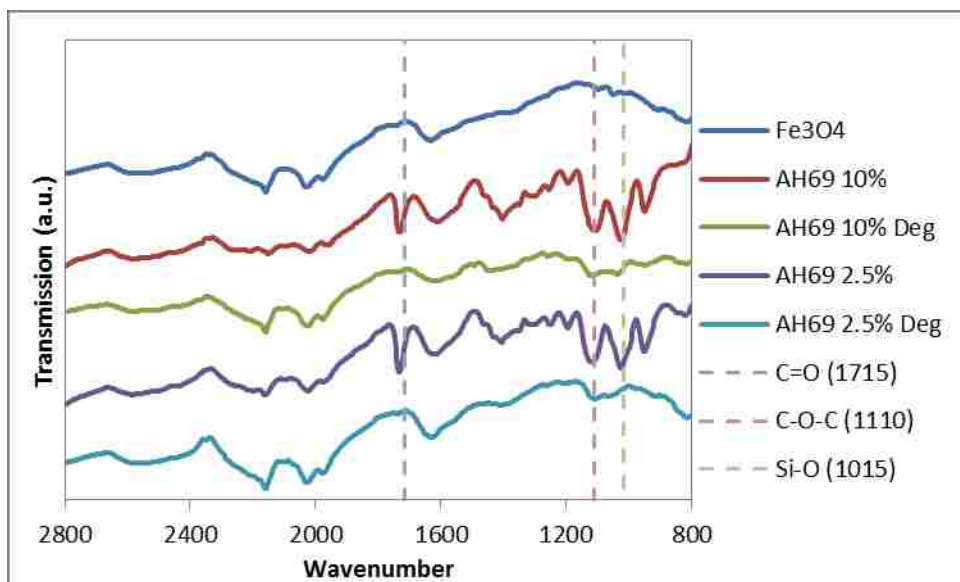
Figure 7.1. FTIR spectra of functionalized nanoparticles. Vertical lines at 1715 cm^{-1} and 1130 cm^{-1} indicate the location of the C=O and C-O-C bonds from the PBAE backbone; 1015 cm^{-1} attributed to the Si-O bond from the anchor molecule.
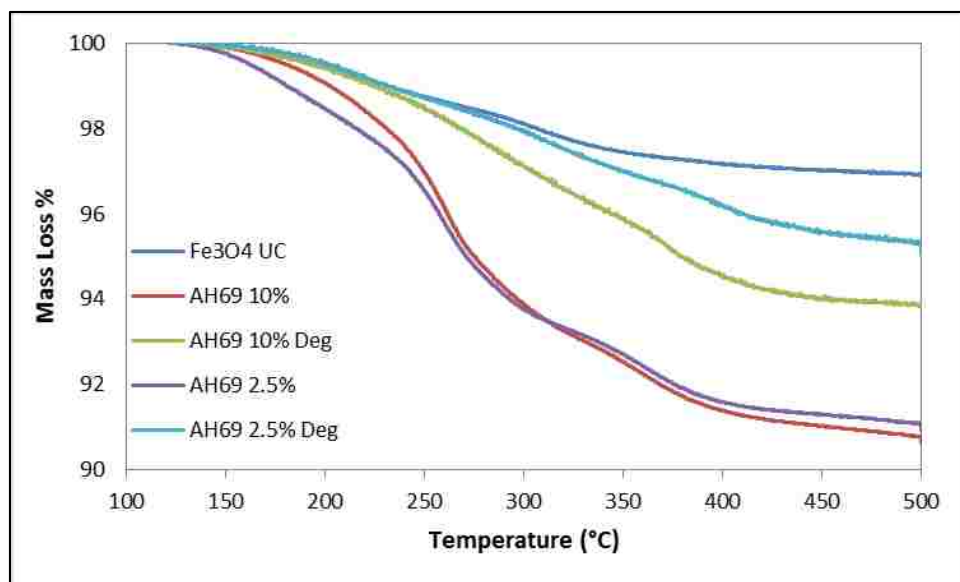
Figure 7.2. Mass loss profile of uncoated iron oxide and AH69 coated iron oxide before and after degradation with different amount of anchoring group.

Table 7.1. Results from DLS measurements over 40 minutes, the equivalent time involved in the methylene blue assay.

Sample	Time	Zavg (D-nm)	PDI	% change
Fe3O4 UC	Initial	94.69	0.172	106.2
	40 min	100.6	0.179	
AH69 10%	Initial	126.7	0.358	110.1
	40 min	139.5	0.317	
AH69 10% Degraded	Initial	88.01	0.315	108.7
	40 min	95.63	0.251	
AH69 2.5%	Initial	109.2	0.373	111.9
	40 min	122.2	0.292	
AH69 2.5% Degraded	Initial	86.02	0.263	116.6
	40 min	100.3	0.252	
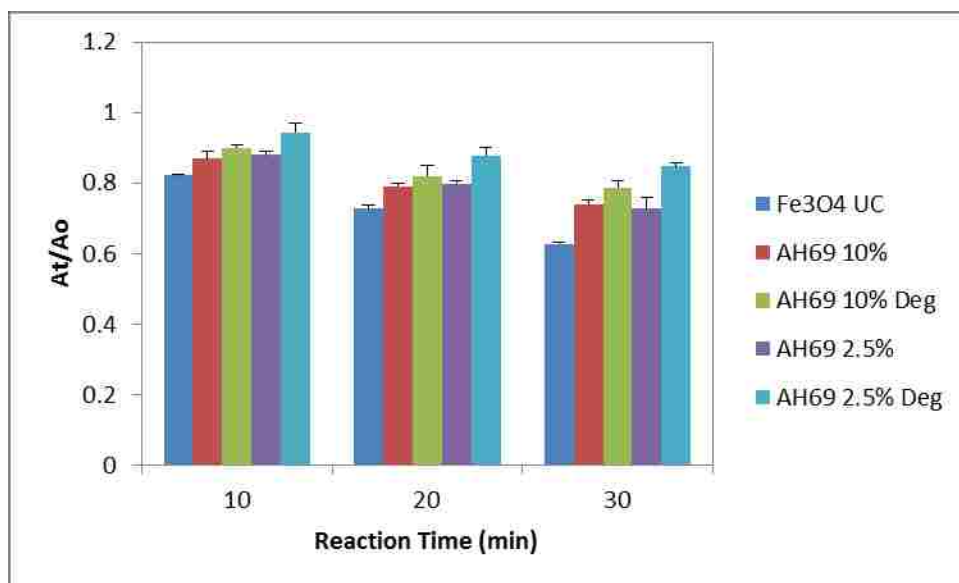
Figure 7.3. Extent of methylene blue degradation over different reaction times of 75 µg/ml nanoparticles at 34 °C. Initial concentration of methylene blue was 5 µg/ml and H_2O_2 was used at 245 mM.

The hydrodynamic size of the particles was determined with DLS and reported as Z-average in **Table 7.1**. The core uncoated nanoparticle are on the order of 100 nm in diameter with a PDI of 0.172%. The nanoparticles increase 20-30 nm with the addition of AH69 as further evidence of the successful coating. With coating degradation, the increase in hydrodynamic size recedes, and the nanoparticles loses close to 8 nm in size compared to the core uncoated nanoparticles. While not significant, it is an interesting result as one would expect the potential for agglomeration with the additional dialysis and handling steps. A possible explanation would be an etching of the outer layer of iron oxide by the local acidic environment created during the PBAE degradation. Over the course of 40 minutes, corresponding to the length of the methylene blue degradation assay, all samples experience a similar ~10% increase in size due to agglomeration.

7.3.2 Surface ROS Generation

After determining the addition and degradation of the AH69 coating, the nanoparticles were tested for their reactivity with a methylene blue degradation assay. In the presence of hydrogen peroxide, the surfaces of iron oxide nanoparticles are capable of catalytically generating highly reactive hydroxyl and superoxide radicals through the Fenton and Haber-Weiss reactions. These radicals attack bonds on methylene blue fracturing the molecule into colorless intermediates which can be measured colorimetrically. **Figure 7.3** below displays the reactivity of the various systems at 75 µg/ml at 34 °C. Without any functionalization, the uncoated nanoparticles are the most reactive displaying 38% degradation over 30 minutes of reaction. The AH69 coated Fe_3O_4 nanoparticles were still reactive but at a diminished 25% over 30 minutes. Previously, with citric acid stabilized nanoparticles, the reactivity was completely inhibited (submitted to

Acta Biomaterlia). In this case, the nanoparticle system involves coating with semi-mobile polymeric chains as opposed to a monolayer of stabilizing groups. The mobility of the coating would facilitate diffusion of the reactants to the catalytic surface allowing the reaction to occur.

However, with degradation of the AH69 coating, there was no improvement in reactivity. Recall, the initial hypothesis was that with degradation the nanoparticle system should return to similar behavior of the uncoated nanoparticles allowing these nanoparticles a range of therapeutic applications. When observing concentrated suspensions of nanoparticles, the degraded samples had a slight brown hue compared to the black suspension of uncoated Fe_3O_4. A brown shift would be indicative of oxidation of the nanoparticles to Fe_2O_3. Fe_2O_3 is less reactive than Fe_3O_4 as a Fenton-like catalyst, since only Fe^{3+} ions are initially present on the particle surface [36]. When diluted to a transmittable concentration, there is no measurable shift in UV-vis absorbance to quantify this observable color change. An alternative approach is to study the inductive heating property of the nanoparticles. If there is a measurable surface oxidation, the nanoparticle systems would heat less than uncoated Fe_3O_4. **Figure 7.4** displays the heating profile of uncoated and degraded nanoparticle systems and specific absorption ratio (SAR) values were tabulated in **Table 7.2**. SAR is a means of quantifying the heat generated per mass of nanoparticle and is calculated using the following equation:

$$SAR = (\textstyle\sum_i C_i m_i)/m * (\Delta T/\Delta t) \qquad\qquad \textbf{Equation 7.1}$$

where C_i is the heat capacity, m_i is the individual mass of the components heated (water and iron oxide nanoparticles), m is the mass of the component generating heat (iron oxide), and $\Delta T/\Delta t$ is the initial slope of the heating profile (the 25 and 35 second time points were

used to calculate the slope). Based on the results in **Figure 7.4** and **Table 7.2**, there is negligible differences between the various nanoparticle systems tested suggesting whatever surface oxidation is present does not affect the physical properties of the nanoparticles. Future work is warranted to investigate potential surface oxidation. Additionally, the 10 and 2.5% anchoring group was selected relatively arbitrarily, and based on the TGA evidence future work should investigate lowering the amount to determine the role of the residual β-amino acid-silane on the nanoparticle surface.

7.4. Conclusion

This study explores the use of PBAE coated nanoparticles for biological enhanced ROS generation. Biodegradable AH69 macromer was successfully added to and subsequently degraded from iron oxide nanoparticles. However, when determining the reactivity, the degraded nanoparticles did not return to the performance of uncoated iron oxide as expected. The macromer system can further be modified to incorporate targeting ligands. To date, we have incorporated amine-PEG-carboxyl spacers into the PBAE backbone. The intent was to functionalize the carboxyl groups with epithelial cell adhesion molecule (EpCAM) antibodies via an amine-carboxyl coupling reaction. EpCAM was selected since it has been observed to be over expressed in majority of colorectal cancer cell lines [37, 38]. By comparison it has also been documented that adult, non-regenerating hepatocytes do not express EpCAM [39]. Thus, EpCAM is an attractive target for colorectal cancer liver metastases, however local delivery through hepatic perfusion must be considered to prevent unintended delivery to healthy epithelium. If future work overcomes the obstacles of decreased reactivity, this novel nanoparticle system has promising applications to detect and treat cancer through enhanced ROS generation.
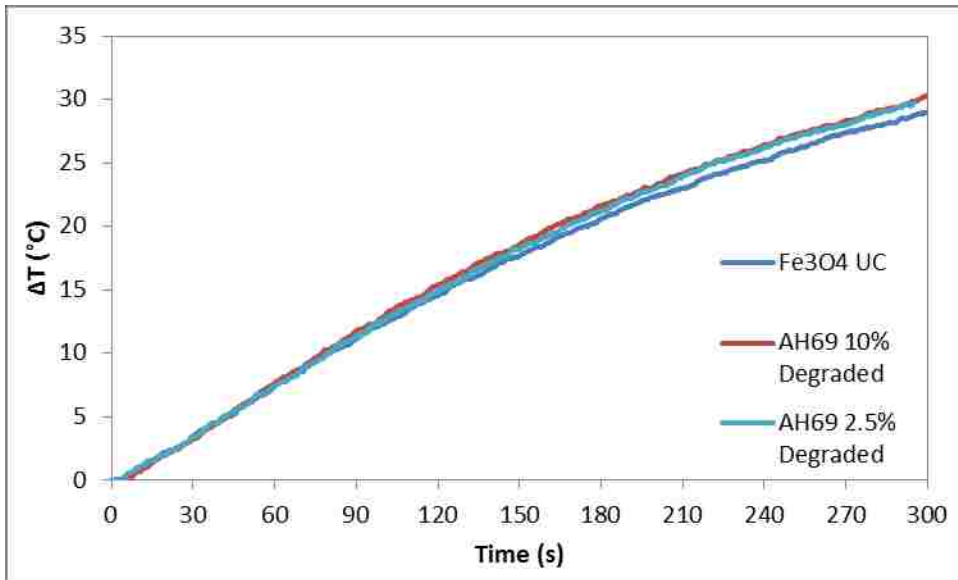
Figure 7.4. Heating profile of various systems tested

Table 7.2. Calculated SAR values using the estimated slope between 25 and 35 second time points.

System	SAR (W/kg)
Fe3O4 UC	317.8
AH69 10% Degraded	319.9
AH69 2.5% Degraded	309.4

7.5. References

References are located at the end of the dissertation subdivided by chapters.

Chapter 8: Conclusion

In this dissertation, the use of iron oxide nanoparticles for cancer therapy applications was explored. When exposed to an alternating magnetic field (AMF), iron oxide nanoparticles absorb energy from the magnetic field and convert it into heat. Traditionally, this energy was used to heat the bulk surroundings for thermal therapy. As explored in the first section of this dissertation, poly(ethylene glycol)-coated nanoparticles were able to heat cancer cells to the thermoablation range inducing necrosis. While effective in the lab, there are major translational hurdles for implementing thermoablation or magnetic fluid hyperthermia in the clinic. Current research focuses on targeted nanoparticles and their intracellular nanoscale effects to treat metastatic lesions previously considered untreatable. Now instead of heating the bulk surrounding, the energy is dissipated locally to eliminate individual cancer cells. Possible mechanisms of cytotoxicity at play are local heating effects, physical-mechanical effects (rotational or vibrational movements), or chemical effects (e.g., the generation of reactive oxygen species, ROS)). When exposed to an AMF, the Fenton-like generation of ROS was enhanced. To our knowledge, this is the first time Fenton-like reaction kinetics were studied with AMF exposure and adds relevant literature to the ongoing controversy over the existence of nanoscale heating effects. With biological applications, nanoparticle coatings are essential, and thus far these coatings either inhibit or retard the generation of ROS. Using enhanced ROS is an intriguing new route of therapy, and the work described here lays the groundwork for exciting future studies.

8.1. Significant Findings

There are several findings in this work that contribute to the scientific community's understanding of iron oxide nanoparticles for biomedical applications. The focus here was on cancer therapy, but the knowledge can be extended to other diseases or fields such as environmental remediation. Magnetically mediated energy delivery is a relatively new concept in the literature, and thus, our findings contribute directly to a growing field. The specific conclusions and relevance of this work is presented below.

- The successful thermoablation of A549 demonstrates the potential use of polymer coated particles for thermal therapy

- Uncoated nanoparticles display enhanced ROS generation with AMF compared with the Arrhenius prediction due to nanoscale heating effects

- Cyclical field exposure prevents nanoparticles from agglomerating allowing for sustained ROS enhancement

- Glucose coated iron oxide nanoparticles are internalized at a greater rate than non-targeted nanoparticles and induce enhanced cellular ROS with AMF exposure leading to apoptosis

- Stabilizing groups can inhibit the surface generation of ROS suggesting a thermal or mechanical effect is more likely the source of observed toxicity

- Residual anchoring groups from a bio-degradable poly(beta-amino ester) coating retards the surface generation of ROS

- Composite monoglyceride-based thermo-responsive cubosomes release a model protein when heated past their transition temperature

Appendix 1: Co-delivery of Heat Shock Protein 90 Inhibitors and Iron Oxide Nanoparticle Induced Hyperthermia for Dual Cancer Therapy

In this study, iron oxide nanoparticles were prepared to concurrently deliver a heat shock protein (HSP) inhibitor to cancer cells for chemotherapeutic/hyperthermic dual cancer therapy. The dual cancer therapy involves the use of magnetic nanoparticles raising the temperature of a tumor between 40-45°C through energy dissipation in an alternating magnetic field (AMF), while HSP inhibitors down-regulate chaperoning signal transduction for cancer cell survival under heat-mediated stress. We hypothesized that HSP inhibition prior to hyperthermia would make cancer cells more susceptible to thermal damage delivered by the nanoparticles. The nanoparticles utilized were citric acid coated with the intent to study core-shell nanoparticles that were prepared using atomic transfer radical polymerization as described in Chapter 4. In our preliminary study, 90 kDa heat shock protein (HSP90) was targeted by using the chemotherapeutics geldanamycin and 17-N-Allylamino-17-demethoxygeldanamycin. Combinational therapy of HSP90 inhibitors and hyperthermia on lung carcinoma cells was then investigated to explore potential enhancements in therapeutic effect. This work was done in conjunction with Sarah E. Seger as part of her NSF-REU research.

A1.1. Introduction

Thermal therapy is the process of elevating tumor tissue temperature for therapeutic gains and is traditionally divided into two regimes, hyperthermia and thermoablation, based on temperature achieved. Hyperthermia therapy, heating tumor tissue to 40-45 °C, is of interest in conjunction with traditional therapies for enhanced efficacy as opposed to a stand-alone treatment [1, 2]. Increasing the temperature of tumor tissue can be done with

focused ultrasound waves, warmed chemotherapy or blood perfusion, and magnetic fluid hyperthermia [3]. Magnetic fluid hyperthermia involves the introduction of magnetic nanoparticles to a tumor site that remotely heated when exposed to an alternating magnetic field (AMF) by dissipating the absorbed energy as heat through Neel and Brownian relaxations [4-6]. This approach avoids causing damage to surrounding tissue by localizing the heat delivery within the tumor and opens the possibility to treat tumors that are deep within the body and unreachable with current techniques. Numerous clinical trials have demonstrated that hyperthermia has additive and sometimes synergistic effects when combined with conventional radiotherapy or chemotherapy [7]. Elevated temperatures can increase the effects of chemotherapy by increasing rates of alkylation by alkylating agents, increasing drug uptake into tumor tissue, and inhibiting DNA repair mechanisms [8].

While hyperthermia has been proven beneficial in numerous trials, it can also be antagonistic by inducing cell-protective mechanisms. The dominant response depends on the magnitude of the temperature change, the resulting levels of denatured proteins, and the order of therapy delivered [9]. Activating cell-protective responses to hyperthermia include increased enzyme activity and induction of the heat shock response. The heat shock response is the increased expression of various heat shock proteins (HSPs) or molecular chaperones within the cell [10]. These proteins can re-fold denatured proteins, prevent proteasomal degradation of proteins, and protect the cell from subsequent stresses, leaving the cell in a transient thermotolerant state.

Of the HSPs identified, HSP90 is the most abundantly expressed stress protein in the eukaryotic cytosol and has been highly studied [11]. Included in HSP90's client proteins are signal transduction molecules related to cell growth and nuclear receptors of

126

steroid hormones [12]. Signal transduction clients are significant because cancer cells express altered signal transduction pathways that enable the avoidance of apoptosis and unlimited cell division. Additionally, HSP90 is involved with the heat shock response protecting the cell from stress- induced death. Many tumor environments are acidic, hypoxic, and nutrient deprived, therefore the HSP90 are overexpressed in cancer cells relative to normal tissue cells [13, 14]. Already being overexpressed, HSP90 can protect cells from traditional cancer therapies. Thus, targeting HSP90 for cancer therapy provides a way of sensitizing cancer cells to therapy [15, 16].

This study investigated co-delivery of hyperthermia and the HSP90 inhibitors, geldanamycin (GA) and 17-N-allylamino-17-demethoxygeldanamycin (17-AAG) on lung carcinoma cells. Cytotoxicity studies were carried out to determine the concentrations of the HSP90 inhibitors required to sensitize lung carcinoma cells to subsequent a hyperthermia treatment. Hyperthermia was delivered to the cells in two different ways. Ambient incubation was used to create bulk heating of the media, and magnetic fluid hyperthermia was used to create localized heating of the cells. It was expected that pre-incubation of cells with the inhibitors, in addition to hyperthermia, would be more cytotoxic than each treatment alone, and that magnetic fluid hyperthermia would be more toxic than incubator-mediated hyperthermia.

A1.2. Materials and Methods

A1.2.1 Materials

Iron (III) chloride hexahydrate ($FeCl_3 \cdot 6H_2O$) and iron (II) chloride tetrahydrate ($FeCl_2 \cdot 4H_2O$) were obtained from Sigma Aldrich (St Louis, MO). Citric acid monohydrate (CA) was obtained from Fisher Scientific and ammonium hydroxide (NH_4OH) from EMD

Chemicals (Gibbstown, NJ). Geldanamycin (GA) and 17-N-allylamino-17-demethoxygeldanamycin (17-AAG) were purchased from LC Laboratories (Woburn, MA). Both drugs were dissolved in dimethyl sulfoxide at a concentration of 500 μM and stored at -20 °C. For experimentation, the stock solutions were diluted to the desired concentrations in A549 cell medium immediately before use. Unless noted, all materials were used as received.

A1.2.2 Iron Oxide Nanoparticle Synthesis

A one-pot co-precipitation method was used to prepare the core citric acid coated iron oxide nanoparticles [17]. Aqueous solutions of $FeCl_3 \cdot 6H_2O$ and $FeCl_2 \cdot 4H_2O$ were combined in a 2:1 molar ratio in a sealed three-neck flask under vigorous stirring and an inert N_2 environment. Once 85 °C was reached, 5 mL of NH_4OH was injected into the vessel followed by 4 ml of 2 M citric acid. The reaction was carried out for 1 hour. The particles were washed with ethanol and retrieved with magnetic decanting.   Following the wash the particles were dried and stored under vacuum.

A1.2.3 Cell culture

All cell culture reagents were purchased from American Type Culture Collection (ATCC). A549 and PC-9 lung carcinoma cells at passages 4-13 were cultured in F-12K medium supplemented with 10% fetal bovine serum, 10 μg/ml Fungizone, and 2 μg/ml Penicillin-Streptomycin-Glutamine at 37 °C under an atmosphere of 5% CO_2 humidified incubator. Confluent (80% confluence) cells were detached with a Trypsin-EDTA solution (0.05% Trypsin and 0.02% EDTA; ATCC) and subcultured at least once prior to seeding.

A1.2.4 HSP90 Inhibitor Therapy Combined with Incubator-mediated Hyperthermia

Lung carcinoma cells were seeded in 6-well plates and 96-well plates at 6000 cells/cm^2 and were incubated overnight to facilitate attachment. After, the cell culturing medium was removed and replaced with 2 mL or 180 µL of the drug-containing medium. Two 6-well plates and two 96-well plates were prepared identically. One plate from each set was kept at 37°C for the entire study, and the other plates were exposed to 30 minutes of 43 °C hyperthermia treatment in an incubator at elevated temperature after 48 hours of drug exposure. The viability of the cells was assessed immediately after treatment. The 6-well plates were assessed using the Live/dead assay, and the 96-well plates were assessed using the resazurin blue assay.

The Molecular Probes Live/Dead Cytotoxicity kit used to assess 6-well plate viability was purchased from Invitrogen (Carlsbad, CA). This assay was chosen to determine changes in cellular morphology, cell count, and number of necrotic cells present within each sample. After the 48 hour exposure to drug or directly after the 30 minute hyperthermia treatment, the culture medium was removed and discarded. A 2 ml DPBS wash was performed to ensure the removal of residual medium. Then 1 ml of live/dead assay solution was added to each well, and the plates were incubated for 20 minutes. Five image sights (live and dead) were taken of each well using a fluorescence microscope (Nikon Eclipse LV 100, Melville, NY). The number of live and dead cells in each image were counted using NIS-Elements BR 3.0 imaging software. All 6-well experiments were performed in triplicate. Viability was determined by dividing the average number of live cells by the total number of cells in each cohort. Normalized concentration was determined as average live number of cells divided by the seeding density of the picture area.

The resazurin sodium salt used for the resazurin blue assay of the 96-well plates was purchased from Sigma-Aldrich (Milwaukee, WI). This assay was chosen to evaluate mitochondrial activity as a means of quantifying viability. The resazurin sodium salt was dissolved in 1x PBS to a 10 mM concentration and stored at -20 °C. After the 48 hour drug exposure or directly after the 30 minute hyperthermia treatment, culture medium was removed and discarded. A 180 µl DPBS wash was performed to remove residual drug medium prior to adding 90 µl fresh drug-free medium and 10 µL resazurin solution to each well. The plates were incubated for 3 hours before reading fluorescence. The fluorescence was read with a Cary Eclipse bottom-reading fluorescence spectrophotometer (5 nm slit; 560ex/590em wavelength). Data from this assay is presented as percent mitochondrial activity compared to the control.

A1.2.5 HSP90 Inhibitor Therapy Combined with AMF-mediated Hyperthermia

A549 lung carcinoma cells were seeded in 35 mm dishes (2 mL cell culture medium) at 6000 cells/cm^2. Cells were cultured and doped with drug containing media as above. 6-well plates were prepared identically but were kept at 37 °C for the entire study. After 48 hours of drug exposure, the medium in the 35 mm dishes was removed and replaced with medium containing 5 mg/ml suspended citric acid coated iron oxide nanoparticles. The dishes were placed on the stage, centered on the coil, and exposed to the alternating magnetic field for 30 minutes. After termination of the alternating magnetic field, the dishes were stained and imaged with the live/dead assay described above.

A1.3. Results and Discussion

A1.3.1 A549 HSP90 Efficacy Screen

This study was utilized to determine an effective concentration of each inhibitor that would sensitize the A549 cells to hyperthermia. Viability was assessed with resazurin blue stain which is reduced within metabolically active cells producing the highly fluorescent resofurin. The results from the assay can be found below in **Figure A1.1** for both GA (**Figure A1.1a**) and 17-AAG (**Figure A1.1b**). Based on these results, 125 nM concentrations of both GA and 17-AAG were selected for future studies. At this concentration, there was the most dramatic decrease in mitochondrial activity after the cells were exposed to 30 minute of 43 °C hyperthermia treatment indicating sensitization to hyperthermia.

A1.3.2 A549 Cytotoxicity with Active Agents

Following the selection of a working concentration, A549 cells were exposed to every combination of variables. Based on previous working knowledge of citric acid coated iron oxide, a 5 mg/ml concentration was selected [18]. This concentration is capable of heating to the hyperthermia range while having minimal toxicity over the short time frame selected. To facilitate the AMF-induced studies, the viability assay was changed from resazurin to live/dead. Since the 35 mm dishes utilized are larger than the 0.625"ID coil, there will be a distinct region in the center of the well where the field was the strongest and the particles heat more [19]. When determining the viability, images were taken from both the periphery and the center to distinguish between the two regions. Live/dead also provides representational images allowing for discussion on the morphology of the cells.

A normalized live cell concentration was also calculated to give insight on the proliferation potential of the cells instead of only absolute live/dead viability.

The percent viability and normalized cell concentration for A549 cells exposed to 125 nM concentrations of GA or 17-AAG with or without a 45 min exposure to citric acid coated Fe_3O_4 nanoparticles are displayed in **Figure A1.2**. By initially only calculating the percent viability, it appeared that 125 nM no longer has an effect on the cells despite the resazurin results discussed above. By including a normalized cell concentration, we in part calculated a proliferation potential of the cells. Here, 17-AAG and peripheral GA display minimal cell proliferation as the relative concentration only increases 1-2 fold over the seeding density, confirming the inhibitory concentration selected. The representative images from this assay are displayed in **Figures A1.3** and **A1.4** where **Figure A1.4** contains the cells exposed to 5 mg/ml citric acid coated iron oxide nanoparticles. Based on these images and the results above, the nanoparticles have negligible effect on A549 cells. Compared to the control group, cells receiving 125 nM of inhibitor displayed an altered morphology. The cells are sparsely packed and some examples seem bloated with a larger cell radius. Parallel results were displayed in **Figures A1.5-7** where a 30 minute exposure to 43 °C incubator-mediated hyperthermia was applied in combination with 125 nM GA or 17-AAG and 45 min exposure to citric acid coated Fe_3O_4 nanoparticles. Similarly, we observed minimal change in percent viability. However, with the inclusion of hyperthermia all samples exposed to the inhibitor displayed minimal cell proliferation as the relative concentration only increased 1-3 fold over the seeding density. In the case of GA, this would add support to the increased sensitivity of the cells to hyperthermia. Similar altered morphologies appear in the representative cell images.
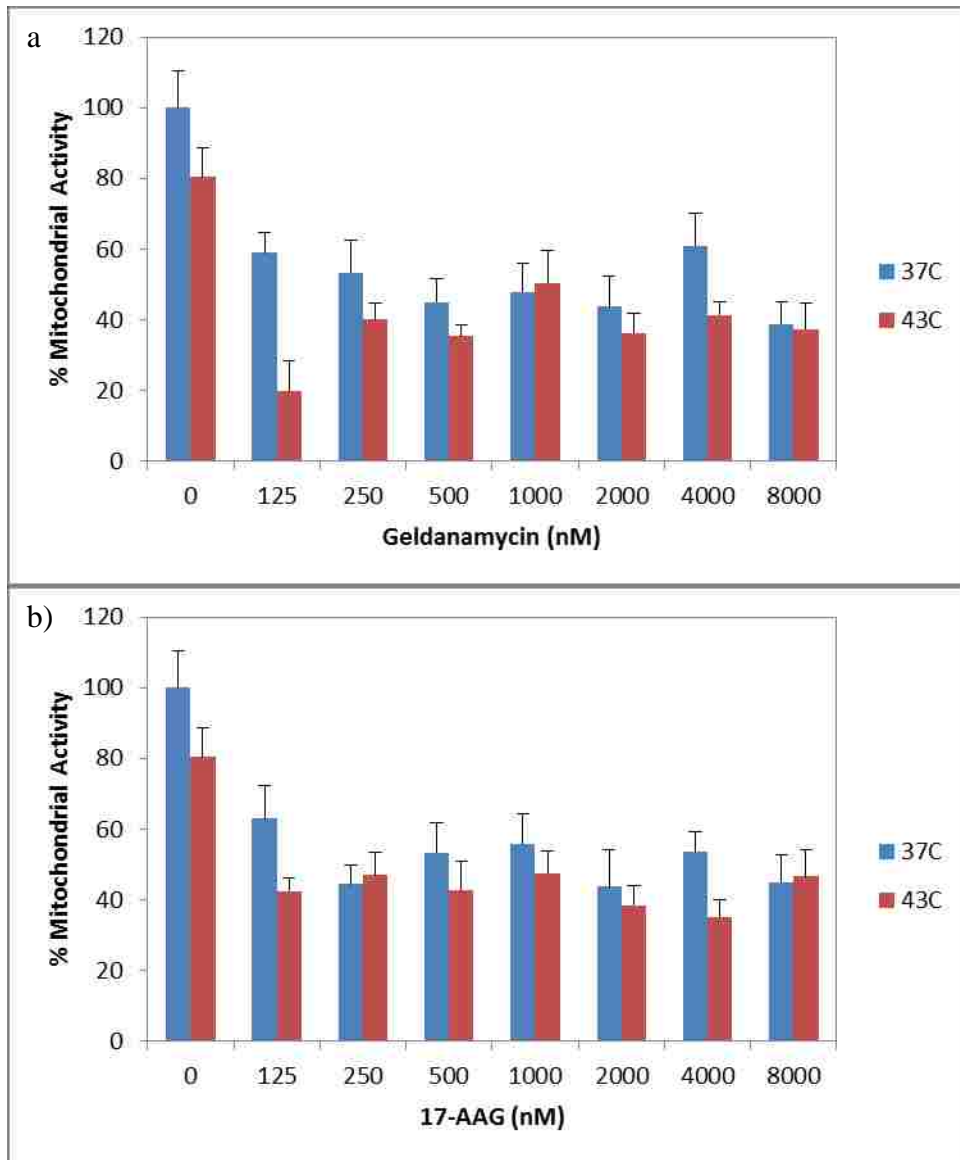
Figure A1.1. Relative mitochondrial activity of A549 cells after exposure to GA (a) and

17-AAG (b) with or without hyperthermia treatments. Results are presented as means ± SE

(n = 6).
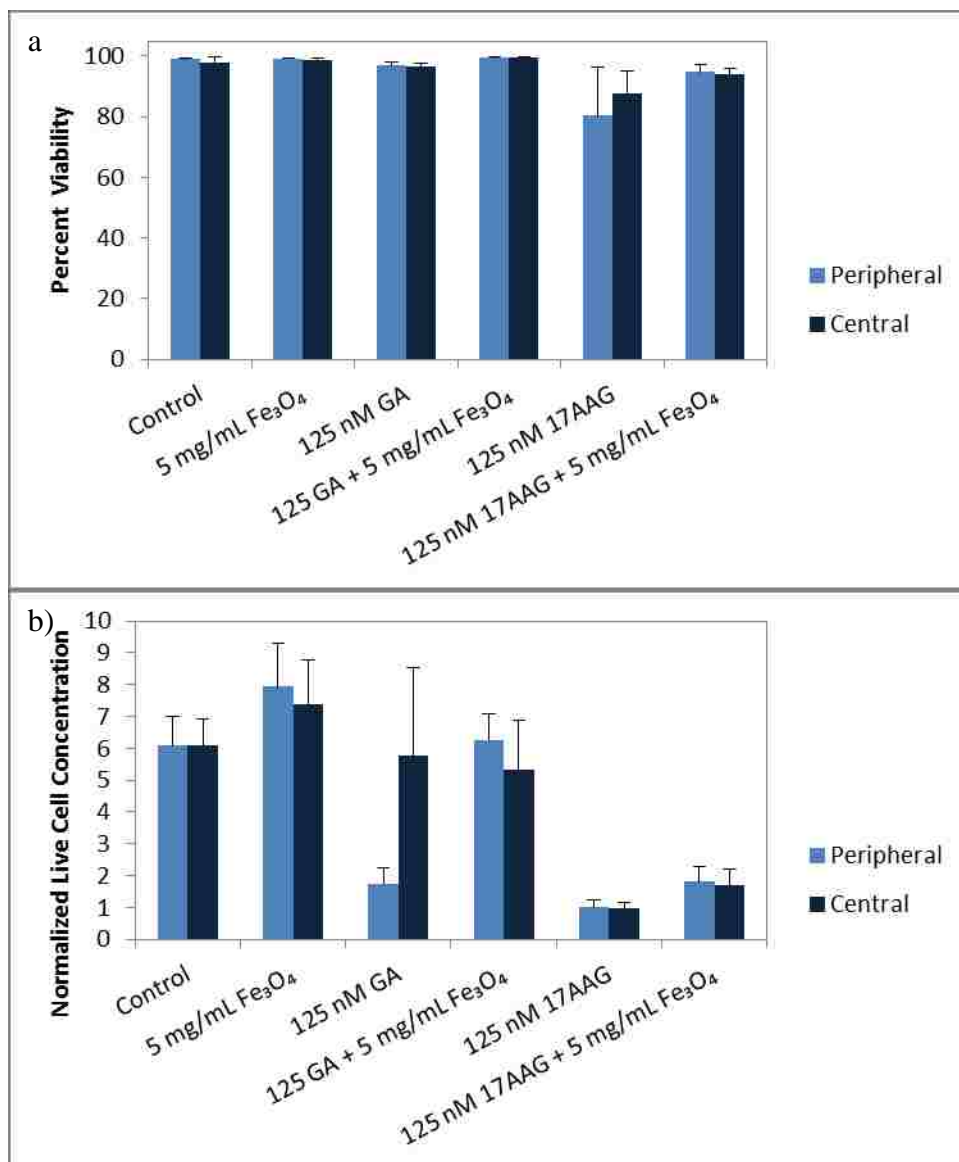
Figure A1.2. Percent Viability (a) and normalized cell concentration of A549 cells after 48 h exposure to 125 nM concentrations of GA or 17-AAG with or without a 45 min exposure to citric acid coated Fe_3O_4 nanoparticles. Results are presented as means ± SE (n=3).
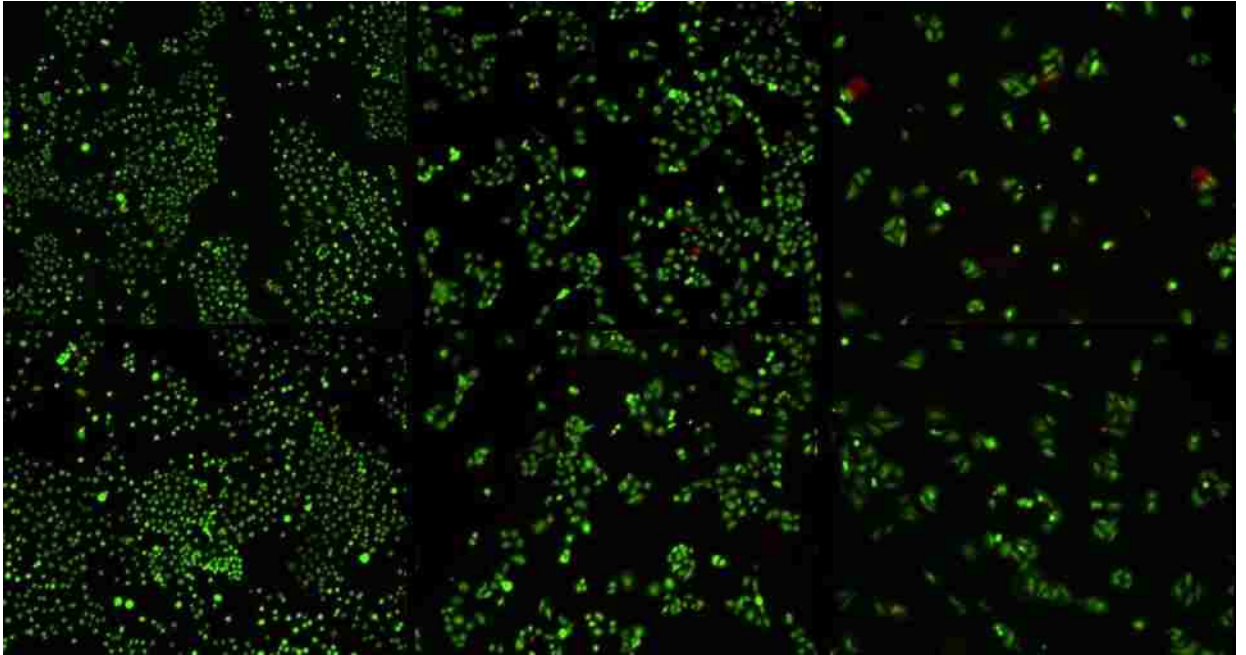
Figure A1.3. Representative images of A549 cells after 48 h exposure to 125 nM concentration of each inhibitor. Peripheral images (top, left to right): control, 125 nM GA, 125 nM 17-AAG. Central images (bottom, left to right): control, 125 nM GA, 125 nM 17-AAG.
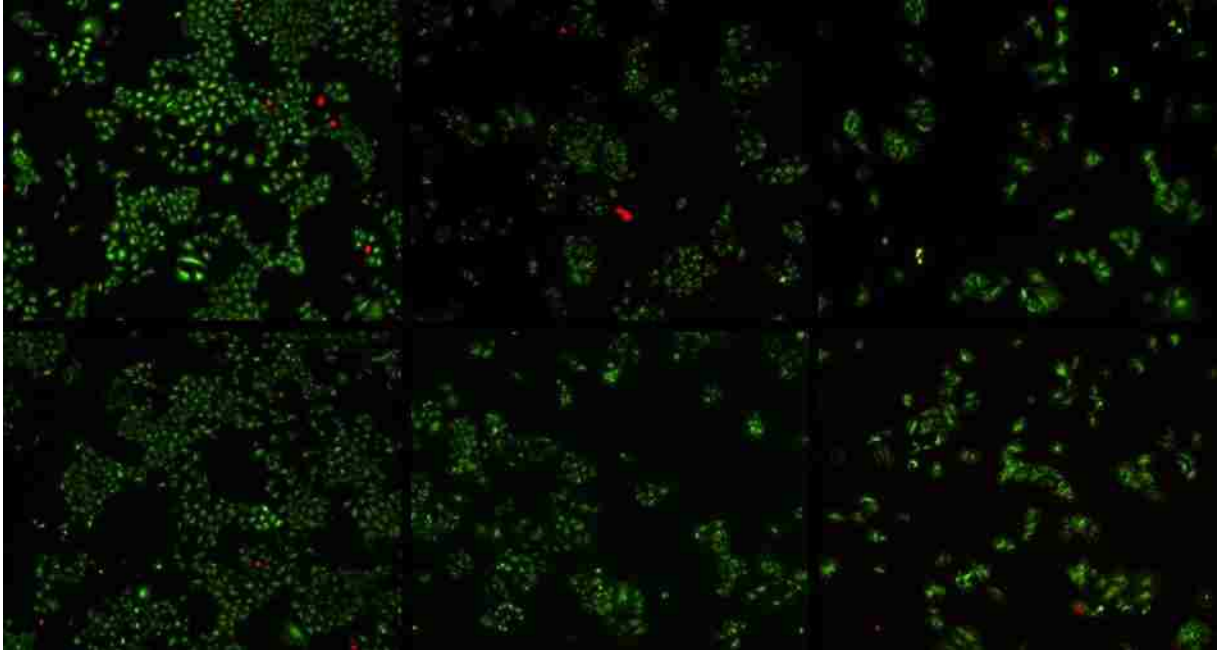
Figure A1.4. Representative images of A549 cells after 45 min exposure to 5 mg/ml citric acid coated Fe₃O₄ nanoparticles with or without 48 h exposure to inhibitors. Peripheral images (top, left to right): 5 mg/mL Fe₃O₄, 125 nM GA + 5 mg/mL Fe₃O₄, 125 nM 17-AAG + 5 mg/mL Fe₃O₄. Central images (bottom, left to right): 5 mg/mL Fe₃O₄, 125 nM GA + 5 mg/mL Fe₃O₄, 125 nM 17-AAG + 5 mg/mL Fe₃O₄.
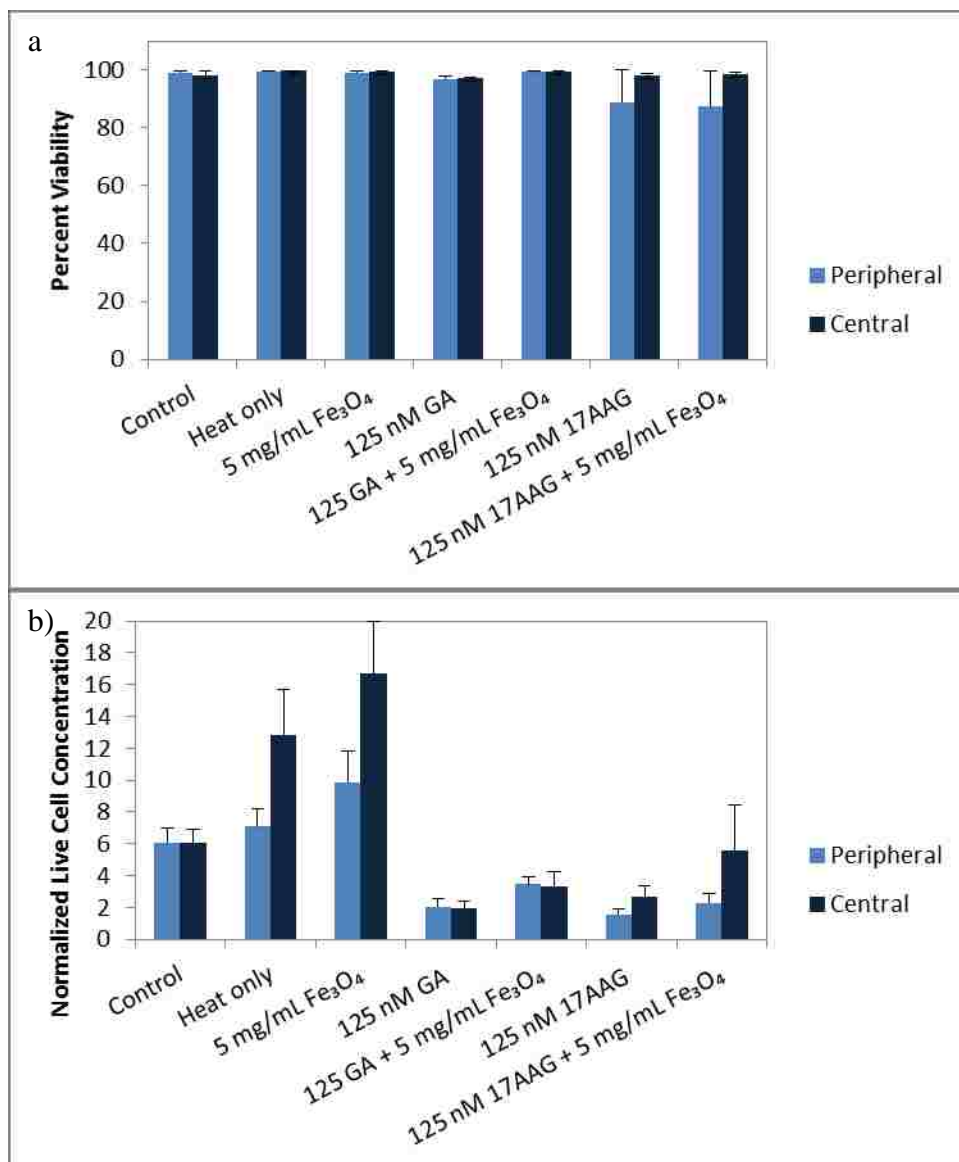
Figure A1.5. Percent viability (a) and normalized cell concentration (b) of A549 cells after 48 h exposure to 125 nM concentrations of GA or 17-AAG with or without a 45 min exposure to citric acid coated Fe_3O_4 nanoparticles. All systems were then exposed to a 30 min 43°C incubator-mediated hyperthermia treatment. Results are presented as means ± S E of 3 replicates (n=3).
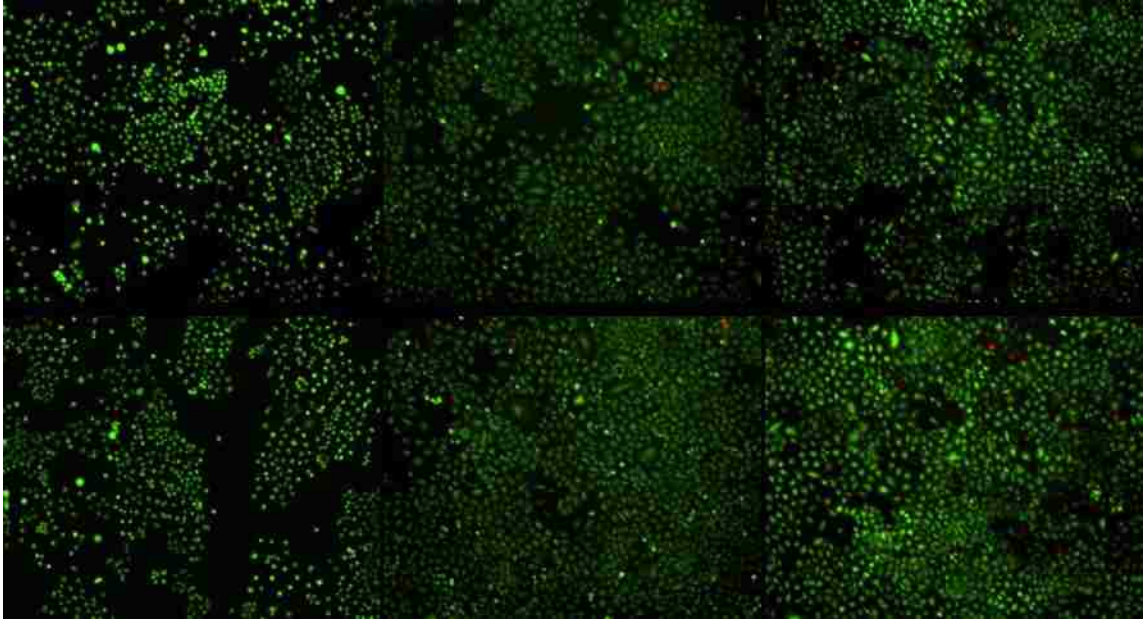
Figure A1.6. Representative images of A549 cells exposed to incubator-mediated hyperthermia. Peripheral images (top, left to right): control, hyperthermia treatment only, 5 mg/mL Fe_3O_4. Central images (bottom, left to right): control, hyperthermia treatment only, 5 mg/mL Fe_3O_4.
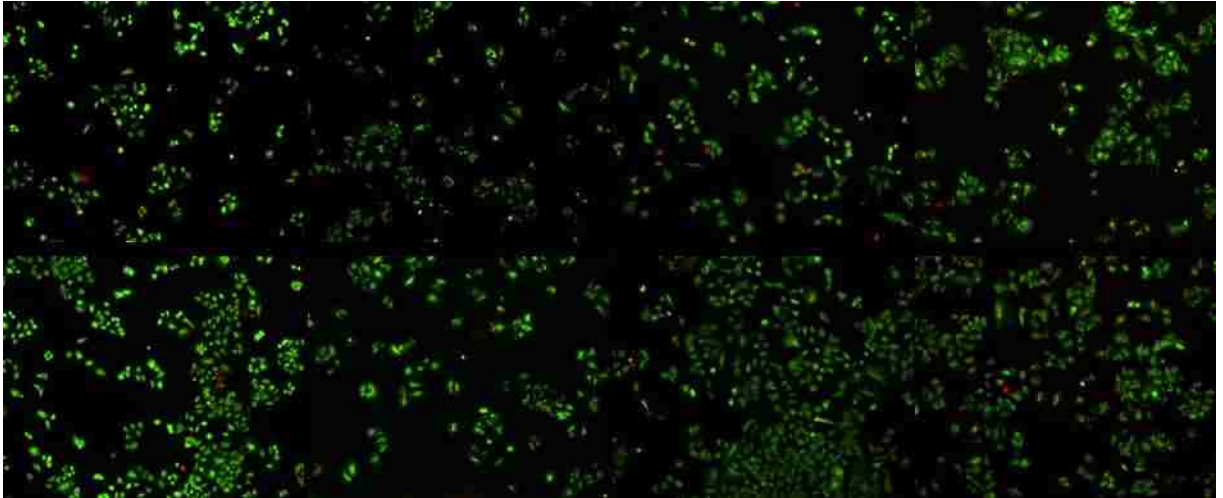
Figure A1.7. Representative images of A549 cells exposed to incubator-mediated hyperthermia. Peripheral images (top, left to right): 125 nM GA, 125 nM GA + 5 mg/mL Fe_3O_4, 125 nM 17-AAG, 125 nM 17-AAG + 5 mg/mL Fe_3O_4. Central images (bottom, left to right): 125 nM GA, 125 nM GA + 5 mg/mL Fe_3O_4, 125 nM 17-AAG, 125 nM 17-AAG + 5 mg/mL Fe_3O_4.

Since our working hypothesis was that the local delivery of hyperthermia through nanoparticle delivery would be more effective than bulk we went forward with AMF-mediated studies. With incubator-mediated hyperthermia, we observed a decrease in cell proliferation but no changes in absolute viability. With AMF exposure, we hoped to demonstrate that the local heat delivery would render cells necrotic and quantifiable with the live/dead assay. In the preliminary study (results not shown), the 125 nM GA AMF-mediated hyperthermia sample overshot the goal temperature of 43 °C and heated to 46 °C. The resulting viability was 100% in the peripheral and 60% in the center where the field is the strongest. Similarly, the iron oxide alone AMF-mediated hyperthermia overshot the goal temperature but to 45 °C. The peripheral viability remained at 100% and the center decreased slightly to 90%. Despite exceeding the typical hyperthermia range, this study demonstrated the possibility of local heat delivery inducing necrosis in cells sensitized to hyperthermia with HSP90 inhibitors. Rethinking our strategy, we increased the hyperthermia temperature from 43 to 45 °C. Since GA was the only sample to show differences in proliferation with incubator-mediated hyperthermia, the gamut of studies was only repeated at 125 nM GA.

Figure A1.8 displays the cell viability and relative cell concentration of all the variables tested. The real time temperature profile of the AMF-mediated hyperthermia samples is displayed in **Figure A1.9**. The temperature did not exceed 45 °C as the steady state averages were 44.72 ± 0.66 °C for iron oxide nanoparticles and 44.56 ± 0.51 °C for GA plus iron oxide nanoparticles. With greater control over the temperature, we did not observe any decreases in absolute viability below 90% indicating no cytotoxic effect. In
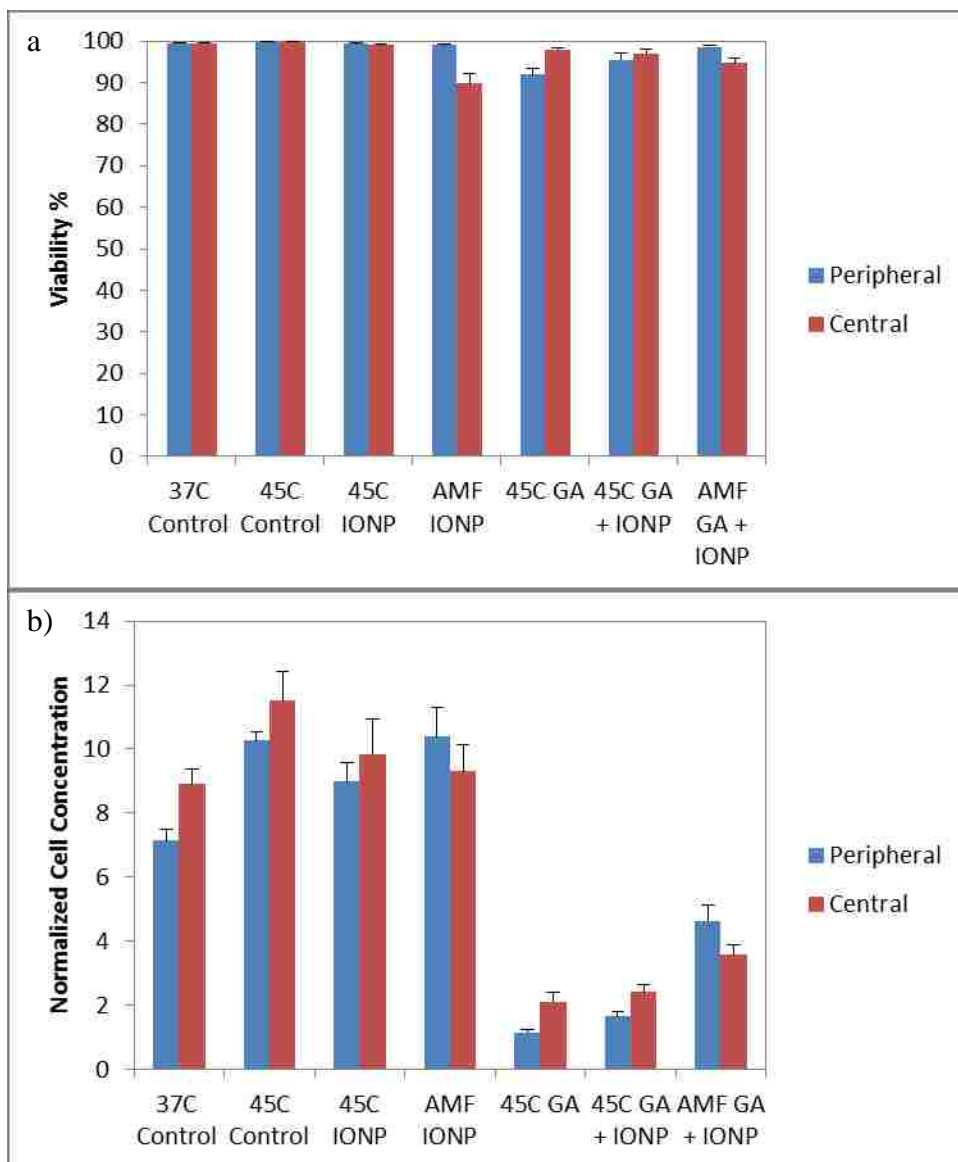
Figure A1.8. Percent viability (a) and normalized cell concentration (b) of A549 cells with or without 48 h exposure to 125 nM concentrations of GA, with or without 45 min exposure to citric acid coated iron oxide nanoparticles (IONP), and with or without 30 minutes of 45 °C hyperthermia.

141
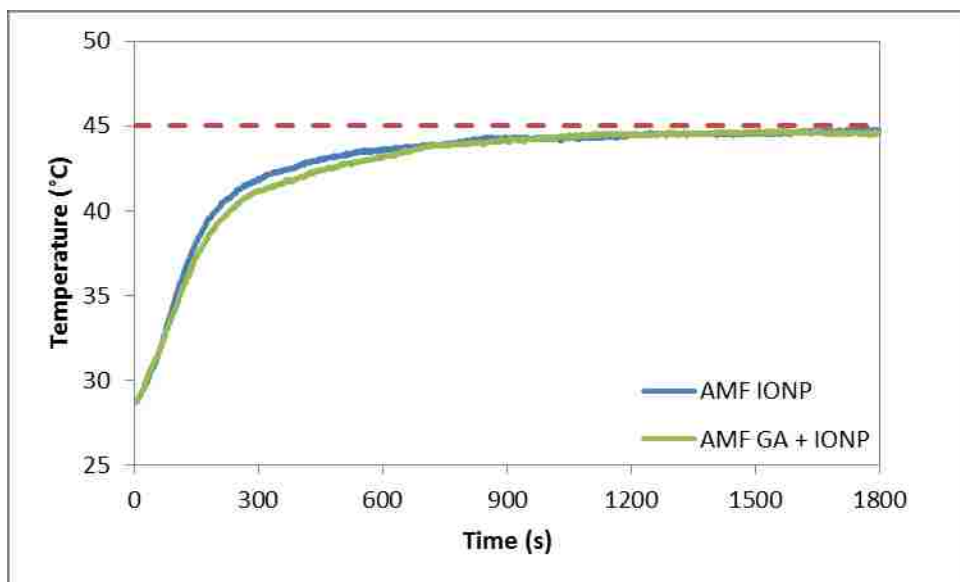
Figure A1.9. Real-time solution temperature obtained using Luxtron FOT. Field

parameters were held constant at 17.0 kA/m at 306 kHz.
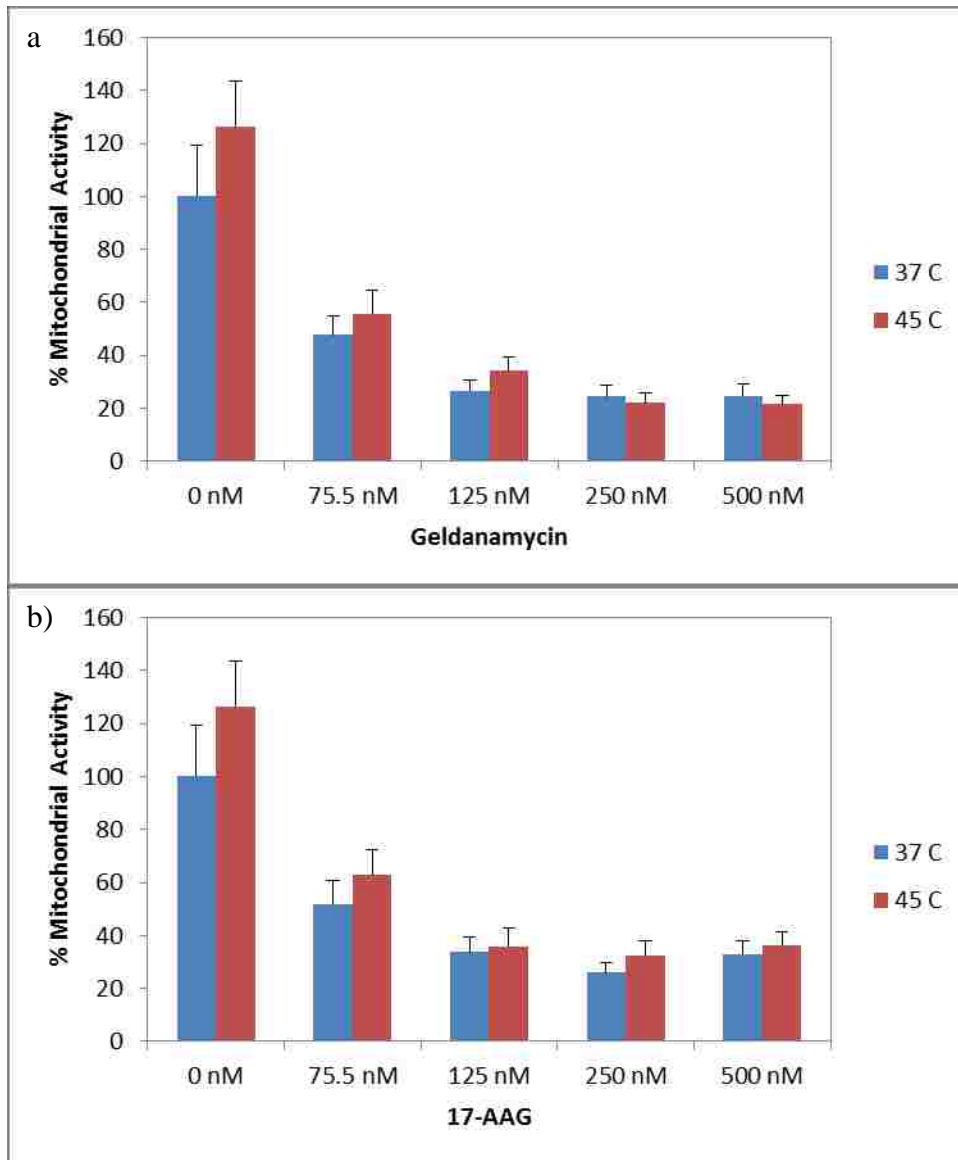
Figure A1.10. Relative mitochondrial activity of PC-9 cells after exposure to GA (a) and

17-AAG (b) with or without hyperthermia treatments. Results are presented as means ± SE

(n = 6).

the case of A549 cells, decreased viability was only observed during the accidental overheating of the sample beyond the hyperthermia range.

The decrease in cellular proliferation observed with the live/dead assay can be explained by the cancer cells entering senescence as a result of the inhibitors. Recall that cancer cells typically overexpress HSP90 to maintain routine cell functions. By inhibiting the function of HSP90, the cells enter a dormant state where they remain in the Gap phase since DNA replication is impaired and they cannot go forward with cell division. Thus, the initial cells seeded would appear live using live/dead assay, however proliferation would be minimized resulting in decreased overall mitochondrial compared to the control.

A1.3.3 PC-9 HSP90 Efficacy Screen

Around the time the AMF-mediated hyperthermia studies were being concluded, Kobayashi et al. published a paper examining the effects of HSP90 inhibitors on non-small-cell lung cancers [20]. They studied 17-dimethylaminoethylamino-17-demethoxygeldanamycin, a variant of 17-AAG with better oral availability, and determined that A549 cells are resistant to the inhibitor. PC-9 cells were shown to be sensitive and were available for an initial screen displayed in **Figure A1.9**. The initial screen found the cells to be more sensitive to the inhibitors, with 50% reduction in activity in the neighborhood of 75.5 nM. However, there was no enhancement with 45 °C incubator-mediated hyperthermia. Future work should investigate PC-9 or other EGFR mutant cell lines which would be more sensitive to HSP90 inhibitors.

A1.4. Conclusion

The results displayed here represent the exhaustive work performed in conjunction with Sarah Seger during her time as an undergrad. Unfortunately, by the time PC-9 cells

became available to us, funds and patience were wearing thin. A few beneficial take home results were determined during the course of this project. The first is the careful selection of a cellular assay. As demonstrated here, a significant decrease in mitochondrial activity does not necessarily mean a decrease in live cells, and multiple assays may be needed to understand what is happening at the cellular level. In the case of A549 cells, they become non-proliferative with HSP90 inhibitors and with the application of intense heat (46 °C) the cells can become necrotic. While the goal was to explore hyperthermia, interesting future work should investigate temperatures just outside the typically defined range. Beyond hyperthermia ranges, HSP90 inhibitors can be used in conjunction with other chemotherapeutics, such as erlotnib, to provide multimodal therapies.

A1.5. References

References are located at the end of the dissertation subdivided by chapters.

Appendix 2: Determining the Effects of Nanoparticle Agglomeration on the Generation of Free Radicals in the Presence of an Alternating Magnetic Field

In chapter 5, we explored the enhanced surface reactivity of iron oxide nanoparticles in the presence of an alternating magnetic field (AMF). We observed that the enhanced generation of free radicals through Fenton-like chemistry decreased with concentration and exposure time. This was attributed to possible AMF-induced nanoparticle agglomeration, which reduced the amount of surface area available for reaction. In this study, we investigated ways of minimizing agglomeration, namely a cyclical field exposure and immobilizing the nanoparticles in a crosslinked network of a poly(ethylene) glycol (PEG)-based hydrogel. Part of this work was done in conjunction with Helen Yao as part of her NSF-REU research.

A2.1. Introduction

The surfaces of iron oxide nanoparticles are capable of catalytically generating reactive oxygen species (ROS) through the Fenton and Haber-Weiss reactions. Advanced oxidation processes (AOP) beneficially use ROS generated through this mechanism to degrade contaminants in the environment [1]. In an aqueous environment, the catalytic generation would be heterogeneous: surface bound Fe^{2+} and Fe^{3+} ions react with H_2O_2 via the Fenton and Haber-Weiss reactions. This Fenton-like process has been used to break down model pollutants, such as methylene blue, a dye utilized by the textile industry [2, 3]. Previous work with AOP have used free iron ions in the reaction environment and they left behind an iron hydroxide sludge waste products [4]. By using heterogeneous catalysts, the waste stream could safely be magnetically decanted to remove byproducts.

Iron oxide nanoparticles are an interesting candidate because not only do they have high surface area to volume ratio for catalytic purposes, but they remotely heat when exposed to an alternating magnetic field (AMF). The heating mechanism is typically attributed to two relaxations: Brownian relaxation and Neel relaxation [5]. There is debate in the literature in terms of the potential application of nanoscale heating effects. The theoretical calculations from Rabin suggest the heat generated from a single nanoparticle or cluster of nanoparticles would be negligible to a surrounding environment [6]. However, Polo-Corrales and Rinaldi provided experimental evidence demonstrating nanoscale heating [7]. Specifically, they designed a core-shell nanoparticle with a temperature responsive polymer coating. With AMF exposure, the surface temperature of the nanoparticles was shown to instantly increase and to drive a temperature responsive polymer beyond its lower critical solution temperature without an immediate increase in solution temperature.

In previous work, we utilized this nanoscale heating effect to enhance ROS generation through the Fenton-like chemistry. This enhancement was determined by measuring methylene blue degradation and comparing it to the Arrhenius prediction at that steady state temperature. However, it was also demonstrated that this enhancement effect decreases as AMF exposure time and IONP concentration increases. We postulated that this may have been caused by AMF-induced nanoparticle agglomeration, which reduced the amount of surface area available for reaction with H_2O_2 [8]. In this study, we investigated methylene blue degradation while trying to minimize agglomeration influence through cyclical field exposure and nanoparticle immobilization in a hydrogel. By cycling the AMF on/off we explore whether the agglomeration is reversible. As illustrated in

147

Scheme A2.1a, the nanoparticles align in chains along the magnetic field but break up from Brownian effects when the magnetic moment is removed. The second technique utilized was immobilizing the nanoparticles in a hydrogel. A hydrogel is a hydrophilic cross-linked polymeric network. Iron oxide nanoparticles can be entrapped in this network and then hydrophilic small molecules, such as methylene blue, can freely diffuse in and out, as diagramed in **Scheme A2.1b**.

A2.2. Materials and Methods

A2.2.1 Materials

Iron (III) chloride hexahydrate ($FeCl_3 \cdot 6H_2O$); iron (II) chloride tetrahydrate ($FeCl_2 \cdot 4H_2O$); hydrogen peroxide (H_2O_2); poly(ethylene glycol) methyl ether methacrylate (PEG1000MA, Mn = 1100.13 g/mol); and methylene blue (MB) were obtained from Sigma Aldrich (St Louis, MO). Ammonium hydroxide (NH_4OH) was obtained from EMD Chemicals (Gibbstown, NJ) and poly(ethylene glycol) dimethacrylate (PEG400DMA, Mn = 454.18 g/mol) was obtained from Polysciences Inc. All materials were used as received.

A2.2.2 Iron Oxide Nanoparticle Synthesis

A one-pot co-precipitation method was used to prepare the iron oxide nanoparticles as similarly reported previously.[9] Briefly, aqueous solutions of $FeCl_3 \cdot 6H_2O$ and $FeCl_2 \cdot 4H_2O$ were combined in a 2:1 molar ratio in a sealed three-neck flask under vigorous stirring and an inert N_2 environment. Once 85 °C was reached, a 1.5 M solution of NH_4OH was injected into the vessel and the reaction was carried out for 1 hour. The nanoparticles were initially decanted via magnetic decantation to remove majority of the impurities. After, they were resuspended in water and transferred to a dialysis bag for 48 hours of dialysis. Following the washing steps, the particles were stored in suspension.
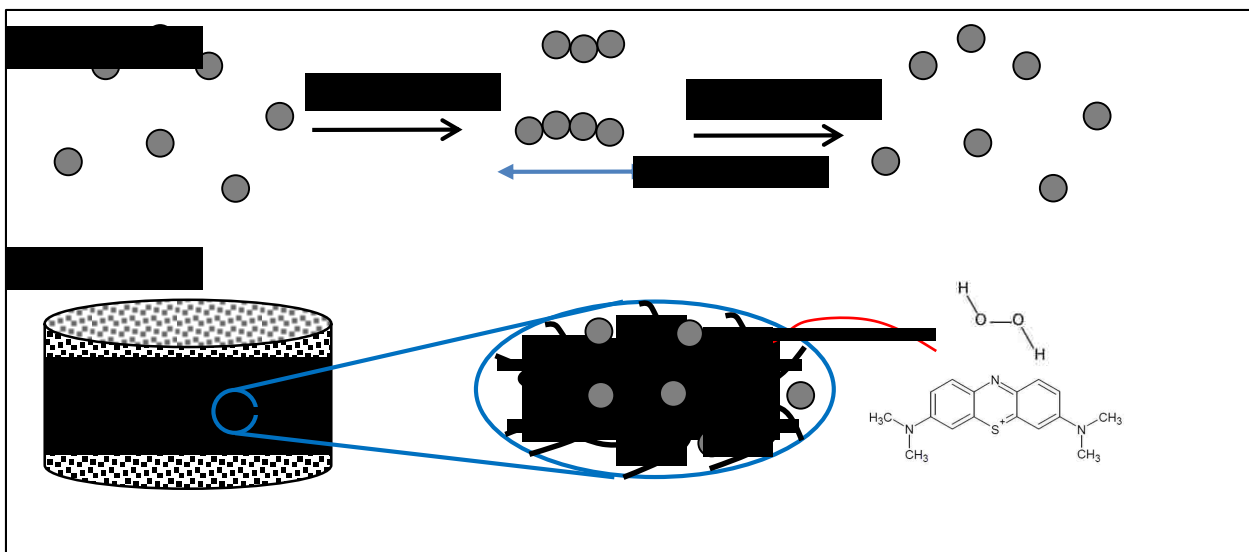
Scheme A2.1. Proposed reversible agglomeration of iron oxide nanoparticles aligning in chains with the application of a magnetic field (a). The immobilization of iron oxide nanoparticles in a hydrogel and the diffusion of hydrogen peroxide and methylene blue into the matrix to interact with the particle surface (b).

A2.2.3 Nanocomposite Hydrogel Synthesis

Nanocomposite hydrogels were synthesized via free radical polymerization using a 4:1 molar ratio of PEG1000MA to PEG400DMA. Iron oxide nanoparticles (1, 2.5, 5 wt%) and DMSO (50 wt%) were added to the macromers, and the mixture was sonicated to disperse the nanoparticles uniformly. Two different methods were used to initiate the hydrogel cross-linking reaction based on iron oxide loading. Photoinitiation with 1.5 wt% 2,2-dimethoxy-2-phenylacetophenone (Sigma-Aldrich) was used to synthesize hydrogels of low iron oxide concentration (< 5 wt%). While at the high concentration, 5 wt%, chemical initiation with 4 wt% of accelerator N, N, N', N'-tetramethylethane-1,2-diamine (Sigma-Aldrich) and 2 wt% of initiator ammonium persulfate (Sigma-Aldrich) was used. After addition of the initiator, the mixture was vortexed for 10 s before transferring to a template. Photoinitiated hydrogels were exposed to an ultraviolet light source (14.0 mW/cm2) for 5 min, while chemically initiated hydrogels were allowed to react overnight. After the reaction was complete, the hydrogels were washed for 48 hours in water. Upon removal from the water bath, the hydrogels were washed for 2 hours in ethanol. The hydrogels were transferred to a freeze-dryer to remove excess solvent. Freeze-dried hydrogels were mechanically ground and sieved to obtain composite microparticles in the size range of 150–500 μm and stored under vacuum.

A2.2.4 Methylene Blue Degradation Assay

The methylene blue degradation experiments were performed in 2 ml microcentrifuge tubes in either temperature controlled water baths at four temperatures (28, 30, 34, 37°C) or exposed to an AMF. One ml samples were prepared by diluting stock concentrations of methylene blue to 5 μg/ml and iron oxide nanoparticles to 75 μg/ml. The

samples were placed in the water bath for 10 min to equilibrate to the expected temperature. The degradation was initiated by spiking the samples with 25 μl of 30% H_2O_2 to a working concentration of 245 mM. The samples were exposed to a 30 s on/off cyclical field of approximately 51.0 kA/m in strength at 292 kHz frequency. The temperature was measured with a Luxtron FOT Lab Kit. After given time intervals the samples were centrifuged for 30 s using a Phenix Quickspin Centrifuge, magnetically decanted, and measured using UV-visible spectroscopy (maximum absorbance at 665 nm) with a Varian Cary. To account for nanoparticle scattering from the nanoparticles that remain in suspension, samples containing only nanoparticles were measured and subtracted out from the sample absorbance.

Similarly, nanocomposite hydrogel particles of different iron oxide loading densities were combined with 1 ml of 5 μg/ml methylene blue. The samples were placed in the water bath for 10 min to equilibrate to the set temperature. The degradation was initiated by spiking the samples with hydrogen peroxide at a working concentration of 1.5 or 3%. After given time intervals the samples were centrifuged for 1 min, magnetically decanted, and measured using UV-visible spectroscopy. The controls prepared were nanocomposite hydrogel suspended in methylene blue solution, nanocomposite hydrogel suspended in water, and pure hydrogel suspended in methylene blue solution. The working concentrations of iron oxide were back calculated from the concentration of nanocomposite to 750 and 1067 μg/mL iron oxide.

Nanocomposites exposed to the AMF were prepared as described above. The AMF was operated at a field of approximately 30.6 kA/m in strength at 296 kHz frequency. The samples were first pre-heated for 10 min in a water bath to 32°C. Pre-heated samples were

placed inside the magnetic coil for 15 min of pre-exposure to the AMF to allow the sample to reach a steady state temperature. After pre-exposure, 30°C pre-heated hydrogen peroxide was added to the suspension, and the reaction was allowed to run for 5, 10, 15, 20, and 30 min under the AMF. After the allotted time for AMF exposure, the sample was analyzed for degradation using the UV-vis spectrometer.

To quantify the enhancement of ROS production, an enhancement factor (EF) defined in chapter 5 was utilized. Recall, the EF is the ratio between experimental degradation (exp) and theoretical degradation (theo) from the Arrhenius prediction:

$$EF = (1-(A_t/A_o)_{exp}) \, / \, (1-(A_t/A_o)_{theo}) \qquad \textbf{Equation A2.1}$$

Where A_t is the measured absorbance at a given time normalized to the initial absorbance, A_o. If the sample did not reach steady state at the end of the time interval (as was the case for 5 min exposure time), an average temperature over the time period was used instead.

A2.2.5 Statistical Analysis

Statistical analysis of the enhancement factor was determined using a one sample t-test where the hypothetical mean was set to 1. To indicate significant enhancement a single, double, or triple asterisk corresponding to $p < 0.05$, 0.01, and 0.001 respectively were included in the figure.

A2.3. Results and Discussion

A2.3.1. Cyclical Field Exposure

The kinetics of colloidal iron oxide reacting with hydrogen peroxide to degrade methylene blue was explored in Chapter 5. In that chapter, we explored three iron oxide concentrations based on their ability to heat a solution with AMF exposure. In this experiment, we focused on the 75 µg/ml iron oxide concentration. At this concentration,

there was minimal (i.e., 1.5 °C) temperature rise with prolonged AMF exposure. The system displayed an initial enhancement at 5 minutes of field exposure but decreased to no statistical difference by 15 minutes. With cyclical field exposure, the temperature profile never deviated from room temperature. 30 s intervals were not long enough for the radiant heat from the copper coil to heat the solution of methylene blue to 32-32.5 °C. Initial studies were performed with a 34 °C water bath pre-heat, but over the course of reaction time the temperature plummeted. The protocol was revised to keep all reactants at room temperature during sample preparation. The Arrhenius analysis was done using the constants from Chapter 5 (A = 1.05e14 s-1, -Ea = 9.91e4 J/mol) at the steady state temperature measured during field exposure.

The EF results can be found in **Figure A2.1** comparing cyclical field exposure to the static field exposure data from Chapter 5. The cyclical field exposure EF remained statistically different from the hypothetical mean throughout the three reaction times and never statistically deviated from each other. Note, unlike the static field where reaction time corresponds to length of AMF exposure, in this case the field was cycled 30 s on/off so total length of AMF exposure would be 50% of the reaction time. Despite 50% of the length of AMF exposure, the cyclical samples displayed a greater EF compared to the static field. Recall the steady state temperature was room temperature so the theoretical degradation value, the denominator in the EF equation, would be much lower than the theoretical degradation at 34 °C. Despite no fluctuations in perceived temperature, the local temperature surrounding the nanoparticles with field exposure would immediately exceed 34 °C driving the reaction kinetics. If we were to compare net degradation, the static field would perform better due to the elevated steady state temperature.
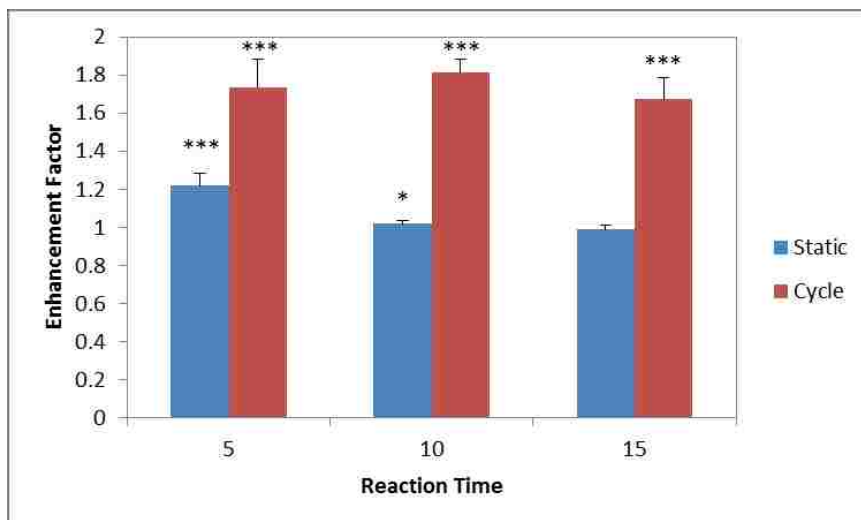
Figure A2.1. Enhancement factor comparing extent of methylene blue degradation based on experimental and theoretical values at 75 μg/ml of iron oxide nanoparticles in a static or cyclical field exposure over varying lengths of reaction time. The field cycle was 30 s on/off.

In chapter 5, we attributed the decrease in EF with time to the agglomeration of nanoparticles decreasing the available surface area for reactivity. In the case of cyclical field exposure, there is no decrease in EF with time suggesting that the agglomeration effect is not taking place. The 30 s AMF exposure is either not long enough to induce measurable agglomeration or the agglomeration induced is reversible allowing the nanoparticles to disperse during the off period. In both cases, there are minimal fluctuations in available surface area allowing the EF to remain constant over the three reaction times measured.

A2.3.2 Nanocomposite Immobilization

Initial experiments explored the use of hydrogel nanocomposite discs to degrade methylene blue. The discs proved to have a large diffusional barrier, as the methylene blue degradation was very low and did not fit well to any of the three kinetic models (zeroth, first, and second order) considered in this experiment. Additionally, the hydrogel discs produced inconsistent methylene blue degradation levels, as it was observed for some of the time points the absorbance of the methylene blue was larger at a later time than an earlier time. This would suggest that less methylene blue has degraded over a longer time period which is inherently false based on our knowledge of the reaction kinetics. The study was revised to use nanocomposite microparticles to minimize the diffusion length and obtain more reproducible results.

Kinetics data for zeroth, first, and second order models obtained for 5 wt% Fe_3O_4 nanocomposite microparticles with a loading density of 750 μg/mL and 1.5 wt% hydrogen peroxide are displayed in **Figure A2.2** and summarized in **Table A2.1**. Based on the fit of the data to the zeroth, first, and second order reaction models, it was concluded that the reaction most closely followed a second order model as the fit had high R2 coefficients and

a y-intercept close to 1. A general observation was that the zeroth and second order models were the best fit to the kinetics data for other loading densities. However, based on a physical model it would be more logical for the degradation to be concentration-dependent; i.e. the amount of methylene blue in the solution should affect its degradation rate. This makes the second order reaction model the most feasible. This matches the kinetic model used in Chapter 5 for colloidal iron oxide nanoparticles. The four temperature trials also yielded the relevant Arrhenius constants (derived from **Figure A2.3**), where the exponential prefactor, *A*, was found to be 2.53e11 and the activation energy, *-Ea*, was found to be 91,800 J/mol.

This kinetics data was used to determine the EF (**Figure A2.4**) and it was found that the AMF enhanced ROS production and methylene blue degradation at all times tested. Similar to Chapter 5, the enhancement factor for methylene blue degradation due to AMF exposure decreased as AMF exposure time increased. The decrease in EF from 5 min was statistically significant ($p < 0.01$) starting at 15 min. Despite the observed decrease, the enhancement factor observed at 30 min remained relatively high (1.8 ± 0.3) compared to data obtained for free nanoparticles in suspension, where at 15 min and 75 and 150 μg/mL loading density the enhancement had dropped to 1 (no enhancement). The increased enhancement factor, relative to that observed in the free nanoparticle system would suggest that the hydrogel entrapment of the nanoparticles was able to prevent agglomeration. However, there was still a decrease in enhancement factor with AMF exposure time.

The elevated EF could be in part explained by the inconsistencies in obtaining reliable temperature data. The loading density of the microparticles was 750 μg/ml which would lead to local temperatures greater than 37 °C. The temperature measurement used
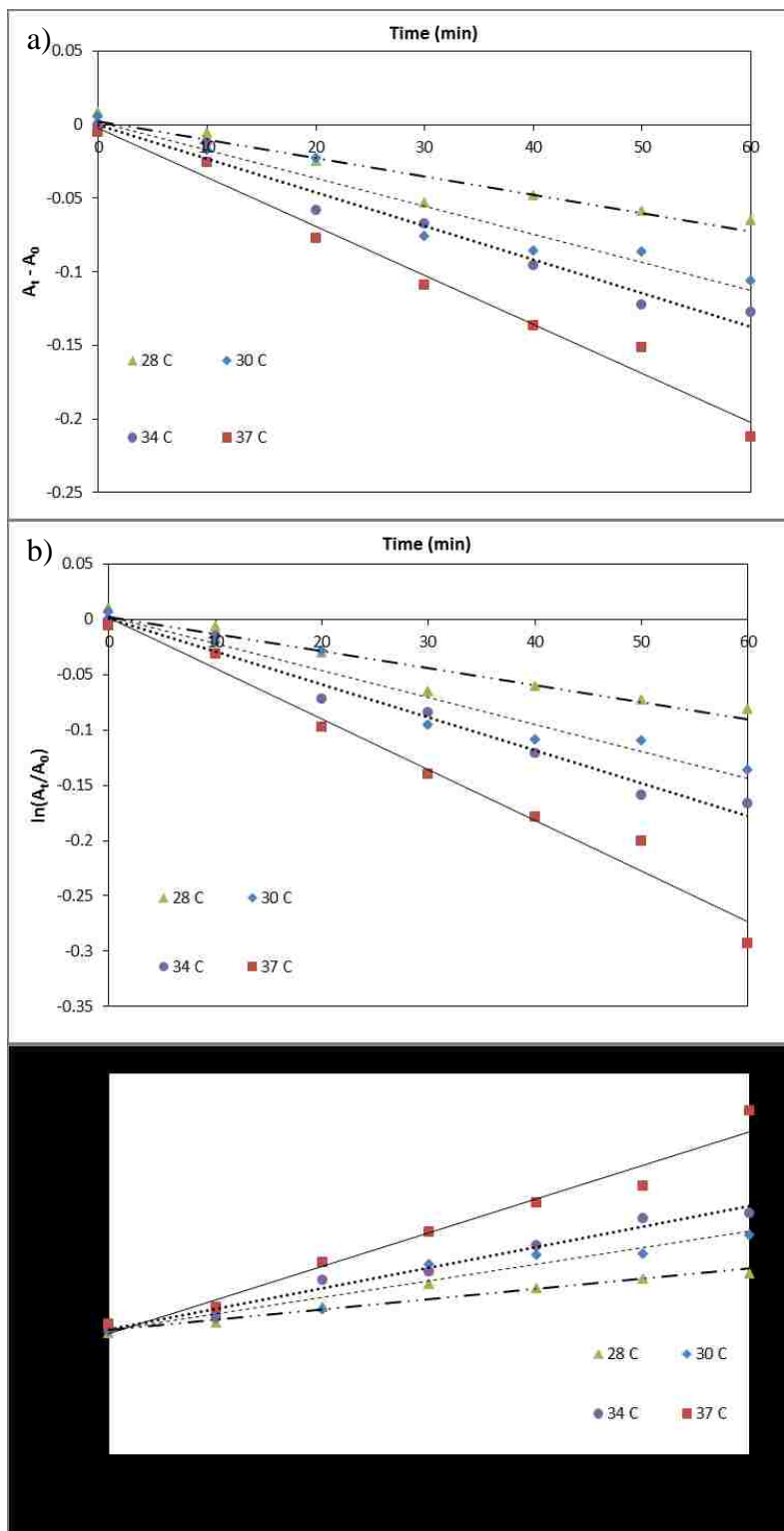
Figure A2.2. Zero- (a), First- (b), and Second-order (c) kinetic plots of methylene blue degradation using 5 wt% nanocomposite microparticles at 750 μg/mL loading density iron oxide.

Table A2.1. Rate constants for MB Degradation derived from Figure 2.

Temperature (°C)	Zero Order			First Order			Second Order		
	k (A min^{-1})	R^2	y-intercept	k (min^{-1})	R^2	y-intercept	k (A^{-1} min^{-1})	R^2	y-intercept
28	0.00125	0.908	0.00208	0.00155	0.911	0.00274	0.00161	0.914	0.997
30	0.00191	0.926	0.00189	0.00245	0.928	0.00324	0.00262	0.931	0.996
34	0.00228	0.971	-0.00054	0.00298	0.974	0.00112	0.00324	0.976	0.997
37	0.00333	0.980	-0.00260	0.00458	0.976	0.00201	0.00529	0.968	0.991
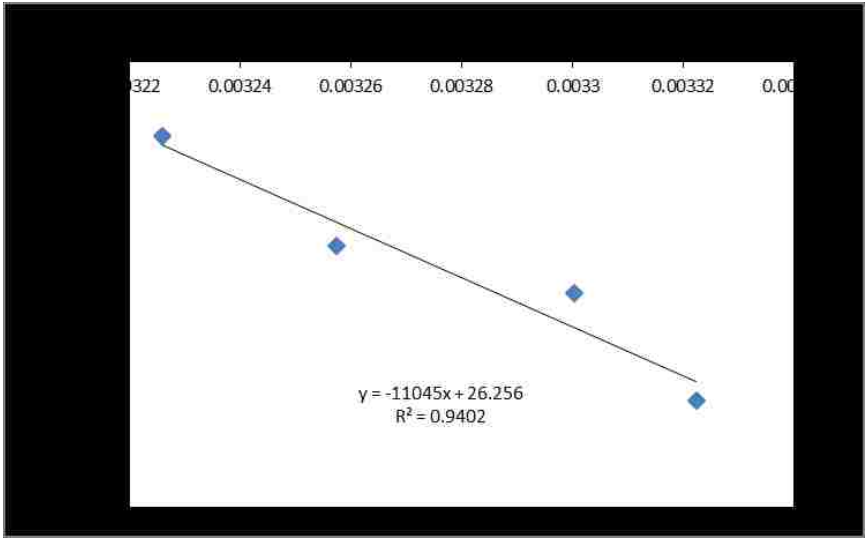
Figure A2.3. Arrhenius plots derived from second order kinetic model from methylene blue degradation.
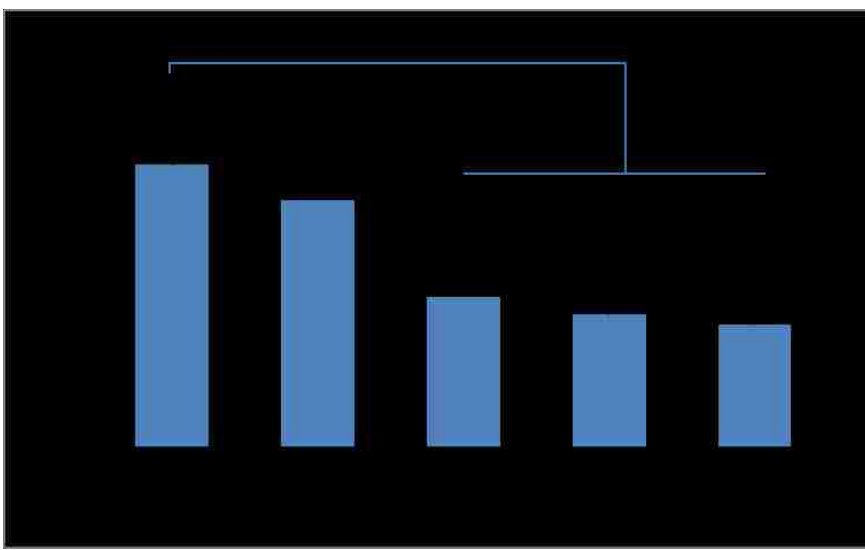
Figure A2.4. Comparison of enhancement factor of methylene blue degradation using nanocomposite microparticles based on experimental and theoretical values at different durations of AMF exposure. Samples were compared to 5 minutes to indicate very significant ($p < 0.01$) declines in enhancement with time.

to calculate enhancement factor was not the local temperature of the hydrogel particles but rather, the average solution temperature with the probe placed in the center of the centrifuge tube. Typically, the microparticles settled to the bottom of the vial and were allowed 15 minutes of AMF exposure to reach steady state prior to spiking the reaction with hydrogen peroxide. During the reaction, the microparticles would become entrapped in oxygen bubbles (byproduct of the Fenton reaction) and circulate in the tube disturbing the flexible fiber optic thermoprobe. Therefore, the calculated enhancement factor is not the true enhancement factor reflecting the local reaction kinetics but rather a relative enhancement factor to this nanocomposite microparticle system.

The decrease in EF at 15 min could most likely be explained by the decrease in available hydrogen peroxide. Hydrogen peroxide would be consumed by both the reaction and natural degradation into hydrogen and oxygen at elevated temperatures. The observable presence of bubbles in the reaction chamber would indicate a more hydrogen peroxide is being consumed compared to the colloidal experiment. Future research should consider a secondary injection of hydrogen peroxide to see if the EF can be sustained for a longer period of time. Another possible reason for the decrease in enhancement factor could be a permanent change in the oxidation state of the surface to γ-Fe2O3. At a higher temperature and in the presence of oxygen, this change in oxidation state occurs more readily. This would render the nanoparticles less reactive as Fe3+ would become the predominant ion present at the surface.

Despite the decrease in EF with time, in the section we demonstrated the potential to immobilize iron oxide nanoparticles in a polymeric matrix and display enhanced reactivity with AMF exposure. For AOP applications, future work should investigate the

use of nanocomposite films or membranes to study the degradation in a flow system. By using an AMF to heat only the local environment there is limited risk of premature hydrogen peroxide decomposition compared to bulk heating of the entire fluid.

A2.4. Conclusion

This study investigates means of preventing nanoparticle agglomeration to sustain the enhanced reactivity of iron oxide in the presence of AMF. In the first section, we cycled the AMF 30 s on/off to prevent the nanoparticles from agglomerating in chains along the magnetic field minimizing the available surface area. The results displayed sustained enhancement demonstrating reversible agglomeration with magnetic field exposure. In the second section, we immobilized iron oxide nanoparticles in nanocomposite hydrogel microparticles. While we observed enhanced reactivity, the enhancement was not sustained with time. Future work is needed to investigate the cause of the decrease in enhancement. However, this demonstration opens up the possibility of creating different nanocomposite systems for environmental remediation.

A2.5. References

References are located at the end of the dissertation subdivided by chapters.

Appendix 3: Composite GMO-GMS Cubosomes Loaded with Iron Oxide Nanoparticles for the Controlled Delivery of Therapeutics

The focus of this work explores the use of thermo-responsive materials for controlled drug release applications. Previous work has demonstrated that oleic acid coated iron oxide nanoparticles can be incorporated into a monoglyceride-based thermo-responsive matrix and be used as a controllable drug release depot. Shifting the material from the bulk to nanoscale, GMO-GMS cubosomes were prepared through a dispersion method. Demonstrating the controlled release of a model protein raises the possibility of designing multi-functional nanoparticle systems in the future.

A3.1. Introduction

Magnetic nanoparticles are being studied for a wide range of biomedical applications such as diagnostic imaging, drug delivery, and thermal therapy of cancer [1-4]. Recently, we developed a novel monoglyceride-based thermo-responsive matrix for the controlled delivery of therapeutics [5]. The monoglycerides, glyceryl monooleate (GMO) and glyceryl monostearate (GMS), are amphiphilic molecules that self-assemble into a variety of crystalline structures that can be utilized for drug delivery [6, 7]. By mixing GMO and GMS in different compositions, the melting and crystallization points can be systematically tuned. Oleic acid coated iron oxide nanoparticles were incorporated into the lipid matrix for the magnetic actuated release of the drug. When exposed to the alternating magnetic field (AMF), the iron oxide nanoparticles remotely heat, driving the matrix past a melting point triggering the drug release.

Colloidal lyotropic liquid crystalline nanoparticles represent a growing area of advanced nanoparticles for drug delivery [8-11]. Based on the local environment, lyotropic

liquid crystals can form a variety of morphologies, of which the non-lameller inverse cubic phases, or cubosomes, are of interest. Mulet et al. identified four advantages of cubosomes over liposomes: loading of a range of agents including hydrophobic, hydrophilic, and amphiphilic; high loading extant due to increased lipid per particle and surface area; rigid internal structure facilitating the loading of imaging agents; and the mesophase has been shown to significantly affect release rates [8]. Beyond bioactive agent loading and release, researchers are interested in loading nanoparticles into the biocontinuous phase particles. With phytantriol-based nanoparticles, Fong et al. was able to successfully load gold nanorods into the liquid crystal structure [12]. When excited with NIR light, the nanoparticles underwent a reversible switch through different phase transitions. Acharya et al. integrated iron oxide nanoparticles into a phytantriol matrix for use as an enhanced MRI contrast agent [13]. To date, no one has studied the triggered release of therapeutic with composite cubosomes.

In this study, we synthesized composite cubosomes based on the aftermentioned GMO-GMS matrix blend. As before, oleic acid coated nanoparticles were synthesized with a one-pot co-precipitation method. Various blends of composite GMO-GMS cubosomes (based on the previous work, 75-25 wt% was the preliminary starting point) were created by dispersion using ultrasonication and stabilized with Pluronic F-127. Lysozyme was used as a model protein and drug release assessed with and without alternating magnetic field exposure. We hypothesized that the protein will preferentially partition into the matrix facilitating loading and when exposed to the alternating magnetic field, the thermal energy will trigger a phase change altering the release of the drug.

A3.2. Materials and Methods

A3.2.1 Materials

Iron (III) chloride hexahydrate ($FeCl_3 \cdot 6H_2O$), iron (II) chloride tetrahydrate ($FeCl_2 \cdot 4H_2O$), oleic acid (OA), Pluronic F-127, lysozyme, and fluorescein isothiocyanate (FITC) were obtained from Sigma Aldrich (St Louis, MO), and used as received. Glycerol monooleate (in the form of Myverol 18-99) and glycerol monostearate (Myverol 18-04) were kindly donated by Kerry Scientific (Beloit, WI).

A3.2.2 Synthesis of Oleic Acid Coated Iron Oxide Nanoparticles

A one-pot co-precipitation method was used to prepare the oleic acid coated iron oxide nanoparticles as previously reported [14]. Briefly, aqueous solutions of $FeCl_3 \cdot 6H_2O$ and $FeCl_2 \cdot 4H_2O$ were combined in a 2:1 molar ratio in a sealed three-neck flask under vigorous stirring and an inert N_2 environment. Once 85 °C was reached, 5 mL of NH_4OH was injected into the vessel followed by 2 ml of oleic acid and the reaction was carried out for 1 hour. The particles were washed and retrieved with magnetic decanting. Following the wash the particles were dried and stored under vacuum.

A3.2.3 Synthesis of GMO-GMS Composite Nanoparticles

Nanoparticle composite blends of GMO-GMS were prepared as previously reported [5]. Briefly, compositions of 75 and 80 w/w% GMO-GMS were prepared by a fusion method. These lipid matrices were prepared with and without 0.5 or 2.0 wt% dried oleic acid coated iron oxide nanoparticles. The mixtures were homogenized by a cycle of melting in an oven at 75 °C, vortexing, and chilling in the freezer. Typical 4-5 cycles were required to obtain a homogeneous blend

Blends of GMO-GMS at 75:25 and 80:20 and composite blends of oleic acid coated iron oxide nanoparticles were used to synthesis cubosomes. The blends were added to an aqueous solution of 0.5 w/v% Pluronic F-127 at a working concentration of 25 mg/ml. The suspension was probe sonicated at 0.5 Hz on/off for 5 minutes resulting in a milky dispersion.

A3.2.4 GMO-GMS Characterization

Differential scanning calorimitry (DSC). The thermal behavior and phase diagrams of the GMO-GMS blends were investigated with using a differential scanning colorimeter (DSC-2920, TA Instruments). DSC thermograms were produced by hermetically sealing samples in aluminum pans and heated at 5 °C/min from 5 °C to 90 °C, cooled back to 5 °C, and reaheated to 90 °C

Dynamic Light Scattering (DLS). DLS measurements were obtained using a Malvern Zetasizer, Nano ZS90 instrument. Post synthesis, samples were diluted to 0.5 mg/ml in DI-water for DLS measurements.

Alternating Magnetic Field heating. The AMF heating profile was observed using a custom made Taylor Winfield magnetic induction source and temperature was measured with a Luxtron FOT Lab Kit. Particles were diluted in DI water to a concentration of 2 mg/mL. One ml of solution was placed in a 2 ml centrifuge tube and placed in the center of the coil. The solution was heated in a field of approximately 58.1 kA/m in strength at 292 kHz frequency for 5 minutes.

A3.2.5 Drug Loading and Release

Drug release behavior was studied by using lysozyme as a model protein. Lysozyme was tagged with FITC following a similar protocol from Takahashi et al. [15].

Lysozyme was dispersed into a 0.1 M sodium phosphate buffer solution with 3% DMSO co-solvent. A 100 mM solution of FITC in anhydrous DMSO was made and slowly added to the lysozyme such that the final molar ratio was 5:1 FITC-lysozyme. The workup was placed in the refrigerator overnight to facilitate the reaction between the amino N-terminus and the isothiocyanate group. The workup was purified with dialysis for 24 hours and lyophilized to remove water.

The dried lysozyme was incorporated into the GMO-GMS matrices at 1 wt%. Previously prepared GMO-GMS were added to lysozyme in a centrifuge tube and underwent similar melt-mixing cycles to incorporate. Cubosomes from the blends were prepared as described above. Drug loaded cubosomes were diluted to 2 mg/ml in PBS at room temperature or pre-heated to 43 °C. At prescribed periods, 0.4 ml samples were taken and placed into Amicon Ultra centrifugal filters (100kDA MWCO) at centrifuged for 10 minutes at 18000xg. 200 µl sample of filtrate was transferred to a black 96 well plate and fluorescent intensity was measured at 495 nm/520 nm.

A3.2.6 AMF-triggered Release

Drug loaded cubosomes were prepared as described above. The sample was kept at room temperature for the first two hours to facilitate initial release. After this time, the sample was transferred to the AMF and exposed at a field of approximately 58.1 kA/m in strength at 292 kHz frequency for 30 minutes. The sample was returned to room temperature for one hour followed by another 30 minute field exposure. As described above, 0.4 ml samples were taken per time point and centrifuged.
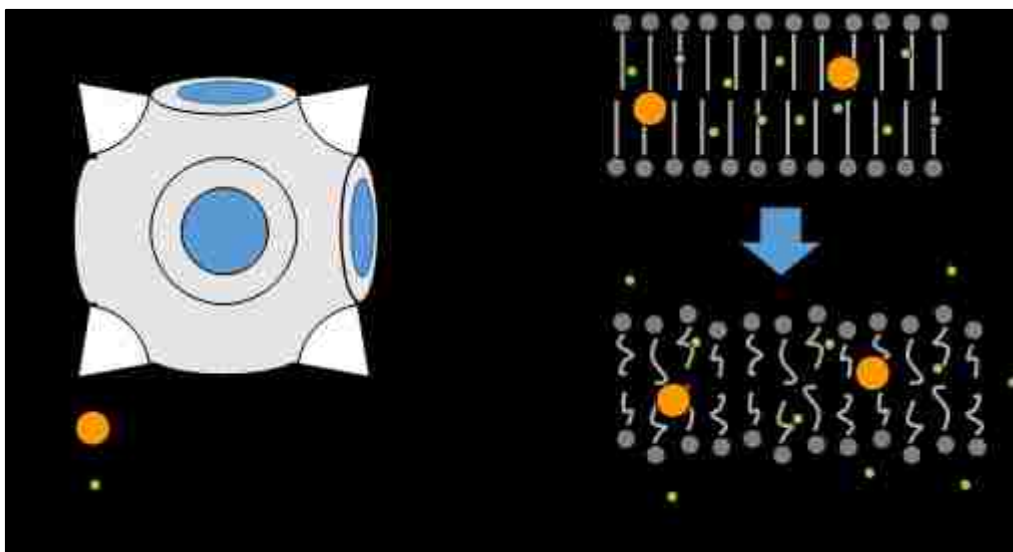
Scheme A3.1. Illustration of the proposed cubosome system with oleic acid coated iron oxide and drug molecules loaded into the GMO-GMS matrix. When the temperature exceeds the melting point, either through water bath or AMF activation, the matrix will undergo a phase change releasing the drug.

A3.3. Results and discussion

A3.3.1 Nanoparticle Characterization

Developing a thermos-responsive matrix combined with the remote heating of iron oxide nanoparticle provides the opportunity for controlled release of a therapeutic. The proposed inverse cubic phase is illustrated in **Scheme A3.1**. The oleic acid iron oxide nanoparticles and drug molecules initially reside within the ordered structure of the GMO-GMS matrix. When the system is heated, the matrix will undergo a phase transition allowing for the actuated release of the drug molecules. Different ratios of GMO-GMS and iron oxide loading were evaluated to determine key physical properties.

The phase behavior of the GMO-GMS blends was determined using differential scanning calorimetry. **Figure A3.1** displays the thermograms of two ratios of GMO-GMS, 75:25 and 80:20, with and without oleic acid coated nanoparticles at 0.5wt% loading. Along the initial heating cycle, two endothermic melting, T_m, values were observed. Previously, these two T_m were attributed to the GMO-rich and GMS-rich phases in the gel, owing to the fact that pure GMO has a Tm of 36.8 °C and pure GMS has a T_m or 82.7 °C [5]. The values of T_m are displayed in **Table A3.1**, and despite slight changes in ratio and the presence of nanoparticles there is minimal difference in reported temperatures observed on the first pass. Upon cooling, the crystallization temperature, T_c, of the 72:25 blend was 36.3 °C compared to 34.5 °C. For repeated activation cycles such as pulsatile delivery, it is important that this value is near physiological so that the delivery system recrystallizes constricting drug release. To simulate multiple cycles, a second heating pass was studied and T_{m2} is reported in **Table A3.1**. During the second heating, the T_{m2} better blend into a single defined point. The T_{m2} of 75:25 is 41.5 °C which would correspond to a mild
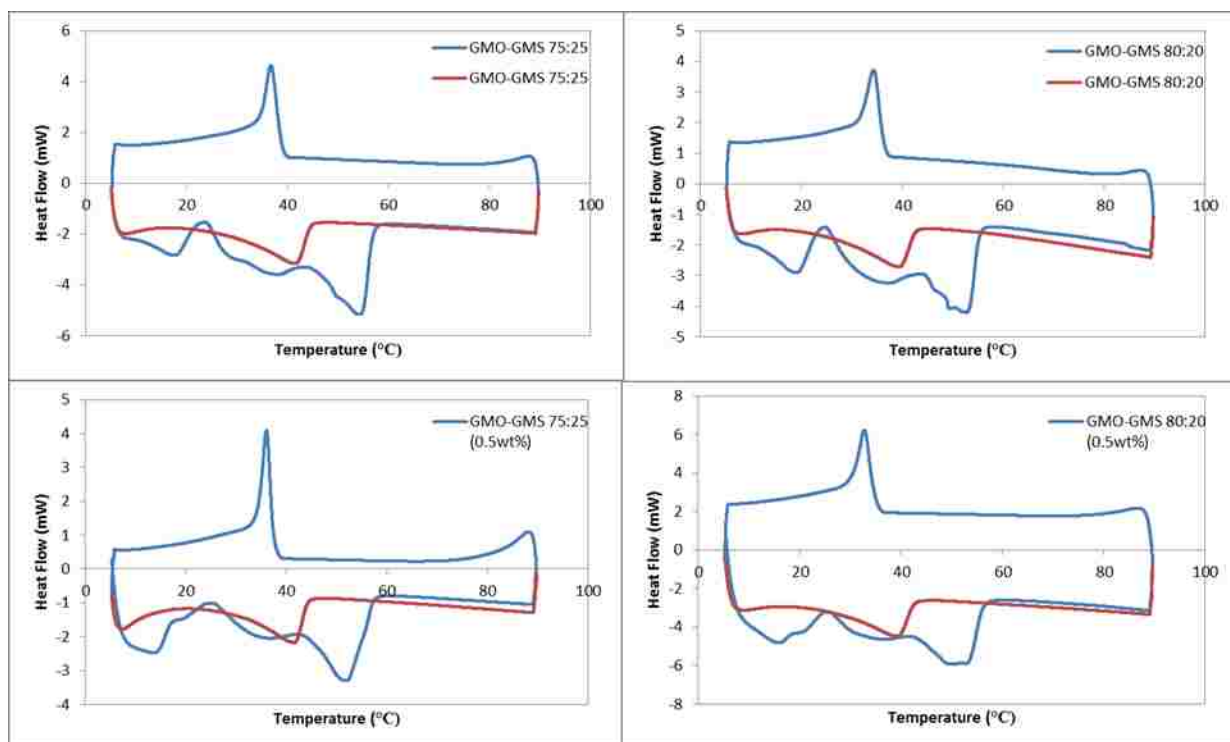
Figure A3.1. DSC thermogram of GMO-GMS mixtures with the second heating cycle trend in red

Table A3.1. Phase behavior of GMO-GMS mixtures

GMO-GMS	T_m GMO rich phase	T_m GMS rich phase	T_c	T_{m2}
75:25	37.3	53.8	36.3	41.5
80:20	37.3	51.7	34.5	39.9
75:25 (0.5wt%)	37.3	51.3	36.1	41.8
80:20 (0.5wt%)	37.3	51.7	32.4	39.6

Table A3.2. Particle size determined by DLS

	Zavg	PDI
75:25	154.0	0.239
75:25 0.5wt%	164.5	0.383
75:25 2wt%	213.5	0.330
80:20	189.3	0.241
80:20 0.5wt%	152.1	0.223
80:20 2wt%	212.6	0.329
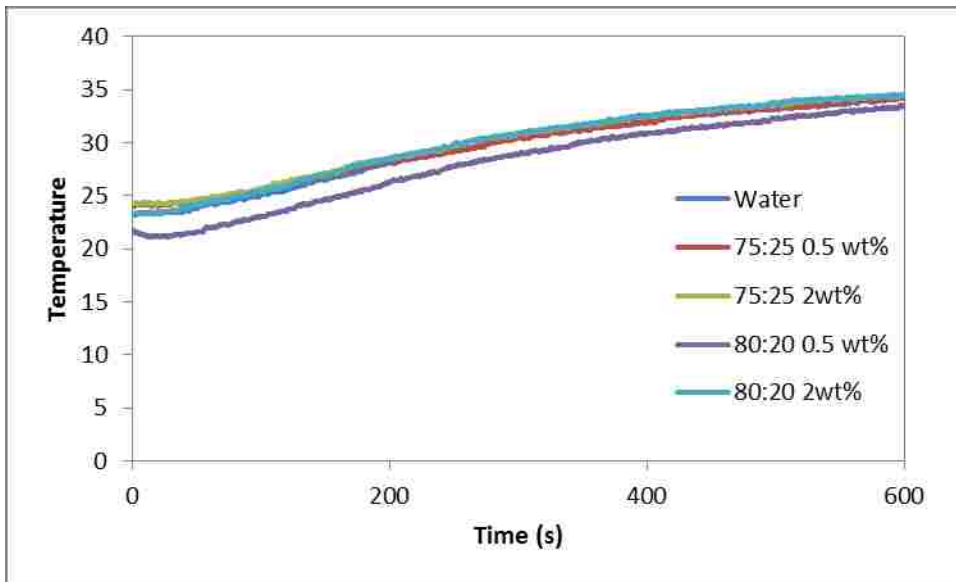
Figure A3.2. Heating profile of composite GMO-GMS samples exposed to the AMF at different ratios of GMO:GMS and iron oxide loading percentages.

hyperthermia range. When used as cubosomes, Pluronic F-127 stabilizers are added to the GMO-GMS matrix for aqueous stability. DSC measurements were performed on these systems and minimal deviation from the pure system were observed.

Prepared cubosomes were analyzed with DLS to determine the hydrodynamic particle size reported as Z-average in **Table A3.2**. The particle sizes are on the order of 150-200 nm with an increase in particle size with increase in nanoparticle loading. The iron oxide nanoparticles were exposed to the AMF, as discussed below, and were reanalyzed with DLS. After AMF exposure, there was no change in particle size indicating that any local phase change is reversible and does not induce agglomeration.

The heating profiles of the cubosomes loaded with iron oxide nanoparticles are displayed in **Figure A3.2**. The concentration selected (i.e., 2 mg/ml) corresponds to the concentrations used in the drug loading and release studies. At this concentration, there is a relatively low level of iron oxide present, and thus, it is not surprising that the heating profiles did not deviate from water in the coil. The measured temperature rise is attributed to the radiant heat from the induction source copper coil. Despite no temperature rise, we predict the local nanoscale heating of the nanoparticles are capable of influencing the surrounding cubosomes.

A3.3.2 Drug Loading and Release

Based on the DSC results, the GMO-GMS 75:25 0.5wt% iron oxide nanoparticle was selected for the preliminary drug loading and release study. The release profile of F-lysozyme is displayed in **Figure A3.3** at temperatures above and below the predicted phase transition temperature. Both samples display a burst type of release over the first hour. This could be attributed to unincorporated lysozyme diffusing through bicontinous matrix.
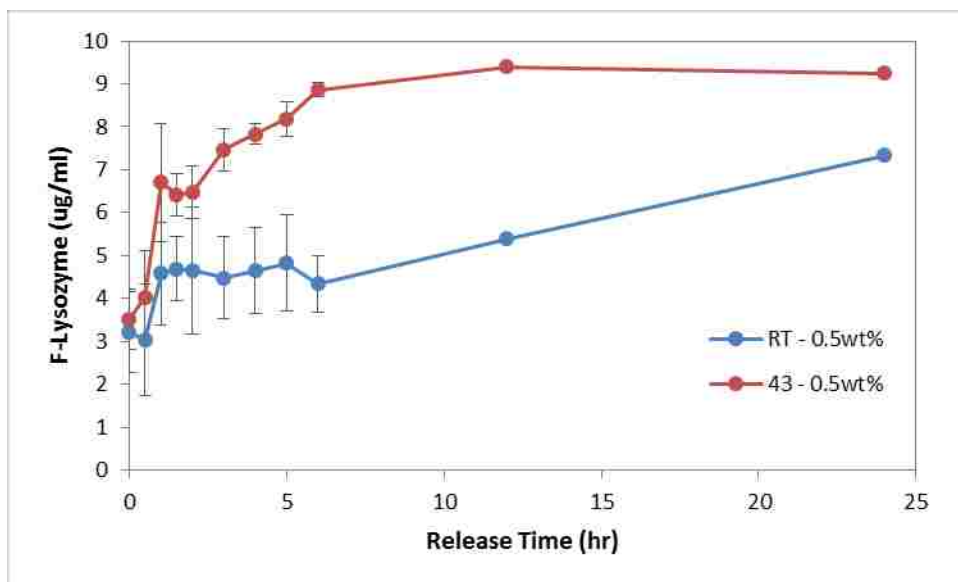
Figure A3.3. Release profile of lysozyme from GMO-GMS 0.5wt% iron oxide cubosomes over 24 hours at room temperature (RT) or 43 °C water bath. For the first 6 hours n = 3 and error is reported as standard deviation. 12 and 24 hour time points are n = 1.
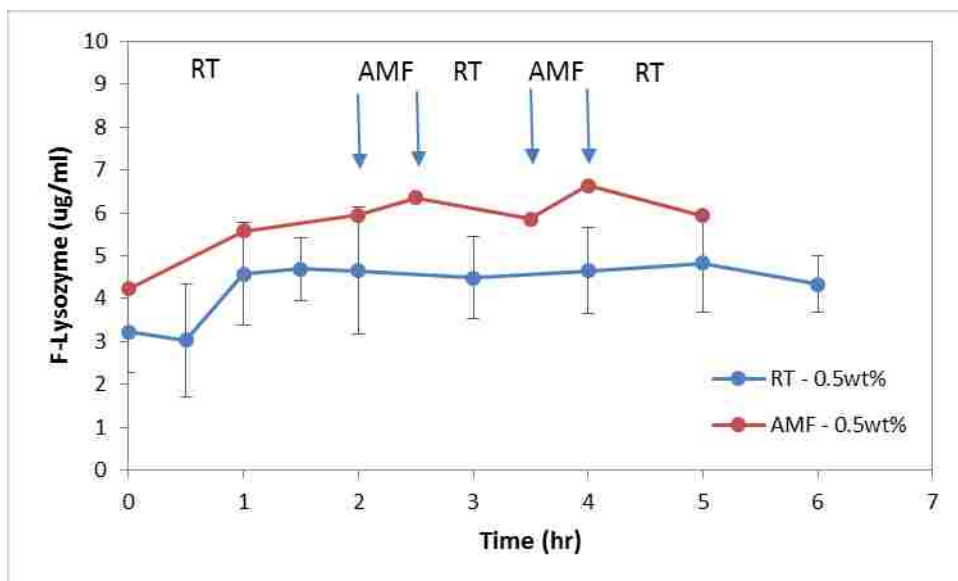
Figure A3.4. AMF-triggered release profile. GMO-GMS 75:25 0.5wt% iron oxide was held at room temperature for 2 hours before being exposed to two cycles of 30 minutes AMF and 60 minutes returned to room temperature.

After the first hour, the release profile at room temperature remains relatively constant for the next 5 hours before the slow diffusion of the drug becomes measureable over 24 hours. At 43 °C, above the phase transition temperature, the release profile continues rapidly until 6 hours where it plateaus over the next 18 hours. The maximum lysozyme release measured was around 9.5 µg/ml. Considering the initial loading density was 1wt%, the theoretical max would be 20 µg/ml resulting in nearly 50% released over 24 hours.

To test the ability of iron oxide triggering the drug release, an exploratory sample underwent two cycles of 30 minute AMF exposure followed by 1 hour at room temperature. The measured release profile is displayed in **Figure A3.4** with the room temperature release profile included for reference. With AMF exposure there appears to be a 0.5-0.6 µg/ml spike in lysozyme release compared to the previous time point. However, after 1 hour, the lysozyme release returns to the statistical range of room temperature release. If there had there been an actual spike in release, one would expect to see the prototypical stair-step profile of pulsatile release. Future work is warranted to investigate systems with a higher iron oxide nanoparticle loading density.

A3.4. Conclusion

This study presents preliminary work attempted to develop composite GMO-GMS cubosomes for the controlled release of therapeutics. Building off our previous work, we looked to translate binary blends of monoglyceride thermo-responsive material from the bulk to nanoscale. Initial characterizations indicated melting and crystallization temperatures which should correspond well for biological use. The release profile of a model drug, lysozyme, demonstrated promising results of distinct differences below and above the materials melting point. However, when AMF triggered release was attempted,

there was negligible increases in drug release. While future work should investigate higher loading densities, ideally the system would operate in the nanoscale heating regime – where the energy output is sufficient to modify the surrounding chemistry but the bulk solution temperature remains constant.

A3.5. References

References are located at the end of the dissertation subdivided by chapters.

References

Chapter 2: Polymeric Coatings and Additives on Nanoparticles for Biomedical Applications

[1] Schaertl W. Current directions in core-shell nanoparticle design. Nanoscale 2010;2:829-43.

[2] Berry CC. Progress in functionalization of magnetic nanoparticles for applications in biomedicine. J Phys D-Appl Phys 2009;42:9.

[3] Gupta AK, Gupta M. Synthesis and surface engineering of iron oxide nanoparticles for biomedical applications. Biomaterials 2005;26:3995-4021.

[4] Pankhurst QA, Thanh NKT, Jones SK, Dobson J. Progress in applications of magnetic nanoparticles in biomedicine. J Phys D-Appl Phys 2009;42:15.

[5] Prijic S, Sersa G. Magnetic nanoparticles as targeted delivery systems in oncology. Radiol Oncol 2011;45:1-16.

[6] Rosensweig RE. Heating magnetic fluid with alternating magnetic field. J Magn Magn Mater 2002;252:370-4.

[7] Daniel MC, Astruc D. Gold nanoparticles: Assembly, supramolecular chemistry, quantum-size-related properties, and applications toward biology, catalysis, and nanotechnology. Chemical Reviews 2004;104:293-346.

[8] Huang HC, Barua S, Sharma G, Dey SK, Rege K. Inorganic nanoparticles for cancer imaging and therapy. J Control Release 2011;155:344-57.

[9] Pyykko P. Theoretical chemistry of gold. Angew Chem-Int Edit 2004;43:4412-56.

[10] Khlebtsov N, Dykman L. Biodistribution and toxicity of engineered gold nanoparticles: a review of in vitro and in vivo studies. Chem Soc Rev 2011;40:1647-71.

[11] Hu M, Chen JY, Li ZY, Au L, Hartland GV, Li XD, et al. Gold nanostructures: engineering their plasmonic properties for biomedical applications. Chem Soc Rev 2006;35:1084-94.

[12] Slowing II, Vivero-Escoto JL, Wu C-W, Lin VSY. Mesoporous silica nanoparticles as controlled release drug delivery and gene transfection carriers. Adv Drug Deliv Rev 2008;60:1278-88.

[13] Vallet-Regi M, Balas F, Arcos D. Mesoporous materials for drug delivery. Angew Chem-Int Edit 2007;46:7548-58.

[14] Edmondson S, Osborne VL, Huck WTS. Polymer brushes via surface-initiated polymerizations. Chem Soc Rev 2004;33:14-22.

[15] Fan QL, Neoh KG, Kang ET, Shuter B, Wang SC. Solvent-free atom transfer radical polymerization for the preparation of poly(poly(ethyleneglycol) monomethacrylate)-grafted Fe_3O_4 nanoparticles: Synthesis, characterization and cellular uptake. Biomaterials 2007;28:5426-36.

[16] Pyun J, Matyjaszewski K. Synthesis of nanocomposite organic/inorganic hybrid materials using controlled/"living" radical polymerization. Chem Mat 2001;13:3436-48.

[17] Dong HC, Huang JY, Koepsel RR, Ye PL, Russell AJ, Matyjaszewski K. Recyclable Antibacterial Magnetic Nanoparticles Grafted with Quaternized Poly(2-(dimethylamino)ethyl methacrylate) Brushes. Biomacromolecules 2011;12:1305-11.

[18] Advincula RC. Surface initiated polymerization from nanoparticle surfaces. J Dispersion Sci Technol 2003;24:343-61.

[19] Barbey R, Lavanant L, Paripovic D, Schuwer N, Sugnaux C, Tugulu S, et al. Polymer Brushes via Surface-Initiated Controlled Radical Polymerization: Synthesis, Characterization, Properties, and Applications. Chemical Reviews 2009;109:5437-527.

[20] Radhakrishnan B, Ranjan R, Brittain WJ. Surface initiated polymerizations from silica nanoparticles. Soft Matter 2006;2:386-96.

[21] Goodwin JW. Colloids and Interfaces with Surfactants and Polymers - An Introduction. Chichester, UK: John Wiley & Sons, Ltd; 2004.

[22] Romero-Cano MS, Martin-Rodriguez A, de las Nieves FJ. Electrosteric stabilization of polymer colloids with different functionality. Langmuir 2001;17:3505-11.

[23] He YT, Wan JM, Tokunaga T. Kinetic stability of hematite nanoparticles: the effect of particle sizes. J Nanopart Res 2008;10:321-32.

[24] Kim T, Lee C-H, Joo S-W, Lee K. Kinetics of gold nanoparticle aggregation: Experiments and modeling. J Colloid Interface Sci 2008;318:238-43.

[25] Gref R, Domb A, Quellec P, Blunk T, Muller RH, Verbavatz JM, et al. THE CONTROLLED INTRAVENOUS DELIVERY OF DRUGS USING PEG-COATED STERICALLY STABILIZED NANOSPHERES. Adv Drug Deliv Rev 1995;16:215-33.

[26] Golas PL, Louie S, Lowry GV, Matyjaszewski K, Tilton RD. Comparative Study of Polymeric Stabilizers for Magnetite Nanoparticles Using ATRP. Langmuir 2010;26:16890-900.

[27] Xiao K, Li Y, Luo J, Lee JS, Xiao W, Gonik AM, et al. The effect of surface charge on in vivo biodistribution of PEG-oligocholic acid based micellar nanoparticles. Biomaterials 2011;32:3435-46.

[28] Kim M, Jung J, Lee J, Na K, Park S, Hyun J. Amphiphilic comblike polymers enhance the colloidal stability of Fe3O4 nanoparticles. Colloid Surf B-Biointerfaces 2010;76:236-40.

[29] Zhang GD, Yang Z, Lu W, Zhang R, Huang Q, Tian M, et al. Influence of anchoring ligands and particle size on the colloidal stability and in vivo biodistribution of polyethylene glycol-coated gold nanoparticles in tumor-xenografted mice. Biomaterials 2009;30:1928-36.

[30] Lewinski N, Colvin V, Drezek R. Cytotoxicity of nanoparticles. Small 2008;4:26-49.

[31] Peppas NA, Hilt JZ, Khademhosseini A, Langer R. Hydrogels in biology and medicine: From molecular principles to bionanotechnology. Adv Mater 2006;18:1345-60.

[32] Otsuka H, Nagasaki Y, Kataoka K. PEGylated nanoparticles for biological and pharmaceutical applications. Adv Drug Deliv Rev 2003;55:403-19.

[33] Gupta AK, Curtis ASG. Surface modified superparamagnetic nanoparticles for drug delivery: Interaction studies with human fibroblasts in culture. J Mater Sci-Mater Med 2004;15:493-6.

[34] Gupta AK, Wells S. Surface-modified superparamagnetic nanoparticles for drug delivery: Preparation, characterization, and cytotoxicity studies. IEEE Trans Nanobiosci 2004;3:66-73.

[35] Hu FX, Neoh KG, Cen L, Kang ET. Cellular response to magnetic nanoparticles "PEGylated" via surface-initiated atom transfer radical polymerization. Biomacromolecules 2006;7:809-16.

[36] Rayavarapu RG, Petersen W, Hartsuiker L, Chin P, Janssen H, van Leeuwen FWB, et al. In vitro toxicity studies of polymer-coated gold nanorods. Nanotechnology 2010;21:10.

[37] Petri-Fink A, Chastellain M, Juillerat-Jeanneret L, Ferrari A, Hofmann H. Development of functionalized superparamagnetic iron oxide nanoparticles for interaction with human cancer cells. Biomaterials 2005;26:2685-94.

[38] Hao R, Xing RJ, Xu ZC, Hou YL, Gao S, Sun SH. Synthesis, Functionalization, and Biomedical Applications of Multifunctional Magnetic Nanoparticles. Adv Mater 2010;22:2729-42.

[39] Wotschadlo J, Liebert T, Heinze T, Wagner K, Schnabelrauch M, Dutz S, et al. Magnetic nanoparticles coated with carboxymethylated polysaccharide shells-Interaction with human cells. J Magn Magn Mater 2009;321:1469-73.

[40] Lemarchand C, Gref R, Passirani C, Garcion E, Petri B, Muller R, et al. Influence of polysaccharide coating on the interactions of nanoparticles with biological systems. Biomaterials 2006;27:108-18.

[41] Wang YXJ, Hussain SM, Krestin GP. Superparamagnetic iron oxide contrast agents: physicochemical characteristics and applications in MR imaging. Eur Radiol 2001;11:2319-31.

[42] Creixell M, Herrera AP, Latorre-Esteves M, Ayala V, Torres-Lugo M, Rinaldi C. The effect of grafting method on the colloidal stability and in vitro cytotoxicity of carboxymethyl dextran coated magnetic nanoparticles. J Mater Chem 2010;20:8539-47.

[43] Gupta AK, Gupta M. Cytotoxicity suppression and cellular uptake enhancement of surface modified magnetic nanoparticles. Biomaterials 2005;26:1565-73.

[44] Tan WB, Zhang Y. Surface modification of gold and quantum dot nanoparticles with chitosan for bioapplications. J Biomed Mater Res Part A 2005;75A:56-62.

[45] Bhattarai SR, Remant BKC, Aryal S, Bhattarai N, Kim SY, Yi HK, et al. Hydrophobically modified chitosan/gold nanoparticles for DNA delivery. J Nanopart Res 2008;10:151-62.

[46] Yoo JW, Chambers E, Mitragotri S. Factors that Control the Circulation Time of Nanoparticles in Blood: Challenges, Solutions and Future Prospects. Curr Pharm Design 2010;16:2298-307.

[47] Alexis F, Pridgen E, Molnar LK, Farokhzad OC. Factors affecting the clearance and biodistribution of polymeric nanoparticles. Mol Pharm 2008;5:505-15.

[48] De la Fuente JM, Penades S. Glyconanoparticles: Types, synthesis and applications in glycoscience, biomedicine and material science. Biochim Biophys Acta-Gen Subj 2006;1760:636-51.

[49] Sunderland CJ, Steiert M, Talmadge JE, Derfus AM, Barry SE. Targeted nanoparticles for detecting and treating cancer. Drug Development Research 2006;67:70-93.

[50] Byrne JD, Betancourt T, Brannon-Peppas L. Active targeting schemes for nanoparticle systems in cancer therapeutics. Adv Drug Deliv Rev 2008;60:1615-26.

[51] Islam T, Josephson L. Current state and future applications of active targeting in malignancies using superparamagnetic iron oxide nanoparticles. Cancer Biomark 2009;5:99-107.

[52] Mahon E, Salvati A, Bombelli FB, Lynch I, Dawson KA. Designing the nanoparticle-biomolecule interface for "targeting and therapeutic delivery". J Control Release 2012;161:164-74.

[53] Muro S. Challenges in design and characterization of ligand-targeted drug delivery systems. J Control Release 2012;164:125-37.

[54] Yang SJ, Lin FH, Tsai KC, Wei MF, Tsai HM, Wong JM, et al. Folic Acid-Conjugated Chitosan Nanoparticles Enhanced Protoporphyrin IX Accumulation in Colorectal Cancer Cells. Bioconjugate Chem 2010;21:679-89.

[55] Bhattacharya D, Das M, Mishra D, Banerjee I, Sahu SK, Maiti TK, et al. Folate receptor targeted, carboxymethyl chitosan functionalized iron oxide nanoparticles: a novel ultradispersed nanoconjugates for bimodal imaging. Nanoscale 2011;3:1653-62.

[56] Moros M, Pelaz B, Lopez-Larrubia P, Garcia-Martin ML, Grazu V, de la Fuente JM. Engineering biofunctional magnetic nanoparticles for biotechnological applications. Nanoscale 2010;2:1746-55.

[57] Xiong F, Zhu Z-y, Xiong C, Hua X-q, Shan X-h, Zhang Y, et al. Preparation, Characterization of 2-Deoxy-D-Glucose Functionalized Dimercaptosuccinic Acid-Coated Maghemite Nanoparticles for Targeting Tumor Cells. Pharm Res 2012;29:1087-97.

[58] Zhuang H, Sinha P, Pourdehnad M, Duarte PS, Yamamoto AJ, Alavi A. The role of positron emission tomography with fluorine-18-deoxyglucose in identifying colorectal cancer metastases to liver. Nucl Med Commun 2000;21:793-8.

[59] Laskin JJ, Sandier AB. Epidermal growth factor receptor: a promising target in solid tumours. Cancer Treat Rev 2004;30:1-17.

[60] Creixell M, Bohorquez AC, Torres-Lugo M, Rinaldi C. EGFR-Targeted Magnetic Nanoparticle Heaters Kill Cancer Cells without a Perceptible Temperature Rise. ACS Nano 2011;5:7124-9.

[61] Kievit FM, Stephen ZR, Veiseh O, Arami H, Wang T, Lai VP, et al. Targeting of Primary Breast Cancers and Metastases in a Transgenic Mouse Model Using Rationally Designed Multifunctional SPIONs. ACS Nano 2012;6:2591-601.

[62] Kruse AM, Meenach SA, Anderson KW, Hilt JZ. Synthesis and characterization of CREKA-conjugated iron oxide nanoparticles for hyperthermia applications. Acta Biomaterialia 2014;10:2622-9.

[63] Wei QS, Ji J, Shen JC. Synthesis of near-infrared responsive gold nanorod/PNIPAAm core/shell nanohybrids via surface initiated ATRP for smart drug delivery. Macromol Rapid Commun 2008;29:645-50.

[64] Purushotham S, Chang PEJ, Rumpel H, Kee IHC, Ng RTH, Chow PKH, et al. Thermoresponsive core-shell magnetic nanoparticles for combined modalities of cancer therapy. Nanotechnology 2009;20:11.

[65] Purushotham S, Ramanujan RV. Modeling the performance of magnetic nanoparticles in multimodal cancer therapy. J Appl Phys 2010;107:9.

[66] Purushotham S, Ramanujan RV. Thermoresponsive magnetic composite nanomaterials for multimodal cancer therapy. Acta Biomaterialia 2010;6:502-10.

[67] Hayashi K, Ono K, Suzuki H, Sawada M, Moriya M, Sakamoto W, et al. High-Frequency, Magnetic-Field-Responsive Drug Release from Magnetic Nanoparticle/Organic Hybrid Based on Hyperthermic Effect. ACS Appl Mater Interfaces 2010;2:1903-11.

[68] Yallapu MM, Maher DM, Sundram V, Bell MC, Jaggi M, Chauhan SC. Curcumin induces chemo/radio-sensitization in ovarian cancer cells and curcumin nanoparticles inhibit ovarian cancer cell growth. J Ovarian Res 2010;3:12.

[69] Slowing II, Trewyn BG, Giri S, Lin VSY. Mesoporous silica nanoparticles for drug delivery and biosensing applications. Adv Funct Mater 2007;17:1225-36.

[70] Hong CY, Li X, Pan CY. Smart core-shell nanostructure with a mesoporous core and a stimuli-responsive nanoshell synthesized via surface reversible addition-fragmentation chain transfer polymerization. J Phys Chem C 2008;112:15320-4.

Chapter 3: Magnetic Nanoparticle Mediated Energy Delivery for Cancer Therapy

[1] Frimpong RA, Hilt JZ. Magnetic nanoparticles in biomedicine: synthesis, functionalization and applications. Nanomedicine 2010;5:1401-14.

[2] Berry CC. Progress in functionalization of magnetic nanoparticles for applications in biomedicine. Journal of Physics D-Applied Physics 2009;42:9.

[3] Ito A, Shinkai M, Honda H, Kobayashi T. Medical application of functionalized magnetic nanoparticles. Journal of Bioscience and Bioengineering 2005;100:1-11.

[4] Sun C, Lee JSH, Zhang MQ. Magnetic nanoparticles in MR imaging and drug delivery. Advanced Drug Delivery Reviews 2008;60:1252-65.

[5] Moroz P, Jones SK, Gray BN. Magnetically mediated hyperthermia: current status and future directions. International Journal of Hyperthermia 2002;18:267-84.

[6] Kittel C. Introduction to solid state physics. 8th ed. Hoboken, NJ: John Wiley & Sons; 2005.

[7] Dutz S, Hergt R. Magnetic nanoparticle heating and heat transfer on a microscale: basic principles, realities and physical limitations of hyperthermia for tumour therapy. International Journal of Hyperthermia 2013;29:790-800.

[8] Hergt R, Dutz S. Magnetic particle hyperthermia—biophysical limitations of a visionary tumour therapy. Journal of Magnetism and Magnetic Materials 2007;311:187-92.

[9] Heider F, Dunlop DJ, Sugiura N. Magnetic properties of hydrothermally recrystallized magnetite crystals. Science 1987;236:1287-90.

[10] Krishnan KM. Biomedical Nanomagnetics: A Spin Through Possibilities in Imaging, Diagnostics, and Therapy. Ieee Transactions on Magnetics 2010;46:2523-58.

[11] Purushotham S, Ramanujan RV. Modeling the performance of magnetic nanoparticles in multimodal cancer therapy. Journal of Applied Physics 2010;107:9.

[12] Rosensweig RE. Heating magnetic fluid with alternating magnetic field. Journal of Magnetism and Magnetic Materials 2002;252:370-4.

[13] Falk MH, Issels RD. Hyperthermia in oncology. International Journal of Hyperthermia 2001;17:1-18.

[14] Issels RD. Hyperthermia adds to chemotherapy. European Journal of Cancer 2008;44:2546-54.

[15] Wust P, Hildebrandt B, Sreenivasa G, Rau B, Gellermann J, Riess H, et al. Hyperthermia in combined treatment of cancer. Lancet Oncology 2002;3:487-97.

[16] Wust P, Gneveckow U, Johannsen M, Bohmer D, Henkel T, Kahmann F, et al. Magnetic nanoparticles for interstitial thermotherapy - feasibility, tolerance and achieved temperatures. International Journal of Hyperthermia 2006;22:673-85.

[17] Hildebrandt B, Wust P, Ahlers O, Dieing A, Sreenivasa G, Kerner T, et al. The cellular and molecular basis of hyperthermia. Critical Reviews in Oncology Hematology 2002;43:33-56.

[18] Jordan A, Scholz R, Wust P, Fahling H, Felix R. Magnetic fluid hyperthermia (MFH): Cancer treatment with AC magnetic field induced excitation of biocompatible superparamagnetic nanoparticles. Journal of Magnetism and Magnetic Materials 1999;201:413-9.

[19] Hilger I, Andra W, Hergt R, Hiergeist R, Schubert H, Kaiser WA. Electromagnetic heating of breast tumors in interventional radiology: In vitro and in vivo studies in human cadavers and mice. Radiology 2001;218:570-5.

[20] Silva AC, Oliveira TR, Mamani JB, Malheiros S, Malavolta L, Pavon LF, et al. Application of hyperthermia induced by superparamagnetic iron oxide nanoparticles in glioma treatment. Int J Nanomedicine 2011;6:591-603.

[21] Thiesen B, Jordan A. Clinical applications of magnetic nanoparticles for hyperthermia. International Journal of Hyperthermia 2008;24:467-74.

[22] Minev BR. Cancer Management in Man: Chemotherapy, Biological Therapy, Hyperthermia and Supporting Measures: Chemotherapy, Biological Therapy, Hyperthermia and Supporting Measures: Springer Science & Business Media; 2011.

[23] Torres-Lugo M, Rinaldi C. Thermal potentiation of chemotherapy by magnetic nanoparticles. Nanomedicine 2013;8:1689-707.

[24] Hao R, Xing RJ, Xu ZC, Hou YL, Gao S, Sun SH. Synthesis, Functionalization, and Biomedical Applications of Multifunctional Magnetic Nanoparticles. Advanced Materials 2010;22:2729-42.

[25] Prijic S, Sersa G. Magnetic nanoparticles as targeted delivery systems in oncology. Radiology and Oncology 2011;45:1-16.

[26] Zhou LL, Yuan JY, Wei Y. Core-shell structural iron oxide hybrid nanoparticles: from controlled synthesis to biomedical applications. Journal of Materials Chemistry 2011;21:2823-40.

[27] Lee SM, Park H, Yoo KH. Synergistic Cancer Therapeutic Effects of Locally Delivered Drug and Heat Using Multifunctional Nanoparticles. Advanced Materials 2010;22:4049-53.

[28] Purushotham S, Chang PEJ, Rumpel H, Kee IHC, Ng RTH, Chow PKH, et al. Thermoresponsive core-shell magnetic nanoparticles for combined modalities of cancer therapy. Nanotechnology 2009;20:11.

[29] Hayashi K, Ono K, Suzuki H, Sawada M, Moriya M, Sakamoto W, et al. High-Frequency, Magnetic-Field-Responsive Drug Release from Magnetic Nanoparticle/Organic Hybrid Based on Hyperthermic Effect. Acs Applied Materials & Interfaces 2010;2:1903-11.

[30] Babincova M, Altanerova V, Altaner C, Bergemann C, Babinec P. In vitro analysis of cisplatin functionalized magnetic nanoparticles in combined cancer chemotherapy and electromagnetic hyperthermia. Ieee Transactions on Nanobioscience 2008;7:15-9.

[31] Valeriote F, Lin H. SYNERGISTIC INTERACTION OF ANTICANCER AGENTS - CELLULAR PERSPECTIVE. Cancer Chemotherapy Reports Part 1 1975;59:895-900.

[32] Meenach SA, Shapiro JM, Hilt JZ, Anderson KW. Characterization of PEG–iron oxide hydrogel nanocomposites for dual hyperthermia and paclitaxel delivery. Journal of Biomaterials Science, Polymer Edition 2012;24:1112-26.

[33] Kruse AM, Meenach SA, Anderson KW, Hilt JZ. Synthesis and characterization of CREKA-conjugated iron oxide nanoparticles for hyperthermia applications. Acta Biomaterialia 2014;10:2622-9.

[34] Jordan A, Scholz R, Maier-Hauff K, van Landeghem FKH, Waldoefner N, Teichgraeber U, et al. The effect of thermotherapy using magnetic nanoparticles on rat malignant glioma. Journal of Neuro-Oncology 2006;78:7-14.

[35] Johannsen M, Jordan A, Scholz R, Koch M, Lein M, Deger S, et al. Evaluation of magnetic fluid hyperthermia in a standard rat model of prostate cancer. Journal of Endourology 2004;18:495-500.

[36] Iyer AK, Khaled G, Fang J, Maeda H. Exploiting the enhanced permeability and retention effect for tumor targeting. Drug Discovery Today 2006;11:812-8.

[37] Yang LL, Mao H, Wang YA, Cao ZH, Peng XH, Wang XX, et al. Single Chain Epidermal Growth Factor Receptor Antibody Conjugated Nanoparticles for in vivo Tumor Targeting and Imaging. Small 2009;5:235-43.

[38] Gordon RT, Hines JR, Gordon D. INTRACELLULAR HYPERTHERMIA - BIOPHYSICAL APPROACH TO CANCER-TREATMENT VIA INTRACELLULAR TEMPERATURE AND BIOPHYSICAL ALTERATIONS. Medical Hypotheses 1979;5:83-102.

[39] De la Fuente JM, Penades S. Glyconanoparticles: Types, synthesis and applications in glycoscience, biomedicine and material science. Biochimica Et Biophysica Acta-General Subjects 2006;1760:636-51.

[40] Sunderland CJ, Steiert M, Talmadge JE, Derfus AM, Barry SE. Targeted nanoparticles for detecting and treating cancer. Drug Development Research 2006;67:70-93.

[41] Byrne JD, Betancourt T, Brannon-Peppas L. Active targeting schemes for nanoparticle systems in cancer therapeutics. Advanced Drug Delivery Reviews 2008;60:1615-26.

[42] Islam T, Josephson L. Current state and future applications of active targeting in malignancies using superparamagnetic iron oxide nanoparticles. Cancer Biomarkers 2009;5:99-107.

[43] Mahon E, Salvati A, Bombelli FB, Lynch I, Dawson KA. Designing the nanoparticle-biomolecule interface for "targeting and therapeutic delivery". Journal of Controlled Release 2012;161:164-74.

[44] Muro S. Challenges in design and characterization of ligand-targeted drug delivery systems. Journal of Controlled Release 2012;164:125-37.

[45] McCarthy JR, Weissleder R. Multifunctional magnetic nanoparticles for targeted imaging and therapy. Advanced Drug Delivery Reviews 2008;60:1241-51.

[46] Xie J, Lee S, Chen XY. Nanoparticle-based theranostic agents. Advanced Drug Delivery Reviews 2010;62:1064-79.

[47] Kelkar SS, Reineke TM. Theranostics: Combining Imaging and Therapy. Bioconjugate Chemistry 2011;22:1879-903.

[48] Jordan A, Wust P, Scholz R, Tesche B, Fahling H, Mitrovics T, et al. Cellular uptake of magnetic fluid particles and their effects on human adenocarcinoma cells exposed to AC magnetic fields in vitro. International Journal of Hyperthermia 1996;12:705-22.

[49] Amorino GP, Fox MH. Effects of hyperthermia on intracellular chloride. Journal of Membrane Biology 1996;152:217-22.

[50] Kalambur VS, Longmire EK, Bischof JC. Cellular level loading and heating of superparamagnetic iron oxide nanoparticles. Langmuir 2007;23:12329-36.

[51] Jordan A, Scholz R, Wust P, Schirra H, Schiestel T, Schmidt H, et al. Endocytosis of dextran and silan-coated magnetite nanoparticles and the effect of intracellular hyperthermia on human mammary carcinoma cells in vitro. Journal of Magnetism and Magnetic Materials 1999;194:185-96.

[52] Fortin JP, Gazeau F, Wilhelm C. Intracellular heating of living cells through Neel relaxation of magnetic nanoparticles. European Biophysics Journal with Biophysics Letters 2008;37:223-8.

[53] Sharifi I, Shokrollahi H, Amiri S. Ferrite-based magnetic nanofluids used in hyperthermia applications. Journal of Magnetism and Magnetic Materials 2012;324:903-15.

[54] Brazel CS. Magnetothermally-responsive Nanomaterials: Combining Magnetic Nanostructures and Thermally-Sensitive Polymers for Triggered Drug Release. Pharmaceutical Research 2009;26:644-56.

[55] Rabin Y. Is intracellular hyperthermia superior to extracellular hyperthermia in the thermal sense? International Journal of Hyperthermia 2002;18:194-202.

[56] Creixell M, Bohorquez AC, Torres-Lugo M, Rinaldi C. EGFR-Targeted Magnetic Nanoparticle Heaters Kill Cancer Cells without a Perceptible Temperature Rise. ACS nano 2011;5:7124-9.

[57] Kievit FM, Stephen ZR, Veiseh O, Arami H, Wang T, Lai VP, et al. Targeting of Primary Breast Cancers and Metastases in a Transgenic Mouse Model Using Rationally Designed Multifunctional SPIONs. ACS nano 2012;6:2591-601.

[58] Kozissnik B, Bohorquez AC, Dobson J, Rinaldi C. Magnetic fluid hyperthermia: Advances, challenges, and opportunity. International Journal of Hyperthermia 2013;29:706-14.

[59] Huang H, Delikanli S, Zeng H, Ferkey DM, Pralle A. Remote control of ion channels and neurons through magnetic-field heating of nanoparticles. Nature Nanotechnology 2010;5:602-6.

[60] Polo-Corrales L, Rinaldi C. Monitoring iron oxide nanoparticle surface temperature in an alternating magnetic field using thermoresponsive fluorescent polymers. Journal of Applied Physics 2012;111:3.

[61] Amstad E, Kohlbrecher J, Muller E, Schweizer T, Textor M, Reimhult E. Triggered Release from Liposomes through Magnetic Actuation of Iron Oxide Nanoparticle Containing Membranes. Nano Letters 2011;11:1664-70.

[62] Cho MH, Lee EJ, Son M, Lee JH, Yoo D, Kim JW, et al. A magnetic switch for the control of cell death signalling in in vitro and in vivo systems. Nature Materials 2012;11:1038-43.

[63] Mannix RJ, Kumar S, Cassiola F, Montoya-Zavala M, Feinstein E, Prentiss M, et al. Nanomagnetic actuation of receptor-mediated signal transduction. Nature Nanotechnology 2008;3:36-40.

[64] Hughes S, El Haj AJ, Dobson J. Magnetic micro- and nanoparticle mediated activation of mechanosensitive ion channels. Medical Engineering & Physics 2005;27:754-62.

[65] Johansson AC, Appelqvist H, Nilsson C, Kagedal K, Roberg K, Ollinger K. Regulation of apoptosis-associated lysosomal membrane permeabilization. Apoptosis 2010;15:527-40.

[66] Erdal H, Berndtsson M, Castro J, Brunk U, Shoshan MC, Linder S. Induction of lysosomal membrane permeabilization by compounds that activate p53-independent apoptosis. Proceedings of the National Academy of Sciences of the United States of America 2005;102:192-7.

[67] Kirkegaard T, Jaattela M. Lysosomal involvement in cell death and cancer. Biochimica Et Biophysica Acta-Molecular Cell Research 2009;1793:746-54.

[68] Jaattela M. Multiple cell death pathways as regulators of tumour initiation and progression. Oncogene 2004;23:2746-56.

[69] Creixell M, Herrera AP, Ayala V, Latorre-Esteves M, Perez-Torres M, Torres-Lugo M, et al. Preparation of epidermal growth factor (EGF) conjugated iron oxide nanoparticles and their internalization into colon cancer cells. Journal of Magnetism and Magnetic Materials 2010;322:2244-50.

[70] Domenech M, Marrero-Berrios I, Torres-Lugo M, Rinaldi C. Lysosomal Membrane Permeabilization by Targeted Magnetic Nanoparticles in Alternating Magnetic Fields. ACS nano 2013;7:5091-101.

[71] Zhang EM, Kircher MF, Koch M, Eliasson L, Goldberg SN, Renstrom E. Dynamic Magnetic Fields Remote-Control Apoptosis via Nanoparticle Rotation. ACS nano 2014;8:3192-201.

[72] Sanchez C, El Hajj Diab D, Connord V, Clerc P, Meunier E, Pipy B, et al. Targeting a G-protein-coupled receptor overexpressed in endocrine tumors by magnetic nanoparticles to induce cell death. ACS nano 2014;8:1350-63.

[73] Connord V, Clerc P, Hallali N, El Hajj Diab D, Fourmy D, Gigoux V, et al. Real-Time Analysis of Magnetic Hyperthermia Experiments on Living Cells under a Confocal Microscope. Small 2015:n/a-n/a.

[74] Wang B, Yin JJ, Zhou XY, Kurash I, Chai ZF, Zhao YL, et al. Physicochemical Origin for Free Radical Generation of Iron Oxide Nanoparticles in Biomicroenvironment: Catalytic Activities Mediated by Surface Chemical States. Journal of Physical Chemistry C 2013;117:383-92.

[75] Singh N, Manshian B, Jenkins GJS, Griffiths SM, Williams PM, Maffeis TGG, et al. NanoGenotoxicology: The DNA damaging potential of engineered nanomaterials. Biomaterials 2009;30:3891-914.

[76] Naqvi S, Samim M, Abdin MZ, Ahmed FJ, Maitra AN, Prashant CK, et al. Concentration-dependent toxicity of iron oxide nanoparticles mediated by increased oxidative stress. International Journal of Nanomedicine 2010;5:983-9.

[77] Mahmoudi M, Hofmann H, Rothen-Rutishauser B, Petri-Fink A. Assessing the In Vitro and In Vivo Toxicity of Superparamagnetic Iron Oxide Nanoparticles. Chemical Reviews 2012;112:2323-38.

[78] Cochran DB, Wattamwar PP, Wydra R, Hilt JZ, Anderson KW, Eitel RE, et al. Suppressing iron oxide nanoparticle toxicity by vascular targeted antioxidant polymer nanoparticles. Biomaterials 2013;34:9615-22.

[79] Voinov MA, Pagan JOS, Morrison E, Smirnova TI, Smirnov AI. Surface-Mediated Production of Hydroxyl Radicals as a Mechanism of Iron Oxide Nanoparticle Biotoxicity. Journal of the American Chemical Society 2011;133:35-41.

[80] Klein S, Sommer A, Distel LVR, Neuhuber W, Kryschi C. Superparamagnetic iron oxide nanoparticles as radiosensitizer via enhanced reactive oxygen species formation. Biochemical and Biophysical Research Communications 2012;425:393-7.

[81] Valko M, Rhodes CJ, Moncol J, Izakovic M, Mazur M. Free radicals, metals and antioxidants in oxidative stress-induced cancer. Chemico-Biological Interactions 2006;160:1-40.

[82] Joshi-Barr S, Lux CD, Mahmoud E, Almutairi A. Exploiting Oxidative Microenvironments in the Body as Triggers for Drug Delivery Systems. Antioxidants & Redox Signaling 2014;21:730-54.

[83] Schieber M, Chandel NS. ROS Function in Redox Signaling and Oxidative Stress. Current Biology 2014;24:R453-R62.

[84] Malvindi MA, De Matteis V, Galeone A, Brunetti V, Anyfantis GC, Athanassiou A, et al. Toxicity Assessment of Silica Coated Iron Oxide Nanoparticles and Biocompatibility Improvement by Surface Engineering. Plos One 2014;9.

[85] Wydra RJ, Oliver CE, Anderson KW, Dziubla TD, Hilt JZ. Accelerated generation of free radicals by iron oxide nanoparticles in the presence of an alternating magnetic field. RSC Adv 2015;5:18888-93.

[86] Ito A, Honda H, Kobayashi T. Cancer immunotherapy based on intracellular hyperthermia using magnetite nanoparticles: a novel concept of "heat-controlled necrosis" with heat shock protein expression. Cancer Immunology Immunotherapy 2006;55:320-8.

Chapter 4: Synthesis and Characterization of PEG-Iron Oxide Core-shell Composite

Nanoparticles for Thermal Therapy

[1] Berry CC. Progress in functionalization of magnetic nanoparticles for applications in biomedicine. J Phys D-Appl Phys 2009;42:9.

[2] Gupta AK, Gupta M. Synthesis and surface engineering of iron oxide nanoparticles for biomedical applications. Biomaterials 2005;26:3995-4021.

[3] Pankhurst QA, Thanh NKT, Jones SK, Dobson J. Progress in applications of magnetic nanoparticles in biomedicine. J Phys D-Appl Phys 2009;42:15.

[4] Frimpong RA, Hilt JZ. Magnetic nanoparticles in biomedicine: synthesis, functionalization and applications. Nanomedicine 2010;5:1401-14.

[5] Rosensweig RE. Heating magnetic fluid with alternating magnetic field. J Magn Magn Mater 2002;252:370-4.

[6] Fortin JP, Gazeau F, Wilhelm C. Intracellular heating of living cells through Neel relaxation of magnetic nanoparticles. European Biophysics Journal with Biophysics Letters 2008;37:223-8.

[7] Hergt R, Dutz S, Muller R, Zeisberger M. Magnetic particle hyperthermia: nanoparticle magnetism and materials development for cancer therapy. Journal of Physics-Condensed Matter 2006;18:S2919-S34.

[8] Hilger I, Dietmar E, Linss W, Streck S, Kaiser WA. Developments for the minimally invasive treatment of tumours by targeted magnetic heating. Journal of Physics-Condensed Matter 2006;18:S2951-S8.

[9] Gupta AK, Wells S. Surface-modified superparamagnetic nanoparticles for drug delivery: Preparation, characterization, and cytotoxicity studies. IEEE Trans Nanobiosci 2004;3:66-73.

[10] Majewski P, Thierry B. Functionalized magnetite nanoparticles - Synthesis, properties, and bio-applications. Crit Rev Solid State Mat Sci 2007;32:203-15.

[11] Zhou LL, Yuan JY, Wei Y. Core-shell structural iron oxide hybrid nanoparticles: from controlled synthesis to biomedical applications. J Mater Chem 2011;21:2823-40.

[12] Laurent S, Forge D, Port M, Roch A, Robic C, Elst LV, et al. Magnetic iron oxide nanoparticles: Synthesis, stabilization, vectorization, physicochemical characterizations, and biological applications. Chemical Reviews 2008;108:2064-110.

[13] Hao R, Xing RJ, Xu ZC, Hou YL, Gao S, Sun SH. Synthesis, Functionalization, and Biomedical Applications of Multifunctional Magnetic Nanoparticles. Adv Mater 2010;22:2729-42.

[14] Peppas NA, Hilt JZ, Khademhosseini A, Langer R. Hydrogels in biology and medicine: From molecular principles to bionanotechnology. Adv Mater 2006;18:1345-60.

[15] Pyun J, Matyjaszewski K. Synthesis of nanocomposite organic/inorganic hybrid materials using controlled/"living" radical polymerization. Chem Mat 2001;13:3436-48.

[16] Frimpong RA, Hilt JZ. Poly(n-isopropylacrylamide)-based hydrogel coatings on magnetite nanoparticles via atom transfer radical polymerization. Nanotechnology 2008;19.

[17] Xu FJ, Neoh KG, Kang ET. Bioactive surfaces and biomaterials via atom transfer radical polymerization. Prog Polym Sci 2009;34:719-61.

[18] Neoh KG, Kang ET. Functionalization of inorganic nanoparticles with polymers for stealth biomedical applications. Polymer Chemistry 2011;2:747-59.

[19] Oh JK, Park JM. Iron oxide-based superparamagnetic polymeric nanomaterials: Design, preparation, and biomedical application. Prog Polym Sci 2011;36:168-89.

[20] Hu FX, Neoh KG, Cen L, Kang ET. Cellular response to magnetic nanoparticles "PEGylated" via surface-initiated atom transfer radical polymerization. Biomacromolecules 2006;7:809-16.

[21] Fan QL, Neoh KG, Kang ET, Shuter B, Wang SC. Solvent-free atom transfer radical polymerization for the preparation of poly(poly(ethyleneglycol) monomethacrylate)-grafted Fe3O4 nanoparticles: Synthesis, characterization and cellular uptake. Biomaterials 2007;28:5426-36.

[22] Zhou Y, Wang SX, Ding BJ, Yang ZM. Modification of magnetite nanoparticles via surface-initiated atom transfer radical polymerization (ATRP). Chem Eng J 2008;138:578-85.

[23] Miles WC, Goff JD, Huffstetler PP, Reinholz CM, Pothayee N, Caba BL, et al. Synthesis and Colloidal Properties of Polyether-Magnetite Complexes in Water and Phosphate-Buffered Saline. Langmuir 2009;25:803-13.

[24] Miles WC, Huffstetler PP, Goff JD, Chen AY, Riffle JS, Davis RM. Design of Stable Polyether-Magnetite Complexes in Aqueous Media: Effects of the Anchor Group, Molecular Weight, and Chain Density. Langmuir 2011;27:5456-63.

[25] Issels RD. Hyperthermia adds to chemotherapy. European Journal of Cancer 2008;44:2546-54.

[26] Ito A, Honda H, Kobayashi T. Cancer immunotherapy based on intracellular hyperthermia using magnetite nanoparticles: a novel concept of "heat-controlled necrosis" with heat shock protein expression. Cancer Immunol Immunother 2006;55:320-8.

[27] Wust P, Gneveckow U, Johannsen M, Bohmer D, Henkel T, Kahmann F, et al. Magnetic nanoparticles for interstitial thermotherapy - feasibility, tolerance and achieved temperatures. Int J Hyperthermia 2006;22:673-85.

[28] Falk MH, Issels RD. Hyperthermia in oncology. Int J Hyperthermia 2001;17:1-18.

[29] Hildebrandt B, Wust P, Ahlers O, Dieing A, Sreenivasa G, Kerner T, et al. The cellular and molecular basis of hyperthermia. Critical Reviews in Oncology Hematology 2002;43:33-56.

[30] Wust P, Hildebrandt B, Sreenivasa G, Rau B, Gellermann J, Riess H, et al. Hyperthermia in combined treatment of cancer. Lancet Oncology 2002;3:487-97.

[31] Jordan A, Scholz R, Wust P, Fahling H, Felix R. Magnetic fluid hyperthermia (MFH): Cancer treatment with AC magnetic field induced excitation of biocompatible superparamagnetic nanoparticles. J Magn Magn Mater 1999;201:413-9.

[32] Hilger I, Andra W, Hergt R, Hiergeist R, Schubert H, Kaiser WA. Electromagnetic heating of breast tumors in interventional radiology: In vitro and in vivo studies in human cadavers and mice. Radiology 2001;218:570-5.

[33] Moroz P, Jones SK, Gray BN. Magnetically mediated hyperthermia: current status and future directions. Int J Hyperthermia 2002;18:267-84.

[34] Rodriguez-Luccioni HL, Latorre-Esteves M, Mendez-Vega J, Soto O, Rodriguez AR, Rinaldi C, et al. Enhanced reduction in cell viability by hyperthermia induced by magnetic nanoparticles. Int J Nanomed 2011;6:373-80.

[35] Frimpong RA, Dou J, Pechan M, Hilt JZ. Enhancing remote controlled heating characteristics in hydrophilic magnetite nanoparticles via facile co-precipitation. J Magn Magn Mater 2010;322:326-31.

[36] Yallapu MM, Othman SF, Curtis ET, Gupta BK, Jaggi M, Chauhan SC. Multi-functional magnetic nanoparticles for magnetic resonance imaging and cancer therapy. Biomaterials 2011;32:1890-905.

[37] Meenach SA, Hilt JZ, Anderson KW. Poly(ethylene glycol)-based magnetic hydrogel nanocomposites for hyperthermia cancer therapy. Acta Biomaterialia 2010;6:1039-46.

Chapter 5: Accelerated Generation of Free Radicals by Iron Oxide Nanoparticles in the Presence of an Alternating Magnetic Field

[1] Frimpong RA, Hilt JZ. Magnetic nanoparticles in biomedicine: synthesis, functionalization and applications. Nanomedicine 2010;5:1401-14.

[2] Berry CC. Progress in functionalization of magnetic nanoparticles for applications in biomedicine. J Phys D-Appl Phys 2009;42:9.

[3] Dhakshinamoorthy A, Navalon S, Alvaro M, Garcia H. Metal Nanoparticles as Heterogeneous Fenton Catalysts. ChemSusChem 2012;5:46-64.

[4] Krishnan KM. Biomedical Nanomagnetics: A Spin Through Possibilities in Imaging, Diagnostics, and Therapy. IEEE Trans Magn 2010;46:2523-58.

[5] McCormack PL. Ferumoxytol In Iron Deficiency Anaemia in Adults With Chronic Kidney Disease. Drugs 2012;72:2013-22.

[6] Yallapu MM, Othman SF, Curtis ET, Gupta BK, Jaggi M, Chauhan SC. Multi-functional magnetic nanoparticles for magnetic resonance imaging and cancer therapy. Biomaterials 2011;32:1890-905.

[7] Wydra RJ, Kruse AM, Bae Y, Anderson KW, Hilt JZ. Synthesis and characterization of PEG-iron oxide core-shell composite nanoparticles for thermal therapy. Mater Sci Eng C-Mater Biol Appl 2013;33:4660-6.

[8] Hilger I, Dietmar E, Linss W, Streck S, Kaiser WA. Developments for the minimally invasive treatment of tumours by targeted magnetic heating. Journal of Physics-Condensed Matter 2006;18:S2951-S8.

[9] Ursachi I, Stancu A, Vasile A. Magnetic alpha-Fe2O3/MCM-41 nanocomposites: Preparation, characterization, and catalytic activity for methylene blue degradation. J Colloid Interface Sci 2012;377:184-90.

[10] Cochran DB, Wattamwar PP, Wydra R, Hilt JZ, Anderson KW, Eitel RE, et al. Suppressing iron oxide nanoparticle toxicity by vascular targeted antioxidant polymer nanoparticles. Biomaterials 2013;34:9615-22.

[11] Naqvi S, Samim M, Abdin MZ, Ahmed FJ, Maitra AN, Prashant CK, et al. Concentration-dependent toxicity of iron oxide nanoparticles mediated by increased oxidative stress. Int J Nanomed 2010;5:983-9.

[12] Stroh A, Zimmer C, Gutzeit C, Jakstadt M, Marschinke F, Jung T, et al. Iron oxide particles for molecular magnetic resonance imaging cause transient oxidative stress in rat macrophages. Free Radic Biol Med 2004;36:976-84.

[13] Malvindi MA, De Matteis V, Galeone A, Brunetti V, Anyfantis GC, Athanassiou A, et al. Toxicity Assessment of Silica Coated Iron Oxide Nanoparticles and Biocompatibility Improvement by Surface Engineering. PLoS One 2014;9.

[14] Mahmoudi M, Hofmann H, Rothen-Rutishauser B, Petri-Fink A. Assessing the In Vitro and In Vivo Toxicity of Superparamagnetic Iron Oxide Nanoparticles. Chemical Reviews 2012;112:2323-38.

[15] van den Bos EJ, Wagner A, Mahrholdt H, Thompson RB, Morimoto Y, Sutton BS, et al. Improved efficacy of stem cell labeling for magnetic resonance imaging studies by the use of cationic liposomes. Cell Transplant 2003;12:743-56.

[16] Yu M, Huang SH, Yu KJ, Clyne AM. Dextran and Polymer Polyethylene Glycol (PEG) Coating Reduce Both 5 and 30 nm Iron Oxide Nanoparticle Cytotoxicity in 2D and 3D Cell Culture. Int J Mol Sci 2012;13:5554-70.

[17] Pignatello JJ, Oliveros E, MacKay A. Advanced oxidation processes for organic contaminant destruction based on the Fenton reaction and related chemistry. Crit Rev Environ Sci Technol 2006;36:1-84.

[18] Voinov MA, Pagan JOS, Morrison E, Smirnova TI, Smirnov AI. Surface-Mediated Production of Hydroxyl Radicals as a Mechanism of Iron Oxide Nanoparticle Biotoxicity. J Am Chem Soc 2011;133:35-41.

[19] Wang B, Yin JJ, Zhou XY, Kurash I, Chai ZF, Zhao YL, et al. Physicochemical Origin for Free Radical Generation of Iron Oxide Nanoparticles in Biomicroenvironment: Catalytic Activities Mediated by Surface Chemical States. J Phys Chem C 2013;117:383-92.

[20] Rosensweig RE. Heating magnetic fluid with alternating magnetic field. J Magn Magn Mater 2002;252:370-4.

[21] Jordan A, Scholz R, Wust P, Fahling H, Felix R. Magnetic fluid hyperthermia (MFH): Cancer treatment with AC magnetic field induced excitation of biocompatible superparamagnetic nanoparticles. J Magn Magn Mater 1999;201:413-9.

[22] Moroz P, Jones SK, Gray BN. Magnetically mediated hyperthermia: current status and future directions. Int J Hyperthermia 2002;18:267-84.

[23] Rabin Y. Is intracellular hyperthermia superior to extracellular hyperthermia in the thermal sense? Int J Hyperthermia 2002;18:194-202.

[24] Creixell M, Bohorquez AC, Torres-Lugo M, Rinaldi C. EGFR-Targeted Magnetic Nanoparticle Heaters Kill Cancer Cells without a Perceptible Temperature Rise. ACS Nano 2011;5:7124-9.

[25] Polo-Corrales L, Rinaldi C. Monitoring iron oxide nanoparticle surface temperature in an alternating magnetic field using thermoresponsive fluorescent polymers. J Appl Phys 2012;111:3.

[26] Melgoza D, Hernandez-Ramirez A, Peralta-Hernandez JM. Comparative efficiencies of the decolourisation of Methylene Blue using Fenton's and photo-Fenton's reactions. Photochem Photobiol Sci 2009;8:596-9.

[27] Chan KH, Chu W. Modeling the reaction kinetics of Fenton's process on the removal of atrazine. Chemosphere 2003;51:305-11.

[28] Chu W, Chan KH, Kwan CY, Choi KY. Degradation of atrazine by modified stepwise-Fenton's processes. Chemosphere 2007;67:755-61.

[29] Zhang SX, Zhao XL, Niu HY, Shi YL, Cai YQ, Jiang GB. Superparamagnetic Fe3O4 nanoparticles as catalysts for the catalytic oxidation of phenolic and aniline compounds. J Hazard Mater 2009;167:560-6.

[30] Ghosh P, Kumar C, Samanta AN, Ray S. Comparison of a new immobilized Fe3+ catalyst with homogeneous Fe3+-H2O2 system for degradation of 2,4-dinitrophenol. Journal of Chemical Technology and Biotechnology 2012;87:914-23.

[31] Frimpong RA, Dou J, Pechan M, Hilt JZ. Enhancing remote controlled heating characteristics in hydrophilic magnetite nanoparticles via facile co-precipitation. J Magn Magn Mater 2010;322:326-31.

[32] de Souza WF, Guimaraes IR, Guerreiro MC, Oliveira LCA. Catalytic oxidation of sulfur and nitrogen compounds from diesel fuel. Appl Catal A-Gen 2009;360:205-9.

[33] Zhang J, Hu FT, Liu QQ, Zhao X, Liu SQ. Application of heterogenous catalyst of tris(1,10)-phenanthroline iron(II) loaded on zeolite for the photo-Fenton degradation of methylene blue. React Kinet Mech Catal 2011;103:299-310.

[34] Hsieh SC, Lin PY. FePt nanoparticles as heterogeneous Fenton-like catalysts for hydrogen peroxide decomposition and the decolorization of methylene blue. J Nanopart Res 2012;14.

[35] Shahwan T, Abu Sirriah S, Nairat M, Boyaci E, Eroglu AE, Scott TB, et al. Green synthesis of iron nanoparticles and their application as a Fenton-like catalyst for the degradation of aqueous cationic and anionic dyes. Chem Eng J 2011;172:258-66.

[36] Biswal SL, Gast AP. Micromixing with linked chains of paramagnetic particles. Anal Chem 2004;76:6448-55.

[37] Byrom J, Biswal SL. Magnetic field directed assembly of two-dimensional fractal colloidal aggregates. Soft Matter 2013;9:9167-73.

[38] Sharma G, Kodali V, Gaffrey M, Wang W, Minard KR, Karin NJ, et al. Iron oxide nanoparticle agglomeration influences dose rates and modulates oxidative stress-mediated dose-response profiles in vitro. Nanotoxicology 2014;8:663-75.

[39] Stone JR, Yang SP. Hydrogen peroxide: A signaling messenger. Antioxid Redox Signal 2006;8:243-70.

[40] Nogueira V, Park Y, Chen CC, Xu PZ, Chen ML, Tonic I, et al. Akt Determines Replicative Senescence and Oxidative or Oncogenic Premature Senescence and Sensitizes Cells to Oxidative Apoptosis. Cancer Cell 2008;14:458-70.

Chapter 6: The Role of ROS Generation from Magnetic Nanoparticles in an Alternating Magnetic Field on Cytotoxicity

[1] Frimpong RA, Hilt JZ. Magnetic nanoparticles in biomedicine: synthesis, functionalization and applications. Nanomedicine 2010;5:1401-14.

[2] Berry CC. Progress in functionalization of magnetic nanoparticles for applications in biomedicine. J Phys D-Appl Phys 2009;42:9.

[3] Ito A, Shinkai M, Honda H, Kobayashi T. Medical application of functionalized magnetic nanoparticles. J Biosci Bioeng 2005;100:1-11.

[4] Sun C, Lee JSH, Zhang MQ. Magnetic nanoparticles in MR imaging and drug delivery. Adv Drug Deliv Rev 2008;60:1252-65.

[5] Hilger I, Dietmar E, Linss W, Streck S, Kaiser WA. Developments for the minimally invasive treatment of tumours by targeted magnetic heating. Journal of Physics-Condensed Matter 2006;18:S2951-S8.

[6] Iyer AK, Khaled G, Fang J, Maeda H. Exploiting the enhanced permeability and retention effect for tumor targeting. Drug Discovery Today 2006;11:812-8.

[7] De la Fuente JM, Penades S. Glyconanoparticles: Types, synthesis and applications in glycoscience, biomedicine and material science. Biochim Biophys Acta-Gen Subj 2006;1760:636-51.

[8] Sunderland CJ, Steiert M, Talmadge JE, Derfus AM, Barry SE. Targeted nanoparticles for detecting and treating cancer. Drug Development Research 2006;67:70-93.

[9] Kruse AM, Meenach SA, Anderson KW, Hilt JZ. Synthesis and characterization of CREKA-conjugated iron oxide nanoparticles for hyperthermia applications. Acta Biomaterialia 2014;10:2622-9.

[10] Kievit FM, Stephen ZR, Veiseh O, Arami H, Wang T, Lai VP, et al. Targeting of Primary Breast Cancers and Metastases in a Transgenic Mouse Model Using Rationally Designed Multifunctional SPIONs. ACS Nano 2012;6:2591-601.

[11] Creixell M, Bohorquez AC, Torres-Lugo M, Rinaldi C. EGFR-Targeted Magnetic Nanoparticle Heaters Kill Cancer Cells without a Perceptible Temperature Rise. ACS Nano 2011;5:7124-9.

[12] Kozissnik B, Bohorquez AC, Dobson J, Rinaldi C. Magnetic fluid hyperthermia: Advances, challenges, and opportunity. Int J Hyperthermia 2013;29:706-14.

[13] Rabin Y. Is intracellular hyperthermia superior to extracellular hyperthermia in the thermal sense? Int J Hyperthermia 2002;18:194-202.

[14] Polo-Corrales L, Rinaldi C. Monitoring iron oxide nanoparticle surface temperature in an alternating magnetic field using thermoresponsive fluorescent polymers. J Appl Phys 2012;111:3.

[15] Voinov MA, Pagan JOS, Morrison E, Smirnova TI, Smirnov AI. Surface-Mediated Production of Hydroxyl Radicals as a Mechanism of Iron Oxide Nanoparticle Biotoxicity. J Am Chem Soc 2011;133:35-41.

[16] Cochran DB, Wattamwar PP, Wydra R, Hilt JZ, Anderson KW, Eitel RE, et al. Suppressing iron oxide nanoparticle toxicity by vascular targeted antioxidant polymer nanoparticles. Biomaterials 2013;34:9615-22.

[17] Naqvi S, Samim M, Abdin MZ, Ahmed FJ, Maitra AN, Prashant CK, et al. Concentration-dependent toxicity of iron oxide nanoparticles mediated by increased oxidative stress. Int J Nanomed 2010;5:983-9.

[18] Sadhukha T, Niu L, Wiedmann TS, Panyam J. Effective Elimination of Cancer Stem Cells by Magnetic Hyperthermia. Mol Pharm 2013;10:1432-41.

[19] Ghosh P, Kumar C, Samanta AN, Ray S. Comparison of a new immobilized Fe3+ catalyst with homogeneous Fe3+-H2O2 system for degradation of 2,4-dinitrophenol. Journal of Chemical Technology and Biotechnology 2012;87:914-23.

[20] Seton-Rogers S. CANCER STEM CELLS Survival skills. Nat Rev Cancer 2009;9:147-.

[21] Wydra RJ, Oliver CE, Anderson KW, Dziubla TD, Hilt JZ. Accelerated generation of free radicals by iron oxide nanoparticles in the presence of an alternating magnetic field. RSC Adv 2015;5:18888-93.

[22] Marradi M, Chiodo F, Garcia I, Penades S. Glyconanoparticles as multifunctional and multimodal carbohydrate systems. Chem Soc Rev 2013;42:4728-45.

[23] El-Boubbou K, Huang XF. Glyco-Nanomaterials: Translating Insights from the "Sugar-Code" to Biomedical Applications. Curr Med Chem 2011;18:2060-78.

[24] Li X, Bao MM, Weng YY, Yang K, Zhang WD, Chen GJ. Glycopolymer-coated iron oxide nanoparticles: shape-controlled synthesis and cellular uptake. J Mat Chem B 2014;2:5569-75.

[25] Li X, Zhou H, Yang L, Du G, Pai-Panandiker AS, Huang X, et al. Enhancement of cell recognition in vitro by dual-ligand cancer targeting gold nanoparticles. Biomaterials 2011;32:2540-5.

[26] Schmidtke C, Kreuziger AM, Alpers D, Jacobsen A, Leshch Y, Eggers R, et al. Glycoconjugated Amphiphilic Polymers via Click-Chemistry for the Encapsulation of Quantum Dots. Langmuir 2013;29:12593-600.

[27] Moros M, Pelaz B, Lopez-Larrubia P, Garcia-Martin ML, Grazu V, de la Fuente JM. Engineering biofunctional magnetic nanoparticles for biotechnological applications. Nanoscale 2010;2:1746-55.

[28] Shan XH, Hu H, Xiong F, Gu N, Geng XD, Zhu W, et al. Targeting Glut1-overexpressing MDA-MB-231 cells with 2-deoxy-d-g1ucose modified SPIOs. European Journal of Radiology 2012;81:95-9.

[29] Xiong F, Zhu Z-y, Xiong C, Hua X-q, Shan X-h, Zhang Y, et al. Preparation, Characterization of 2-Deoxy-D-Glucose Functionalized Dimercaptosuccinic Acid-Coated Maghemite Nanoparticles for Targeting Tumor Cells. Pharm Res 2012;29:1087-97.

[30] Geng F, Song K, Xing JZ, Yuan CZ, Yan S, Yang QF, et al. Thio-glucose bound gold nanoparticles enhance radio-cytotoxic targeting of ovarian cancer. Nanotechnology 2011;22.

[31] Zhuang H, Sinha P, Pourdehnad M, Duarte PS, Yamamoto AJ, Alavi A. The role of positron emission tomography with fluorine-18-deoxyglucose in identifying colorectal cancer metastases to liver. Nucl Med Commun 2000;21:793-8.

[32] Frimpong RA, Dou J, Pechan M, Hilt JZ. Enhancing remote controlled heating characteristics in hydrophilic magnetite nanoparticles via facile co-precipitation. J Magn Magn Mater 2010;322:326-31.

[33] Moros M, Hernaez B, Garet E, Dias JT, Saez B, Grazu V, et al. Monosaccharides versus PEG-Functionalized NPs: Influence in the Cellular Uptake. ACS Nano 2012;6:1565-77.

[34] Wang B, Yin JJ, Zhou XY, Kurash I, Chai ZF, Zhao YL, et al. Physicochemical Origin for Free Radical Generation of Iron Oxide Nanoparticles in Biomicroenvironment: Catalytic Activities Mediated by Surface Chemical States. J Phys Chem C 2013;117:383-92.

[35] Singh N, Manshian B, Jenkins GJS, Griffiths SM, Williams PM, Maffeis TGG, et al. NanoGenotoxicology: The DNA damaging potential of engineered nanomaterials. Biomaterials 2009;30:3891-914.

[36] Domenech M, Marrero-Berrios I, Torres-Lugo M, Rinaldi C. Lysosomal Membrane Permeabilization by Targeted Magnetic Nanoparticles in Alternating Magnetic Fields. ACS Nano 2013;7:5091-101.

[37] Zhang EM, Kircher MF, Koch M, Eliasson L, Goldberg SN, Renstrom E. Dynamic Magnetic Fields Remote-Control Apoptosis via Nanoparticle Rotation. ACS Nano 2014;8:3192-201.

[38] Klein S, Sommer A, Distel LVR, Neuhuber W, Kryschi C. Superparamagnetic iron oxide nanoparticles as radiosensitizer via enhanced reactive oxygen species formation. Biochem Biophys Res Commun 2012;425:393-7.

[39] Valko M, Rhodes CJ, Moncol J, Izakovic M, Mazur M. Free radicals, metals and antioxidants in oxidative stress-induced cancer. Chem-Biol Interact 2006;160:1-40.

[40] Joshi-Barr S, Lux CD, Mahmoud E, Almutairi A. Exploiting Oxidative Microenvironments in the Body as Triggers for Drug Delivery Systems. Antioxid Redox Signal 2014;21:730-54.

[41] Schieber M, Chandel NS. ROS Function in Redox Signaling and Oxidative Stress. Curr Biol 2014;24:R453-R62.

[42] Malvindi MA, De Matteis V, Galeone A, Brunetti V, Anyfantis GC, Athanassiou A, et al. Toxicity Assessment of Silica Coated Iron Oxide Nanoparticles and Biocompatibility Improvement by Surface Engineering. PLoS One 2014;9.

[43] Keblinski P, Cahill DG, Bodapati A, Sullivan CR, Taton TA. Limits of localized heating by electromagnetically excited nanoparticles. J Appl Phys 2006;100.

[44] Huang H, Delikanli S, Zeng H, Ferkey DM, Pralle A. Remote control of ion channels and neurons through magnetic-field heating of nanoparticles. Nat Nanotechnol 2010;5:602-6.

[45] Amstad E, Kohlbrecher J, Muller E, Schweizer T, Textor M, Reimhult E. Triggered Release from Liposomes through Magnetic Actuation of Iron Oxide Nanoparticle Containing Membranes. Nano Lett 2011;11:1664-70.

[46] Persson HL. Iron-dependent lysosomal destabilization initiates silica-induced apoptosis in murine macrophages. Toxicol Lett 2005;159:124-33.

[47] Johansson AC, Appelqvist H, Nilsson C, Kagedal K, Roberg K, Ollinger K. Regulation of apoptosis-associated lysosomal membrane permeabilization. Apoptosis 2010;15:527-40.

[48] Persson HL. Radiation-induced lysosomal iron reactivity: Implications for radioprotective therapy. IUBMB Life 2006;58:395-401.

[49] Yu M, Huang SH, Yu KJ, Clyne AM. Dextran and Polymer Polyethylene Glycol (PEG) Coating Reduce Both 5 and 30 nm Iron Oxide Nanoparticle Cytotoxicity in 2D and 3D Cell Culture. Int J Mol Sci 2012;13:5554-70.

Chapter 7: Synthesis and Characterization of Magnetic Nanoparticles with

Biodegradable Polymer Coatings for the Treatment of Cancer

[1] Frimpong RA, Hilt JZ. Magnetic nanoparticles in biomedicine: synthesis, functionalization and applications. Nanomedicine 2010;5:1401-14.

[2] Berry CC. Progress in functionalization of magnetic nanoparticles for applications in biomedicine. Journal of Physics D-Applied Physics 2009;42:9.

[3] Ito A, Shinkai M, Honda H, Kobayashi T. Medical application of functionalized magnetic nanoparticles. Journal of Bioscience and Bioengineering 2005;100:1-11.

[4] Sun C, Lee JSH, Zhang MQ. Magnetic nanoparticles in MR imaging and drug delivery. Advanced Drug Delivery Reviews 2008;60:1252-65.

[5] Iyer AK, Khaled G, Fang J, Maeda H. Exploiting the enhanced permeability and retention effect for tumor targeting. Drug Discovery Today 2006;11:812-8.

[6] De la Fuente JM, Penades S. Glyconanoparticles: Types, synthesis and applications in glycoscience, biomedicine and material science. Biochimica Et Biophysica Acta-General Subjects 2006;1760:636-51.

[7] Sunderland CJ, Steiert M, Talmadge JE, Derfus AM, Barry SE. Targeted nanoparticles for detecting and treating cancer. Drug Development Research 2006;67:70-93.

[8] Kruse AM, Meenach SA, Anderson KW, Hilt JZ. Synthesis and characterization of CREKA-conjugated iron oxide nanoparticles for hyperthermia applications. Acta Biomaterialia 2014;10:2622-9.

[9] Sanchez C, El Hajj Diab D, Connord V, Clerc P, Meunier E, Pipy B, et al. Targeting a G-protein-coupled receptor overexpressed in endocrine tumors by magnetic nanoparticles to induce cell death. ACS nano 2014;8:1350-63.

[10] Iovino N, Bohorquez AC, Rinaldi C. Magnetic nanoparticle targeting of lysosomes: a viable method of overcoming tumor resistance? Nanomedicine (London, England) 2014;9:937-9.

[11] Kozissnik B, Bohorquez AC, Dobson J, Rinaldi C. Magnetic fluid hyperthermia: Advances, challenges, and opportunity. International Journal of Hyperthermia 2013;29:706-14.

[12] Creixell M, Bohorquez AC, Torres-Lugo M, Rinaldi C. EGFR-Targeted Magnetic Nanoparticle Heaters Kill Cancer Cells without a Perceptible Temperature Rise. ACS nano 2011;5:7124-9.

[13] Polo-Corrales L, Rinaldi C. Monitoring iron oxide nanoparticle surface temperature in an alternating magnetic field using thermoresponsive fluorescent polymers. Journal of Applied Physics 2012;111:3.

[14] Domenech M, Marrero-Berrios I, Torres-Lugo M, Rinaldi C. Lysosomal Membrane Permeabilization by Targeted Magnetic Nanoparticles in Alternating Magnetic Fields. ACS nano 2013;7:5091-101.

[15] Zhang EM, Kircher MF, Koch M, Eliasson L, Goldberg SN, Renstrom E. Dynamic Magnetic Fields Remote-Control Apoptosis via Nanoparticle Rotation. ACS nano 2014;8:3192-201.

[16] Wydra RJ, Oliver CE, Anderson KW, Dziubla TD, Hilt JZ. Accelerated generation of free radicals by iron oxide nanoparticles in the presence of an alternating magnetic field. RSC Advances 2015;5:18888-93.

[17] Klein S, Sommer A, Distel LVR, Neuhuber W, Kryschi C. Superparamagnetic iron oxide nanoparticles as radiosensitizer via enhanced reactive oxygen species formation. Biochemical and Biophysical Research Communications 2012;425:393-7.

[18] Valko M, Rhodes CJ, Moncol J, Izakovic M, Mazur M. Free radicals, metals and antioxidants in oxidative stress-induced cancer. Chemico-Biological Interactions 2006;160:1-40.

[19] Joshi-Barr S, Lux CD, Mahmoud E, Almutairi A. Exploiting Oxidative Microenvironments in the Body as Triggers for Drug Delivery Systems. Antioxidants & Redox Signaling 2014;21:730-54.

[20] Wang B, Yin JJ, Zhou XY, Kurash I, Chai ZF, Zhao YL, et al. Physicochemical Origin for Free Radical Generation of Iron Oxide Nanoparticles in Biomicroenvironment: Catalytic Activities Mediated by Surface Chemical States. Journal of Physical Chemistry C 2013;117:383-92.

[21] Schieber M, Chandel NS. ROS Function in Redox Signaling and Oxidative Stress. Current Biology 2014;24:R453-R62.

[22] Wang B, Wang Y, Wu H, Song X, Guo X, Zhang D, et al. A mitochondria-targeted fluorescent probe based on TPP-conjugated carbon dots for both one- and two-photon fluorescence cell imaging. RSC Advances 2014;4:49960-3.

[23] Marrache S, Dhar S. Engineering of blended nanoparticle platform for delivery of mitochondria-acting therapeutics. Proceedings of the National Academy of Sciences 2012;109:16288-93.

[24] Foy SP, Labhasetwar V. Oh the irony: Iron as a cancer cause or cure? Biomaterials 2011;32:9155-8.

[25] Huang G, Chen H, Dong Y, Luo X, Yu H, Moore Z, et al. Superparamagnetic Iron Oxide Nanoparticles: Amplifying ROS Stress to Improve Anticancer Drug Efficacy. Theranostics 2013;3:116-26.

[26] Voinov MA, Pagan JOS, Morrison E, Smirnova TI, Smirnov AI. Surface-Mediated Production of Hydroxyl Radicals as a Mechanism of Iron Oxide Nanoparticle Biotoxicity. Journal of the American Chemical Society 2011;133:35-41.

[27] Hawkins AM, Puleo DA, Hilt JZ. Effect of macromer synthesis time on the properties of the resulting poly(β-amino ester) degradable hydrogel. Journal of Applied Polymer Science 2011;122:1420-6.

[28] Hawkins AM, Milbrandt TA, Puleo DA, Hilt JZ. Synthesis and analysis of degradation, mechanical and toxicity properties of poly(β-amino ester) degradable hydrogels. Acta Biomaterialia 2011;7:1956-64.

[29] Hawkins AM, Tolbert ME, Newton B, Milbrandt TA, Puleo DA, Hilt JZ. Tuning biodegradable hydrogel properties via synthesis procedure. Polymer 2013;54:4422-6.

[30] Fang C, Kievit FM, Veiseh O, Stephen ZR, Wang T, Lee D, et al. Fabrication of magnetic nanoparticles with controllable drug loading and release through a simple assembly approach. Journal of Controlled Release 2012;162:233-41.

[31] Peppas NA, Hilt JZ, Khademhosseini A, Langer R. Hydrogels in biology and medicine: From molecular principles to bionanotechnology. Advanced Materials 2006;18:1345-60.

[32] Frimpong RA, Dou J, Pechan M, Hilt JZ. Enhancing remote controlled heating characteristics in hydrophilic magnetite nanoparticles via facile co-precipitation. Journal of Magnetism and Magnetic Materials 2010;322:326-31.

[33] Anderson DG, Tweedie CA, Hossain N, Navarro SM, Brey DM, Van Vliet KJ, et al. A combinatorial library of photocrosslinkable and degradable materials. Advanced Materials 2006;18:2614-8.

[34] Wydra RJ, Kruse AM, Bae Y, Anderson KW, Hilt JZ. Synthesis and characterization of PEG-iron oxide core-shell composite nanoparticles for thermal therapy. Materials Science & Engineering C-Materials for Biological Applications 2013;33:4660-6.

[35] Galeotti F, Bertini F, Scavia G, Bolognesi A. A controlled approach to iron oxide nanoparticles functionalization for magnetic polymer brushes. Journal of Colloid and Interface Science 2011;360:540-7.

[36] Pereira MC, Oliveira LCA, Murad E. Iron oxide catalysts: Fenton and Fenton-like reactions--a review. Clay Materials 2012;47:285-302.

[37] Went P, Vasei M, Bubendorf L, Terracciano L, Tornillo L, Riede U, et al. Frequent high-level expression of the immunotherapeutic target Ep-CAM in colon, stomach, prostate and lung cancers. British Journal of Cancer 2006;94:128-35.

[38] Shigdar S, Lin J, Yu Y, Pastuovic M, Wei M, Duan W. RNA aptamer against a cancer stem cell marker epithelial cell adhesion molecule. Cancer Science 2011;102:991-8.

[39] de Boer CJ, Van Krieken J, Janssen-Van Rhijn CM, Litvinov SV. Expression of Ep-CAM in normal, regenerating, metaplastic, and neoplastic liver. Journal of Pathology 1999;188:201-6.

Appendix 1: Co-delivery of Heat Shock Protein 90 Inhibitors and Iron Oxide

Nanoparticle Induced Hyperthermia for Dual Cancer Therapy

[1] Wust P, Gneveckow U, Johannsen M, Bohmer D, Henkel T, Kahmann F, et al. Magnetic nanoparticles for interstitial thermotherapy - feasibility, tolerance and achieved temperatures. International Journal of Hyperthermia 2006;22:673-85.

[2] Falk MH, Issels RD. Hyperthermia in oncology. International Journal of Hyperthermia 2001;17:1-18.

[3] Wust P, Hildebrandt B, Sreenivasa G, Rau B, Gellermann J, Riess H, et al. Hyperthermia in combined treatment of cancer. Lancet Oncology 2002;3:487-97.

[4] Rosensweig RE. Heating magnetic fluid with alternating magnetic field. Journal of Magnetism and Magnetic Materials 2002;252:370-4.

[5] Fortin JP, Gazeau F, Wilhelm C. Intracellular heating of living cells through Neel relaxation of magnetic nanoparticles. European Biophysics Journal with Biophysics Letters 2008;37:223-8.

[6] Hergt R, Dutz S, Muller R, Zeisberger M. Magnetic particle hyperthermia: nanoparticle magnetism and materials development for cancer therapy. Journal of Physics-Condensed Matter 2006;18:S2919-S34.

[7] Hildebrandt B, Wust P, Ahlers O, Dieing A, Sreenivasa G, Kerner T, et al. The cellular and molecular basis of hyperthermia. Critical Reviews in Oncology Hematology 2002;43:33-56.

[8] Issels RD. Hyperthermia adds to chemotherapy. European Journal of Cancer 2008;44:2546-54.

[9] Lepock JR. How do cells respond to their thermal environment? International Journal of Hyperthermia 2005;21:681-7.

[10] Yavelsky V, Vais O, Piura B, Wolfson M, Rabinovich A, Fraifeld V. The role of Hsp90 in cell response to hyperthermia. Journal of Thermal Biology 2004;29:509-14.

[11] Schneider C, SeppLorenzino L, Nimmesgern E, Ouerfelli O, Danishefsky S, Rosen N, et al. Pharmacologic shifting of a balance between protein refolding and degradation mediated by Hsp90. Proceedings of the National Academy of Sciences of the United States of America 1996;93:14536-41.

[12] Stebbins CE, Russo AA, Schneider C, Rosen N, Hartl FU, Pavletich NP. Crystal structure of an Hsp90-geldanamycin complex: Targeting of a protein chaperone by an antitumor agent. Cell 1997;89:239-50.

[13] Pearl LH, Prodromou C, Workman P. The Hsp90 molecular chaperone: an open and shut case for treatment. Biochemical Journal 2008;410:439-53.

[14] Whitesell L, Lindquist SL. HSP90 and the chaperoning of cancer. Nature Reviews Cancer 2005;5:761-72.

[15] Ito A, Saito H, Mitobe K, Minamiya Y, Takahashi N, Maruyama K, et al. Inhibition of heat shock protein 90 sensitizes melanoma cells to thermosensitive ferromagnetic particle-mediated hyperthermia with low Curie temperature. Cancer Science 2009;100:558-64.

[16] Bae Y, Buresh RA, Williamson TP, Chen THH, Furgeson DY. Intelligent biosynthetic nanobiomaterials for hyperthermic combination chemotherapy and thermal drug targeting of HSP90 inhibitor geldanamycin. Journal of Controlled Release 2007;122:16-23.

[17] Frimpong RA, Dou J, Pechan M, Hilt JZ. Enhancing remote controlled heating characteristics in hydrophilic magnetite nanoparticles via facile co-precipitation. Journal of Magnetism and Magnetic Materials 2010;322:326-31.

[18] Wydra RJ, Kruse AM, Bae Y, Anderson KW, Hilt JZ. Synthesis and characterization of PEG-iron oxide core-shell composite nanoparticles for thermal therapy. Materials Science & Engineering C-Materials for Biological Applications 2013;33:4660-6.

[19] Meenach SA, Hilt JZ, Anderson KW. Poly(ethylene glycol)-based magnetic hydrogel nanocomposites for hyperthermia cancer therapy. Acta Biomaterialia 2010;6:1039-46.

[20] Kobayashi N, Toyooka S, Soh J, Yamamoto H, Dote H, Kawasaki K, et al. The anti-proliferative effect of heat shock protein 90 inhibitor, 17-DMAG, on non-small-cell lung cancers being resistant to EGFR tyrosine kinase inhibitor. Lung cancer 2012;75:161-6.

Appendix 2: Determining the Effects of Nanoparticle Agglomeration on the

Generation of Free Radicals in the Presence of an Alternating Magnetic Field

[1] Pereira MC, Oliveira LCA, Murad E. Iron oxide catalysts: Fenton and Fenton-like reactions--a review. Clay Materials 2012;47:285-302.

[2] Feng J, Hu X, Yue PL. Degradation of Azo-dye Orange II by a Photoassisted Fenton Reaction Using a Novel COmposite of Iron Oxide and Silicate Nanoparticles as a Catalyst. Industrial & Engineering Chemistry Research 2003;42:2058-66.

[3] Shahwan T, Sirriah SA, Nairat M, Boyaci E, Eroglu AE, Scott TB, et al. Green synthesis of iron nanoparticles and their application as a Fenton-like catalyst for the degradation of aqueous cationic and anionic dyes. Chemical Engineering Journal 2011;172:258-66.

[4] Garrido-Ramirez EG, Theng BKG, Mora ML. Clays and oxide minerals as catalysts and nanocatalysts in Fenton-like reactions--A review. Applied Clay Science 2010;47:182-92.

[5] Kotitz R, Weitschies W, Trahms L, Semmler W. Investigation of Brownian and Neel relaxation in magnetic fluids. Journal of Magnetism and Magnetic Materials 1999;201:102-4.

[6] Rabin Y. Is intracellular hyperthermia superior to extracellular hyperthermia in the thermal sense? International Journal of Hyperthermia 2002;18:194-202.

[7] Polo-Corrales L, Rinaldi C. Monitoring iron oxide nanoparticle surface temperature in an alternating magnetic field using thermoresponsive fluorescent polymers. Journal of Applied Physics 2012;111:3.

[8] Sharma G, Kodali V, Gaffrey M, Wang W, Minard KR, Karin NJ, et al. Iron oxide nanoparrticle agglomeration influences dose rates and modulates oxidative stress-mediated dose-response profiles in vitro. Nanotoxicology 2014;8:663-75.

[9] Frimpong RA, Dou J, Pechan M, Hilt JZ. Enhancing remote controlled heating characteristics in hydrophilic magnetite nanoparticles via facile co-precipitation. Journal of Magnetism and Magnetic Materials 2010;322:326-31.

Appendix 3: Composite GMO-GMS Cubosomes Loaded with Iron Oxide Nanoparticles for the Controlled Delivery of Therapeutics

[1] Frimpong RA, Hilt JZ. Magnetic nanoparticles in biomedicine: synthesis, functionalization and applications. Nanomedicine 2010;5:1401-14.

[2] Berry CC. Progress in functionalization of magnetic nanoparticles for applications in biomedicine. Journal of Physics D-Applied Physics 2009;42:9.

[3] Ito A, Shinkai M, Honda H, Kobayashi T. Medical application of functionalized magnetic nanoparticles. Journal of Bioscience and Bioengineering 2005;100:1-11.

[4] Sun C, Lee JSH, Zhang MQ. Magnetic nanoparticles in MR imaging and drug delivery. Advanced Drug Delivery Reviews 2008;60:1252-65.

[5] Mengesha AE, Wydra RJ, Hilt JZ, Bummer PM. Binary Blend of Glyceryl Monooleate and Glyceryl Monostearate for Magnetically Induced Thermo-Responsive Local Drug Delivery System. Pharmaceutical Research 2013;30:3214-24.

[6] Sato K. Crystallization behaviour of fats and lipids—a review. Chemical Engineering Science 2001;56:2255-65.

[7] Batte HD, Wright AJ, Rush JW, Idziak SH, Marangoni AG. Phase behavior, stability, and mesomorphism of monostearin–oil–water gels. Food Biophysics 2007;2:29-37.

[8] Mulet X, Boyd BJ, Drummond CJ. Advances in drug delivery and medical imaging using colloidal lyotropic liquid crystalline dispersions. Journal of Colloid and Interface Science 2013;393:1-20.

[9] Rizwan SB, Boyd BJ, Rades T, Hook S. Bicontinuous cubic liquid crystals as sustained delivery systems for peptides and proteins. Expert opinion on drug delivery 2010;7:1133-44.

[10] Barauskas J, Johnsson M, Joabsson F, Tiberg F. Cubic phase nanoparticles (cubosome): principles for controlling size, structure, and stability. Langmuir 2005;21:2569-77.

[11] Guo C, Wang J, Cao F, Lee RJ, Zhai G. Lyotropic liquid crystal systems in drug delivery. Drug Discovery Today 2010;15:1032-40.

[12] Fong WK, Hanley TL, Thierry B, Kirby N, Boyd BJ. Plasmonic Nanorods Provide Reversible Control over Nanostructure of Self-Assembled Drug Delivery Materials. Langmuir 2010;26:6136-9.

[13] Acharya DP, Moffat BA, Polyzos A, Waddington L, Coia G, Wright DK, et al. Cubic mesophase nanoparticles doped with superparamagnetic iron oxide nanoparticles: a new class of MRI contrast agent. Rsc Advances 2012;2:6655-62.

[14] Frimpong RA, Hilt JZ. Poly(n-isopropylacrylamide)-based hydrogel coatings on magnetite nanoparticles via atom transfer radical polymerization. Nanotechnology 2008;19.

[15] Takahashi D, Nishimoto E, Murase T, Yamashita S. Protein-protein interaction on lysozyme crystallization revealed by rotational diffusion analysis. Biophysical journal 2008;94:4484-92.

Robert John Wydra Vita

Personal Information:

Place of Birth: Park Ridge, Illinois, United States of America

Education:
Rice University, Houston, Texas, May 2009
B.S. Chemical Engineering with focus in Material Science

Research Positions:
NCI CNTC Research Fellow in Chemical Engineering
University of Kentucky, June 2012 to Present
Advisor: Dr. J. Zach Hilt, Associate Professor of Chemical Engineering
Clinical Mentor: Dr. B. Mark Evers, Professor and Vice Chair in the Department of Surgery

NSF IGERT Research Fellow in Chemical Engineering
University of Kentucky, November 2009 to June 2012
Advisor: Dr. J. Zach Hilt, Associate Professor of Chemical Engineering
Co-advisors: Dr. Kimberly W. Anderson, Gill Eminent Scholar Professor of Chemical Engineering and Dr. Younsoo Bae, Assistant Professor of Pharmaceutical Sciences

Undergraduate Researcher in Chemical and Biomolecular Engineering
Rice University, June 2007 to May 2009
Advisor: Dr. Sibani Lisa Biswal, Assistant Professor of Chemical and Biomolecular Engineering

NSF REU Researcher in Chemical and Biological Engineering
University of Colorado, June 2008 to August 2008
Advisor: Dr. Christopher N. Bowman, Patten Professor of Chemical and Biological Engineering
Mentor: Dr. Neil Cramer, Senior Research Associate

Publications:
1. Robert J. Wydra, Piotr Rychahou, B. Mark Evers, Kimberly W. Anderson, Thomas D. Dziubla, J. Zach Hilt. The Role of ROS Generation from Magnetic Nanoparticles in an Alternating Magnetic Field on Cytotoxicity. Acta Biomaterialia. (In Review).

2. Robert J. Wydra, Catherine E. Oliver, Kimberly W. Anderson, Thomas D. Dziubla, J. Zach Hilt. Accelerated Generation of Free Radicals by Iron Oxide Nanoparticles in the Presence of an Alternating Magnetic Field. RSC Advances. 2015. 5: 18888-18893, 2015.

3. Abebe E. Mengesha, Robert J. Wydra, J. Zach Hilt, Paul M. Bummer. Binary Blend of Glyceryl Monooleate and Glyceryl Monostearate for Magnetically Induced Thermo-

Responsive Local Drug Delivery System. Pharmaceutical Research, 30(12): 3214-3224, 2013.

4. Robert J. Wydra, Anastasia M. Kruse, Younsoo Bae, Kimberly W. Anderson, J. Zach Hilt. Synthesis and Characterization of PEG-Iron Oxide Core-Shell Nanoparticles for Thermal Therapy. Materials Science and Engineering C: Materials for Biological Applications, 33(8): 4660-4666, 2013.

5. David B. Cochran, Paritosh P. Wattamwar, Robert J. Wydra, J. Zach Hilt, Kimberly W. Anderson, Thomas D. Dziubla. Suppressing Iron Oxide Nanoparticle Toxicity by Vascular Targeted Antioxidant Nanoparticles. Biomaterials, 34(37): 9615-9622, 2013.

6. Daniel F. Scott, Yihwa Beabout, Robert J. Wydra, J. Zach Hilt, Younsoo Bae. Block Copolymer Cross-linked Nanoassemblies for Combination Delivery of Iron Oxide and Doxorubicin to Cancer Tumors. Journal of Applied Pharmaceutical Science, 3(6): 21-28, 2013.

7. Mo Dan, Daniel F. Scott, Peter A. Hardy, Robert J. Wydra, J. Zach Hilt, Robert A. Yokel, Younsoo Bae. Block Copolymer Cross-linked Nanoassemblies Improve Particle Stability and Biocompatibility of Superparamagnetic Iron Oxide Nanoparticles. Pharmaceutical Research, 30(2): 552-561, 2013.

8. Neil B. Cramer, Charles L. Couch, Kathleen M. Schreck, Jordan E. Boulden, Robert J. Wydra, Jeffery W. Stansbury, Chrisopher N. Bowman. Properties of methacrylate-thiol-ene formulations as dental restorative materials. Dental Materials, 26(8): 799-806, 2010.

Presentations (Presenter is first):
1. Robert J. Wydra, Younsoo Bae, Kimberly W. Anderson, J. Zach Hilt. Internalization pattern of functionalized magnetic nanoparticles and the prospects of intracellular hyperthermia. 2012 American Institute of Chemical Engineers Annual Meeting, Pittsburgh, PA, October 28 – November 2, 2012.

2. Robert J. Wydra, Sarah E. Seger, Younsoo Bae, Kimberly W. Anderson, J. Zach Hilt. Co-delivery of Heat Shock Protein 90 Inhibitors and Composite Iron Oxide Nanoparticle for Dual Cancer Therapy. SFB Biomaterials Day at the University of Kentucky, Lexington, KY, September 22, 2012.

3. Robert J. Wydra, Sarah E. Seger, Anastasia M. Kruse, Younsoo Bae, Kimberly W. Anderson, J. Zach Hilt. Synthesis and Characterization of PEG-Iron Oxide Core-shell Nanoparticles for Dual Hyperthermia and Chemotherapy Treatment of Cancer. 2011 American Institute of Chemical Engineers Annual Meeting, Minneapolis, MN, October 16-21, 2011.

4. Robert J. Wydra, Samantha A. Meenach, Kimberly W. Anderson, Younsoo Bae, J. Zach Hilt. Synthesis and Characterization of Polymer-Iron Oxide Composite

Nanoparticles for Medical Applications. 2010 American Institute of Chemical Engineers Annual Meeting, Salt Lake City, UT, November 7-12, 2010.

Posters (Presenter is first):

1. Robert J. Wydra, Kimberly W. Anderson, Thomas D. Dziubla, J. Zach Hilt. Accelerated Generation of Free Radicals by Iron Oxide Nanoparticles in the Presence of an Alternating Magnetic Field. 2014 American Institute of Chemical Engineers Annual Meeting, Atlanta, GA, November 18, 2014.

2. Helen Yao, Robert J. Wydra, Thomas D. Dziubla, Kimberly W. Anderson, J. Zach Hilt. Determining the Rate of ROS Generation from Composite Magnetic Nanoparticle Hydrogels in an Alternating Magnetic Field. 2014 American Institute of Chemical Engineers Student Meeting, Atlanta, GA, November 14-17, 2014.
   *Awarded 3rd Place Materials Engineering and Sciences Division

3. Catherine E. Oliver, Robert Wydra, Kim Anderson, J. Zach Hilt. Analyzing ROS Generation from Magnetic Nanoparticles in an Alternating Magnetic Field and its Role in Intracellular Hyperthermia. 2014 Biomedical Engineering Society, San Antonio, TX, October 22-25, 2014.

4. Robert J. Wydra, Kimberly W. Anderson, Thomas D. Dziubla, J. Zach Hilt. Accelerated Generation of Free Radicals by Iron Oxide Nanoparticles in the Presence of an Alternating Magnetic Field. SFB Biomaterials Day at the University of Kentucky, Lexington, KY, September 27, 2014.

5. Robert J. Wydra, Kimberly W. Anderson, J. Zach Hilt. Determining the Role of ROS Generation from Glucose Functionalized Magnetic Nanoparticles in an Alternating Magnetic Field on Intracellular Hyperthermia Toxicity. 2014 Markey Cancer Center Research Day, Lexington, KY, May 22, 2014.

6. Catherine E. Oliver, Robert Wydra, Kim Anderson, J. Zach Hilt. Analyzing ROS Generation from Magnetic Nanoparticles in an Alternating Magnetic Field and its Role in Intracellular Hyperthermia. 2013 American Institute of Chemical Engineers Student Meeting, San Francisco, CA, November 2-3, 2013.
   *Awarded 2nd Place Materials Engineering and Sciences Division III

7. Robert J. Wydra, Piotr Rychahou, B. Mark Evers, Kimberly W. Anderson, J. Zach Hilt. Internalization Pattern of Functionalized Magnetic Nanoparticles and the Prospect of Intracellular Hyperthermia. 2013 Markey Cancer Center Research Day, Lexington, KY, April 15, 2013.

8. Robert J. Wydra, Sarah E. Seger, Younsoo Bae, Kimberly W. Anderson, J. Zach Hilt. Co-delivery of Heat Shock Protein 90 Inhibitors and Composite Iron Oxide Nanoparticle for Dual Cancer Therapy. 2012 Markey Cancer Center Research Day, Lexington, KY, May 16, 2012.

9. Robert J. Wydra, Sarah E. Seger, Anastasia M. Kruse, Younsoo Bae, Kimberly W. Anderson, J. Zach Hilt. PEG-Iron Oxide Core-Shell Nanoparticles for Dual Cancer Therapy. SFB Biomaterials Day at Purdue University. West Lafayette, IN, October 29, 2011.

10. Robert J. Wydra, David S. Spencer, J. Zach Hilt. PEG-based Functionalization of Iron Oxide Nanoparticles Using the ISOFURE Methodology. 2011 American Institute of Chemical Engineers Annual Meeting, Minneapolis, MN, October 16-21, 2011.

11. Anastasia M. Kruse, Robert J. Wydra, J. Zach Hilt, Kimberly W. Anderson. Biocompatibility Analysis and Cancer Therapy Application of Core-Shell Composite Magnetic Nanoparticles. 2011 American Institute of Chemical Engineers Student Meeting, Minneapolis, MN, October 14-16, 2011.

12. Sarah E. Seger, Robert J. Wydra, Kimberly W. Anderson, J. Zach Hilt. In Vitro Sensitization of Cancer Cells to Hyperthermia via Hsp90 Inhibition. 2011 American Institute of Chemical Engineers Student Meeting, Minneapolis, MN, October 14-16, 2011.

13. Robert J. Wydra, Anastasia M. Kruse, Kimberly W. Anderson, Younsoo Bae, J. Zach Hilt. Synthesis and Characterization of PEG-Iron Oxide Core-Shell Nanoparticles for Cancer Applications. 2011 Society of Biomaterials Annual Meeting, Orlando, FL, April 13-16, 2011.

14. Robert J. Wydra, Anastasia M. Kruse, Younsoo Bae, Kimberly W. Anderson, J. Zach Hilt. Synthesis and Characterization of PEG-Iron Oxide Core-Shell Nanoparticles for Cancer Applications. 2011 Markey Cancer Center Research Day, Lexington, KY, March 22, 2011.

15. Anastasia M. Kruse, Robert J. Wydra, J. Zach Hilt, Kimberly W. Anderson. Biocompatibility Analysis and Cancer Therapy Application of Core-Shell Composite Magnetic Nanoparticles. 2010 American Institute of Chemical Engineers Student Meeting, Salt Lake City, UT, November 5-8, 2010.
    *Awarded 2nd Place Food, Pharmaceutical, and Biotechnology Division

16. Robert Wydra, Neil Cramer, Chipper Couch, Christopher Bowman. Methacrylate-Thiol-Ene Systems for Dental Applications. 2008 American Institute of Chemical Engineers Student Meeting, Philadelphia, PA, November 2008.